University of Nottingham
UK | CHINA | MALAYSIA

Encapsulation of metal complex into apoferritin for drug delivery and prodrug activation

Maria Letizia Cassioli

Thesis submitted to the University of Nottingham for the degree of Doctor of Philosophy

March 2022

“Never forget that until the day when God shall deign to reveal the future to man, all human wisdom is summed up in these two words, ‘Wait and hope’.”

A. Dumas, The Count of Montecristo

Acknowledgements

I would like to thank my supervisors: Dr Anca Pordea, Dr Tracey Bradshaw and Prof Neil Thomas. You have all been great mentors. I am grateful for the opportunity to have met and worked with you. I also want to express my heartfelt gratitude to Dr Lyudmila Turyanska, with whom I had the pleasure to work for my Master's thesis and this PhD project.

A particular thank you goes to all the members of the SPT group, past and present. All the help, advice and support received since my first day in the lab from each and every one of you has been essential to completing this thesis. A huge thank you goes to Elora, a great colleague who contributed to collecting the results reported in Chapter 4, Sections 4.2 and 4.3.

I would like to thank all the members of the apoferritin group, for their valuable help throughout this project.

I would also like to express my gratitude to all the technicians that have helped with my experimental work across the University: Steve, Rachael, Amy, Ben, Mike and Saul.

To all the friends I have made in these four years inside and outside the lab. You've enriched this experience with a lot of wonderful memories, which I will always cherish and remember with gratitude.

To conclude, I would like to thank the BBSRC and the University of Nottingham for sponsoring this PhD project.

Abstract

Cancer is one of the principal causes of mortality and the onset of new cases is estimated to increase from 19.3 million new cases in 2020 to 28.4 million by 2040 worldwide. Brain tumours represent a group of diseases characterised by high aggressiveness and poor prognosis. Glioblastoma represents 47% of cases and is currently treated with the anticancer agent temozolomide. This agent can induce tumour regression and promote patients' survival but is characterised by low specificity and premature conversion into its metabolites causing severe side effects. Recent research has focused on the improvement of the tumour-targeted delivery of drugs such as temozolomide for anticancer chemotherapy exploiting nanocapsules. The protein shell apoferritin is biocompatible, biodegradable, non-immunogenic and pH-responsive and can be preferentially internalised by tumour cells. These features make apoferritin an ideal nanocarrier. However, when small molecules like temozolomide are encapsulated within apoferritin, they can easily leak through the interprotein channels that connect the core of the nanocage with the external environment. This problem can lead to reduced nanoparticle uptake into the brain, consequent decrease in drug efficacy and higher probability of undesired toxicity.

This work aims to exploit the natural affinity of apoferritin for transition metals and their complexes, to improve the retention of temozolomide inside apoferritin when exposed to physiological environments. It was hypothesised that the loading of apoferritin with both Cu^{2+}-phenanthroline complex and temozolomide could promote the coordination of the metal and prevent the escape of the anticancer agent. Furthermore, Cu^{2+}-phenanthroline itself is the precursor of a family of anticancer compounds currently under clinical evaluation. Therefore, Cu^{2+}-phenanthroline has the potential to both prevent temozolomide leakage from apoferritin and contribute to the anticancer activity of the formulation. The work presented in this thesis evaluates the viability of this dual-drug delivery approach by using either horse spleen or human heavy chain apoferritin to achieve temozolomide delivery only in cancer cells and achieve enhanced anticancer activity. The metal affinity of the Apoferritin cage is essential to this approach. Horse spleen apoferritin is employed to evaluate the encapsulation of Cu^{2+}-phenanthroline using the nanoreactor method and its effect on temozolomide loading and retention. With human heavy chain apoferritin, site-specific covalent conjugation of the Cu^{2+}-phenanthroline complex has been undertaken before temozolomide encapsulation given the lower metal accumulation capacity of this apoferritin variant. The nano-formulations are characterised by UV-vis, high

resolution transmission electron microscopy (HRTEM), inductively coupled plasma mass spectrometry (ICP-MS), Ellman's assay, Matrix-assisted Laser Desorption/ionization Time of Flight (MALDI-TOF MS) and tested for *in vitro* anticancer activity by cell viability 3-(4,5-Dimethylthiazol-2-yl)-2,5-Diphenyltetrazolium Bromide (MTT) and clonogenic assays.

The encapsulation of Cu^{2+}-phenanthroline into horse spleen apoferritin led to the formation of different copper(II) species some of them organised into crystal patterns visible by HRTEM and stable for up to 4 months. Upon loading of 339 temozolomide molecules per cage by nanoreactor route, the nano-formulation was able to protect the drug from degradation but the introduction of the metal complex had no effect on drug retention. *In vitro* results reported enhanced cytotoxicity of the apoferritin encapsulated agents with a 30-fold decrease in GI_{50} for glioblastoma cell lines compared to temozolomide treatment. The covalent conjugation of Cu^{2+}-phenanthroline to human heavy chain apoferritin was challenging and robust confirmation of bioconjugation could not be achieved due the heterogeneity of the purified reaction mixtures. Consequently, no significant metal accumulation was observed even when 1,10-phenanthroline was detected. Temozolomide was entrapped within human apoferritin with encapsulation efficiency of 43 % of the total temozolomide added (moles) and drug loading of 12.9 % of the total nano-formulation weight (encapsulated drug and protein).

This work illustrates the potential of horse spleen apoferritin as an efficient drug delivery vehicle for the anticancer agent temozolomide, able to protect it from premature degradation and favour intracellular delivery. The anticancer activity of the metallodrug Cu^{2+}-phenanthroline showed promising results for the treatment of glioblastoma multiforme alone and in combination with temozolomide. However, this application would require functionalisation of the apoferritin cage for precise tumour targeting, given the *in vitro* toxicity caused by the metallodrug to non-tumour cells. In summary, although none of the nano-formulations studied resulted in improved temozolomide retention into apoferritin, this work provided additional evidence to support the use of this protein nanocage as a valuable drug delivery tool.

Table of contents

List of abbreviations and acronyms

5-FU	5-fluorouracil
Ac	Acetate
ADC	Antibody-drug conjugates
ADEPT	Antibody-directed enzyme prodrug therapy
AFt	Apoferritin
AIC	5-Aminoimidazole-4-carboxamide
AP-2	Adaptor complex 2
APS	Ammonium persulfate
ArM	Artificial metalloenzyme
bac	Bromoacetamidecaproyl
BBB	Blood brain barrier
BME	β-mercaptoethanol
BSA	Bovine serum albumin
CNTs	Carbon nanotubes
CO	Carbon monoxide
Cu(phen)	Copper-1,10-phenanthroline complex
CuAAC	Copper mediated alkyne-azide cycloaddition
DCM	Dichloromethane
DDS	Drug delivery system
DIPEA	N,N-Diisopropylethylamine
DLS	Dynamic light scattering
DL	Drug Loading
DNA	Deoxyribonucleic acid
dNTPs	Deoxynucleoside triphosphates
DPS	DNA-binding protein from starved-cells
ds	Double-strand
DTT	Dithiothreitol
EDTA	Ethylenediaminetetraacetic acid
EE	Encapsulation efficiency
EELS	Electron energy loss spectroscopy
EGFR	Epidermal growth factor receptor (HER1)
EMA	European Medicinal Agency
EPR	Enhanced permeability and retention effect
ESI-MS	Electrospray ionisation mass spectrometry
FBS	Foetal bovine serum

FDA	Food and drug administration
FMNH	Dihydroriboflavin 5'-phosphate flavin mononucleotide (reduced form)
FRET	Fluorescence (Förster) resonance energy transfer
Ft	Ferritin
GBM	Glioblastoma multiforme
GDEPT	Gene-directed enzyme prodrug therapy
GI50	Growth inhibition concentration 50 %
h	Hour(s)
HER2	Human Epidermal Growth Factor Receptor 2
His-tag	Hexahistidine tag
HRTEM	High resolution transmission electron microscopy
HSA	Human Serum Albumin
HSAFt	Horse spleen apoferritin
HSFt	Horse spleen ferritin
HSPG	Heparan sulfate proteoglycan
HuFt	Human ferritin
HuHAFt	Human heavy chain apoferritin
ICAM-1	Intercellular Adhesion Molecule 1
ICP-MS	Inductively coupled plasma mass spectrometry
IgG	Immunoglobulin
IMAC	Immobilised metal ion affinity chromatography
IPTG	Isopropyl β-*D*-1-thiogalactopyranoside
LB	Lysogeny broth
mAb	Monoclonal antibody
MALDI-TOF	Matrix assisted laser desorption ionisation-time of flight
mc	Maleimidocaproyl
MeCN	Acetonitrile
MeOH	Methanol
MGMT	O^6-methylguanine-DNA methyltransferase
min	Minute(s)

miRNA	Micro RNA
MMR	Mismatch repair machinery
MRI	Magnetic resonance imaging
MSNs	Mesoporous silica nanoparticles
MTIC	5-(3-methyltriazen-1-yl)imidazol-4-carboxamide
MTT	(3-(4,5-Dimethylthiazol-2-yl)-2,5-Diphenyltetrazolium Bromide)
MWCO	Molecular weight cut-off
NHS	N-hydroxysuccinimide
NMR	Nuclear magnetic resonance
NPs	Nanoparticles
OD (OD_{600})	Optical density (measured at 600 nm)
PBS	Phosphate buffer saline
PCR	Polymerase chain reaction
PEG	Polyethylene glycol
PLA	Poly(lactic acid)
PLGA	Poly(lactic-co-glycolide)
pnpa	*para*-nitrophenyl acetate
PTD	Photodynamic therapy
QDs	Quantum dots
RES	Reticuloendothelial system
rMeTIR	Reverse-templated interface redesign
ROS	Reactive oxygen species
rpm	Rotation per minute
SANS	Small-angle neutral scattering
SAXS	Synchrotron small-angle X-ray scattering
SCARA5	Scavenger receptor class A member 5
SDS PAGE	Sodium dodecyl sulfate-polyacrylamide gel electrophoresis
SeCT	Selective cell tagging therapy
siRNA	Small interfering RNA
SLNs	Solid-lipid nanoparticles
SMDCs	Small molecule-drug conjugates
SOC	Super optimal broth
SPIO	Small particle iron oxide

SPION	Super magnetic iron oxide nanoparticle
ss	Single-strand
T3P	Propanephosphonic acid anhydride
TCEP	Antibody drug conjugates
TEM	Transmission electron microscopy
TEMED	N,N,N',N'-tetramethylethylenediamine
TEV	Tobacco Etch Virus
TfR-1	Transferrin receptor 1
THF	Tetrahydrofuran
TMZ	Temozolomide
Tris base	Tris(hydroxymethyl)aminomethane
Tris-HCl	Tris(hydroxymethyl)aminomethane chloride
U	Unit of activity = µmol of substrate per minute
UAAs	Unnatural amino acids
USPIO	Ultra-small particle iron oxide
UV-vis	Ultraviolet and visible light
v/v	Volume/volume ratio
w/v	Weight/volume ratio

List of apoferritin samples

Name	Description	Chapter reference
HSAFt	Horse spleen apoferritin shell devoid of the iron core	2,3
HSAFt-Cu(phen)	HSAFt shell with copper-1,10-phenanthroline encapsulated by nanoreactor method	2,3
HSAFt-Cu(phen)-TMZ	HSAFt-Cu(phen) stored at -20 °C for 1 month and loaded with TMZ by nanoreactor method	2,3
AFt_WT His	HuHAFt shell with no cysteines with His-tag	4
AFt_WT	HuHAFt shell with no cysteines without His-tag	4
AFt_WT(Cu)	AFt_WT with encapsulated $Cu(NO_3)_2$ by nanoreactor method	4
AFt_WT-Phen	AFt_WT incubated with 2-bromo-*N*-(1,10-phenanthrolin-5-yl)acetamide in urea-tris buffer pH 8.5 at 4 °C overnight and purified by dialysis	4
AFt_WT-Phen(Cu)	AFt_WT-Phen with encapsulated $Cu(NO_3)_2$ by nanoreactor method	4
AFt_K68C His	HuHAFt with Cys68 mutation with His-tag	4
AFt_K68C	HuHAFt with Cys68 mutation without His-tag	4
AFt_K68C-Phen	AFt_K68C incubated with 2-bromo-*N*-(1,10-phenanthrolin-5-yl)acetamide in urea-tris buffer pH 8.5 at 4 °C overnight and purified by dialysis for covalent conjugation	4
AFt_K68C-Phen(Cu)	AFt_K68C-Phen with encapsulated $Cu(NO_3)_2$ by nanoreactor method	4
AFt_K68C-Phen(Cu)-TMZ	AFt_K68C-Phen(Cu) with encapsulated TMZ by nanoreactor method	4

1. Introduction and Literature Review

1.1 Background and motivation

Pharmaceutical treatments represent a fine balance between benefit and risk. In most cases the risk is related to the unintended consequences of drug administration to normal body tissues. This is especially true for anticancer chemotherapy. Tumour heterogeneity even within the same patient makes the development of effective therapies extremely challenging. This can be further exacerbated by the location of the primary tumour and its speed of progression. In this context tumours of the central nervous system only include over one hundred distinct entities.[1] Among them glioblastoma multiforme (GBM) accounts for 46.6 % of the cases,[1] is very aggressive and is incurable at diagnosis with an average survival time of 15 months.[1] This condition is aggravated by the tumour localisation in the brain, which makes any medical treatment or procedure challenging and potentially hazardous. The approved treatment involves surgical resection with post-surgical radiotherapy and chemotherapy with the alkylating agent temozolomide (TMZ), the active component of the drug Temodal®.[1,2]

Treatment of brain tumours like GBM is hindered by the presence of the blood brain barrier (BBB) whose physiological function aims to prevent the penetration of harmful substances into the brain. However, this also constitutes an obstacle for most therapeutic agents.[2] TMZ is able to cross the BBB[2] at the cost of systemic distribution which causes a number of side effects: increased risk of infection, bruising, bleeding gums, nose bleeds, loss of appetite, headache, sickness, constipation or diarrhoea, fatigue, seizures, hair loss, skin rashes.[3] These undesired toxicities would be limited by allowing the drug to exert its pharmacological action only to the tumour site. This is the main objective of the research currently conducted in the field of drug delivery.

Drug delivery aims to achieve the desired therapeutic effect with minimal toxicities by developing systems able to discharge the drug molecules only at their site of action (in this case the tumour), the Ehrlich's 'magic bullet'.[4] The ideal drug delivery system should be biocompatible, biodegradable, nonimmunogenic, highly specific, cost-effective, able to carry a significant amount of drug molecules and to be orally administered. Nanoparticles are emerging as viable devices to accomplish this task. A wide array of biomedical tools using inorganic and organic nano structures is under development with some of them already approved by regulatory agencies for

anticancer treatment.[5] However, the design of a delivery system able to incorporate all the features listed above is still very challenging.

Protein nanoparticles, and in particular the apoferritin (AFt) nanocage already possess many of the advantages desirable in a drug delivery device. The protein cage is biocompatible and biodegradable, can be easily functionalised to target specific tissues, has a natural ability to cross the BBB[6], it can encapsulate different organic and inorganic molecules and its pH-responsiveness provides a selective drug release mechanism.[7] Furthermore, its physiological function as an iron storage protein makes it naturally stable in the systemic circulation, acting as a protective scaffold to its cargo. All these features make apoferritin a good candidate for the development of a TMZ delivery system for the treatment of GBM. Although promising compared to other systems, optimisation is still required to improve the ability of the protein cage apoferritin to prevent the leakage of TMZ while in the systemic circulation and to deliver it selectively to cancer cells. Improving the control over drug release from AFt is critical for its translation into clinical application. So far, the use of helper molecules like metal complexes able to stabilise the drug when inside the protein until internalisation into cancer cells have produced encouraging results.[8] The development of an apoferritin optimised cage, with improved TMZ retention ability would favour the study of this delivery system for therapeutic application and provide the basis for the use of this protein scaffold for the targeted delivery of other anticancer agents.

1.2 Anticancer chemotherapy and drug delivery

1.2.1 The burden of cancer diseases

According to the World Health Organisation (WHO) cancer constitutes one of the leading causes of death worldwide. In 2020, ~10 million patients died of cancer (Figure 1.1).[9,10] Although the most common cancers can vary depending on the country, those which are connected to the highest mortality are lung (1.80 million deaths), colon and rectum (916 000 deaths), liver (830 000 deaths), stomach (769 000 deaths) and breast cancer (685 000 deaths).[9] Of the total number of new cancer cases arising per year, 400 000 are paediatric cancers.[9] In 2020 in Europe 1.9 million cancer deaths and 4.0 million new cases were reported.[11]

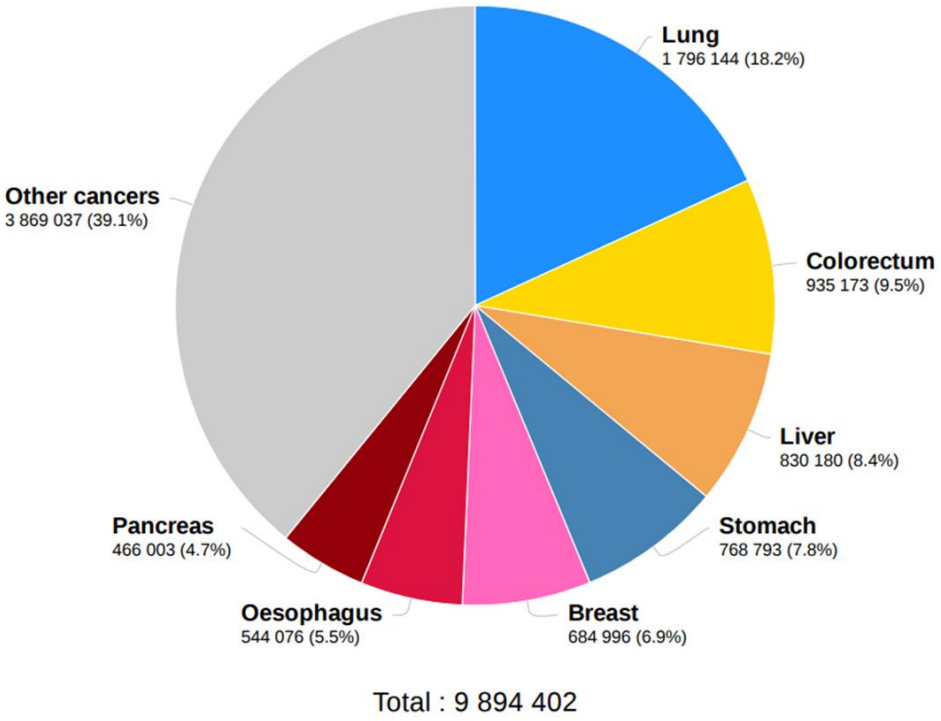

Figure 1.1. Estimated number of cancer deaths in 2020 worldwide reproduced from the International Agency for Research on Cancer (WHO).[12]

The global cancer burden is expected to rise by 47% by 2040, with an overall increase of up to 28.4 million cases.[10] These estimates are likely to grow as the full impact of the severe acute respiratory syndrome coronavirus 2 (SARS-CoV-2) that caused the COVID-19 pandemic is not yet known in many countries. The importance of the incidence of cancer and its mortality are also related to the impact on global economies, given the heterogeneity of cancer disease and the connected comorbidities. For example, in 2018 in Europe it was estimated that cancer diseases had an economic impact of 97 billion euros.[11]

Cancer is a disease caused by the progressive alteration of normal cells into tumour cells promoted by a mixture of genetic factors and external stimuli including physical carcinogens (ultraviolet and ionising radiation), chemical carcinogens (asbestos, components of tobacco smoke, alcohol, food and water contaminants), and infections from certain viruses, bacteria, or parasites. Early detection and efficacy of the treatment are essential to cure many cancers. More is required by individual governments to improve the screening systems and prevention.[10,11] However, the development of affordable and highly specific anticancer chemotherapy would play a crucial role with effective prevention in reducing the mortality associated with cancer diseases.

1.2.2 Anticancer agents

In the recent past, remarkable progress has been achieved in the pharmacological treatment of tumour diseases, leading to an increase in the life expectancy of patients with malignancies and to an extension in the use of chemotherapeutic agents for the treatment of non-malignant diseases such as autoimmune diseases.[13] Most anticancer agents exert their cytotoxic activity by targeting different phases of the cell cycle. Although tumour cells can be heterogeneous, they rely on the constitutive activation of common ancestral biochemical pathways to promote survival and proliferation.[14] Consequently, a significant portion of these medications is still characterised by a low therapeutic index which reflects in their potential to cause drug-related toxicities. This phenomenon occurs because the cells most susceptible to chemotherapy are those in a highly proliferative state: this includes some types of cancer, but healthy cells as well (bone marrow, hair follicles, intestinal epithelium). Furthermore, the severity of these side effects might not be limited to the time in which the patient undergoes treatment, but there can be a negative effect on the functions of vital organs also after its completion. [15]

Anticancer agents can be grouped into three main categories, each being further divided into smaller classes according to the drug targets (Figure 1.2): cytotoxic agents, targeted therapeutics, and hormonal agents.[16] Cytotoxic agents constitute the oldest class of anticancer chemotherapeutics characterised by a remarkable potency. Often these agents can produce significant dose-related toxicities including myelosuppression, gastrointestinal disturbances, alopecia and uncomfortable inflammatory reactions at the site of injection.[16] Targeted therapeutics have been developed to achieve a higher selectivity for tumour cell targets. Targeted therapeutics can be further classified into two main groups of molecular entities: monoclonal antibodies and small molecules.[16] Monoclonal antibodies (mAb) have the advantage of being more stable in the blood and of providing the specific targeting moiety on more complex therapeutic systems. They can be used as conjugates with toxins or radionuclides to enhance the specificity of their cytotoxic action.[16] The major issue of small-targeted therapeutics is related to their hepatic CYP450 metabolism and the consequent drug-drug interactions that can take place if the patient is subjected to a multitherapy regimen, which is a plausible condition in the case of cancer.[16] Hormonal agents constitute a class of chemotherapeutics whose application is restricted to specific tumour types such as prostate and breast cancers.[16] All the anticancer agents used in chemotherapy can be hampered in their pharmacological effect because of the mounting of drug resistance by the targeted

tumour cells by employing mechanisms leading to poor drug absorption and delivery, genetic alteration of drug transport, activation and clearance as well as mutations, amplifications or deletions of the drug target.[17]

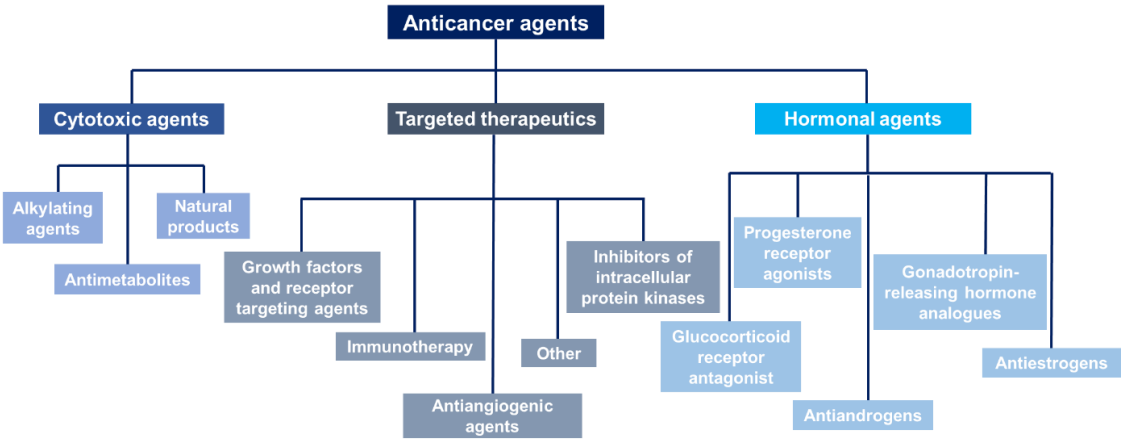

Figure 1.2. Diagram of the anticancer agents currently employed in pharmacological chemotherapy, grouped into different classes according to their mechanism of action.

The complexity of cancer cells' biology as well as the enormous variability according to which cancer disease develops among different individuals highlights the need for complex, personalised therapies carefully tuned not only to the disease but also, and more importantly, to the patient. Targeted agents are characterised by a higher specificity, but many of them still rely on the ability of the immune response of the patient to determine therapeutic success and can suffer the rapid development of resistance mechanisms.[16] On the other hand, cytotoxic agents do not bear the specificity of mAb or small molecules but have established efficacy in the clinic despite the severe drug-related toxicities that they are likely to cause.[16]

1.2.3 Drug delivery systems (DDSs) and their pharmacokinetics in anticancer chemotherapy

Drug delivery can be valuable in oncology where the administration of anticancer agents in a controlled fashion can improve their therapeutic efficacy and prevent non-specific interactions that can cause major toxicities to patients. Drug delivery systems (DDSs) are designed to stabilise therapeutics agents *in vivo* in a way to achieve localised controlled release of the active compound and to minimise systemic exposure.[18] The growing interest developed for DDSs in the past 50 years has led to the identification of those features that must be considered during their evaluation: chemical structure, shape, size and the possible interactions with the body.[5,18,19] DDSs aim to address some of the major issues responsible for decreased efficacy of

drug therapies such as poor patient adherence, enzymatic degradation, poor bioavailability, insufficient concentration at the target site and onset of off-target toxicities. Although the common aim might lead to the conclusion that also prodrugs can be considered DDSs it is important to highlight that while DDSs are materials whose physicochemical properties determine a specific interaction with the pharmaceutical compound, prodrugs are chemical derivatives of a drug molecule able to exert a therapeutic effect only if "triggered".[20,21]

Several materials have been artificially developed to achieve controlled release of their "cargo" (Figure 1.3). Of particular relevance are those systems exploiting the size of the DDS for passive accumulation at the target site and/or the response of the DDS material to various stimuli such as pH[22], temperature or light.[23] Since 1986 with the discovery of the enhanced permeability and retention effect (EPR) the use of nanocarrier formulations for drug delivery has been widely investigated.[24] The EPR effect is the consequence of the irregular and defective vasculature growing around the tumour mass. The surrounding blood vessels have large pores created by the sparse distribution of their epithelial cells which make the tumour vasculature porous.[25] Nanocarriers within 20-200 nm can passively accumulate within the tumour tissue because of the EPR effect.[26,7] Passive tumour targeting is one of the reasons for which size is crucial for nanocarriers. Larger particles are too big to allow extravasation at the tumour site and can be recognised and removed by the reticuloendothelial system (RES). Smaller particles can leak also from normal vascular tissue.[26,7]

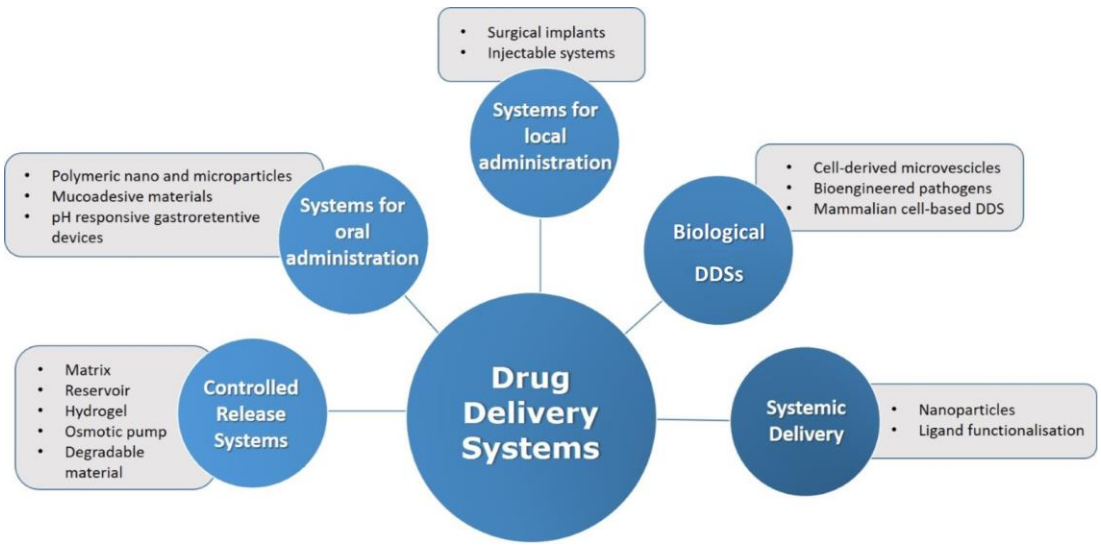

Figure 1.3. Different DDSs produced according to the physicochemical features of their "cargo" and the intended administration route.

Among essential features of drug delivery nanocarriers, charge and hydrophobicity can determine the efficiency of cellular uptake and the probability of clearance from the blood circulation. The nanocarrier's surface charge should avoid interactions with serum proteins and water and reduce clearance from the blood circulation by reticuloendothelial system (RES), hepatic and renal excretion.[7] In addition to this, specific internalisation by cancer cells should be provided by surface motifs recognised by receptors (biomarkers) that are overexpressed on tumour cells.[26,7] In practice, the EPR effect produces only a 20-30% increase in tumour accumulation due to the high interstitial pressure in the tumour environment exacerbated by the entry of more nanocarriers.[26] The ability to encapsulate a high number of drug molecules and their homogeneous distribution within the nanocarrier, without premature drug release are essential to ensure the efficacy of the drug delivery system.[27] Biodegradability of the nanocarrier and its biocompatibility are also necessary to prevent unwanted immunogenic responses or other undesired side effects.

The main smart carriers studied for biotech applications, including drug delivery (Figure 1.4) can be divided into inorganic (carbon nanotubes, gold nanoparticles and quantum dots etc) and organic nanocarriers (polymer-based micelles, liposomes, dendrimers, exosomes).[5,7] Inorganic nanocarriers are characterised by a central core formed by metal NPs or loaded with active molecules, stabilised by a surface coating that can be functionalised for targeting. Organic nanocarriers are delivery vehicles derived from living systems (pathogen-based, mammalian-cell based) recently recognised as a more advantageous tool for clinical purposes.[18]

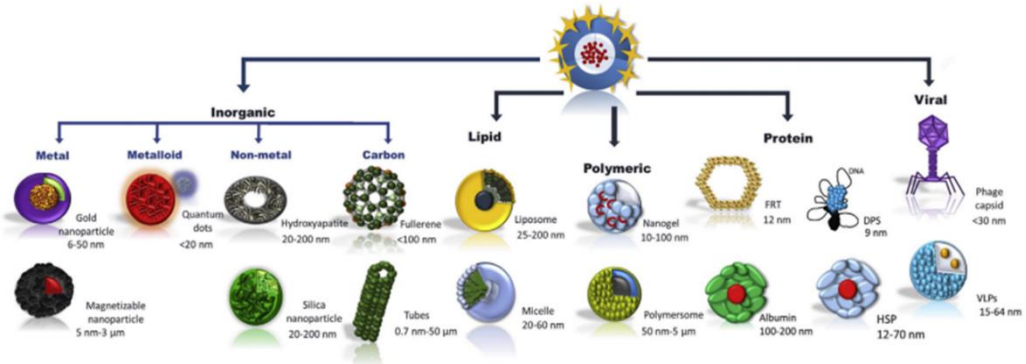

Figure 1.4 Nanocarriers currently studied for drug delivery and diagnostics and their size reproduced from Tesarova *et al.*[7]

The structure of inorganic nanocarriers is characterised by an inorganic core which constitutes the active agent and an outer shell to improve stability in biological environments (Figure 1.5). The core is used for the loading of drugs or inorganic materials such as gold, quantum dots, silica or iron oxide that are responsible for the magnetic and plasmonic properties of the nano-formulation.[28,29] The outer shell is usually composed of organic polymers or metals which can be conjugated to biomacromolecules for targeting and protecting the core (usually a metal, depending on the formulation) from non-specific interactions (Figure 1.5).[28,29] Gold nanoparticles (NPs),[30] quantum dots (QDs),[31] carbon nanotubes (CNTs),[32] supermagnetic iron-oxide nanoparticles (SPIONs)[33] and mesoporous silica nanoparticles (MSNs)[34] are the inorganic nanocarriers mostly employed for clinical applications and drug delivery.[5]

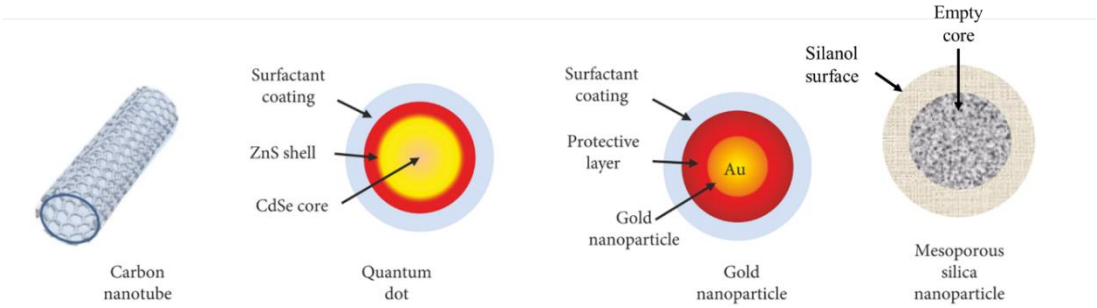

Figure 1.5 Example of inorganic nanocarriers used in biotechnology as reported by Lombardo *et al.*[5]

QDs are inorganic nanoparticles formed of three layers: an inner semiconductor core (usually CdSe), coated by a semiconductor layer (usually ZnS) with an outer surfactant coating (Figure 1.5). Their unique photophysical properties and their fluorescence allow for real-time monitoring of drug delivery and tumour imaging.[35,36] Gold NPs are characterised by higher biocompatibility and low toxicity. Furthermore, they can be easily functionalised for therapeutic and diagnostic purposes.[37] CNTs are characterised by a nano-needle shaped structure that favours internalisation by endocytosis and has successfully delivered doxorubicin, methotrexate, paclitaxel, cisplatin and siRNA.[38,39,40] SPIONs are formed by magnetite (Fe_3O_4) and maghemite (Fe_2O_3) which can be concentrated at the target tumour tissue with the use of an external high-gradient magnetic field.[41] MSNs have been used for the delivery of paclitaxel, doxorubicin and methotrexate using a variety of systems responsive to temperature, light, pH, magnetic, electric and mechanical stimuli.[42,43]

Among the smart inorganic carriers described above, only gold NPs and MSNs showed encouraging biocompatibility and biodegradability. The main challenges are correlated to the translation of these systems in the clinic, especially for MSNs.[5] QDs, CNTs and SPIONs are all characterised by significant toxicity and poor biocompatibility which in some cases has been improved by surface coating with polyethylene glycol (PEG).[5] Although PEGylation is a standard technique to improve the biocompatibility and stability of drug compounds, recent studies have outlined the formation of anti-PEG antibodies over time in patients upon administration of PEGylated treatments.[44] The production of such antibodies can lead to accelerated blood clearance, low drug efficacy, hypersensitivity and life-threatening side effects.[44] Of these inorganic systems only the NanoTherm® formulation had been approved by the FDA for the treatment of glioblastoma through magnetic hyperthermia induced by the superparamagnetic iron oxide.[5] Other similar iron oxide nanoparticles have been withdrawn from the market, while gold NPs and MSNs showed critical issues related to toxicity and stability in early phase clinical trials.[5] As mentioned previously, the clinical application of DDSs requires them to be biodegradable to prevent their accumulation in the body and the onset of harmful effects. However, biodegradability constitutes one of the major drawbacks of inorganic nanocarriers and the reason why organic structures such as liposomes and albumin are instead used and approved in clinical practice.[45,46]

In contrast to inorganic DDSs, organic nanocarriers such as exosomes, bacteria, viruses and some mammalian cells already possess the right structural features to circulate within organisms and cross physiological membranes. Furthermore, DDSs able to be assembled from pre-functionalised biomaterials can benefit from simplified optimisation and manufacturing steps, compared to DDSs produced from non-natural materials.[47,48] Nanomaterial-based drug delivery is emerging as a widely studied form of DDS, especially for anticancer chemotherapy. The benefits of nano-scale DDSs are controlled drug release, specific tumour targeting, improved drug pharmacokinetics and biodistribution, ability to overcome biological barriers and enhanced tumour tissue accumulation.[27] All these aspects with a detailed description of the organic nanocarriers studies for therapeutic applications will be discussed in the next section.

The large number of pharmaceuticals available and the problems brought by their administration, either related to the dose regimen or pre-existing clinical conditions, underline the need to continue to expand research on drug delivery. The development

of DDSs characterised by simple structures, high specificity, and loading efficiency have the potential to greatly increase the therapeutic effect of drug compounds. By addressing the issues of non-specific distribution, rapid clearance, uncontrolled release and low bioavailability of common drug therapies, DDSs can significantly reduce the onset and the severity of adverse reactions.[5] The introduction of nanotechnology in the field of drug delivery could provide a valuable tool for the improvement of both the pharmacokinetic (solubility, bioavailability, stability) and specificity of the pharmacological activity (cell or tissue-specific delivery, precise intracellular delivery, visualisation of delivery sites).[47]

1.2.4 Nanocapsules used as DDSs: polymeric vesicles, liposomes, exosomes, protein cages and virus-like particles

Liposomal and polymeric nanocapsules formulations are currently the only two categories of nanocarriers approved for therapeutic uses.[5] Liposomes are 50-500 nm vesicles that can be composed of synthetic or natural (phospho-)lipid units consisting of a hydrophilic head and hydrophobic tail that can self-assemble into bilayers in aqueous solution (Figure 1.6).[5] The complexity of these structures can be increased by producing multilamellar vesicles characterised by several concentric lipid bilayers or (in the case of highly hydrophobic drugs) by introducing a core of high melting fat matrix to obtain solid lipid nanoparticles (SLNs).[49,50] The encapsulation of a variety of anticancer agents such as doxorubicin, daunorubicin, cisplatin, paclitaxel and vincristine has been achieved into liposomes due to their ability to store both hydrophilic and hydrophobic molecules.[5] The doxorubicin-containing liposomal formulations Doxil® and Myocet® are currently used for the treatment of Kaposi's sarcoma and breast cancer respectively.[5] Liposomes can be functionalised with the use of PEG polymers and their structures designed to release their cargo to specific stimuli such as light, heat, magnetic field, ultrasound, pH, enzymes and redox.[5] The thermo-sensitive liposome-doxorubicin formulation Thermodox® is currently under phase III clinical trial.[5] Furthermore, a theranostic liposome-based system loaded with the MRI contrast agent Gd-DTPA and doxorubicin showed the ability to simultaneously monitor and allow drug delivery.[51] Liposomes constitute the dominant nanoparticle formulations approved for anticancer treatment.[52] This is owed to the biocompatibility, ease of preparation and size control, low cytotoxicity and hydrophobic/hydrophilic features of these nanocarriers.[5]

Polymer-based nanocarriers can be assembled from natural and synthetic building blocks into micelles or vesicles by balancing the hydrophobic/hydrophilic balance of

the final amphiphilic polymer (Figure 1.6).[53] Micelles provide the ideal microenvironment for the loading of hydrophobic drugs by virtue of their lipophilic core and hydrophilic shell which improves solubility and stability in aqueous media.[5] Vesicles are characterised by a bilayer structure which makes them suitable for the encapsulation of hydrophilic molecules.[5] Chitosan, dextran, heparin and hyaluronan are among the natural polymers which have been studied in the past for drug delivery. Among them, chitosan has been used for the self-assembly of amphiphilic micelles loaded with anticancer agents for drug delivery and theranostic applications.[5] In addition to nanoparticles based on natural polymers, there has been recent interest in the use of biodegradable synthetic polymeric biomaterials like poly(lactic acid) (PLA) and poly(lactic-co-glycolide) (PLGA) copolymers. Both are approved by the US Food and Drug Administration (FDA) and the European Medicinal Agency (EMA) as drug delivery biomaterials.[5] PEG-PLGA micelles were used to conjugate the anticancer agent doxorubicin to produce a slow and controlled release formulation.[54] The functionalisation of PLGA-PEG nanocarriers with folate produced a system more efficient at targeting cancer cells both for imaging and drug delivery.[55] Furthermore polymer-based nanocarriers can also be engineered to release their content upon physical, chemical and biological stimuli. The use of poly(*N*-isopropylacrylamide) (PNIPAm) and the pluronic-type class of poly(ethylene oxide)-poly(propyleneoxide)-po-ly(ethylene oxide) PEO_m-PPO_n-PEO_m triblock copolymers to synthesise thermoresponsive micelles has been extensively used for drug encapsulation and delivery.[56] The drug release is achieved by localised alteration of the temperature to reduce the solubility of the polymers which destabilises the structure of the nanocarrier.[56] Biocompatible polymers are also employed for the design of dendrimers and hydrogels for biomedical applications.[5]

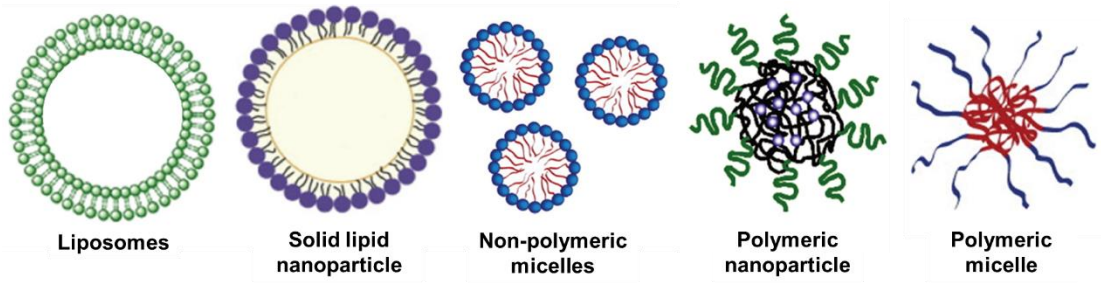

Figure 1.6 Example of lipid and polymeric organic nanocarriers used in biotechnology reproduced from Masserini *et al.*[57]

Although liposomes and polymers are the only nanocarriers that have been able to reach the market, other emerging nanoparticles have attracted interest as potential drug delivery systems like exosomes. Exosomes are membrane-based vesicles ranging from 40 to 100 nm, that can be produced by all cell types and therefore are non-immunogenic.[58] According to the exosome database ExoCarta there are ~8000 proteins and 194 lipids known to be associated with exosomes (Figure 1.7).[59] These nanocarriers have been employed to detect prostate, breast and ovarian cancer and for the diagnosis and detection of active and latent forms of intracellular infections.[58,59] Recent literature illustrated the successful encapsulation of doxorubicin into exosomes and efficient delivery across the BBB using zebrafish embryos.[60] Similar results were achieved in a mouse tumour model both *in vitro* and *in vivo.*[61] Exosomes were proven efficient carriers of proteins for the therapy of Parkinson's disease and of siRNA to achieve gene silencing.[58] Due to the high expression of the epidermal growth factor receptor (EGFR) in many cancer cells, exosomes were tested for the delivery of miRNA also to breast cancer cells.[62] Although promising, further study of the role of exosomes in health and disease conditions is needed to predict long term safety.[58] Many techniques have been developed to isolate and purify exosomes, however their production is still very expensive and difficult to scale up for biomedical application.[58] To overcome this issue the design of artificial or exosomes mimetics is one of the approaches undertaken by researchers.[58]

In addition to lipid and polymer-based drug delivery systems, protein nanocapsules provide a variety of biocompatible and biodegradable tools due to their native presence in the organism. They can be used for drug encapsulation by physical entrapment or covalent conjugation. However, they often cause rapid and uncontrolled drug leakage.[27] Among some of the currently studied natural nanocarriers there are virus-like particles (VLPs) and viral capsids, milk proteins, small heat shock proteins (HSP), silk proteins, albumin, gliadin, gelatin, legumin, lipoproteins, DNA-binding proteins from starved cells (DPS), and the ubiquitous protein ferritin (Ft).[7,63] VLPs are non-infectious nano-capsules formed by the assembly of the proteins that normally form viral capsids.[64] These proteins can be produced from bacteriophages, animal and plant viruses and have been successfully used to encapsulate and deliver small peptide drugs, siRNA, and chemotherapeutic drugs such as Taxol® and doxorubicin.[64] Particularly important is the contribution of VLPs in vaccine delivery.[65,66] In fact, VLPs have been successfully used to display epitopes that can produce an enhanced and long-lasting antibody response to target poorly immunogenic antigens.[65,66]

The inherent transport function of albumin makes it able to bind several peptides and proteins through non-covalent interactions and also presents a variety of residues that can be used for covalent conjugation of drugs like Taxol®, which has been approved as Abraxane® for the treatment of metastatic breast cancer by the FDA.[67] Furthermore it is stable in the pH range 4.0-9.0 and at temperatures up to 60 °C.[64] DPS and ferritin are iron storage proteins composed of a small number of subunits able to assemble into symmetrical nanocages.[68] The presence of a hollow core makes them suitable for the loading of anticancer and theranostic agents.[69,70] Mammalian ferritin has been widely investigated for drug delivery and clinical applications.[68] The loading of doxorubicin into the empty ferritin shell (apoferritin) achieved ten times higher tumour accumulation and significant cytotoxicity compared to free doxorubicin, with lower systemic toxicity compared to the liposomal formulation Doxil®.[63]

The main issues related to the use of nanocarriers for clinical and biotech applications are connected to their employment within the complex biological environment where multiform interactions can occur.[5] The design of liposomes able to evade the host immune system with a long-circulating capability, higher stability, and without toxicity remains challenging.[71] Although polymeric nanoparticles may have better stability, their biocompatibility and long-term potential safety are still a concern for clinical applications.[72] The production of pure and scalable quantities of exosomes makes the development of formulations for clinical applications challenging.[59] Protein-based delivery systems like ferritin have the biocompatibility, uniform size and potential for functionalisation able to overcome the limitations observed with the majority of nano-formulations presented in this section.[73] The natural stability of some protein nanocapsules makes them valuable tools for drug delivery. Their basic structure can be modified and adapted for the loading of different therapeutic agents and to increase their uptake by cancer cells. Successful protein-mediated drug delivery has been achieved through the covalent modification of proteins, to produce pharmacologically active bioconjugates.

1.3 Design and therapeutic applications of protein bioconjugates

The use of bioconjugation to covalently bind drug molecules to protein and peptide systems for drug delivery is characterised by increased chemical stability, protection from *in vivo* degradation and excretion, increased drug half-life, reduced side effects

and increased drug solubility.[74] Beside these benefits the design of protein-drug bioconjugates for clinical applications should be carefully controlled in every aspect of their preparation. For this reason, the choice of the conjugation strategy can be critical for the efficacy and the safety of the bioconjugate system.

1.3.1 Methods for protein conjugation

The applications of protein bioconjugates span from diagnostics, bio-sensors, recyclable catalysts and protein-based therapeutics.[75] Ensuring the selectivity of the protein labelling is essential for bioconjugates designed for clinical applications, as heterogeneous conjugates can negatively affect the pharmacokinetic profile of the formulation.[75] There are two major approaches for the labelling of proteins with exogenous functionalities: pre-engineering of the amino acid sequence and the single-site chemical modification of native proteins.[75] The pre-engineered protein method involves the genetic modification of the amino acids sequence for the incorporation of low frequency occurring residues like cysteine, or noncanonical amino acids with azide functionalities.[75] This method has been further expanded to make the mutated sequence recognisable by a specific reagent or enzyme to achieve labelling.[76] The single-site modification of native proteins instead is based on the selective labelling of a canonical amino acid residue (cysteine, tryptophan, tyrosine, histidine, lysine) without previous protein engineering.[75] Even though the use of the native protein for conjugation can provide better information on its biological function, it comes at the cost of heterogeneity and low specificity of labelling. The presence of amino acid residues with similar nucleophilicity in a reaction mixture containing an excess of the electrophilic label can lead to the formation of bioconjugates at multiple protein sites.[75]

Due to its higher specificity and its potential application to many protein substrates, the pre-engineering of the peptide sequence approach is generally preferred to produce bioconjugates for therapeutic applications. Unnatural amino acids (UAAs) provide site-specific protein conjugation due to their unique chemical and biological features that differentiate them from canonical amino acids.[77] Although employed for many applications including pharmaceuticals manufacturing, the synthesis of UAAs is still challenging and time-consuming.[77,78] Natural amino acids with ionisable side chains that tend to be highly accessible in the protein structure (aspartic acid, glutamic acid, lysine, arginine, cysteine, histidine, tyrosine) can also act as nucleophiles for conjugation purposes. Among them cysteine is characterised by unique nucleophilicity and natural low abundance, combining the advantages of the UAAs

with those of canonical amino acid side chains.[74,78] For these reasons, cysteine is one of the mostly employed amino acid for site-specific protein bioconjugation reactions.[78,74] Its side chain (pKa~ 8.0-9.0) is ionised into a negatively charged thiolate anion at alkaline pH. [78,74] This favours the labelling of the cysteine through different reactions such as alkylation, acylation and maleimide conjugations while keeping protein-compatible conditions.[74]

The principal reaction for protein conjugation through a cysteine residue involves the use of maleimide reagents. The Michael addition of a thiolate anion of cysteine to a maleimide double bond leads to the formation of a thiosuccinimide bond (Figure 1.7).[78,79] This approach is characterised by fast labelling procedures with acceptable selectivity in aqueous environment and no need for heating or catalysts.[78] Furthermore, maleic anhydrides can be easily added to amines to produce functionalised dyes and probes for protein labelling.[80] All these features contributed to the use of maleimide coupling to produce systems such as antibody drug conjugates, some of which are currently used in therapeutic regimens.[78] An example is Brentuximab vedotin formed by the conjugation of an anti-CD30 antibody to the cytotoxic agent monomethyl aurostatin E, approved for the treatment of Hodgkin's lymphoma and systemic anaplastic large cell lymphoma.[81] A more detailed description of the ADC approach is described in the following section.

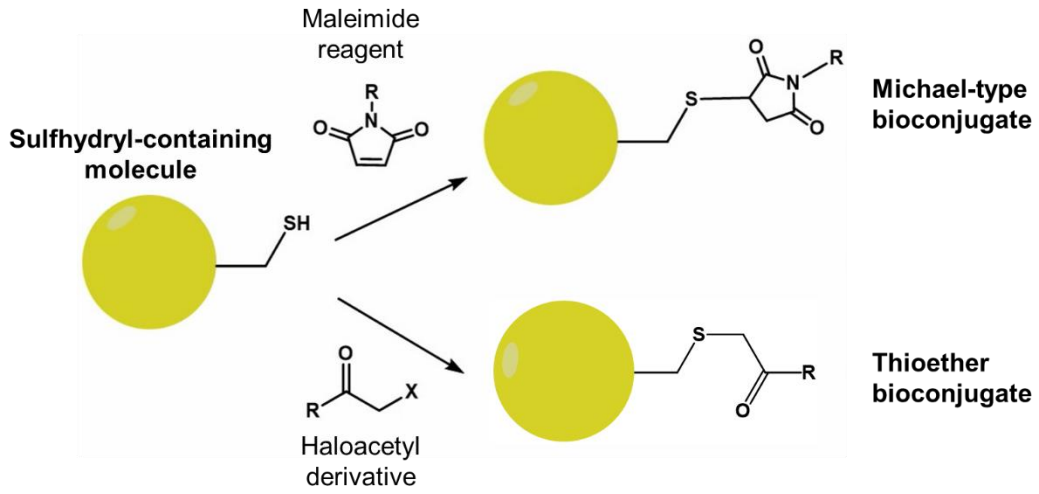

Figure 1.7 Examples of cysteine bioconjugation through maleimide and haloalkyl compounds. Although extensively employed, the maleimide bond can undergo thiol exchange in thiol-rich environment thus leading to non-specific interactions and loss of the targeting ability.[79] Instead the thioether conjugate has the potential for greater stability and better control over release.[82]

Although the maleimide-thiol chemistry has been widely employed for protein bioconjugation due to its chemoselectivity and good reactivity, recent reports have revealed the instability of such linkages with a dramatic effect on the bioconjugate's activity and pharmacokinetics *in vivo*.[19] The presence of high thiol concentration in biological environments can cause a retro-Michael reaction to occur, leading to the group exchange with exogenous thiols and the irreversible cleavage of the thiosuccinimide bond (Figure 1.8).[79] Degradation of the succinimidyl moiety can also occur through irreversible hydrolysis, which stabilizes the maleimide-thiol bond (Figure 1.8).[79] Although less common than maleimides, another valuable and reliable method for cysteine conjugation is the S_N2 reaction with haloalkyl iodide and bromide reagents (Figure 1.7).[78] This method was employed for the synthesis of protein bioconjugates for therapeutic applications and provides a more stable alternative to maleimides even though the conjugation reaction can be slower.[82] The use of this system for covalent conjugation to AFt is described in Chapter 4. Many other reagents have been developed as alternatives to maleimide for protein bioconjugation through cysteine residues. Although promising, most of them still lack substantial *in vivo* evaluation.[80] This is crucial not only to determine their safety and stability in biological environments but also the efficiency of their cargo release.

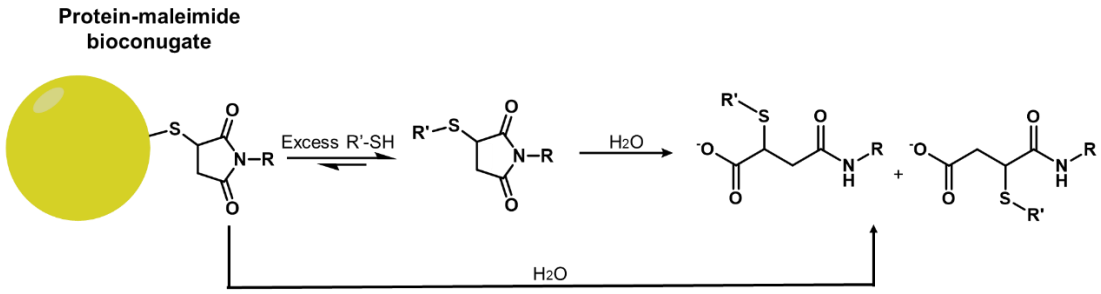

Figure 1.8 Mechanism of protein-maleimide degradation in biological environments. In some cases irreversible hydrolysis can stabilize the maleimide-thiol bond preventing the thiol-exchange reaction.[79]

1.3.2 Antibody drug conjugates and small-molecules drug conjugates

One of the most investigated systems where the covalent conjugation of drug molecules to protein is exploited for targeted drug delivery is the antibody-drug conjugate (ADC).[83] Their effectiveness in specific tumour targeting is confirmed by the fact that there are currently seven ADCs that have been approved by the FDA for the treatment of several cancers.[83] This system is based on the covalent conjugation of the anticancer drug to a monoclonal antibody (mAb) targeting the tumour tissue

(Figure 1.9-a).[84] The selective release of the drug molecule is ensured by the presence of a degradable linker that can be cleaved upon internalisation by the cancer cell (Figure 1.9).[84] The mAbs are engineered murine/humanised antibodies that target specific surface antigens expressed only or in higher quantity by cancer cells to ensure the specificity of the cytotoxic action and reduce drug internalisation by normal cells.[83] To achieve controlled drug release, ADCs are designed with three essential components: the mAb, a biodegradable linker and the drug.[83] The linkers can be usually cleaved by pH-induced hydrolysis or enzymatically.[83] The different drugs delivered through ADCs include anticancer toxins and antimitotic and DNA-binding cytotoxic agents like anthracyclines and auristatins.[83]

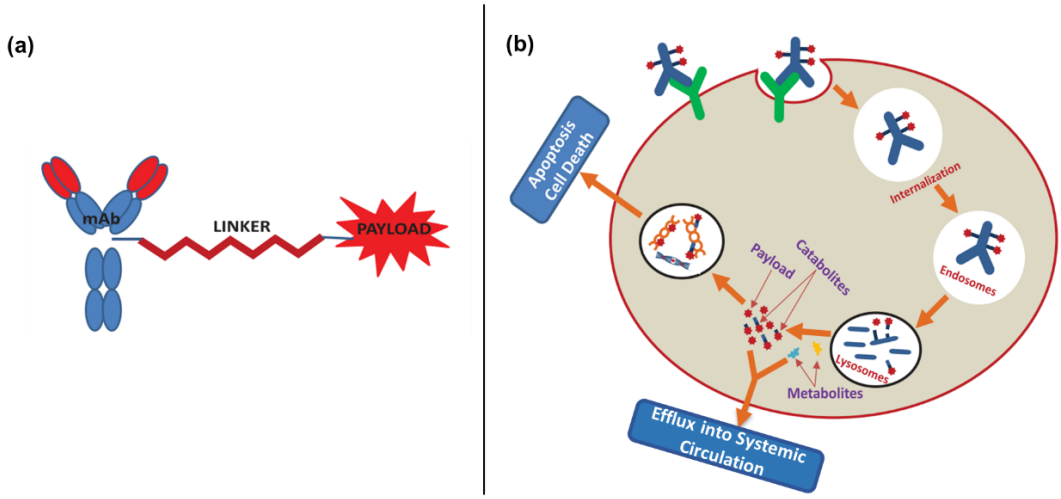

Figure 1.9. Schematic representation of the structure of an ADC (a) with proposed mechanism of drug (payload) release and catabolism (b) as reported by Liu *et al*.[83]

The other protein bioconjugates employed and investigated for drug delivery are the targeted biologics like PEGylated proteins and small peptides employed for cancer treatment and folate-targeted small molecule–drug conjugates (SMDCs).[83] The latter exploit the high expression of the folate receptor on many primary and metastatic cancers to specifically deliver cytotoxic drugs.[85] In addition to the advantages of increased specificity and more favourable safety profiles of ADCs, the SMDCs are cleared from the systemic circulation more efficiently than the larger ADCs thus reducing the chances of off-target side effects.[86] The systems reported in this section suggest that protein and peptide-based DDSs can provide superior target specificity over polymeric and lipid-based systems and for their improvement through functionalisation. However more studies focused on the metabolic fate of these bioconjugate systems could help understanding their long-term impact on the human body.

1.3.3 Antibody directed enzyme prodrug therapy

Although being a successful drug delivery system, the metabolism, non-specific release, and limited delivery capacity per mass of targeting protein of ADCs still constitute a clinical issue.[83,87] In the attempt to overcome such limitations as well as to further improve the benefit over risk profile of the concurrent ADCs system, the antibody directed enzyme prodrug therapy (ADEPT) approach has been developed. ADEPT is based on the delivery of enzymes specifically to tumours, using the selectivity of mAb, to allow the extracellular conversion of prodrugs at the target site upon infusion (Figure 1.10).[88] Prodrugs are a class of therapeutic agents characterised by a markedly reduced pharmacological activity until converted to their active form by either chemical or enzymatic processes within the organism.[21] Differently from ADC, the therapeutic action of ADEPT systems is based on the administration of the Ab-enzyme fusion protein first to ensure binding to target cells and successively of the prodrug which would be activated only where the Ab-enzyme is present.[89] Although several mammalian and non-mammalian enzymes have been employed the only ADEPT system that has been able to reach clinical evaluation has been the one exploiting the carboxypeptidase CPG2 from *Pseudomonas sp.*[88]

CPG2 is a bacterial metalloenzyme responsible for the hydrolytic cleavage of reduced and non-reduced folates, therefore it has no mammalian homologue. With the aid of zinc(II) as a cofactor, it catalyses the hydrolysis of cleavable bonds in aqueous environments[90]. This CPG2 carboxypeptidase has been selected for its ability to cleave glutamate from amidic urethanic and ureidic bonds, so it has been studied for the activation of L-glutamate triazines[90] and nitrogen mustards[91]. Even though this ADEPT system had encouraging preclinical results major challenges were found due to the inadequate localisation of the antibody/enzyme conjugate and humoral immune reaction against the bacterial CPG2, which often required administration of cyclosporine.[88,89] To address such issues the research efforts have also been concentrated on the human *β*-glucuronidase for ADEPT design. *β*-glucuronidases are intracellular lysosomal enzymes[92] responsible for the metabolism of some pharmaceutical agents into more polar compounds, making the xenobiotic easier to be excreted. Due to its polar nature, a glucuronide prodrug will be less likely to enter non-target cells and to produce off-target toxicities. *In vitro* (paclitaxel and camptothecin) and *in vivo* (cyclopamine, monomethyl auristatin E, and doxorubicin) studies have reported the positive results in terms of cancer cell cytotoxicity and safety correlated with the use of glucuronide ADEPT sytems.[92] However, no ADEPT system using *β*- glucuronidases has yet reached the stage of clinical evaluation.

Another approach that follows the lead of ADEPT is gene-directed enzyme prodrug therapy (GDEPT) which is based on the intracellular activation of a prodrug by an enzyme expressed upon gene transduction within the cancer cell (Figure 1.10).[93] Four enzyme/prodrug systems have been evaluated, all reaching clinical stages with promising pre-clinical results. As for the ADEPT system also GDEPT translation into clinical application was limited by the low transduction efficiency of the vector, the lack of an appropriate drug delivery system, prodrug conversion rates and active metabolites diffusion through cancer cells (bystander effect) are still major issues limiting the clinical application of both methods.[93] Ideally a system based on a human protein, able to deliver both the prodrug and its activator at the same time could avoid these challenges.

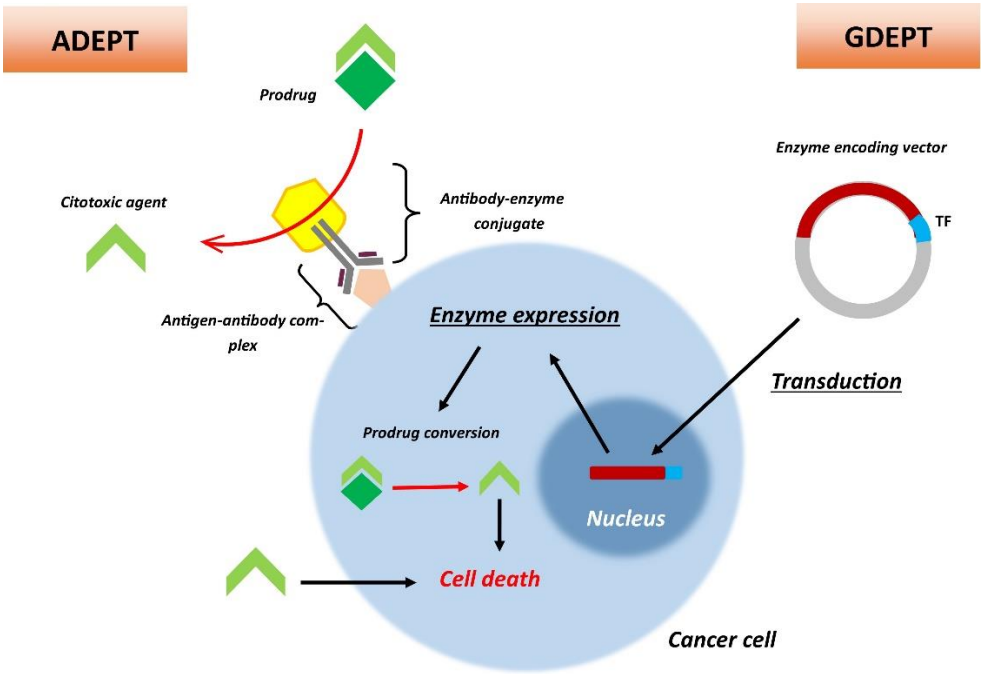

Figure 1.10. Schematic representation of the ADEPT and GDEPT prodrug activation and delivery mechanism.

1.3.4 Metal-protein bioconjugates developed for therapeutic applications

Covalent conjugation constitutes the preferred method of metal incorporation to produce systems for biomedical applications and DDSs, as it limits the metal non-specific interactions between the metal and endogenous molecules.[19] One of the most general structures is the drug-linker-peptidic conjugate in which every element has a crucial role in the stability and pharmacological activity of the construct and which reflects the structure of ADCs (Figure 1.9-a).[19] In the same way as for ADCs

the linker is responsible for the stability of the bioconjugate in the systemic circulation and drug release at the target tissue.[19] In general, the covalent conjugation strategy is based on the presence of highly active groups on specific amino acids within the protein (either natural or unnatural) with selective reactivity towards the metal ligand chosen for the conjugation (Figure 1.11-a). Single amino acid mutations with cysteines or incorporation of unnatural amino acids such as azidomethionine, homopropargylalanine, homoallylglycine etc. [75] can be easily achieved in the protein by genetic engineering. Other strategies also involve the use of the peptide backbone and of the N and C-termini to provide sites for metal incorporation (Figure 1.11-b).[94,95]

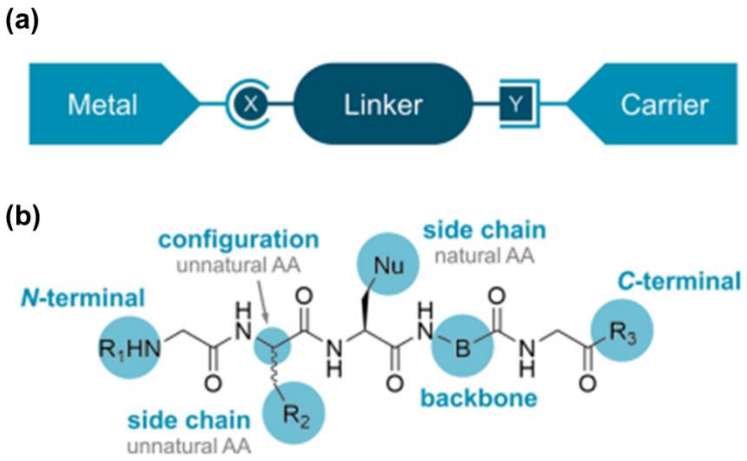

Figure 1.11. Structure of metal-peptide/protein conjugates (a) and detail of peptide/protein conjugation sites used for metal complex binding (b) as described by Meier-Menches *et al.*[19] (a) General structure of a metal-bioconjugate with X and Y representing the common functional groups used to connect either the drug or the peptide to the linker. (b) Sites of metal−peptide conjugation: N-terminal conjugation performed via linker strategies (R1), side chain modifications involving nucleophilic (Nu) or unnatural amino acids (R2), backbone modifications (B) and C-terminal conjugation (R3).

The covalent conjugation of metallodrugs to proteins can increase drug efficacy and reduce the onset of toxicities resulting from non-specific interactions in physiological environments. Platinum-containing drugs cisplatin, carboplatin and oxaliplatin are the most widely used metallodrugs for anticancer chemotherapy worldwide (Figure 1.12).[4] The mechanism through which these metallodrugs cause cancer cell toxicity involves DNA binding and generation of irreversible DNA lesions which block the cell cycle.[4] Platinum (II) derivatives share the same pharmacological activity, but are characterised by improved targeting.[4] Platinum (IV) derivatives are instead prodrugs that can release cisplatin, carboplatin or oxaliplatin upon reduction within the tumour

cell.[4] However, these platinum (IV) complexes can be often subjected to non-specific reduction, which constitute a challenge for clinical application.[96]

Many metal-peptide bioconjugates have been synthesised using platinum anticancer agents cisplatin and oxaliplatin and their derivatives.[19] Recently Imberti *et al.* developed a platinum (IV) *trans,trans*-[$Pt(N_3)_2(Py)_2(OH)(OCO\text{-}(PEG)_2\text{-}NHCSNH\text{-}Ph\text{-}NCS)$] complex conjugated to myoglobin.[96] Release of the metallodrug was controlled by exposing the myoglobin bioconjugate to light.[96] Lippard *et al*. produced platinum (IV) complexes that were conjugated to RGD motives by amide coupling to the peptide N-terminus.[97] A modified oxaliplatin analogue was also conjugated to the monoclonal antibody Herceptin® (trastuzumab). This formulation aimed at specific targeting of human epidermal growth factor receptor 2 (HER2) positive cancers. The ADC improved cellular accumulation and cellular cytotoxicity of the platinum metallodrug.[98] On a similar approach trastuzumab-gold (I) conjugates were synthesised by copper-free alkyne cycloaddition and by amide formation were found to have particularly enhanced anticancer activity (Figure 1.13).[99] Copper mediated alkyne-azide cycloaddition (CuAAC) and "click" chemistry approaches are also used for metal coordination and metalation. The formation of an N-terminal triazole through "click" chemistry favoured the synthesis of a cyclam-tripeptide bioconjugate able to coordinate zinc (II), copper (II) or nickel (II), suitable for imaging purposes.[19] The spontaneous cycloaddition between *p*-ethynylphe with an azido-gold(I) moiety produced a gold bioconjugate with anticancer activity.[100]

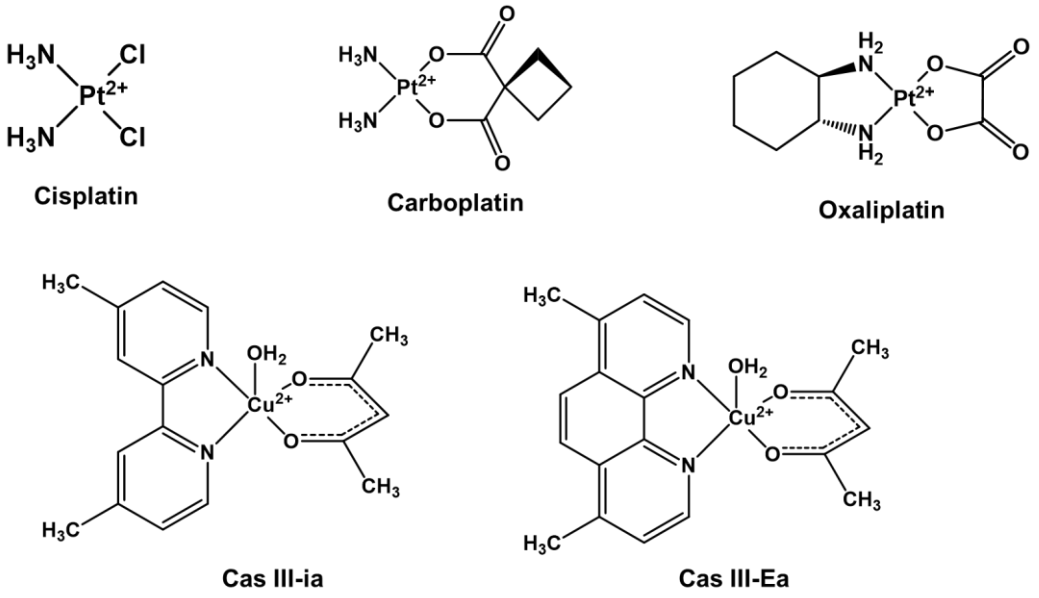

Figure 1.12. Approved platinum anticancer agents and Casiopeinas under clinical evaluation.

Another class of novel metallodrugs under clinical evaluation for anticancer chemotherapy are Casiopeinas (Figure 1.12).[101] These are a class of copper coordination compounds whose ligand is either a bipyridine or a phenanthroline ring.[102] These complexes can induce cancer cell death by ROS-induced DNA oxidation and degradation, depletion of antioxidant defenses, mitochondrial toxicity through CYP450 inhibition and DNA intercalation.[103] The enhanced cytotoxicity exerted by the phenanthroline complexes combined with their low specificity toward cancer cells and the tendency of the metal center to interact with off-target biochemical processes make them ideal candidates for conjugation to targeting proteins and peptides. [102,104,105]

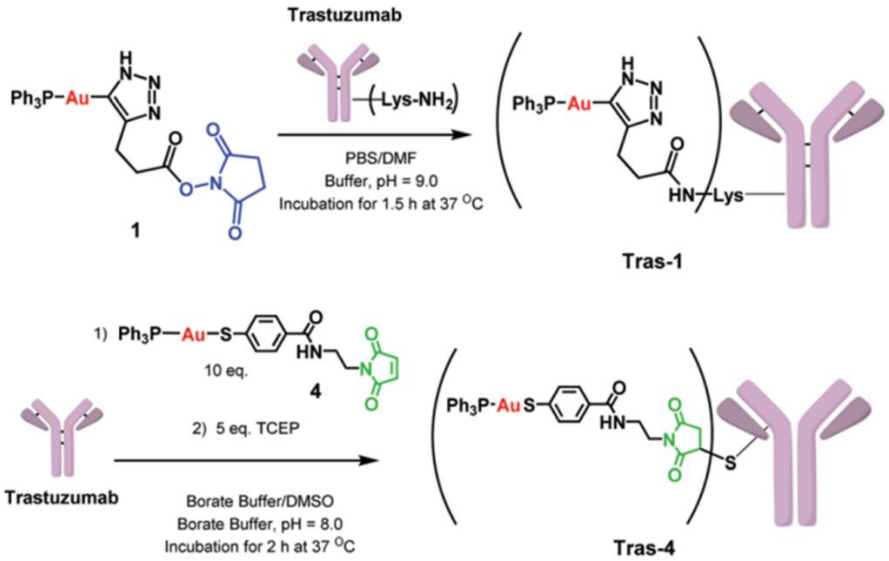

Figure 1.13 Preparation of novel Trastuzumab-gold conjugates as reported by Curado *et al., Trastuzumab gold-conjugates: Synthetic approach and in vitro evaluation of anticancer activities in breast cancer cell lines*, (Chemical Communication, 2019).

Due to the reactivity of metal complexes with nucleophiles exposed on protein covalent conjugation often provides a more stable system for therapeutic application. Serum proteins like human serum albumin (HSA) provide valuable scaffolds that can prevent undesired clearance of the metallodrug from the system circulation.[19] The use of HSA targeted platinum (IV)-maleimide *in vivo* significantly reduced tumour mass.[19] Zhang *et al.* also used HSA to prepare organoiridium (III)-protein conjugates able to exert *in vitro* anticancer activity and to act as photo-sensitiser for photodynamic therapy (PDT).[106] The bioconjugate was prepared through maleimide reaction with the cysteine residue naturally expressed in HSA.[106]

The extended interest and study of protein and peptide-drug conjugates for medical application has highlighted that in many cases constructs with non-cleavable moieties can provide better efficacy. [19] The covalent immobilisation of organometallic species to proteins could result in more inert functionalities that can provide a better alternative for the targeted delivery of therapeutic agents. [19] Furthermore, the potential of bioconjugates formed by metal-peptide and metal-protein interactions can be further expanded from drug delivery to the development of therapeutic catalysts and new imaging techniques.

An interesting approach for the use of protein-metal complex conjugation in biology is represented by the emerging field of artificial metalloenzymes (ArMs).[107] Artificial enzymes are non-natural biocatalysts produced by the incorporation of non-native chemical functionalities within biomolecular scaffolds, often a protein or DNA. Alternatively, *de novo* design of small peptides reproducing the enzyme's active site have also been proposed.[108,109] Using this approach, copper complexes have been explored for *in vitro* catalysis of Diels-Alder cycloaddition reactions.[110] In this case the metal was coordinated by residual 1,10-phenanthroline bound to high affinity antagonists of the human adenosine receptor 2A.[110] The presence of the core structure of the antagonist allowed for the exploitation of its interaction with the receptor to localise the ArM on the cell surface.[110] This work reported the transformation of a membrane receptor into an ArM with the potential to broaden the repertoire of reactions catalysed *in vivo* for the targeted activation of prodrugs or organ specific synthesis of deficient metabolites.[110] Recently the *in vivo* formation of amide bonds between fluorescent probes and the amine groups exposed on proteins was reported using gold complexes bound to coumarin, exploiting its strong affinity for albumin.[111] The further functionalisation of the albumin scaffold with glycans allowed for organ-specific imaging.[111] A promising example of ArM employing albumin as protein scaffold for the protection of the catalytic activity of gold (I) complexes allowed for *in vitro* hydroamination to produce anticancer phenanthridinium derivatives.[112] Following a different approach, the covalent anchoring of copper clusters to bovine serum albumin (BSA) functionalised with tumour-targeting peptides triggered sustained DNA cleavage and chemiluminescent tumour imaging *in vivo*.[112] The application of targeted ArM is also emerging as potential approach for selective cell tagging therapy (SeCT), in which glycosylated ArM can be used to catalyse the labelling of tumour cells *in vivo* with cytotoxic moieties.[113] Although promising, there are still many challenges associated with the introduction of artificial catalysts into *in vitro* and *in vivo* including the permeability of artificial cofactors bound

to the metal ligands, the cofactor localisation, the biocompatibility of the cofactor as well as additives, substrates and products and the mutual inactivation caused by the downstream natural enzyme.[109]

1.4 Ferritin and Apoferritin

Ferritin (Ft) is an iron storage protein that is expressed by many organisms. The main function of Ft is to prevent iron-induced cell damage upon the formation of reactive oxygen species from free iron (II).[114] The possibility to easily remove the iron core by reductive mobilisation,[115] allows for the rapid preparation of the protein-only apoferritin (AFt) which can then be employed for the loading of a wide variety of molecules and functionalities.[116] For this reason, the protein cage AFt can serve as a multimodule platform for drug delivery, diagnostic and theranostic applications.[6] Different protein isoforms have been extensively studied and employed for organic and inorganic agents loading, functionalisation and targeted delivery.[7] As mentioned above, an efficient drug delivery device must possess most of the following characteristics: biocompatibility and biodegradability, low immunogenicity, presence of modifiable groups for active targeting moieties, nano-size that exploits enhanced uptake by EPR, reduced chances of rapid liver and renal clearance or opsonisation.[7] In the case of AFt most of these requirements are met but despite this, no clinical trials are using the protein cage as a DDS. In this section, a detailed description of the uses and features of AFt proteins from different organisms is provided to highlight the gaps in knowledge and the challenges that must be addressed to fully exploit the potential of this nanocage as a multi-functional therapeutic tool.

1.4.1 Ferritin: physiological role and main properties

Ft is a protein cage formed from the assembly of 24 subunits which can be classified as light chain (L) or heavy chain (H) and these can combine into different ratios (from 1:23 H:L to 23:1 H:L) according to the organism and the tissue in which they are expressed.[117] Mammalian Ft cages expressed in the heart are predominantly H-chain, whereas those expressed in the liver a mainly formed of L-chain subunits.[117] The mammalian protein cage has an outer diameter of 12 nm and an inner cavity of 7-8 nm (Figure 1.14) in diameter and an interior volume of 1.4×10^{-19} cm^3.[117] The H and L chain subunits for mammalian Ft share 55% homology and have an average weight of respectively 21 kDa and 19 kDa.[117] Although the amino acid sequence can vary, the tertiary and quaternary structure of the protein cage is highly conserved.[117]

The subunits are composed of five helices (A-E) and can interact with each other along the 2-fold axis to form the protein cage (Figure 1.14).[118] In the 24-mer each subunit can interact with the other six subunits forming four interfaces (C1-C4) through hydrogen bonds and electrostatic interactions, following a 432 symmetry.[6] Among them the C2 interfaces are those characterised by the largest number of interactions and are therefore the most susceptible to sequence modification as they contribute significantly to the formation of the protein cage.[6] At the subunits interfaces there is the formation of two sets of channels (0.4 nm wide) that provide the connection between the interior core of the protein and the external environment: the eight 3-fold hydrophilic channels and the six 4-fold hydrophobic channels (Figure 1.14).[117] The 3-fold channels are formed by the end of helix C and the start of helix D from three subunits, their triangular opening (Figure 1.14) is lined with hydrophilic amino acids which generate an electrostatic gradient that guides the cations toward the protein core.[117,119] The six 4-fold hydrophobic channels are instead formed by 4 inwardly pointing E-helices (Figure 1.14) that have the function to allow the exit route for protons during the mineralisation of the iron core.[119]

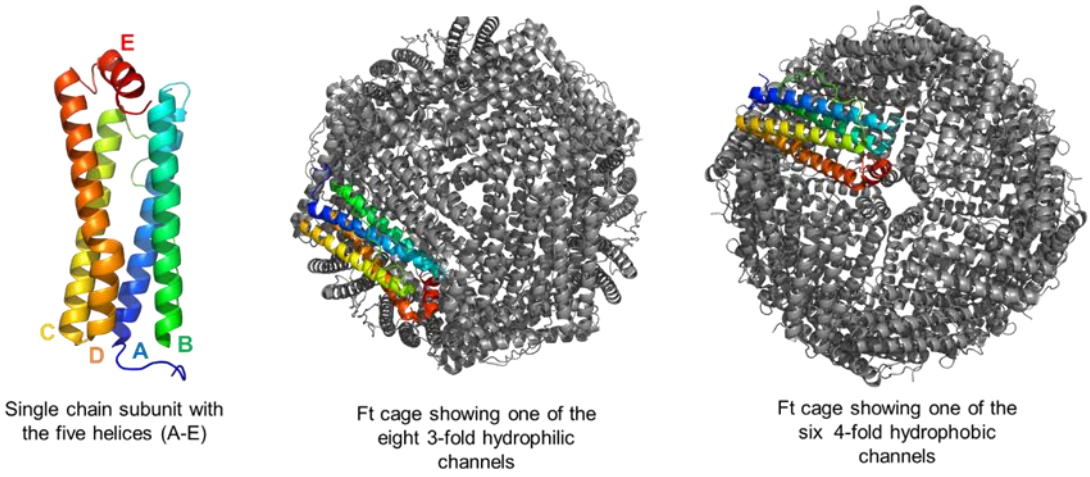

Figure 1.14. Structure of ferritin light-chain subunit and of the 24-mer with 3-fold and 4-fold channels.

Both H and L-chain subunits contribute to the nucleation of iron into Ft although with different roles. The H-chain Ft contains the ferroxidase centre which is responsible for the catalytic oxidation of iron (II) to iron (III).[117] The L-chain Ft instead favours the growth of the mineral core by providing the inner-facing 4-8 carboxylic acid residues that chelate the metal and act as nucleation sites.[117] The entry of iron into Ft heteropolymers is regulated by the saturation of the ferroxidase site. Here occurs the oxidation of 2 iron (II) ions upon consumption of oxygen by the formation of a μ-1,2

diferric peroxo-complex and then its precipitation into diferric-oxo-clusters (Figure 1.15-a).[117] When higher concentrations of iron (II) are present and for L-chain Ft homopolymers the incoming iron can be catalytically deposited on the surface of the growing mineral core.[117] Ft can theoretically accumulate up to 4500 iron atoms in this way as a ferrihydrite mineral core, in which iron has tetrahedral coordination.[117] It is also important to specify that Ft shows an electrochemical signature as a result of the electron transfer step involved in the formation/dissolution of its iron core.[117]

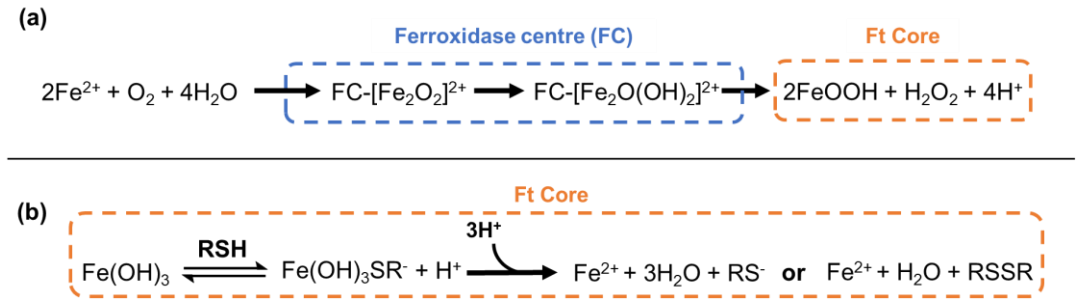

Figure 1.15. Ft iron core mineralisation (a) and demineralisation in the presence of thiols at acidic pH (b).

When the iron core is removed from Ft, the empty shell is referred to as apoferritin. The process of iron mobilisation to prepare AFt for loading of different agents like anticancer drugs can be performed using dithionite, thioglycolate and dihydroriboflavin 5'-phosphate (FMNH) (Figure 1.16).[115] The kinetics of the iron demineralisation can vary depending on the agent used even among thiol compounds. Although the mobilisation of iron is also possible with chelating agents only, the process is generally very slow.[115]

The use of reducing agents able to penetrate the Ft cage helps in the demineralisation of the iron core and prevents further metal deposition. In general, the reduction is favoured at low pH, where there are more protons available for the reduction of iron (III) to iron (II) (Figure 1.15-b).[116] The pH can significantly increase the rate of iron mobilisation exemplified in the case of dithionite where the reaction at pH 4.0 is 100 times faster than at pH 7.0.[115] Iron mobilisation by dithionite usually occurs in presence of a bipyridine chelating agent to aid for iron removal, which significantly reduces the protein recovery.[116] For this reason preparation of AFt from Ft is usually carried out using thioglycolic acid, even though the demineralisation proceeds at a slightly slower rate than with dithionite.[116]

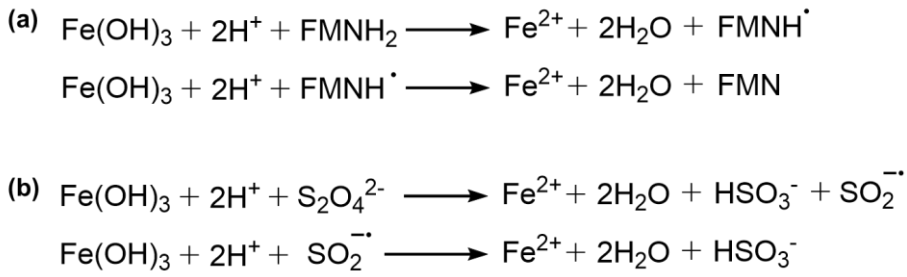

Figure 1.16 Iron (III) reduction into iron (II) by FMNH (a) and dithionite (b).

One of the intrinsic properties of AFt is its pH responsiveness.[6] The protein cage can disassemble and reassemble in a pH-dependent manner, this mechanism has been studied with different techniques like synchrotron small-angle X-ray scattering (SAXS),[6] dynamic light scattering (DLS) and small-angle neutral scattering (SANS),[120] or fluorescence resonance energy transfer (FRET).[121] The process of self-assembly is the result of the spontaneous association of both subunits into a supramolecular structure through hydrogen bonding, electrostatic, hydrophobic and van der Waals interactions, in which low-energy bonds are formed between subunits.[118] FRET studies reported that the presence of different ratios of L-chain and H-chain subunits can contribute to the speed of AFt cage assembly, with a tendency to prefer the formation of H/L heteropolymers over homopolymers.[121] AFt exists as an intact 24-mer spherical cage between pH 3.4 to 10.0, more acidic and more alkaline pH induces its disassembly into single subunits.[122] When the pH drops below 3.4 the disassembly proceeds gradually, forming at first two holes in the sphere until producing rod-like oligomers when the pH reaches 0.8 (Figure 1.17).[6] DLS studies demonstrated that the disassembly of the protein cage is a direct consequence of the progressive protonation of carboxyl and hydroxyl groups of the amino acid residues at the subunit interfaces, which in turn causes the disruption of the tertiary structure of the protein and alters its configuration, sometimes irreversibly.[120] Other studies reported the disassembly of the AFt cage under extreme pH conditions and the successful reassembly of the intact cage structure at pH 7.5.[123,124]

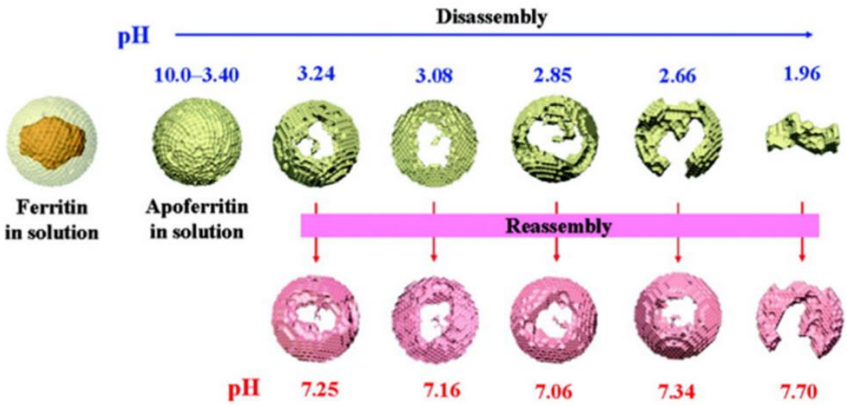

Figure 1.17. Scheme representing the pH-dependent disassembly and reassembly behaviour of AFt process as reported by Mihee *et al.*[122]

The pH-dependent disassembly of AFt becomes especially relevant upon protein internalisation by cells and its ability to release its cargo within the acidic environment of the lysosomes (pH 4.5-5.5) favouring the relaxation of the cage.[6] Receptor-mediated binding is the first step for the internalisation of Ft, then the adaptor complex (AP-2) recruits clathrin polypeptides that internalise the protein cage into a vesicle (Figure 1.18).[7] Upon internalisation the vesicle is converted into an endosome which progressively acidifies to form early endosome (pH 6.5), late endosome (pH 5.5) and then lysosome (pH 4.5).[7] The gradual acidification of the endosome allows for the release of the AFt content as a consequence of the swelling of the protein channels, thus becoming a crucial step to ensure intracellular delivery as of encapsulated therapeutic agents (Figure 1.18). The receptor-binding step for AFt internalisation is determined by the ratio of H and L-chain subunits forming the cage. The H-chain Ft has a high affinity for the transferrin receptor 1 (TfR-1) while the L-chain Ft is recognised by the Scavenger Receptor Class A Member 5 (SCARA5).[119] These receptors are expressed on hepatocytes, reticulocytes, lymphoid cells, erythroid precursors and several cancer cells.[125] In particular, the expression of TfR-1 by some malignant cancer cells was found to be up 100 times higher than in normal cells, suggesting an intrinsic targeting ability of H-chain AFt toward tumour sites.[126] Similarly, high expression of TfR-1 has been reported on the endothelial cells forming the BBB and in macrophages at the atherosclerotic plaques.[127,128] H-chain AFt was also reported to be able to translocate into the nucleus with the potential to be employed as a DDS for nuclear-targeted drug delivery as well.[129] Depending on the subunits' ratio the different Ft cages are predominantly expressed in different tissues. H-subunit rich Ft are found in erythroid cells, heart cells, pancreatic cells, kidney cells, lymphocytes and monocytes, which are characterised by high iron requirements for

their metabolic activities.[114] L-rich subunit Ft tend to accumulate largely in the liver and spleen, whose physiological function mainly requires iron storage.[114]

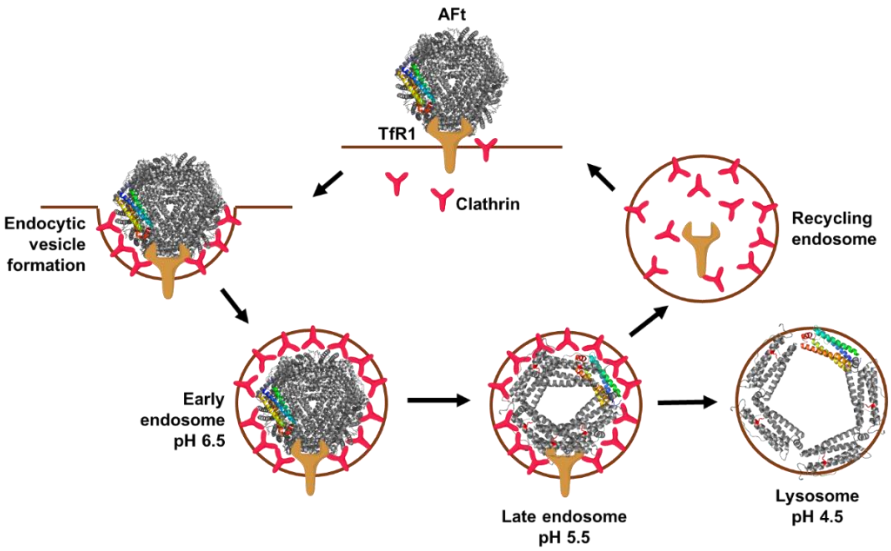

Figure 1.18. TfR1-mediated internalisation of AFt cage.

All the properties described above represent advantages in the potential use of AFt for many applications, as clinical and therapeutic tool. The AFt cage can be loaded with a wide variety of imaging, catalytic or drug molecules using multiple protocols. The protein subunits present an intrinsic tumour targeting ability in addition to the AFt cage nano-size which allows tumour accumulation via the EPR effect. More importantly, AFt can ensure the delivery of the drug-loaded nanoparticle with subcellular precision and to the nuclear compartment through its pH-dependent disassembly. Although promising, some of these features can pose challenges that need to be addressed according to the application envisaged. If on one side pH-dependent disassembly allows for the loading of large molecules into AFt, the harsh pH conditions prevent the encapsulation of acid-sensitive compounds. A similar problem is faced upon the delivery of acid-labile and enzyme-sensitive drugs through receptor-mediated endocytosis.[6] The affinity of AFt subunits for TfR-1 and SCARA5 receptors contributes to the effective and rapid clearance of the loaded cage from the bloodstream, which might hamper efficient drug delivery.[114] However, the external and internal surfaces of AFt are amenable to genetic and chemical modifications, providing a wide range of solutions to the above-mentioned challenges.

1.4.2 Apoferritin isoforms: horse-spleen and human apoferritin

Ft is a ubiquitous protein of which there can be identified three types according to their structural features: classical Ft, bacterioferritin and DNA- binding protein from starved-cells (DPS).[119] The classical Fts composed the largest group present in nature and include the mammalian Fts.[119] Bacterioferritins are composed of 24 identical subunits and bind an heme-like iron protoporphyrin between two subunits.[117] DPS is smaller Fts (typically 12-mers) and functions to protect bacterial chromosomes.[119] In mammals Fts can be found in the cytosol, nucleus and mitochondria for iron storage, but also in blood plasma, synovial and cerebrospinal fluids.[68] The mammalian Fts mainly employed for drug delivery are the horse-spleen (HSFt) and the human (HuFt) isoforms. The sequence homology between HSFt and HuFt is between 83-95 % for L-chain and 55 % for the H-chain subunit.[130] The denaturation temperatures of HSFt and HuFt at pH 7 are 93 and 77 ◦C, respectively.[131] HuFt is preferable as drug delivery capsule due to its reduced immunogenicity and the possibility to be genetically engineered for tumour targeting.[68] While HuFt requires in-house production for its use in experimental procedures, HSFt is a commercially available alternative that has been more extensively used for drug encapsulation studies and also favoured by the comparability of the *in vivo* results.[68] However, it must be highlighted that while the subunits composition of HuFt cages may vary, that of HSFt is 90 % L-chain and 10 % H-chain, a factor that can affect receptor affinity and metal binding.[131]

1.4.3 Apoferritin applications in nanotechnology and drug delivery

The interest in AFt for biotechnology applications can be summarised by two main properties of the protein cage: the possibility to functionalise the external and internal surfaces of the protein shell and its pH responsiveness. In addition to these, AFt is biocompatible, biodegradable, has an ideal nano-size for many applications. These features have been applied to the development of several AFt-based systems in the field of nano theranostics, biorthogonal therapy, gene delivery, vaccines, tissue engineering, food science, catalysis and nanoelectronics.[7,117] The protein cage is especially valuable in the field of anticancer drug delivery and diagnostics. Ft has been extensively studied as endogenous iron storage protein and therefore has well-documented toxicity, biodistribution and excretion profile.[117] AFt particles can be easily obtained using standard biotechnology methods, with encapsulation protocols that can be potentially optimised for the loading of a wide range of therapeutic agents.

1.4.3.1 Preparation of Apoferritin particles by encapsulation

The encapsulation of organic and inorganic compounds into AFt has the advantage of improving their water solubility, thermal stability, photostability, and cellular uptake.[7] The preparation of AFt-drug formulations reported in the literature consists of two methods mainly dictated by the size and pH stability of the cargo: nanoreactor route and reassembly route (Figure 1.19).[132,133,134] The nanoreactor route is usually employed for small molecules able to enter the AFt cage by diffusion through the 8 hydrophilic or 4 hydrophobic channels whose diameter is 0.3-0.5 nm (Figure 1.19).[133] Cisplatin,[135,136] gefitinib[137] and temozolomide[138] have been encapsulated via this route. The reassembly route is based on the ability of AFt to disassemble and reassemble at different pH conditions.[139] The experimental method involves the gradual acidification (pH 2) or alkalinisation (pH 11) of the protein solution and the dropwise addition of the drug.[133,139] The pH would then be restored to neutrality to allow reassembly of the cage. Anticancer agents including doxorubicin[140] and olaparib[124] have been encapsulated via the reassembly route.

The main disadvantages of the reassembly method are the requirement for the loaded agent to withstand harsh pH conditions and the limited recovery of the intact AFt cage as the disassembly process is not fully reversible.[134,122,141,120] Furthermore, recent reports have shown that the AFt cage is not a rigid structure, but rather a flexible macromolecule that can encapsulate larger molecules like uranyl acetate dehydrate, phosphotungstic acid and curcumin by diffusion through its channels.[141] The flexibility of the AFt cage reported by this study opened the possibility to avoid the disassembly-reassembly procedure when necessary even for compounds that wouldn't normally fit through the protein channels.

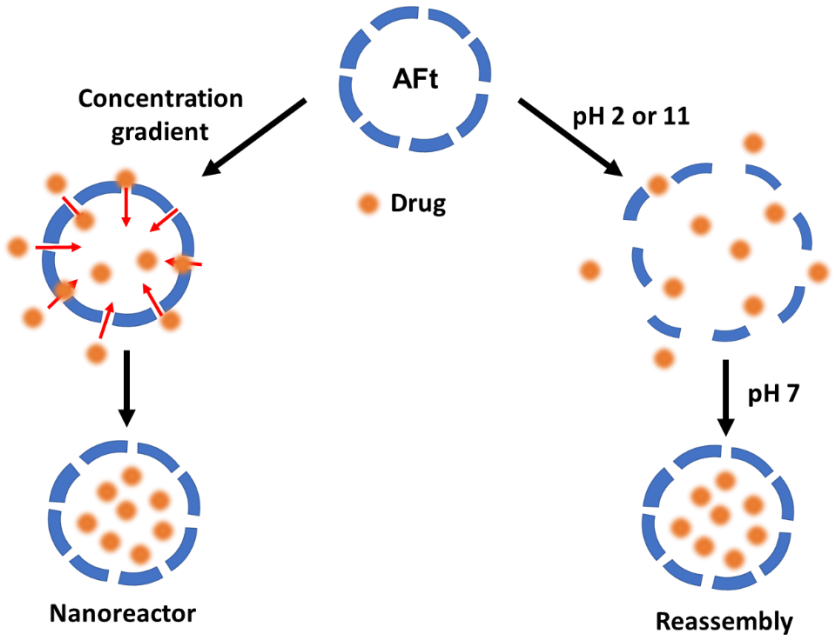

Figure 1.19. Routes for drug encapsulation into AFt: nanoreactor (left) and reassembly (right).

Many groups have tried to address the challenges related to drug encapsulation into AFt using different strategies. In addition to low protein recovery, encapsulation by pH-dependent disassembly/reassembly is not suitable for acid-labile compounds. Two approaches have been developed to resolve this issue: one is to make AFt disassemble under milder pH conditions using denaturing agents or mutation of the protein and the other is to make the protein cage responsive to other stimuli less likely to favour drug degradation. Wang *et al.* developed a protein cage with weaker inter-subunit interactions which was able to disassemble at pH 4.[142] In this work the modification of 2-3 amino acids in the AB loop of the human H-chain AFt subunits influenced the inter-subunit interactions at the C3-C4 interface, thus affecting the disassembly process.[142] In 2016 Chen *et al.* obtained a similar result by deleting 23 amino acids on the DE turn and the E helix on human H-chain AFt.[118] Alternatively, Huard *et al.* reported the production of a copper-responsive AFt cage.[143] Their strategy was based on the alteration of the protein-protein interactions to make them responsive only to metal binding using the reverse-templated interface redesign (rMeTIR).[143] The introduction of His_6 motifs into the 4-fold protein channel interfaces of AFt can make the protein cage responsive to two different types of stimuli: pH and metal ions.[144] The His_6 motifs pH-dependent protonation allow for the disassembly under neutral conditions and reassembly at alkaline pH= 10.0.[144] Alternatively, the ability of histidine to interact with transition metals also drives the reassembly of the protein cage when metals are present in solution.[144]

One of the main challenges of AFt-drug delivery systems is the leakage of small molecules from the cage, which is the main drawback for formulations prepared by the nanoreactor route.[145] Even though this method is less disruptive than reassembly, it can lead to poor control over drug loading and retention. Small molecules can leak from the cage shortly after encapsulation, which prevents the targeted drug delivery strategy on which the rationale for the clinical use of AFt is based.[139] Furthermore, the loading is dependent on the size of the loaded agent compared to the protein channel's diameter. Drug encapsulation and entrapment inside AFt relies on the equilibrium between the protein and the drug. The stability of the AFt-drug formulation is dependent on the hydrophobicity/hydrophilicity of the drug, the interactive sites of AFt under the encapsulation conditions and the nanocage integrity after the preparation.[119] Due to the presence of negatively charged amino acids lining the interior of the AFt cage, metal ions, organic molecules with a net positive charge and reactive precursors can be trapped in significantly higher amounts compared to noncharged drug molecules.[119] Methods exploiting the flexibility of the AFt channels in the presence of denaturants such as urea, guanidine or Triton X-100, and the use of pH stressors like acidic acetic buffer at pH 5.0 have been employed to increase the loading efficiency of the protein without disrupting the cage.[146,147,148] Another interesting approach was taken by Wang *et al.* that attempted to modify the natural hydrophilicity of the AFt cage by substituting the fifth helix of the human H-chain with hydrophobic-hydrophilic RGD peptides.[149] They were able to produce an amphiphilic AFt cage loaded with Epirubicin (hydrophilic) and externally coated with camptothecin (hydrophobic), thus obtaining the highest drug loading capacity reported for human AFt.[149]

To improve drug loading and reduce undesirable drug leakage from AFt formulations it is essential to understand the interactions between the protein cage and the agent to encapsulate. This can guide the optimisation of the encapsulation procedure as well as the choice of the best encapsulation method according to the agent intended for use. Another approach developed to improve the performance of AFt-drug systems was the introduction of helper molecules that can exploit the natural affinity of the AFt core for positively charged species.[119] Many anticancer agents such as doxorubicin and olaparib when complexed with metal ions before encapsulation showed greater drug loading efficiency and stability. The encapsulation of doxorubicin-copper (II) achieved an increase in drug loading rate from 14 % to 73.5 %.[124] In a similar work using olaparib-copper (II) complexes the drug loading increased from 0.69 olaparib molecule per AFt to 4.8 when pre-complexation with the

metal was performed.[150] The loading of 5-fluorouracyl with gold NPs and that of TMZ active drug 5-(3-methyltriazen-1-yl)imidazole-4-carboxamide (MTIC) with copper (II) immobilised the drugs inside the AFt core, dramatically reducing the leakage under storage and physiological conditions.[8,151] Another approach was that of using negatively-charged aspartic acid sequences to stabilise and prevent the leakage of positively charged agents like daunomycin.[145]

Optimisation of AFt-drug formulations procedures is paramount for its application in the clinical setting, especially in the field of anticancer chemotherapy. Significant effort has been made in this direction and a better understanding of the interactions between the protein and different loading agents at different conditions would provide valuable information to future efforts. Although an efficient drug delivery vehicle must be able to load a significant amount of drug molecules and prevent uncontrolled leakage equally important is the development of strategies for efficient targeting of the AFt formulations.

1.4.3.2 Functionalisation of the Apoferritin surface for precision targeting

The need for AFt surface functionalisation derives from the evidence that the innate receptor affinity of the protein cage is not always enough to satisfy the therapeutic targeting needs.[7] AFt pH-sensitivity would make it available almost exclusively for intravenous administration. Therefore, it is critical to reduce the likelihood of the AFt formulations entering non-specific organs or tissues to avoid undesired side effects. The expression of the TfR-1 receptor is present at basal low levels on normal cells, cells requiring high amounts of iron like placental trophoblasts and maturing erythroid cells.[152] Other non-proliferating cells expressing TfR-1 are those forming the brain endothelium, endocrine pancreas, seminiferous tubules of the testes, cells of the pituitary, luminal membranes of the breast, hepatocytes, Kupffer cells of the liver, and tubules of the kidney.[152] Significant levels of SCARA5 expression have been detected in prostate, breast, stomach, lung and cardiac cells.[7]

To increase the targeting ability of AFt beyond its innate receptor affinity it is possible to modify the protein outer surface with ligands with high specificity for the target tissue. The modification of the AFt shell can be performed through covalent binding or genetic engineering of the protein sequence.[6] The study performed by Wetz and Crichton to identify the number of reactive residues expressed by horse spleen AFt showed that there are one cysteine, 4-5 lysines and 11 carboxyl groups available per protein cage.[153] They found that when all of the carboxyl groups were blocked the protein lost its catalytic activity for iron accumulation.[153] This suggested the essential

function of one or more of the carboxylic groups in the oxidation of Fe^{2+} into Fe^{3+}.[153] These functional groups expressed by AFt can be labelled using *N*-hydroxysuccinimide (NHS) esters, NHS/EDC-activated carboxyl groups and maleimide groups.[6] Superior *in vitro* and *in vivo* antiglioma activity was reported for horse spleen AFt after covalent conjugation via sufhydryl-maleimide coupling reaction to the GKRK peptide ligand.[154] The natural affinity of AFt to TfR1 receptors combined with the addition of the ligand for the heparan sulfate proteoglycan (HSPG) over-expressed on endothelial cells during angiogenesis and glioma cells, endowed the protein cage with higher specificity.[154] PEGylation is a clinically approved surface modification of the AFt cage that has demonstrated improved tumour-targeting to melanoma cells and was also employed to increase the protein half-life (Figure 1.20-a).[155]

Functionalisation of AFt through genetic engineering can be carried out at the N-terminal and C-terminal of the sequence of the subunit. The position of the N-terminal makes it the ideal site for genetic modification of the protein external surface.[6] The introduction of the Arg-Gly-Asp (RGD) tripeptide on the surface of AFt is a common modification to target the integrin receptors which are a considered angiogenic tumour biomarkers.[7] Another frequent strategy involves the targeting of the folate receptor, which is overexpressed in many human malignant cells.[7] Falvo *et al.* produced a genetically fused human AFt with a proline (P), serine (S) and alanine (A) rich PAS polypeptide sequence (Figure 1.20-b).[156] The modified protein showed greater solubility and stability in plasma and enhanced encapsulation of doxorubicin, with improved half-life and anticancer activity.[156]

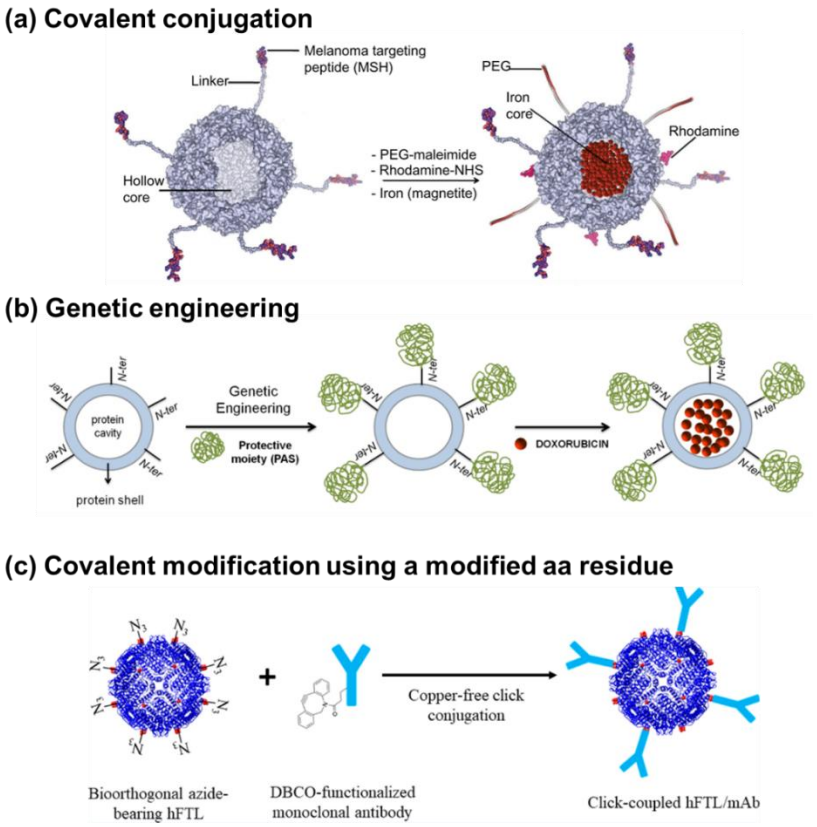

Figure1.20. Examples of surface modification of AFt for targeting (a) Design of an HFt-based nanoplatform for melanoma targeting as reported by Vannucci *et al.*[155] (b) Synthesis of the PAS-fuse human AFt as reported by Falvo *et al.*[156] (c) Genetic incorporation of unnatural functional groups for antibody conjugation as reported by Khoshnejad *et al.*[157]

Notably, chemical modification can also by achieved upon engineering of the AFt amino acid sequence, which avoids the use of coupling reagents.[6] Recently, Wang *et al.* reported the production of a recombinant AFt nanoparticle that can be functionalised with multiple tumour specific antigens through a click-link system for the production of a vaccine nanoparticle.[158] This system used the expression of a SpyCatcher functionality on the AFt outer surface by genetic cloning into the protein sequence which can be easily labelled by formation of an isopeptide bond with tumour specific antigens fused to a SpyTag.[158] This modified AFt was able to enhance by 2-3 fold a tumour specific antigen cytotoxic T-lymphocyte response.[158] Another example of AFt functionalisation by 'clickable' conjugation was reported by Khoshnejad *et al.* with the production of a recombinant AFt L-chain bearing unnatural amino acids expressing azide groups (Figure 1.20-c).[157] The click reaction was used for the conjugation of antibodies for ICAM-1 and was employed for imaging and treatment of pulmonary inflammatory conditions.[157]

Another important observation regarding the functionalisation of the outer AFt surface concerns the potential immunogenicity of the motifs added to the peptide sequence. For native AFt the potential immunogenicity is related to the source from which the protein is isolated which can be horse, pig or a bacterial strain for recombinant AFt.[7] Therefore, careful evaluation of the potential immunogenic reactions induced by the motifs which are used to functionalise the AFt surface needs to be carried out if clinical application is envisaged.

1.4.4 Incorporation of metals and their complexes into Apoferritin

The iron storage function of Ft correlates with the high metal affinity exhibited by the AFt cage. The protein cage can bind cadmium (II), zinc (II), copper (II) and manganese (II) other than iron (II).[117] The electrostatic potential generated in the hydrophilic 3-fold channels plays a significant role not only for the ferrihydrite nucleation but also for the accumulation of nonferrous metals. However, there is no catalytic activity exerted by the ferroxidase centre on the non-native inorganic substrates which correlates with the formation of fewer uniform cores.[117] The encapsulated iron core of Ft provides an effective contrast agent, at the same time the confined space the AFt shell is a biocompatible structure for metal accumulation for diagnostics, therapy and metal nanoparticles synthesis.[117]

Accumulation of metals into AFt has been studied to provide better MRI formulations.[125] The encapsulation of polymer-coated small and ultrasmall particle iron oxide (SPIO and USPIO) was attempted into AFt by Valero *et al.* showing comparable results to the commercially available reference.[159] In addition to iron, AFt can accumulate other metals with some differences depending on the protein electrostatic potential, concentration, buffer pH and time of incubation with the ion of interest.[117] gadolinium (III) and manganese (II) were encapsulated into AFt to provide the targeted visualisation of tumour tissue, angiogenesis and melanin formation.[125] The x-ray crystallography studies performed by Ueno *et al.* reported that palladium (II) ions bind almost exclusively to the 3-fold channel (coordinated by Cys48, 126 and a water molecule) of the horse L-chain AFt subunit and to additional residues in the so-called accumulation site (coordinated by Cys48, Glu45 and His49).[160] They found that the metal coordination mode is influenced by the presence or absence of an external ligand and that the Cys126 and Cys48 are essential for palladium (II) binding.[160] When palladium (II) complexes were incubated with AFt, up to 193 palladium (II) ions were retained by the protein cage.[160] When AFt was incubated with gold (III) the overall number of metal ions retained by the protein cage was 74.[161]

Although the X-ray crystallography of the gold (III)-loaded AFt showed metal binding to similar sites to palladium (II), the two metals have different coordination preferences: palladium (II) has affinity for the carbonyl groups of glutamic and aspartic acid, and for cysteine methionine and histidine.[161] Gold (I) instead binds preferentially to cysteine, methionine and histidine.[161] Horse-spleen AFt loaded with 4-PF_6 of platinum (II)/gold (I) led to the accumulation of 10.3 gold (I) and 16 platinum (II) atoms per subunit.[162] The study of these protein-metal complexes by X-ray crystallography revealed that these 4-PF_6 complexes dissociated during the encapsulation, with the metal ions of gold (I) preferentially binding close to the Cys126, while platinum (II) seemed to be trapped in the bulk of the protein core.[162] Similarly, the dissociation of the metal from its external ligand upon encapsulation was observed for the Auoxo gold complexes (figure 1.20).[133] The encapsulation of the HSAFt with the Au_2Phen and $Auoxo_4$ reported average gold retention of 384 and 432 ions respectively, a value much higher than that obtained by incubating the cage with $AuCl_4$ only.[163] For some Auoxo complexes, the UV spectra observed even suggested the formation of metal gold NPs, similar to those formed by reduction with $NaBH_4$.[164] These findings again supported that the largest proportion of the metal retained was trapped in the bulk forming the core of the protein cage and that part of the metal dissociated from its ligands.[163]

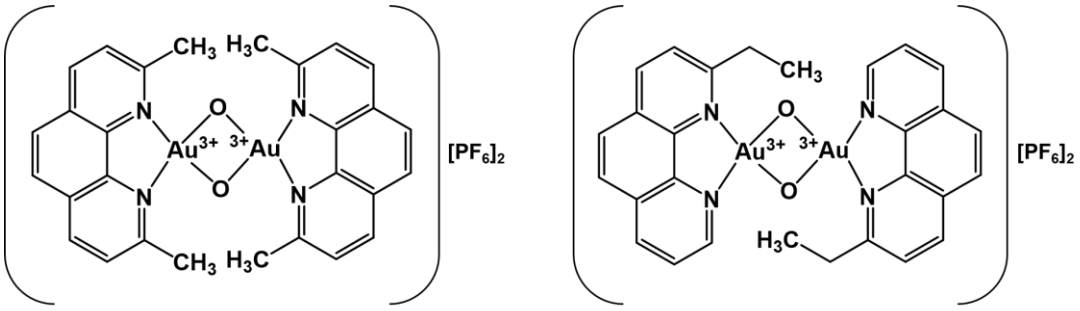

Figure 1.20. Structures of the gold(III)-complexes Au_2Phen and $Auoxo_4$.

The exposure of encapsulated gold to $NaBH_4$ led to the observation of sub-nanoclusters and gold NPs formation into the protein cage.[133] Even though gold binds preferentially the external surface of AFt over the internal core, by a two-step reduction process it was possible to promote the nucleation of gold NPs into native HSAFt.[165] The process of metal NPs formation inside AFt using the nanoreactor route was tracked using a combination of X-ray crystallography, spectroscopy, microscopy techniques.[166] This work outlined the process of gold NPs' formation into recombinant

HSAFt as composed of four phases occurring in the 3-fold hydrophilic channels: metal deposition, nucleation, formation of sub-nanoclusters, growth by aggregation of the clusters to form NPs.[166] One of the most widely used methods for the synthesis of metallic NPs is chemical synthesis, often referred to as bottom-up or seed-mediated growth. This protocol involves the reduction of the metal salts using strong agents ($NaBH_4$, hydrazine, CO, glucose, ascorbic acid) that can provide electrons for the reaction.[167] The product of this reaction is a metal with an oxidation state equal to zero and that will act as a nucleation centre for the growth of NPs. Capping agents are usually added to the reaction mixture as surface stabilisers, to prevent metal NPs oxidation in solution by air.[168,169] In this context, the use of biomolecules such as AFt can afford NPs' synthesis methods that avoid the use of high temperatures or harsh chemicals to produce stable and monodispersed solutions.[170,165]

The negative electrostatic potential generated by the amino acid lining its internal surface and its enclosed structure make AFt a template to restrain NPs growth up to its core size (≤ 7 nm) and as a coating to increase their stability in solution.[171] AFt provides the metal NPs with greater stability toward oxidation, like in the case of silver NPs used as antimicrobial agents.[172] But the protein cage has also been demonstrated to be useful in camouflaging platinum NPs used for their ROS scavenging properties, improving their biocompatibility compared to polymer-coated NPs.[173] Besides the advantages of using protein-coated metal NPs it would be interesting to understand how the AFt-metal NPs themselves can provide valid support for therapeutic agents in improving the control over drug delivery. Anticancer agents with metal coordinating groups could be introduced inside the AFt cage containing the metal NPs to which they will remain bound until AFt internalisation by cancer cells and content release in the endosome. A successful example of this approach was reported by Liu *et al.* who synthesised gold NPs (d= 3 nm) into AFt by *in situ* reduction of the $AuCl_4$ with $NaBH_4$ following the protocol developed by Fan *et al.* (Figure 1.21).[151,165] They then used the void space of the protein core to encapsulate the anticancer agent 5-fluorouracil (5-FU) producing a drug delivery system characterised by higher stability, increased cellular uptake of 5-FU, increased selectivity, ability to increase cancer cell sensitivity to the anticancer agent and almost no drug leakage at pH 7.4.[151] The advantages of preparing AFt-coated metal NPs include the control over their size, composition, morphology as well as improved stability, solubility and biocompatibility.[174]

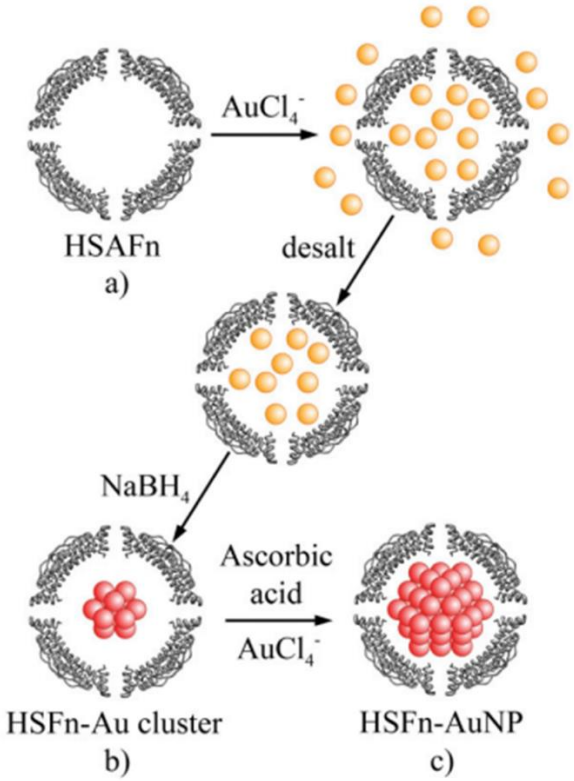

Figure 1.21. Diagram of the two-step synthesis of Au NPs inside HSAFt as reported by Fan *et al.*[165]

When the anticancer platinum (II) complex cisplatin was encapsulated into HSAFt (45 platinum ions /cage) its uptake by cancer cells was significantly improved compared to the agent alone *in vitro* (uptake ratio 0.425% vs 0.095%).[175] However, the cytotoxicity of the AFt-cisplatin complex was lower than that exerted by the naked drug, a phenomenon that was related to the limited release of the drug molecules from the protein cavity in the intracellular environment.[175]

The introduction of metals and their complexes into AFt has been studied for different purposes, ranging from green metal NPs synthesis to drug delivery. The detailed analysis of the X-ray crystallographic structures of the metal-bound subunits has highlighted the differences between the L and H-chain AFt and the preferred binding sites for the metals tested. Given the physiological iron storage function of the AFt cage, the protein-metal complexes showed greater stability than AFt encapsulated with organic compounds. These results can provide valuable information on how to improve the stability of organic therapeutic agents loaded within AFt for drug delivery.

1.5 Research aims

The use of proteins' hollow spaces for the introduction of chemical functionalities to produce artificial metalloenzymes and drug delivery systems has led to increased interest in protein engineering for therapeutic and diagnostic applications. AFt provides a valuable platform having the function of iron storage which requires a wide hollow space for metal accumulation. This feature can be exploited for metal complex accumulation by non-covalent interactions and for covalent protein modification. The potential use of AFt as confined space for metal complexes with catalytic activity is supported by several examples reported in the literature: platinum, palladium and iron-based AFt nanoparticles mimicked catalase and peroxidase enzymes.[176,161] Polymerisation of phenylacetylene into polyphenylacetylene were reported from an AFt-rhodium complex.[177] Furhtermore the affinity of AFt for metals is reported to achieve better control over the retention and release of encapsulated anticancer exposing metal coordinating moieties. Pre-complexation of olaparib with copper favoured drug retention into AFt for up to 6 h in physiological conditions.[124] The active drug of TMZ (MTIC) immobilised using AFt-copper adducts led to increased drug bioavailability and enhanced antitumour effect compared to TMZ treatment.[8]

The aim of the research discussed in this thesis was to understand how the metal affinity of different AFt isoforms (human heavy chain and horse spleen) can be exploited to load copper (II) complexes, through encapsulation and covalent conjugation, to improve the stability and the controlled release of anticancer prodrugs and to assess the *in vitro* stability and cytotoxicity of these formulations. The metal complex copper(II)-1,10-phenathroline was selected given its intrinsic antitumour effect and its ability to interact with temozolomide as reported in previous studies.[8] To achieve this aim, the experimental work was developed to address three major objectives:

1. **Encapsulation of a metal complex with cytotoxic activity inside horse spleen AFt, characterisation of the protein-metal adducts and evaluation of its *in vitro* activity**. Horse spleen AFt is extensively used for the preparation of anticancer agents for drug delivery due to its similarity to the human AFt and ease of preparation.[68] Therefore, it would provide the best option for the non-covalent encapsulation of copper(II)-1,10-phenanthroline. This metal complex can act as helper molecule for the retention of small organic compounds like TMZ into AFt by metal coordination and is also the precursor of a class of anticancer metallodrugs known as Casiopeinas®

(Section 1.3.4). The effectiveness of these copper(II)-phenanthroline derivatives against many cancers is characterised by poor specificity due to interactions of the metal with cellular components.[102,104] Therefore, the negatively charged amino acids lining the internal surface of AFt could stabilise copper(II)-phenanthroline and reduce any undesired toxicities caused by these interactions.[141,178]

2. **Assessment of the ability of AFt-copper(II) adducts in retaining and affecting the accumulation and the release of the anticacer agent TMZ.** The use of the AFt-copper(II) adducts for the nanoreactor encapsulation of TMZ would provide indication on the stability of the anticancer agent during the preparation and upon exposure to physiological (pH 7.4, 37 °C, 24 h) and endosomal conditions (pH 5.5, 37 °C, 24 h). It is hypothesised that upon encapsulation the direct coordination of copper (II) by the deprotonated nitrogen on the imidazole ring of TMZ[179] would promote the formation of bulky copper (II) complexes with two ligands (one phenanthroline and one TMZ molecule) less likely to leak through the AFt channels and with potentially enhanced anticancer activity when tested on GBM cells. The studies that reported the complexation of doxorubicin (543 Da) and olaparib (434 Da) with copper (II) aimed at improving the number of drug molecules loaded into AFt.[124,150] In this case the use of TMZ, a much smaller compound (194 Da) that can easily fit into the protein channels, could provide better indication on the capacity of metal ions to stabilise small drugs into the AFt cage. Furthermore, the use of a copper(II)-phenanthroline complex could prevent the conversion of TMZ into MTIC that was reported when free copper(II) was used to stabilise the drug into AFt.[8]
3. **Production of a human heavy chain AFt cysteine mutant.** Although extensively used, horse spleen AFt could be immunogenic compared to human AFt, an effect that requires attention when studying formulations for clinical application.[68] Furthermore, human AFt could be produced in-house and engineered by insertion of a cysteine mutation to allow for the introduction of the copper(II)-phenanthroline complex by covalent conjugation. In the case of human heavy chain AFt, the insertion of an additional metal binding functionality would help increasing its metal affinity, naturally lower than that of light chain AFt (main component of horse spleen AFt cages).[180,131] The use of haloalkyl reagents provides a valid alternative to maleimides for protein conjugation due to the ease and reliability of the reaction.[78] For this reason it was envisaged that labelling of the cysteine

human AFt mutant with 2-bromo-*N*-(1,10-phenanthrolin-5-yl)acetamide would provide the advantage of greater control over the localization of the coordinating metal and the composition of the AFt labelled cages upon further encapsulation of TMZ. Furthermore, the covalent immobilisation of positively charged species on the interior of AFt would favour the entrapment of TMZ and reduce its leakage when exposing the nano-formulation to physiological and endosomal conditions.

2. Encapsulation of copper-1,10-phenanthroline by Apoferritin and functionality of the resulting adducts

2.1 Background

Ft is an iron storage protein that has been extensively studied as a drug delivery vehicle due to its size (12 nm external diameter and 8 nm inner cavity) and its biocompatibility.[139,181,133] Removal of the iron mineral core leaves the empty protein shell, AFt that can be loaded with anticancer drug molecules, catalysts and nanoparticles.[116] The AFt cage is a 24-mer that can be assembled as a homopolymer or heteropolymer, according to the metabolic requirements of the tissue where the protein is expressed.[114] These isoferritins are formed by different ratios of two subunits: the Ft light chain and the Ft heavy chain. The AFt from horse spleen (HSAFt) is rich in light chain subunits (19 kDa) combined with a minority of heavy chain (22 kDa) subunits and is commonly used for encapsulation studies due to its structural similarity with human Ft.[182]

One of the methods used to load AFt with small molecules is passive diffusion through the protein channels connecting its surface with the protein core (Figure 2.1).[138,183] These channels (0.3-0.5 nm) are formed at the interface between the protein chains forming the cage.[133] Although efficient and easy to perform, the limitation of this method is that the loaded molecules must fit inside the protein channels, which also results in their leakage soon after the encapsulation.[139] The natural affinity of AFt for iron, which is extended to other metals provides a way to address this issue. Due to its physiological function, the internal surface of AFt is lined with acidic amino acid residues which normally stabilise the iron core, but that can also be exploited as binding sites for other metal cations like platinum (II), gold (III) and/or silver (II).[141,178]

The encapsulation of metal complexes and their analysis through X-ray crystallography has confirmed that metal coordination occurs by amino acid residues lining the internal surface of the protein and its channels.[141,163,164] Cytotoxicity studies on the AFt encapsulated with the Auoxo gold (III) complexes showed that the amount of metal required to kill half of the cell population is 30-100 times lower compared to the free complexes, with IC_{50} values ranging from 6-30 μM.[163] *Zhen et al.*[150] produced a copper(II)-doxorubicin metal complex with greater AFt loading efficiency by nanoreactor route (up to 73.5 %) rather than reassembly.[150,140] The integrin targeted AFt-metal-drug system also showed longer half-life, higher tumour growth inhibition

and decreased cardiotoxicity compared to doxorubicin alone (Figure 2.1).[150] Similarly, complexation of the PARP inhibitor olaparib (Figure 2.1) with copper before encapsulation also yielded up to 7 times higher loading efficiency compared to encapsulation without metal, and drug retention for up to 6 h in physiological conditions.[124] AFt-copper adducts were also used to immobilise the active drug of TMZ (Figure 2.1), MTIC, increasing the drug bioavailability and enhancing its antitumour effect compared to treatment with TMZ alone.[8] Another method to increase the stability of the metal-drug adducts inside AFt is to initially form metal NPs inside the protein and then load the drug of interest. The process of gold metal NPs nucleation into AFt was tracked and applied to sequester the cytostatic drug 5-fluoro-uracil (5-FU) to inhibit the growth of liver cancer cells.[151,166]

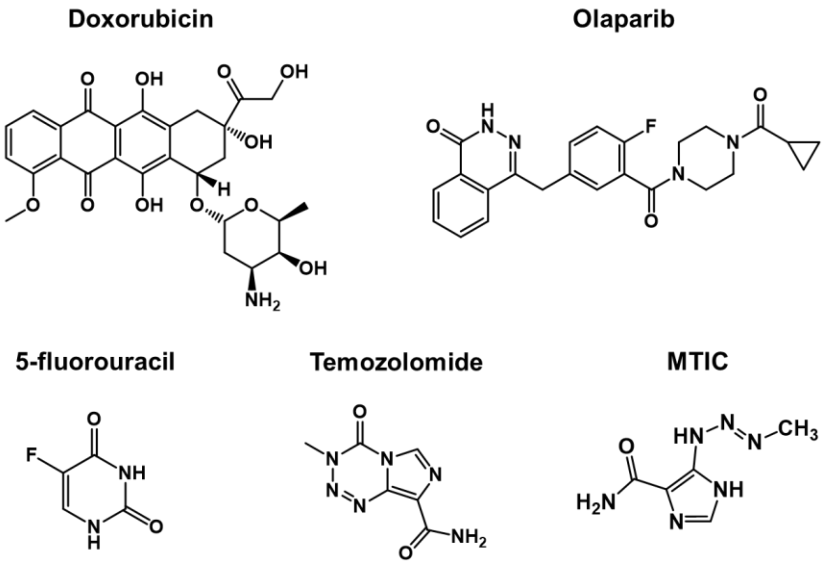

Figure 2.1. Representation of some of the anticancer agents encapsulated into AFt.

In addition to the complexes mentioned above, other metal complexes of phenanthroline and/or bipyridine have been shown to exhibit anticancer properties.[184] On its own, the 1,10-phenanthroline ligand has shown antibacterial activity due to its metal chelating properties and its ability to interact with DNA. Casiopeinas® are a class of copper coordination compounds where the primary ligand is either a bipyridine ring or a phenanthroline ring.[102] They have very potent pharmacological activity against several cancers, with some of these compounds are currently under clinical evaluation.[101] The aromatic nature of the ligands and the metal centre provide a variety of mechanisms of action against cancer cells and microorganisms such as generation of ROS causing DNA oxidation and degradation and depletion of antioxidant defences, mitochondrial toxicity through CYP450 inhibition and DNA

intercalation. Among them, Cas III-ia (Phase I clinical trial) and Cas III-Ea (Chapter 1, Section 1.3.4) have been identified as those baring the best balance between human cells toxicity and efficacy against cancer cells and parasites.[103] However, the cytotoxicity that copper phenanthroline derivatives can exert toward healthy human cells is greater than that of their bipyridine analogues.[102] The poor selectivity of these agents in association with their intercalating, redox and hydrolytic capacity strongly increase their ability to inhibit cell growth compared to their bipyridine analogues.[102,104] The presence of charged metal species favours participation in a variety of chemical and biochemical processes before reaching their target.[105] This feature of the phenanthroline derivatives makes them more efficient at killing cancer cells but very damaging to healthy human cells.

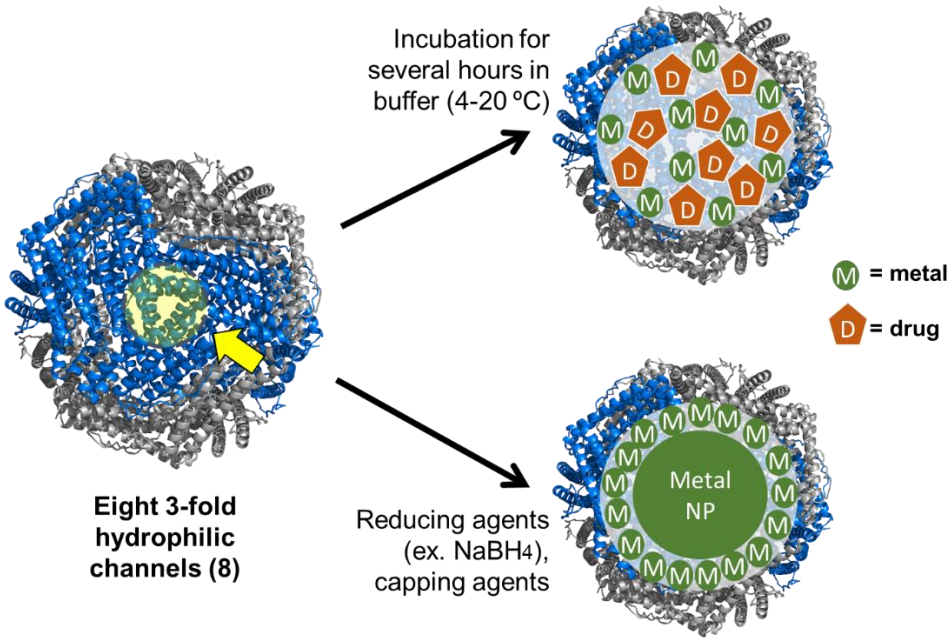

Figure 2.2. Representation of the eight hydrophilic channels used to load HS-AFt for drug encapsulation and the synthesis of nanoparticles (NPs). The AFt from horse spleen has been reported as a potential platform for efficient encapsulation of drug molecules with metal coordinating groups[124] and controlled metal NPs synthesis.[172]

This work investigates the ability of the HSAFt cage to retain a metal complex of copper with 1,10-phenanthroline and tests the effect of encapsulation on its anticancer activity. It was hypothesised that the encapsulation within HSAFt would be beneficial to diminish their toxicity to healthy cells by improving the selective uptake into cancer cells. Furthermore, the possibility to functionalise the external surface of AFt and exploit its enhanced uptake by iron-avid cancer cells can provide better control over the site-specific release of this complex to in selected tissues.[185,186]

Whilst other metal phenanthroline complexes were successfully incorporated into AFt, as drug delivery agents,[163] Casiopeinas® have not been loaded into AFt yet which makes it the aim of the study described in this chapter. It was envisaged that this experimental work would provide valuable information about the impact of the AFt cage on the cytotoxicity and stability of the copper-1,10-phenanthroline complex.

Accordingly, the objectives of this chapter are to achieve the encapsulation of a new metal complex with cytotoxic activity inside AFt and to evaluate the protein effect on its *in vitro* activity and selectivity.

2.2 Production and characterisation of AFt loaded with copper phenanthroline

The test agent selected for encapsulation inside horse spleen AFt is the precursor of a family of metallodrugs for which anticancer and anti-parasitic activity has been reported.[187,103] The planarity of the 1,10-phenanthroline ring contributes to cell cytotoxicity by direct interaction with cellular DNA and was found to be the electron donor ligand with the greatest cytotoxic activity.[104,187] For this reason, copper-1,10-phenanthroline was selected as the candidate test agent to analyse the effect of the AFt cage on this class of metal complexes.

2.2.1 Synthesis and characterisation of the copper-1,10-phenanthroline complex

The metal chelator 1,10-phenanthroline is the parent compound of the 2,2'-bipyridyl system.[102] However, 1,10-phenanthroline is characterised by the presence of a central ring, determining the rigidity of the planar conformation where the position of the two nitrogen atoms is fixed (Figure 2.3).[102] On one hand this makes metal coordination extremely quick and the coplanarity of the lateral rings favours the pharmacological activity of 1,10-phenanthroline as DNA and RNA intercalator. [102,187] However, in some experimental conditions the 3-ring system can cause steric effects that can dramatically slow down the formation of binary and ternary complexes with metal ions like copper.[188]

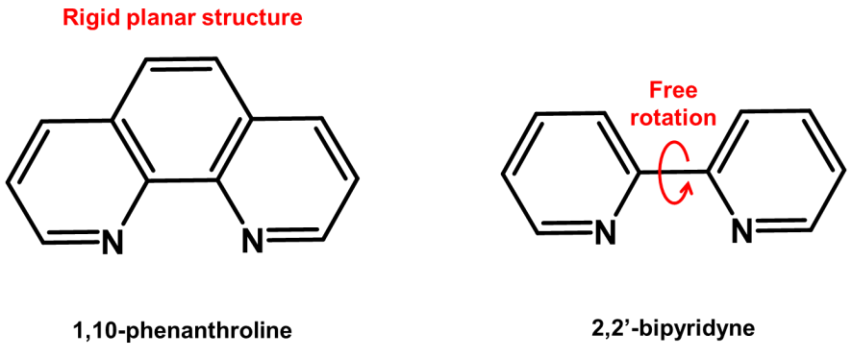

Figure 2.3. Structure of the 1,10-phenanthroline ligand and metal chelator and the 2,2'-bipyridine system.

Few studies report the formation rate, stability and ratio of complexes of copper (II) with 1,10-phenanthroline in aqueous solutions, with and without second ligands.[189,190,191] In general, the coordination number of copper (II) complexes can vary from four to six, usually accompanied by crystallographic structures characterised by tetrahedral distortions.[192] According to Ozutsumi *et al.,* extended X-ray absorption and other spectrophotometric measurements performed in aqueous solution showed that the predominant species found were those of the hexacoordinated copper-1,10-phenanthroline $[Cu(phen)]^{2+}$ and the ternary complex $[Cu(phen)_3]^{2+}$ (Figure 2.4).[190] Given the low stability of $[Cu(H_2O)_6]^{2+}$ in aqueous solution compared to the other complexes, the progressive substitution of the water molecules with ligand leads to the formation of the mono, bis and tris complexes at different rates.[189] Overall, it was shown that the ternary copper (II) complexes with phenanthroline are the species most stable in solution.[191] This is hypothesised to be due to the π-π stacking interaction occurring between the ligand aromatic rings which is mediated by the metal.[191]

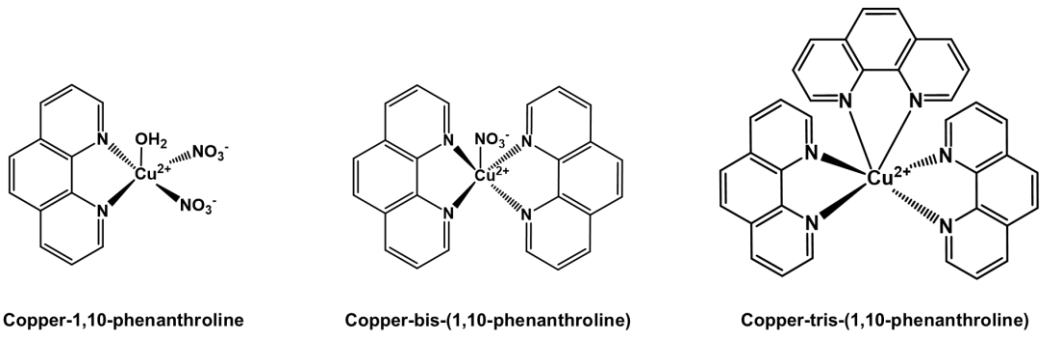

Figure 2.4. Copper(II)-phenanthroline and its complexes in aqueous solution.

Considering the synthesis of $[Cu(phen)]^{2+}$ described in the methods section 7.2.1 it is reasonable to expect the composition of the aqueous solutions of the complex to correspond to that described in the literature, with two water molecules replaced by nitrate ions. According to literature describing the crystallographic structures of bidentate $[Cu(phen)]^{2+}$ ligands in aqueous solution, it emerges that in the presence of water a penta-coordination of the copper ion is most likely to occur.[193] Consequently it is possible to expect copper (II) to be coordinated by the phenanthroline nitrogen atoms, the two nitrate ions and a water molecule[193,194] or by three water molecules displacing the nitrate ions (Figure 2.4).[195] All these observations are valuable in the definition of the species likely to be present within the bulk of the $[Cu(phen)]^{2+}$ complexes constrained within the AFt cage core.

2.2.2 Preliminary encapsulation experiments

The encapsulation of $[Cu(phen)]^{2+}$ inside HSAFt was performed using the nanoreactor method (Figure 2.5).[134] The reaction was performed by incubating a mixture of HSAFt (2.3 µM) with a 22,000 molar excess of $[Cu(phen)]^{2+}$ in 0.1 M sodium acetate buffer at pH 5.5. The reaction was stirred for 3 h at room temperature while the metal complex was added in 5 aliquots every 30 minutes, to avoid protein precipitation. The pH conditions were chosen according to those reported in the literature[135] and to mimic the endosomal environment to which Ft is exposed upon internalisation.[196] After the encapsulation, the solution was transferred into fresh sodium acetate buffer for overnight dialysis (200 volumes, membrane MWCO 14000 Da) to ensure removal of non-internalised copper(II)-phenanthroline complexes, yielding the encapsulated copper phenanthroline-AFt adduct (HSAFt-Cu(phen)). After dialysis, copper analysis by ICP-MS confirmed the encapsulation of 70 to 337 copper ions per protein cage (results of 13 independent experiments). This variation in the number of copper ions retained in the HSAFt-Cu(phen) samples may have been due to the use of different protein batches of commercial horse spleen Ft. Given that only the light chain subunit has the residues responsible for the iron nucleation,[133] it is possible to assume that the fraction of L-chain subunits also drives the copper(II) accumulation. Copper ions have been reported to reach up to 334 metal/AFt cage ratio using the diffusion method in the presence of drug molecules with potential metal coordinating groups.[8] Although the maximum number of copper ions reported by ICP-MS is similar, the average obtained from the HSAFt-Cu(phen) is lower than expected. This can be explained by the different incubation times used for the encapsulation, as in most of these reports AFt is mixed with the metal or metal complex for more

than 3 h. After the ICP-MS analysis the sample was stored at -20 °C for further analysis.

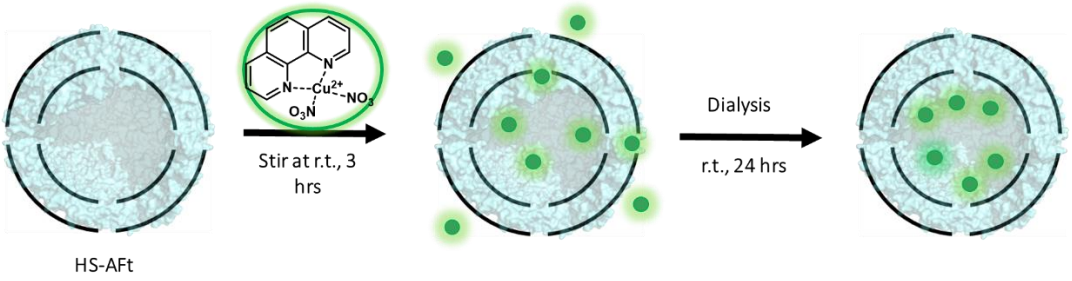

Figure 2.5. Encapsulation of copper(II)-phenanthroline inside horse spleen apoferritin. The removal of the Ft iron core leaves the empty shell AFt which can be loaded with small molecules able to enter its channels (represented as 4 for simplification). There are eight 3-fold hydrophilic channels and 6 4-fold hydrophobic channels for compounds encapsulation. The encapsulation by nanoreactor route is performed by incubating the protein with an excess of test compound for 3 h at room temperature. The sample is then dialysed to ensure the complete removal of residual unencapsulated compound.

2.2.3 Effect of long-term incubation on the copper-1,10-phenanthroline-apoferritin adducts

After the confirmation of copper(II)-phenanthroline loading inside HSAFt, a more detailed analysis of the properties of HSAFt-Cu(phen) was performed. The use of high-resolution transmission electron microscopy (HRTEM) for the characterisation of loaded AFt cages is a widely used technique to confirm the integrity of the protein structure and to observe the distribution of the cargo within different cages in the same sample. [134,173] In this case HRTEM would allow the clear identification of structures (organised or amorphous) formed from the accumulation of the copper (II) complexes inside the protein due to the contrast from the background produced by their higher electron density. For this reason, it was decided to initially avoid staining with uranyl acetate for the imaging. This method would highlight the structure of the protein cages at the cost of visualising the material loaded inside them.

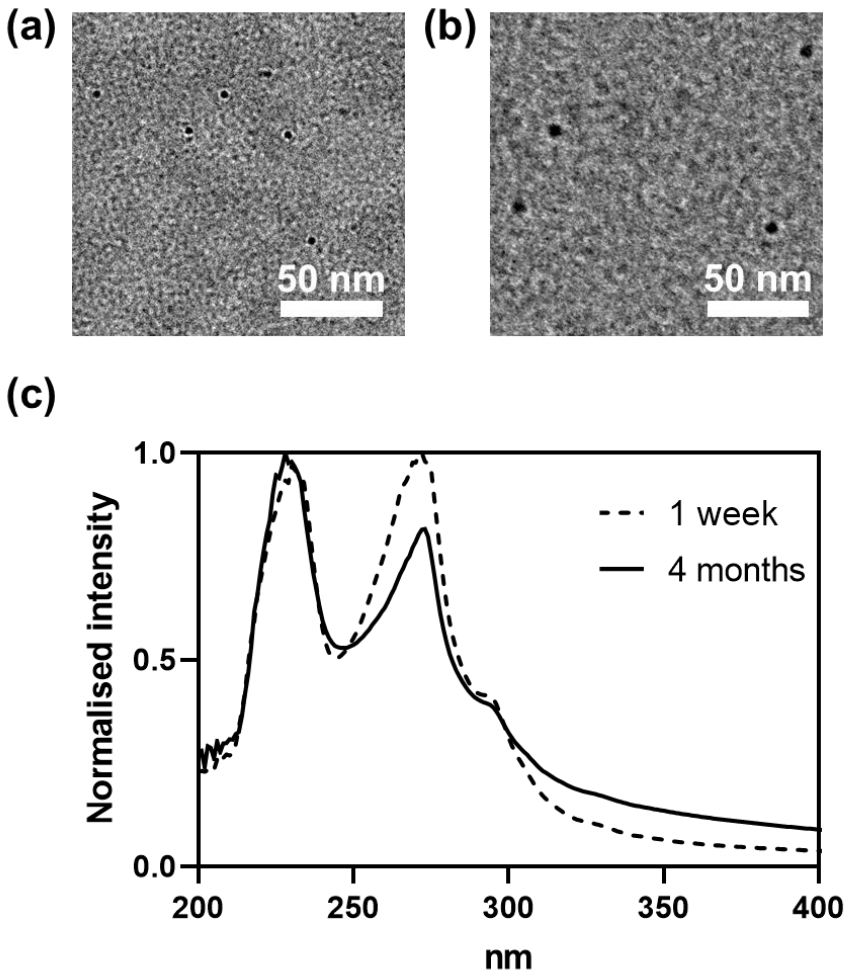

Figure 2.6. HRTEM (scale bar= 50 nm) and UV-vis timeline of HSAFt-Cu(phen) samples in sodium acetate buffer pH 5.5, T= 20 °C. (a) HSAFt-Cu(phen) sample (1 µM) imaged after 1 week from the encapsulation at pH 5.5 showing crystalline structures with an estimated diameter of d= 2.5 ± 0.8 nm. (b) HSAFt-Cu(phen) sample (1 µM) imaged after 4 months from the encapsulation at pH 5.5 showing crystalline structures with an estimated diameter of d= 5.6 ± 1.1 nm. (c) HSAFt-Cu(phen) samples UV-vis taken at the time of HRTEM imaging.

To assess the timescale of the encapsulation and the stability of the adducts, samples were imaged by HRTEM at one week and at four months after the encapsulation, upon storage in sodium acetate buffer at pH 5.5, -20 °C. The images taken after one week revealed the presence of electron-dense copper structures that showed a crystalline organisation upon magnification (Figures 2.6-a). The presence of electron-dense structures was also observed after 4 months of storage at -20 °C (Figure 2.6-b). Furthermore, the average diameter of these copper particles increased from d= 2.5 ± 0.8 nm (n= 805) at 1 week to d= 5.6 ± 1.1 nm (n= 83) at 4 months. Images taken after 6 months showed the loss of such structures suggesting their degradation over

time (Appendix 2.A). No formation of particles was observed by performing the encapsulation and analysis of control agents copper nitrate and 1,10-phenanthroline separately into the AFt cage (Figure 2.7 c and d).

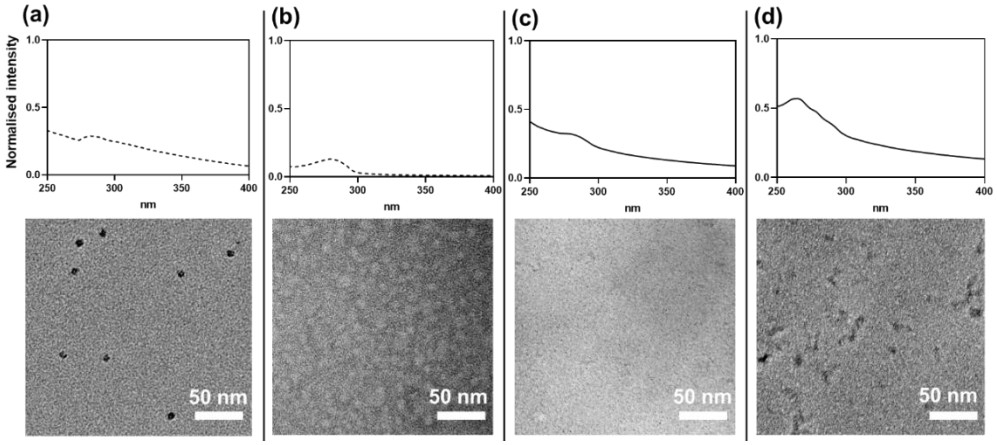

Figure 2.7. UV-vis and HRTEM controls of 11 µM HSFt (a) and HSAFt (b), HSAFt encapsulated with copper nitrate (c) and HSAFt encapsulated with 1,10-phenanthroline at pH 5.5 (d). (a) The presence of iron inside Ft is confirmed by the increased absorbance intensity on the UV spectrum (top) and by the dark high electron-dense cores that are visible in the HRTEM image (bottom). (b) The AFt spectrum (top) shows the expected protein peak at 280 nm confirming protein present in the sample. The HRTEM (bottom) is in this case less clear due to the absence of sufficient contrast between the carbon-based structure of the protein sample and that of the graphene oxide grid. (c) No increase in the absorbance of the AFt is visible upon encapsulation with copper nitrate (top), no clusters or electron-dense structures appear on HRTEM (bottom). (d) AFt-1,10-phenanthroline shows increased absorbance on the UV-vis spectrum (top) but no visible structures on the HRTEM (bottom), confirming their formation only in presence of copper.

To better inform the observations from the HRTEM results UV-Vis spectrum of the HSAFt-Cu(phen) particles was recorded. A new UV-vis spectrum was recorded before every HRTEM analysis (Figure 2.6-c). At each time point, the recorded spectra showed two maxima at 230 nm and 268 nm, together with a shoulder peak at 295 nm (Figure 2.6 c). By comparing these UV spectra with the one of $[Cu(phen)]^{2+}$ in methanol (Appendix 7.B) it is reasonable to conclude that the metal complex has been retained in the HSAFt-Cu(phen) solution after encapsulation and dialysis. The UV-Vis spectrum of HSAFt-Cu(phen) is substantially different to that of HSAFt (Figure 2.7-b) and at the same time very similar to that of $[Cu(phen)]^{2+}$ (Appendix 7.B). By looking at the same data produced using HSFt, HSAFt and the HSAFt treated with either copper nitrate or 1,10-phenanthroline at pH 5.5 it is clear that the structures observed

in the HSAFt-Cu(phen) samples prepared at pH 5.5 are unique and related to the presence of the metal complex (Figure 2.7). The HSFt and the AFt-1,10-phenanthroline sample images confirm that the electron-dense cores observed are directly related to the presence of copper (Figure 2.7-a and d). However, the spectrum of the AFt-1,10-phenanthroline also suggests that the copper can play an important role in the amount of 1,10-phenanthroline retained by the HSAFt cage, as there is a significant difference in the absorbances at 280 nm of the HSAFt-Cu(phen) and AFt-1,10-phenanthroline spectra at the same protein concentration (Figures 2.7-c and d). The ICP-MS data obtained from the encapsulation of $Cu(NO_3)_2$ into AFt show that the maximum metal retention is of 84 metal ions per protein cage. This value is on the lower end of the average measured for HSAFt-Cu(phen), suggesting that also in this case the association of copper (II) and phenanthroline into the metal complex can be mutually beneficial for their loading into HSAFt.

The analysis of the UV-vis spectra at higher wavelengths could prove valuable in informing if the HSAFt-Cu(phen) adducts observed could be copper NPs. Literature reports on the synthesis of copper (0) and copper (I) oxide (Cu_2O) NPs describe a change in colour in the solution and presence of absorbance bands respectively at 573 nm and 360 nm upon metal NPs formation and subsequent oxidation in solution.[197] In the case of the HSAFt-Cu(phen) samples none of these features is present, confirming that the structures observed in the HRTEM images are adducts of HSAFt with $[Cu(phen)]^{2+}$, rather than NPs. It is also important to highlight that in some cases (Figure 2.7-b), even though copper (II) is present in the sample, it cannot be visualised in the form of electron dense cores by HRTEM.

2.2.4 Characterisation of the HSAFt-Cu(phen) adducts

The images collected by HRTEM on the HSAFt-Cu(phen) samples after 4 months of storage allow for the analysis of the lattice visible upon magnification on single copper particles (Figure 2.8-a). The alternation of parallel dark and bright stripes visible in Figure 2.8 a identifies the lattice structure, called lattice fringe, in which copper seems to be organised into a crystalline structure. This arrangement is substantially different from the amorphous iron cores that normally accumulate in Ft (Figure 2.8-b). The dark lines are formed by the aligned atoms and the bright ones represent the space between the atoms (Figure 2.8-a and c). Using the ImageJ analysis tool it is possible to estimate the spacing between the atoms by measuring the thickness of the bright stripes (Appendix 2.B). This value can inform on the arrangement of the copper atoms with their surrounding environment. The d-spacing estimated for the lattice fringes

observed is 0.251 nm (Appendix 2.B, Figure 2.8-c). Crystal structures with a similar d-spacing (0.264 nm) are CuO NPs in which copper and oxygen atoms are packed into what is called a simple cubic unit cell arrangement. [198,199] However, the results presented in this chapter showed no evidence of NPs forming in HSAFt-Cu(phen) solution according to the data from previous literature.

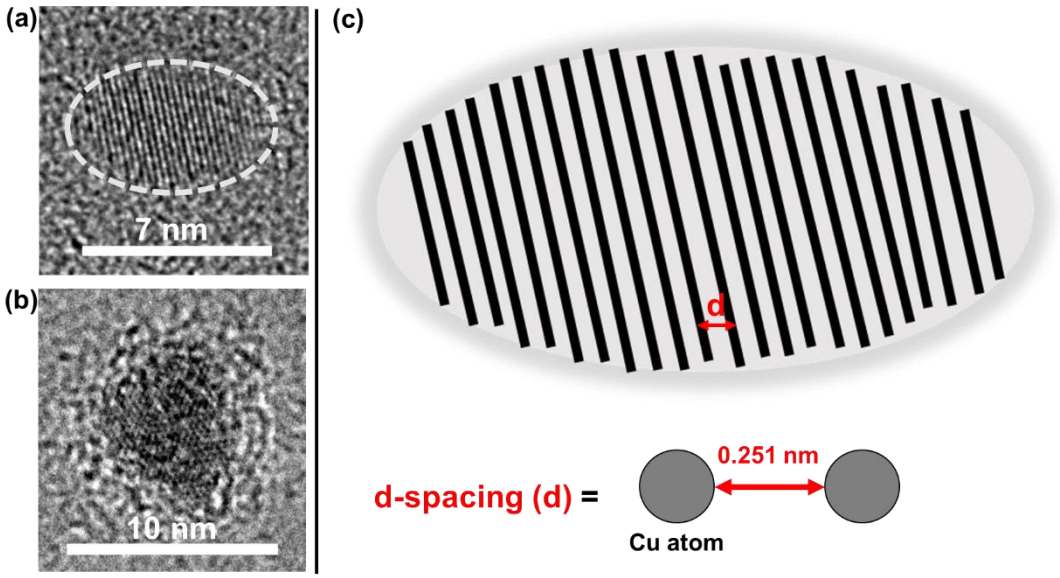

Figure 2.8. Image and drawing of the lattice arrangements of copper atoms in HSAFt-Cu(phen) and image of iron-loaded ferritin. (a) Image of the crystalline adducts formed in HSAFt-Cu(phen) samples (1 µM) where the crystal lattice is visible and highlighted by the dashed line. (b) Image of the amorphous iron core of ferritin (1 µM). (c) Representation of the basic structure of a crystal lattice were the d-spacing is indicated as the distance between the stripes which corresponds to the distance between the copper atoms forming the lattice (0.251 nm in this case).

Even though no NPs are formed inside HSAFt-Cu(phen) the electron energy loss spectroscopy (EELs) analysis provided additional evidence of copper-oxygen interactions occurring (Figure 2.9). This technique allows for the identification of the type of atom present and the chemical properties of the specimen analysed, hence giving information on the state and the neighbouring environment of the copper ions present within the sample. The EELs spectrum of the HSAFt-Cu(phen) sample (Figure 2.9-a) shows the energy edges in the 900-950 eV range which correspond to those present in reference samples of CuO (Figure 2.9-b).

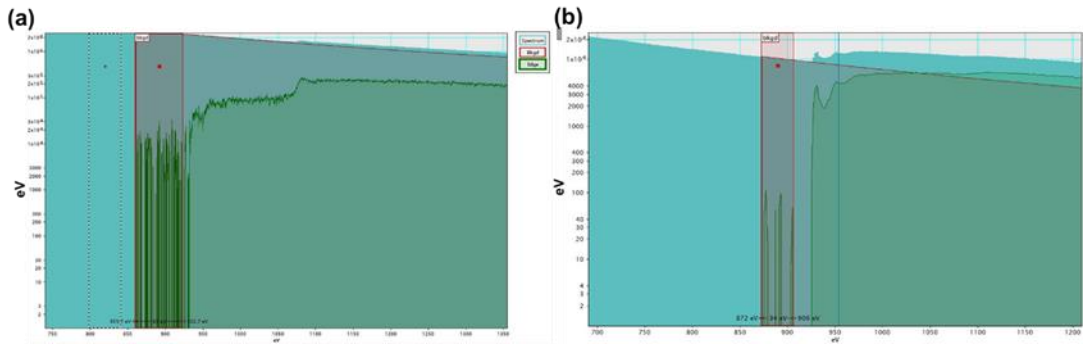

Figure 2.9. EELs spectrum of HSAFt-Cu(phen) (a) compared to a reference spectrum of CuO thin film (b). The spectrum of HSAFt-Cu(phen) sample (a) shows a very low-intensity signal in the 900-950 eV region which corresponds to the energy edge produced by copper oxide as it can be identified in the reference spectrum (b), suggesting copper coordination by oxygen.

By considering the data from the lattice measurements and the EELs it is feasible to hypothesise that the void spaces in the copper crystalline pattern observed by HRTEM are occupied by oxygen atoms provided by neighbouring amino acid side chains. Some of the copper ions present in the HSAFt-Cu(phen) sample may be coordinated to oxygen atoms belonging to the aspartate and glutamate residues lining the internal surface of the AFt cage.[141] Some examples in the literature show how the 1,10-phenanthroline ligand can dissociate from the metal after loading into AFt.[164] This can support the hypothesis in which there are other metal species in addition to $[Cu(phen)]^{2+}$ present inside the protein cage, forming a heterogeneous copper core (Figure 2.10). In addition to the organised structures lining the interior of AFt resulting from the interaction between the metal and the protein amino acid residues, there could be a central bulk formed by a mixture of the different copper(II)-phenanthroline complexes described in section 2.2.1. [160,161,162,190]

The images produced by the copper loaded AFt cages so far has provided information on the copper arrangement in the samples but not on whether the protein shell has maintained its integrity. In the absence of staining, it is very difficult to visualise the protein shell around the metal cores. This is due to the low contrast between the carbon background of the graphene oxide grid used and the carbon-rich structure of the protein itself. In most literature reports, negative staining with uranyl acetate provides a good solution to image the AFt protein shell, but sometimes that can negatively affect the visualisation of the internal cargo.[171] In this case, it was observed that by storing the sample (once deposited on the grid) under vacuum overnight it was possible to significantly increase the contrast and, in some cases, to visualise the protein shell. This method was tested on the Ft control (Figure 2.8-b) in which

both the protein shell (bright white ring) and the features of the iron core were more visible compared to the sample containing copper (Figure 2.8-a).

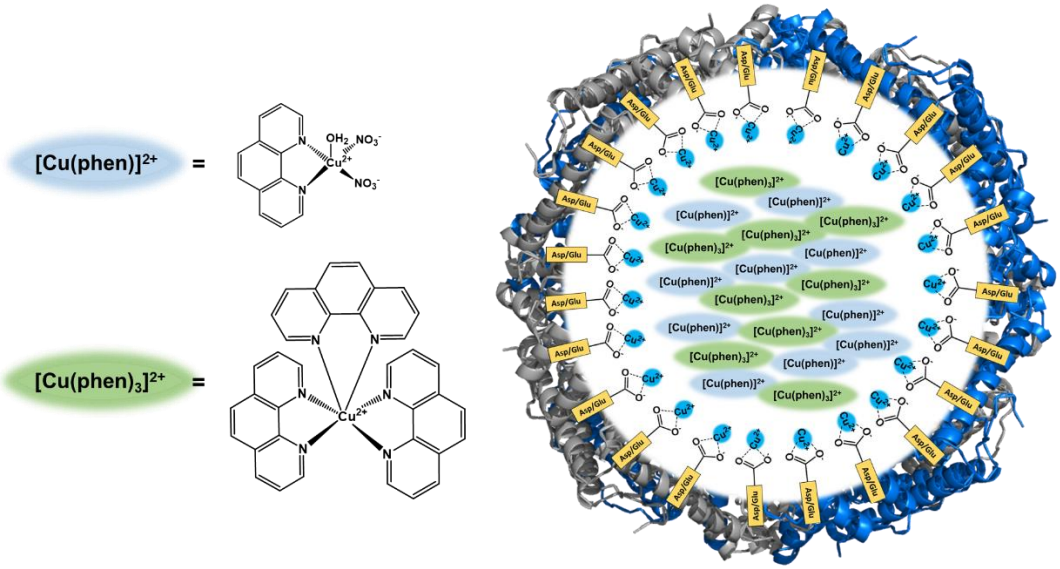

Figure 2.10. Representation of the hypothesised HSAFt-Cu(phen) core composition. L-chain HSAFt subunits were used to represent the protein cage.

To identify the protein shell in the HRTEM images and assess its integrity in the HSAFt-Cu(phen) pH 5.5 samples, uranyl acetate staining was used. By comparing unstained and stained images it is possible to visualise the AFt protein shell and confirm its integrity even in the presence of the copper adducts (Figure 2.11).

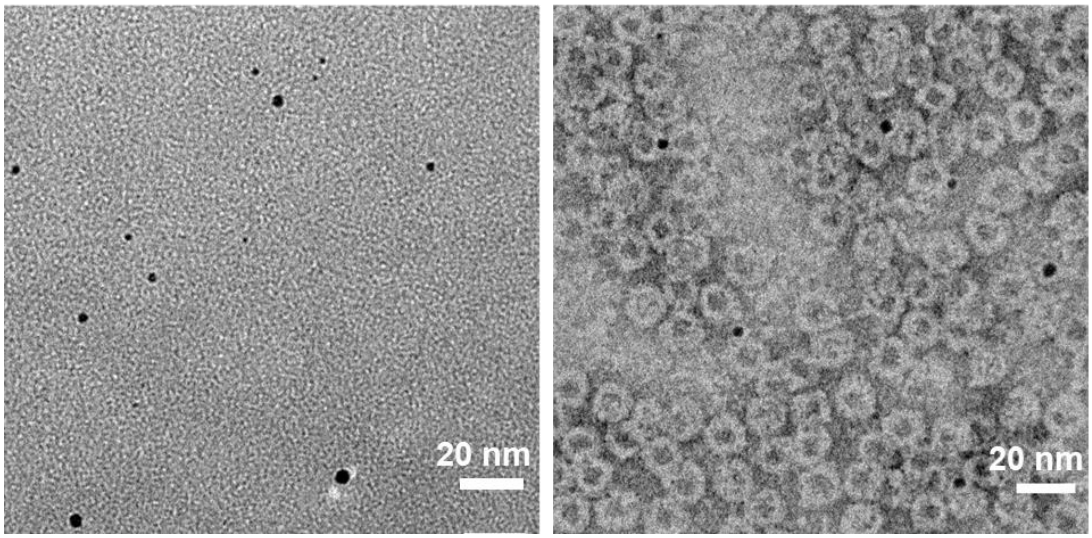

Figure 2.11. HRTEM with (right) and without (left) staining using uranyl acetate of the HSAFt-Cu(phen) encapsulated at pH 5.5 aged 4 months.

Furthermore, the images of the AFt protein with uranyl acetate staining agree with the results from the native PAGE, DLS and zeta potential. By comparing the DLS data from HSAFt and HSAFt-Cu(phen) at pH 5.5 (Figure 2.12-a) the predominant particle species has an estimated hydrodynamic radius of 15.4 ± 2.3 nm for the HSAFt-Cu(phen) and of 17.2 ± 1.3 nm for AFt. The DLS shows that in both HSAFt and HSAFt-Cu(phen) The zeta potential values recorded are -7.79 ± 1.97 mV for AFt and -7.15 ± 0.67 mV for HSAFt-Cu(phen). Even though these values are lower than those reported in the literature[124,138] it is possible to conclude that no significant accumulation of charged species on the outside of the protein cage occurred neither did the protein subunits formed oligomers[200] (Figure 2.12-b). The native PAGE gel showed that all the samples displayed a migration pattern like the protein reference (Figure 2.12-c).

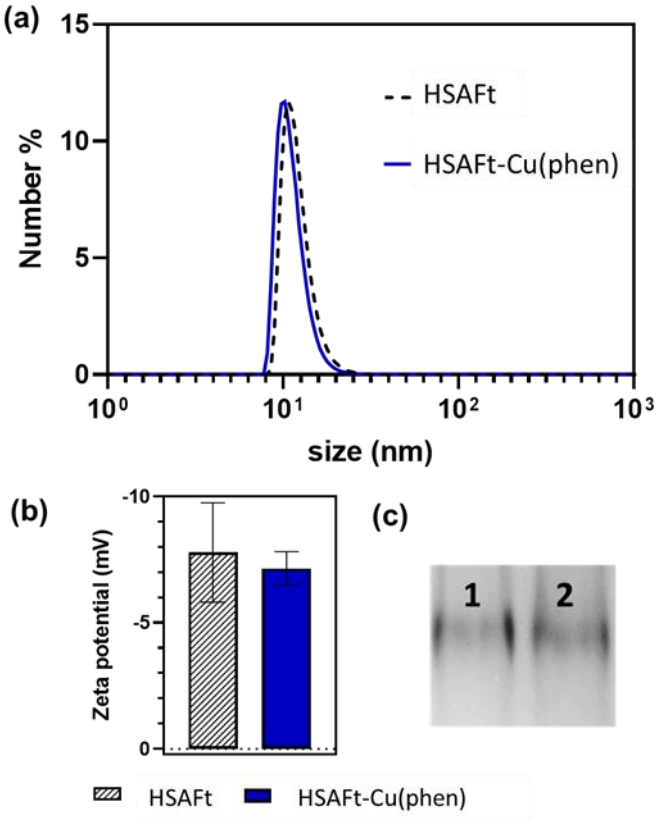

Figure 2.12. Analysis of the HSAFt cage integrity in HSAFt-Cu(phen) samples by DLS (a), zeta potential (b) and native PAGE (c). (a) Size distribution in the HSAFt and HSAFt-Cu(phen) samples at pH 5.5. (b) Zeta potential of the protein cage and the HSAFt-Cu(phen) at 25 ºC. (c) Lane 1: HSAFt reference (440 kDa); Lane 2: HSAFt-Cu(phen).

To summarise, the characterisation of the HSAFt-Cu(phen) indicates a heterogeneous composition of the metal core inside the protein cage. This link can

be enough to justify the presence of organised crystal layers formed by the interaction of copper with amino acid residues inside the protein, but it does not support the formation of NPs. In addition to the copper layers, the UV-vis data clearly show presence of phenanthroline in the HSAFt-Cu(phen) samples, supporting the hypothesis of a central bulk composed by a mixture of $[Cu(phen)]^{2+}$ and $[Cu(phen)_3]^{2+}$ as not all the ligand dissociated form the metal (Figure 2.10). To conclude the DLS, zeta potential and native PAGE results show that the AFt cage is intact, with no indication of charged compounds associated to the external surface of the protein.

2.2.5 Stability of the AFt-Cu(phen) adducts

One of the purposes of introducing metal complexes into AFt is to improve the retention of the pharmacological compounds encapsulated for drug delivery through metal coordination by the drug functional groups.[8,124] For this reason, the stability of the adducts formed in the HSAFt-Cu(phen) sample was tested at physiological conditions, by estimating the time-dependent release profile of 1,10-phenanthroline. A sample (aged 1-4 months) was incubated at 37 ºC for 24 h either at pH 7.4 or at pH 5.5 and the 1,10-phenanthroline released in the dialysis solution was recorded by UV-vis (Figure 2.13). The percentage of phenanthroline release over time was estimated from the intensity recorded from the dialysis solution at the maxima at 268 nm for each time measurement using the Beer-Lambert law (Appendix 2.C, 2.D). The data show a 1,10-phenanthroline release of up to a maximum of 60% of the total loaded amount within 10 h of incubation at 37 °C (Figure 2.13). The percentage of phenanthroline release is lower at pH 7.4, suggesting a greater stability of the complex at physiological conditions. Given that the UV-vis spectra of phenanthroline and of its copper complex are very similar (Appendix 7.B) and given the low absorbance of the peak at 679 nm characteristic of $[Cu(phen)]^{2+}$ it is not possible to verify whether the 1,10-phenanthroline detected in the dialysis buffer was still coordinating copper. For this reason, the dialysis buffer was also analysed by ICP-MS to determine the release of copper ions from AFt (Figure 2.13). The ICP-MS data were in agreement with what observed by UV-vis, as the largest percentage of AFt-internalised copper was released at pH 5.5 (20 %). This suggests a greater stability of the HSAFt-Cu(phen) adducts at pH 7.4. When comparing these data to other nano-formulations with copper-phenanthroline it seems that lipid formulations like liposomes yield better stability at pH 7.4. However, these data report incubation of the nano-formulation for only 90 mins[201] compared to the results reported in this section which span over 24 h.

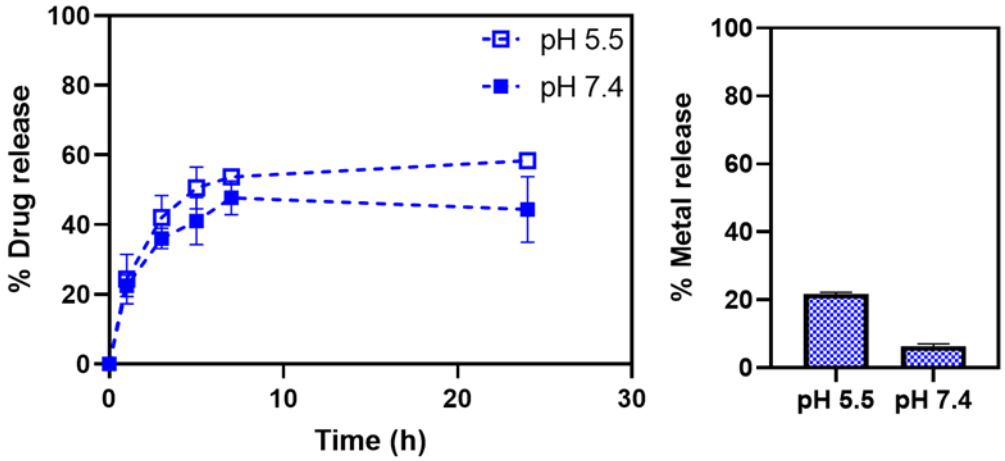

Figure 2.13. Release test of HSAFt-Cu(phen) at 37 °C exposed to pH 5.5 and pH 7.4**.** UV-vis (left) and ICP-MS (right) analyses were performed on the dialysis buffers to estimate the release of the ligand and of copper separately.

The data reported in sections 2.2.3 and 2.2.4 show that the presence of a copper complex in solution with HSAFt at pH 5.5 leads to the formation of specific HSAFt-copper adducts with a peculiar arrangement of the copper atoms inside the protein. The drug release data strongly suggest that accumulation of the 1,10-phenanthroline complex with copper occurs inside HSAFt and it is favoured by the presence of the metal. At this stage, it is difficult to directly measure the stoichiometry between the copper and the 1,10-phenanthroline loaded inside HSAFt. The data from the lattice measurements and the EELs analysis seems to point in the direction of different copper species present in the AFt core. These data suggest the simultaneous presence of copper ions forming the lattice layer(s) upon coordination with acidic amino acid side chains and a central bulk formed by a mixture of copper-1,10-phenanthroline complexes. HRTEM, DLS and native PAGE demonstrated that these structures are inside the protein shell, which preserved its integrity and native features. To investigate the possible factor contributing to the formation of HSAFt-Cu(phen) adducts the effect of pH and temperature were tested in separate experiments (section 2.2.6).

2.2.6 Effect of pH and temperature on NPs growth

Buffer pH and temperature were evaluated as factors with the potential to influence the encapsulation efficiency and the stability of the structures forming inside AFt. Even though it was concluded that the HSAFt-Cu(phen) adducts described in this work were not NPs, literature on copper NPs (metal and oxide) was taken as a

reference to test the adducts growth conditions. The evidence available from other literature reports shows that certain pH conditions can promote the growth into NPs and affect the size of the metal structures formed. Furthermore, some of the data above suggested the decomposition of part of the $[Cu(phen)]^{2+}$ upon encapsulation. In the case of metallic copper, the size of NPs increases up to pH ≥ 5 and probably between pH 9-11 whilst at neutral, slightly alkaline pH, the excess of hydroxide ions causes the formation of copper oxides NPs rather than metallic copper NPs.[170] The temperature was also evaluated, as protocols for the chemical synthesis of copper NPs also supply heat to speed the reaction.[167]

A second encapsulation experiment was performed by diffusion through the protein channels, but with a different reaction buffer: 50 mM glycine at pH 7.4. This pH was chosen according to other studies employing copper-AFt NPs for drug delivery purposes. [8] This time the dialysis buffer was supplied with 10 mg of CHELEX resin to ensure the efficiency of excess $[Cu(phen)]^{2+}$ removal. Copper loading was quantified by ICP-MS giving only 33 copper ions per protein cage, which is much lower compared to the maximum capacity reported in the literature[171] and with the encapsulation performed at pH 5.5. This result was further supported by UV-Vis recorded 2 weeks after the encapsulation. The sample was stored also in this case at -20 °C until the analysis. This time the spectrum profile was like that of the control AFt (Figure 2.14-c). The absence of the second peak at 268 nm suggested that the concentration of the $[Cu(phen)]^{2+}$ complex in the sample was very low or absent.

According to these results, lower pH seemed to yield better loading of $[Cu(phen)]^{2+}$ into AFt than neutral pH. It is difficult to compare such a result with the literature as the buffer pH is reported to have a greater effect on the amount of AFt recovered after encapsulation, rather than on the loading efficiency.[133] However, it is also important to consider the presence of the chelating resin in the dialysis solution which might have favoured faster release of the $[Cu(phen)]^{2+}$ from the protein cage. A solution to this issue could be to dialyse for a shorter amount of time against the buffer containing the CHELEX resin followed by extensive overnight dialysis in storage buffer only.

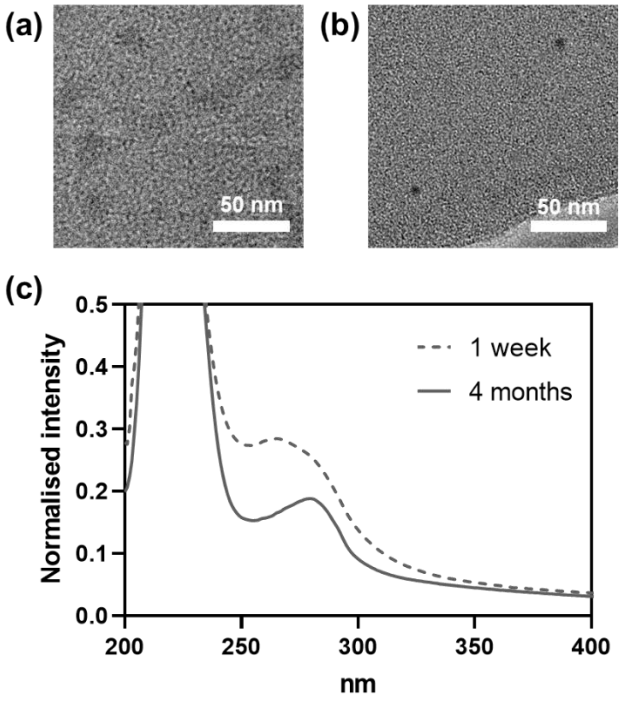

Figure 2.14. HRTEM (scale bar= 50 nm) and UV-vis timeline of HSAFt-Cu(phen) samples at pH 7.4. (a) HSAFt-Cu(phen) sample (1 µM) imaged after 1 week from the encapsulation at pH 7.4 where no copper clusters can be observed. (b) HSAFt-Cu(phen) sample (1 µM) imaged after 4 months from the encapsulation at pH 7.4 showing structures forming with an estimated diameter of d = 9.8 ± 0.9 nm. Further magnification in the 20 nm range was not possible due to low contrast. **(c)** HSAFt-Cu(phen) samples UV-vis taken at the time of HRTEM imaging.

HRTEM analysis was carried out by storing one aliquot of the HSAFt-Cu(phen) sample at pH 7.4 at -20 °C and imaging it at different time intervals. The images recorded showed dark circular structures (9.8 ± 0.9 nm) forming after 4 months of storage (Figure 2.14-b). Due to the low contrast between the particles and the background, it was not possible to magnify the image to a lower nm range to confirm if the nuclei were crystalline or not. Although such images suggest a change in the samples over time the results did not provide enough evidence to confirm the formation of the same adducts that were present in the HSAFt-Cu(phen) samples at pH 5.5.

To further analyse the influence of pH on copper adducts growth, the sample encapsulated in glycine buffer at pH 7.4 was divided into aliquots, each one exchanged into two buffers one at pH 6 and the other at pH 2 (0.1 M NaOAc). In this case, the aliquots were characterised by UV-Vis (Figure 2.15 c) and analysed by HRTEM (Figure 2.15-a and b). UV-Vis confirmed the very low concentration of $[Cu(phen)]^{2+}$ in the original solution as also in this case the peaks at 230 and 268 nm

showed by 1,10-phenanthroline were not visible. Images showed copper clusters at pH 6 and no visible structures were observed at pH 2, where the protein is expected to be disassembled. The behaviour observed at pH 6 could be explained as the effect of low pH on the stability of the $[Cu(phen)]^{2+}$ complex. As reported in section 2.2.5 the release tests suggested the potential tendency of $[Cu(phen)]^{2+}$ to dissociate into 1,10-phenanthroline and the copper ion. This can then lead the subsequent coordination of the free copper to the acidic glutamate and aspartate side chain lining the internal surface of AFt.[141] According to literature reports the size of copper NPs increases up to pH ≥ 5 while at higher pH the excess of hydroxide ions favours the formation of Cu oxides and hydroxides which are more difficult to visualise by HRTEM on a graphene grid due to low contrast. [170]

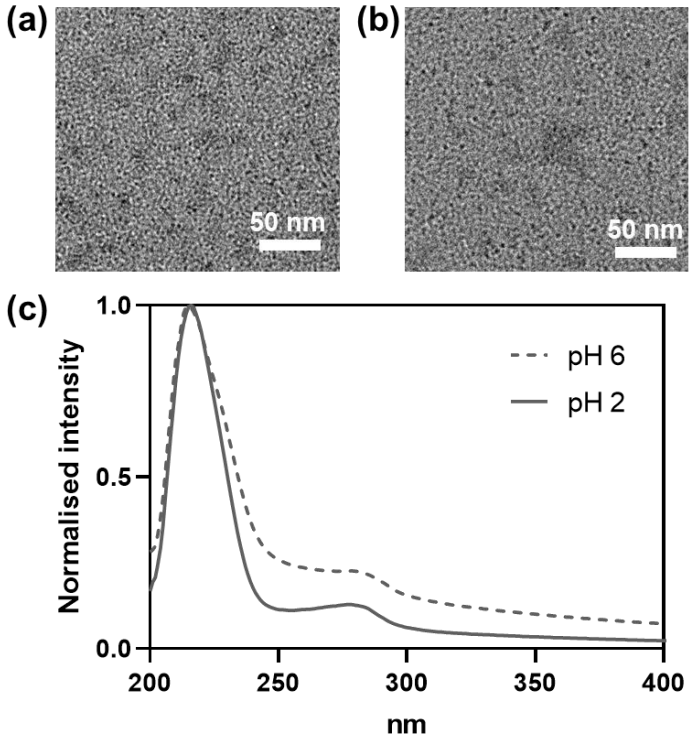

Figure 2.15. HSAFt-Cu(phen) samples treated at pH 6 and pH 2 (scale bar= 50 nm). (a) HRTEM image of the HSAFt-Cu(phen) sample exposed to pH 2. No clear protein and metal clusters could be identified. (b) HRTEM image of the HSAFt-Cu(phen) sample exposed to pH 6. In this case, small copper clusters (average diameter 6.3 ± 2.3 nm) appear, suggesting that the change in pH might drive their formation. (c) UV spectra of the samples treated at different pH showing a different absorbance profile depending on pH.

After observing that pH can have an influence on the accumulation of copper within AFt it was determined whether the temperature was able to accelerate the process. Two aliquots of the HSAFt-Cu(phen) sample were incubated overnight at 37 and 50°C

before examining them by HRTEM. This revealed no difference between the untreated samples and those exposed to higher temperatures (Figure 2.16), thus suggesting that temperature does not have an effect on copper cores formation.

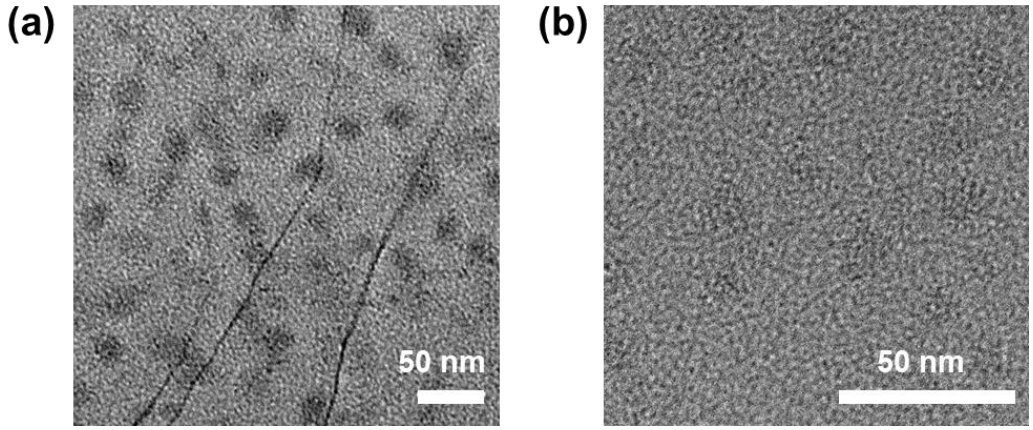

Figure 2.16. HSAFt-Cu(phen) samples treated at 37 (a) and 50 °C (b) overnight. Both samples do not show the presence of high electron-dense copper cores. Scale bar= 50 nm.

2.3 Test of the catalytic activity of copper phenanthroline in solution

The potential for AFt to be employed as a scaffold for catalysis has been extensively demonstrated in the literature for different purposes.[176] The first group that identified the catalytic potential of copper-phenanthroline complexes were Sigman and co-workers that discovered the nuclease activity of bis-(1,10-phenanthroline)copper (II).[202] Copper complexes were found to act by two mechanism of DNA cleavage: oxidative and hydrolytic cleavage. While the majority of the copper-phenanthroline complexes and their derivatives act by oxidative cleavage,[202] which also requires the presence of a reducing agent to convert copper (II) into copper (I), a few along with bipyridine-copper complexes have also shown hydrolytic activity.[193,203, 204, 205] In addition to this DNA nuclease activity, a report from Distefano *et al.* showed that the use of the confined space provided by a protein scaffold was able to promote and accelerate copper (II) mediated hydrolysis of non-activated substrates in aqueous solution and at mild temperature conditions.[206] Many pharmaceutical compounds rely on hydrolysis for their *in situ* activation.[21] The ability to control this reaction through a targeted vehicle like AFt could therefore be highly desirable in clinical settings. Based on this, some assays were attempted using both $[Cu(phen)]^{2+}$ and HSAFt-Cu(phen) to identify any catalytic activity promoted by the confined space of the protein cage.

The assays to test the catalytic activity using $[Cu(phen)]^{2+}$ in solution to promote the hydrolysis of esters showed no significant effect on the reaction rate (Figure 2.17-a). These tests were performed both on the activated ester *para*-nitrophenyl acetate and more stable substrates *N*-methyl-*N*-phenylpicolinamide and ethyl-*N*-phenylcarbamate (Chapter 7, Sections 7.2.2 and 7.2.3). Different pH conditions and metal complex concentrations were screened, and the reaction was monitored up to 24 hrs with no relevant results showing any hydrolytic activity on UV-vis and HNMR.

To validate our observations and the results reported by Distefano *et al.* by verifying if the confined space of AFt could boost the catalytic effect of $[Cu(phen)]^{2+}$ the same assay was performed using the HSAFt-Cu(phen) adduct. The conversion of *para*-nitrophenyl acetate into *para*-nitrophenol was followed by UV-Vis.[207,208]

The reaction mixture was composed of a constant substrate concentration mixed with variable concentrations of the HSAFt-Cu(phen) complex. The reactions were then incubated for up to 24 h in 50 mM phosphate buffer at pH 7.4, 37 °C. The formation of *para*-nitrophenol was monitored by recording the absorbance at 405 nm at different time intervals.

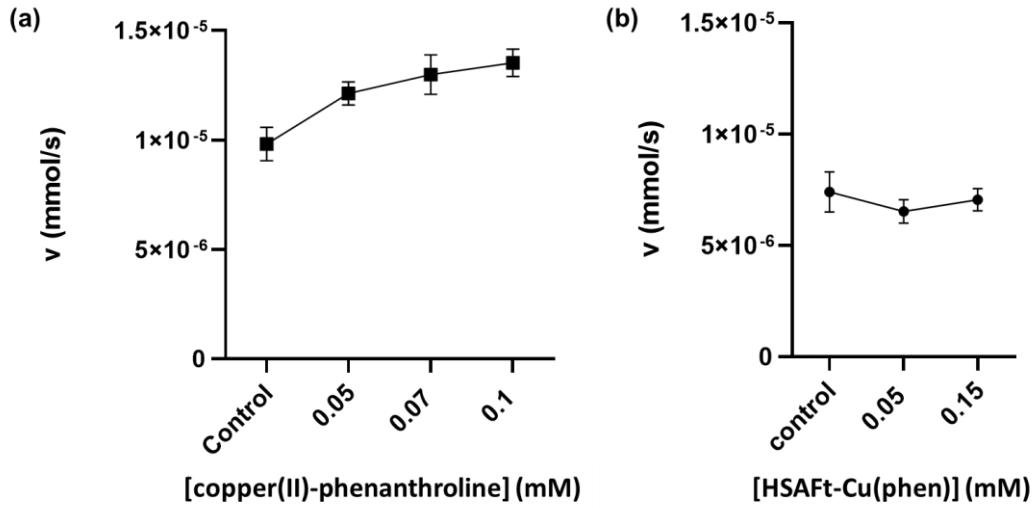

Figure 2.17. Curves representing the hydrolysis rate of *para*-nitrophenyl acetate in solution with $[Cu(phen)]^{2+}$ (a) and with HSAFt-Cu(phen) (b). The plots represent the average rate of the hydrolysis of *para*-nitrophenol in presence of copper-1,10-phenantroline and of the HSAFt-Cu(phen) system. In both cases no significant difference between the rate of the spontaneous hydrolysis of the substrate (control) and the rate in the presence of catalyst could be observed. The catalyst concentration was determined from the AFt/copper ratio.

The data collected from the experiment (Figure 2.17-b) showed no substantial differences from the results reported in the preliminary assays. These results suggest that the confined environment of the AFt cage did not affect the properties of the loaded copper (II) complex. In this case, the contrast from the results reported by Distefano could be related to the effect of the protein surface to which the metal complex is exposed. The adipocyte lipid-binding protein is more hydrophobic than the internal surface of AFt, whose core is lined by acidic amino acid residues.[105, 165] As observed in other systems where the copper ion was used to accelerate the rate of ester hydrolysis the surrounding environment of the ion complex is mostly nonpolar.[209] Consequently, the different interactions between the protein surface and the $[Cu(phen)]^{2+}$ complex are likely to contribute to the different effects on its catalytic activity making AFt an unsuitable scaffold for a hydrolytic artificial enzyme.

2.4 Effect of HSAFt-Cu(phen) adducts on cancer and non-tumourigenic human cells

Preliminary *in vitro* cytotoxicity studies of $[Cu(phen)]^{2+}$ were carried on colorectal cancer cells (HCT-116) and healthy human lung fibroblasts (MRC5) (Figure 2.18). This preliminary assessment of $[Cu(phen)]^{2+}$ activity has led to the estimation of its GI_{50} concentrations as > 5 μM for HCT-116 and of 0.7 μM for MRC5 cells (Table 2.1). Such values suggest that $[Cu(phen)]^{2+}$ causes *in vitro* growth inhibition also in non-cancer cells (Figure 2.18). If compared with the class of Casiopeinas® complexes, currently undergoing Phase I Clinical Trials, it is difficult to find similar results especially for non-cancer cells as their data collected from peripheral blood lymphocytes show very low cytotoxicity.[104]

The preliminary results with $[Cu(phen)]^{2+}$ were used to inform the analysis of the activity of the AFt-Cu(phen) samples prepared at pH 5.5. As for the preliminary cell survival assays the same cell lines were used and the same exposure time of 72 h. The dilutions for the assay were prepared according to the amount of copper per cage estimated in each sample so that the results could be directly comparable with the $[Cu(phen)]^{2+}$ controls. Three replicates were performed. AFt was also tested to confirm the absence of growth inhibition (putative biocompatibility) to the selected cell lines.

	Cell line	$[Cu(phen)]^{2+}$	HSAFt-Cu(phen)
GI_{50} ± SEM (μM)	MRC5	0.75 ± 0.13	0.92 ± 0.34
	HCT-116	> 5	> 2.5
	U373V	2.3 ± 0.067	1.1 ± 0.014
	U373M	2.2 ± 0.068	2.2 ± 0.084

Table 2.1. Table summarising the GI_{50} values of $[Cu(phen)]^{2+}$ and HSAFt-Cu(phen) in μM concentration estimated for the cell lines tested. GI_{50} is expressed as Mean ± SD from Three Independent Trials, Where N = 8.

The outcome of the 3-[4,5-dimethylthiazol-2-yl]-2,5 diphenyl tetrazolium bromide (MTT) assay correlates cell viability with the absorbance at 570 nm detected in the cell solution after exposure to the test compound.[210] The data collected were normalised using the absorbance values recorded 24 h after seeding the cells, before treatment (T_0) and before interpolation. The resulting GI_{50} values were estimated as 0.92 μM for MRC5 and > 2.5 μM for HCT-116 (Table 2.1). As expected HSAFt did not show any effect on HCT-116 and MRC5 cells (Figure 2.18). A similar situation was observed on both cell lines when treated with HSAFt-Cu(phen), in this case the presence of the protein shell had a limited effect on the activity profile of $[Cu(phen)]^{2+}$. Even though AFt provided some protection from the activity of $[Cu(phen)]^{2+}$, the HSAFt-Cu(phen) adduct was more active against healthy fibroblasts than to colorectal cancer cells (Figure 2.19).

To corroborate the results of the MTT assays, a cell count assay was performed in triplicates to assess the effects of two test concentrations of AFt-Cu(phen): 0.5 μM and 1.5 μM. In this assay, cells were seeded at a density of 2 x 10^4 cells/ well, allowed to grow for 24 h and exposed to the test agent for 72 h before counting. This assay highlighted a stark difference between the growth inhibitory activity exerted on both cell lines by $[Cu(phen)]^{2+}$ and HSAFt-Cu(phen). However, it was again evident that the HSAFt-Cu(phen) treatment at 1.5 μM resulted in a greater toxicity on MRC5 cells compared to HCT-116 (Figure 2.19). Colorectal cancer cells did show sensitivity to 1.5 μM HSAFt-Cu(phen), however, this concentration was still not enough to drastically inhibit their viability, whilst it was already very toxic to healthy cells. Similar results were also reported by Ferraro *et al.* which studied the effect of the cytotoxic gold (I) and platinum (II) complex encapsulated int HSAFt and revealed that the

presence of the protein cage significantly reduced the toxicity to cancer cells and did not provide enough selectivity between tumour and normal cells.[162]

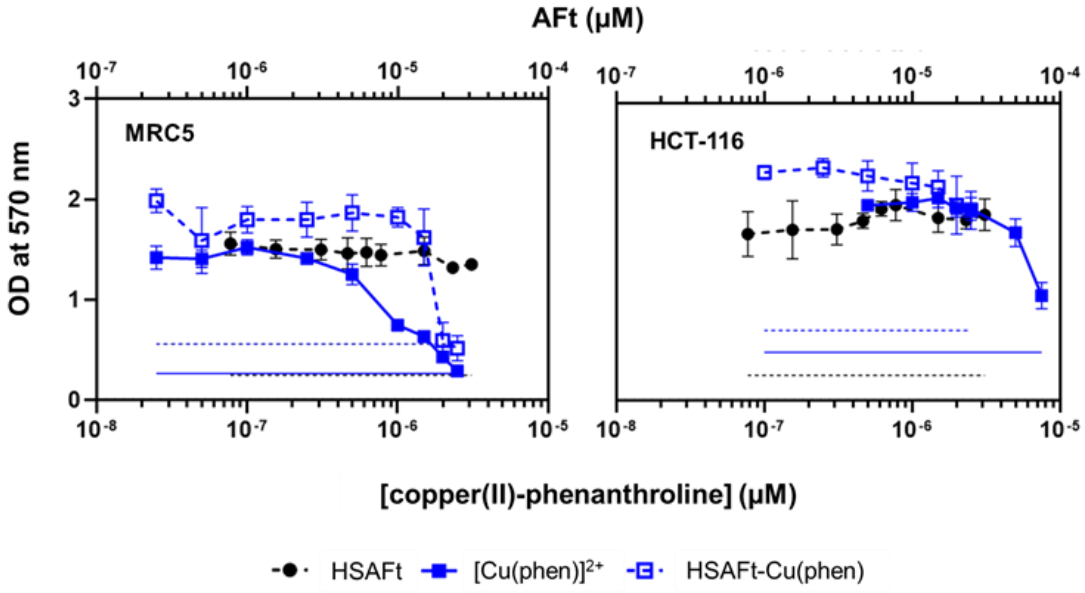

Figure 2.18. Effect of HSAFt, $[Cu(phen)]^{2+}$ and HSAFt-Cu(phen) on MRC5 and HCT-116. MTT assays were performed at time of test agent addition (T_0) and following 6 days treatment of cells with test agents. Representative dose-response curves are shown. Data points are mean ± SD (n=8); 3 independent trials were conducted.

The data presented so far are encouraging in supporting the role of AFt as a biocompatible scaffold, able to protect the cells from the toxic effects of its cargo. However, they also suggest that the effect of AFt on the pharmacological activity of $[Cu(phen)]^{2+}$ is mild. Furthermore, it is important to specify that an increase in the GI_{50} value is yet not enough to satisfy the objective of this study. The data reported here point out that the concentration of HSAFt-Cu(phen) required to kill colorectal cancer is likely to be higher than the minimum safe concentration to avoid toxicity to healthy cells as well. Even though the toxicity to healthy fibroblasts is a concern, the GI_{50} values estimated for HSAFt-Cu(phen) against colorectal cancer cells are comparable with the reported toxic concentrations found for most Casiopeinas® used on HeLa tumour cells.[104] Cytotoxicity in the low micromolar range was also found in studies with other copper-phenanthroline complexes tested on ovarian carcinoma[211] and their liposomal formulations tested on murine melanoma cells.[212]

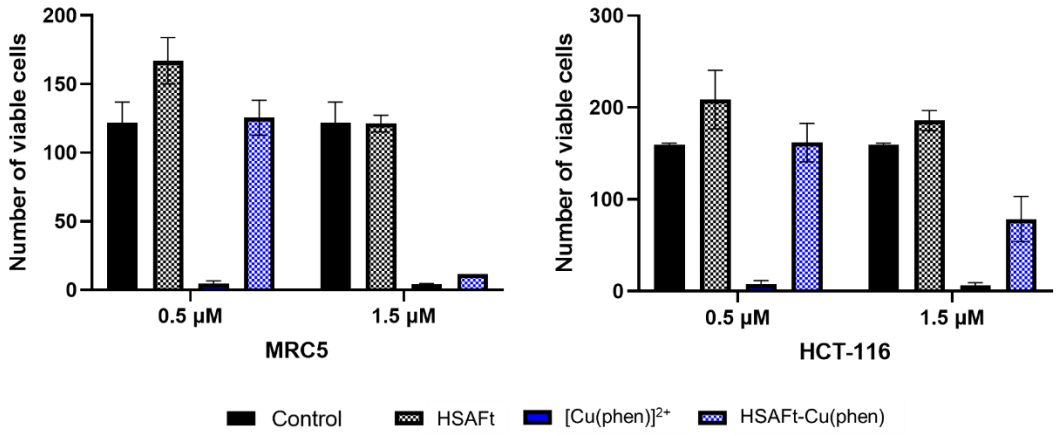

Figure 2.19. Effect of HSAFt, $[Cu(phen)]^{2+}$ and HSAFt-Cu(phen) on MRC5 and HCT-116 cells. Clonogenic assays were performed at time of test agent addition (T_0) and following 72 h treatment of cells with test agents. Representative cell survival data are shown. Data points are mean ± SD (n=2); 3 independent trials were conducted. Control represents cells incubated with media only until colony staining.

To expand the investigation of these effects further, $[Cu(phen)]^{2+}$ and HSAFt-Cu(phen) were tested on two glioblastoma (GBM) cancer cell lines, MGMT-low U373V and MGMT-transfected U373M. These cell lines can be valuable in the study of the pharmacological activity of the AFt co-encapsulated with $[Cu(phen)]^{2+}$ and TMZ which are discussed in Chapter 3. In fact, while U373V carries a control vector, and is sensitive to TMZ treatment, U373M expresses the MGMT protein and is resistant to this anticancer agent.

The MTT assays performed on U373V and U373M showed a similar growth inhibitory profile in both cell lines to $[Cu(phen)]^{2+}$ and HSAFt-Cu(phen), again with a mild effect exerted by the presence of the protein cage on the overall activity of the metal complex (Figure 2.20). The GI_{50} values were 2.3 µM for $[Cu(phen)]^{2+}$ in both cases and only slightly lower for HSAFt-Cu(phen) (Table 2.1). No toxicity was observed when cells were treated with HSAFt only.

To corroborate the results reported above on GBM cancer cell lines a clonogenic assay was set up exposing the cells to HSAFt (0.05 µM), $[Cu(phen)]^{2+}$ (2.5 µM) and HSAFt-Cu(phen) (2.5 µM copper). Differently from the cell count assay employed previously, the clonogenic assay measures the ability of the cell lines tested to form colonies of > 50 cells.[201] For this reason, the cells were seeded in 6-well plates at a low density (400 cells/well) and incubated with test agents until day 6, when the cells were then washed and incubated in fresh media until colonies were observed in the

control wells. The results from the clonogenic assay show that the cytotoxicity of the $[Cu(phen)]^{2+}$ on both cell lines is similar and higher than that exerted by the HSAFt-Cu(phen) adduct (Figures 2.21, 2.22). This further corroborates observations made in the MTT assays: HSAFt-Cu(phen) is still cytotoxic, but in this case the protein cage seems to exert a shielding effect on the cells from its cargo. Even though there is a difference between the effect of the complex alone and encapsulated into AFt these results are encouraging, especially when looking at the toxicity exerted on the U373M resistant cells.

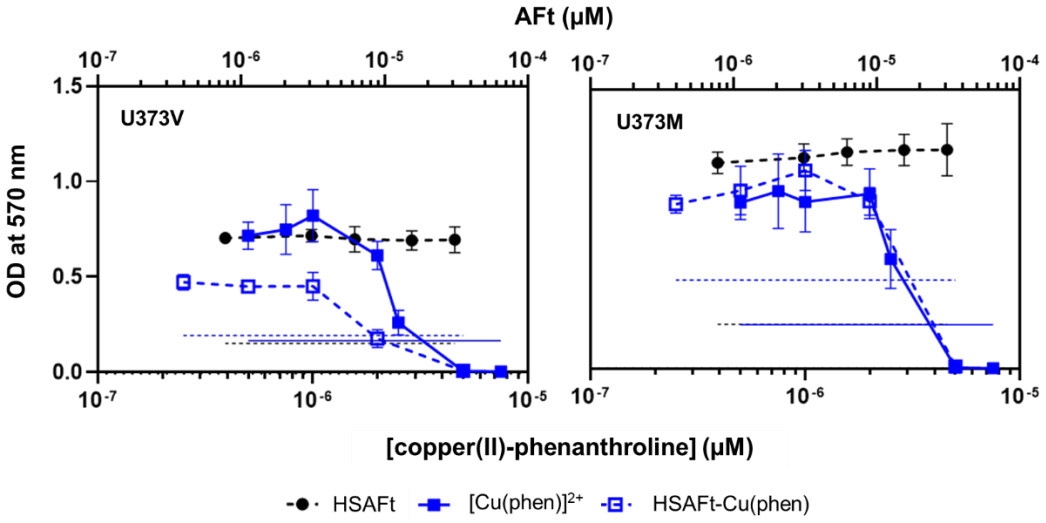

Figure 2.20. Effect of HSAFt, $[Cu(phen)]^{2+}$ and HSAFt-Cu(phen) on U373V and U373M. MTT assays were performed at time of test agent addition (T_0) and following 6 days treatment of cells with test agents. Representative dose-response curves are shown. Data points are mean ± SD (n=8); 3 independent trials were conducted.

The lack of significant effects on cell cytotoxicity observed for HSAFt-Cu(phen) compared to $[Cu(phen)]^{2+}$ is likely to be related to the higher stability provided to the HSAFt-Cu(phen) adducts by the protein corona formed by the AFt shell. Studies on metal complexes like platinum-based anticancer agents showed that their interaction upon loading inside AFt reduces their pharmacological activity.[133]

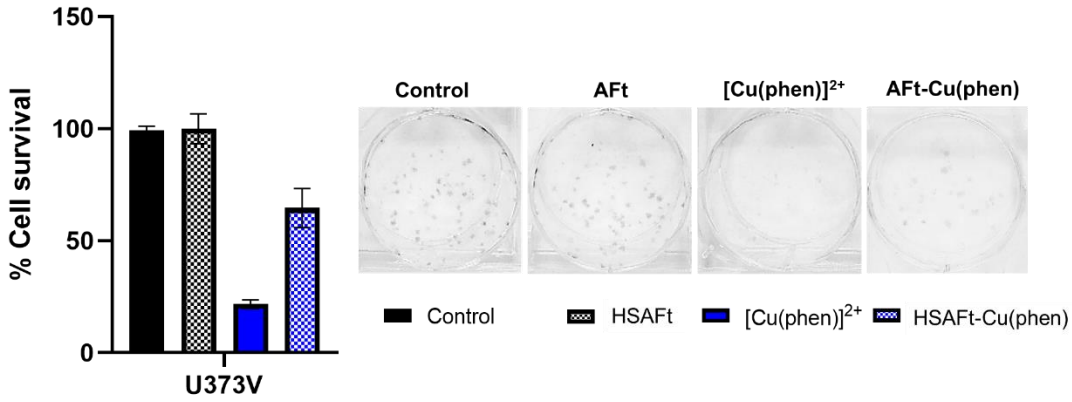

Figure 2.21. Effect of HSAFt, $[Cu(phen)]^{2+}$ and HSAFt-Cu(phen) on U373V GBM cells (72 h exposure). Representative cell survival data are shown. Data points are mean ± SD (n=2); 3 independent trials were conducted. Control represents cells incubated with media only until colony staining.

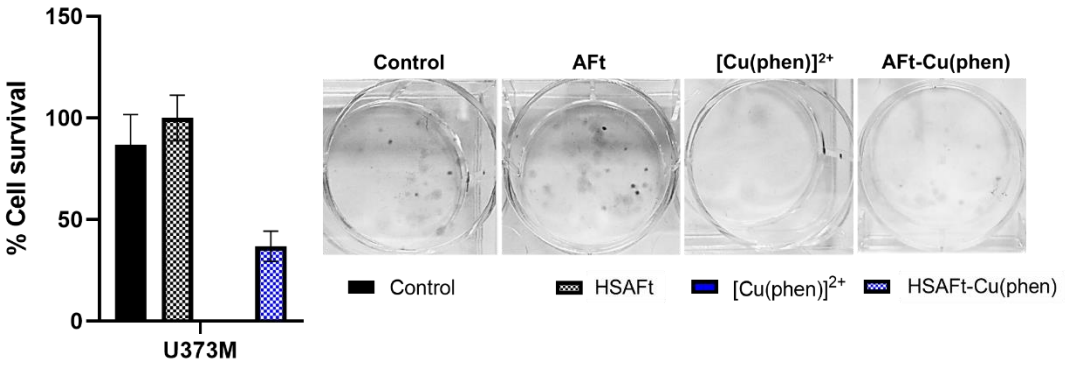

Figure 2.22. Clonogenic assay testing the effect of HSAFt, $[Cu(phen)]^{2+}$ and HSAFt-Cu(phen) on U373V GBM cells (72 h exposure). Representative cell survival data are shown. Data points are mean ± SD (n=2); 3 independent trials were conducted. Control represents cells incubated with media only until colony staining.

These results can be interpreted in light of the data presented in the previous sections of this chapter. At physiological conditions (pH 7.4, 37 ºC) up to 40 % of phenanthroline is released from the cage reaching a plateau at 10 h, which could be the likely cause of the cytotoxicity observed in the assay. If this is the case, AFt would only provide limited control over the anticancer moiety release causing it to exert the same level of cytotoxicity. At the same time, this might also indicate loss of copper coordination by the 1,10-phenanthroline ligand and therefore loss of the combined toxicity of the metal-ligand complex. In fact, the cytotoxicity observed in other studies with $[Cu(phen)]^{2+}$ in solution resulted from the contribution of the metal promoting the production of ROS and the ligand causing DNA damage. [105]

These findings make the analysis of a co-encapsulation system of HSAFt-Cu(phen) with TMZ interesting not only to investigate the effect on drug release but also to investigate the cytotoxic activity compared to literature studies using HSAFt-TMZ and HSAFt-Cu-TMZ. [8,138]

2.5 Summary and Conclusions

This study aimed to investigate in detail the effects of the loading of HSAFt with the complex of copper(II) with 1,10-phenanthroline, the precursor of a family of novel anticancer agents currently under clinical evaluation.[101] Encapsulation by nanoreactor route in sodium acetate buffer at pH 5.5 was identified as the optimal method to produce HSAFt-Cu(phen). Protein characterisation after the encapsulation suggested that $[Cu(phen)]^{2+}$ did not affect the integrity and the properties of the AFt cage. Oscillation in the copper loading within a fixed range was detected by ICP-MS, which could be attributed to the small variability in the heavy to light chain subunits ratio in the protein batches prepared for the experiments. Although UV-vis data confirmed the presence of 1,10-phenanthroline in the sample, the determination of the exact metal to ligand stoichiometry was not possible.

Upon HRTEM analysis crystalline structures could be seen forming in the HSAFt-Cu(phen) samples which remained visible for up to 4 months of storage at -20 ºC. The lattice of the crystal structure formed by copper atoms was measured and with the EELs data it helped informing the hypothesis for the arrangement of the copper inside AFt. It was hypothesised that the copper ions interact with the acidic residues exposed inside AFt forming layers on the internal surface of the protein shell. In addition to these organised layers, the UV-vis and drug release results suggest the presence inside AFt of a central bulk likely formed by mono and tris copper-phenanthroline complexes. This phenomenon was already observed upon characterisation by X-ray crystallography of HSAFt loaded with cisplatin as well as other platinum (II) complexes.[133] These studies reported consistently a higher metal content detected by ICP-MS analysis compared to the crystallographic results, suggesting that a significant number of the encapsulated metal complex was not directly bound to the cage but is probably trapped in the central bulk.[133]

Following from the HRTEM data, other experimental conditions were investigated: pH and temperature. The results collected suggested that the pH conditions could

influence the growth and the size of the HSAFt-Cu(phen) adducts over time. However, they did not provide enough evidence to attribute their formation entirely to the buffer pH conditions. When tested for content release under physiological conditions (37 ºC, PBS pH 7.4), the HSAFt-Cu(phen) samples showed loss of up to 40% of the ligand within 10 h of incubation and of 10% of the metal in 24 h. Although these data did not provide information on the ratio between $[Cu(phen)]^{2+}$ complexes and separate metal and 1,10-phenanthroline released, it showed good retention of metal and ligand by the AFt cage when compared to lipid nano-formulations.[201]

In vitro cell cytotoxicity assays showed that $[Cu(phen)]^{2+}$ was cytotoxic to all cell lines tested, with MRC5 being the most sensitive and HCT-116 being the most resistant. No dramatic change in the cell toxicity was observed by exposing the same cell lines to HSAFt-Cu(phen). This effect could be caused by the release of the intercalating agent 1,10-phenanthroline from the protein cage before internalisation as observed in the release test at physiological conditions. However, HSAFt-Cu(phen) showed very similar growth inhibitory profiles in isogenic TMZ-sensitive and resistant glioblastoma cell lines. This result is promising in view of the study of the effects of co-encapsulation of HSAFt-Cu(phen) with the anticancer agent TMZ to evaluate its drug retention capacity and its effects in particular to MGMT-expressing cancer cells (U373M).

In conclusion, the experiments reported in this chapter confirm HSAFt-Cu(phen) as a cytotoxic agent in solution, whose cargo is composed of a mixture of different copper species associated with 1,10-phenanthroline. These features are likely to contribute to the anticancer activity of HSAFt-Cu(phen), while no catalytic activity towards hydrolysis of prodrug functionalities was detected. These findings allowed the characterisation of HSAFt-Cu(phen) for the next steps of this study involving the co-encapsulation with the anticancer prodrug TMZ.

3. Encapsulation of horse spleen AFt-Cu(phen) with temozolomide: studies on drug stability and *in vitro* anticancer activity

3.1 Background

The intrinsic features of AFt as a biological metal carrier have contributed to its extensive study for the loading of anticancer agents and their controlled release.[139] Many anticancer agents have been encapsulated into AFt: the platinum complex cisplatin,[135,132,136] the antitumour antibiotic doxorubicin,[140] the protein kinase inhibitor gefitinib[137] are some examples. The general method for the encapsulation of small molecules into AFt is the nanoreactor route which involves the diffusion of the drug molecules into the protein cage through its hydrophobic and hydrophilic channels.[133] However, as the drug molecules encapsulated through this route should also be able to fit inside the protein channels (0.3-0.5 nm),[139] they can also leak out of the protein shortly after the encapsulation. A factor that constitutes a significant challenge for their delivery.

TMZ provides a good example of this issue. This prodrug is currently used for the treatment of GBM, an aggressive brain tumour with poor prognosis.[8] TMZ undergoes spontaneous ring-opening at pH > 7 into 5-(3-methyltriazen-1-yl)imidazole-4-carboxamide (MTIC) which is the precursor of a methyl diazonium ion that alkylates cellular DNA (Figure 3.1 a). [8,213,214] Once generated, MTIC is extremely unstable ($t_{1/2}$= 3 min) and quickly degrades into 5-amino-imidazole-4-carboxamide (AIC) at pH < 7 (Figure 3.1 a).[8] Even though TMZ efficacy against sensitive GBM cells is high, the hydrophilicity of its metabolites prevents quantitative crossing of the BBB and favours renal and hepatic clearance, reducing the drug availability to 20-30 % and causing dose-limiting haematological toxicity.[215,216] The half-life of TMZ under physiological conditions (pH 7.4) is 2 h.[8] However, it is important to highlight that only TMZ and MTIC are hydrophobic enough to cross the BBB and that the half-life of MTIC is very short. This causes most of the drug administered to be activated into its metabolites in the blood circulation before reaching the tumour in the brain.

Recent reports show that when TMZ is encapsulated into AFt, the loaded drug is released at pH 5.5 quicker than at pH 7.4,[138] an encouraging result for the controlled

delivery of TMZ to tumour cells (Figure 3.1-b). The protective effect provided by AFt can stabilise the structure of TMZ by slowing down its activation into MTIC and the non-specific toxicity. This protective effect of AFt under experimental conditions mimicking the blood circulation can contribute to its targeted delivery to the brain, prevent its degradation and increase prodrug accumulation into GBM cells, where the lower pH favours both the relaxation of the protein cage and drug release.

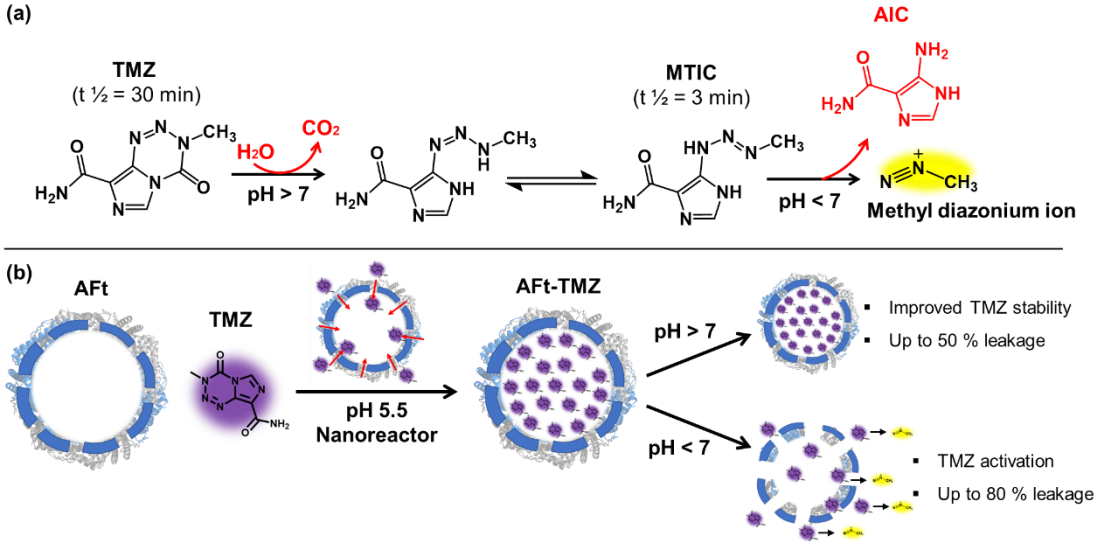

Figure 3.1. Prodrug activation and pH-dependent degradation of TMZ in solution (a) and inside AFt as reported by Bouzinab *et al.* (b).

The natural affinity of AFt for metals can be exploited to improve the retention of small molecules with metal coordinating functionalities. Examples of this were provided in recent literature describing the encapsulation of anticancer agents including doxorubicin,[150] olaparib,[124] 5-fluorouracyl[151] and TMZ[8] with metal ions into AFt. A less frequent approach to this issue involves the use of negatively-charged aspartic acid sequences to stabilise and prevent the leakage of positively charged agents such as daunomycin.[145] Of particular interest is the work of Li *et al.* which reported the formation of a copper-MTIC complex detectable by a UV-vis shift to 355 nm (Appendix 3.A) with improved stability resulting from the encapsulation of TMZ into AFt in presence of free copper(II) as illustrated in Figure 3.2.[8] The result was the immobilisation of MTIC inside the protein and the improvement of its stability at alkaline and acidic pH. In this system drug release was dependent on intracellular availability of glutathione (GSH) able to reduce copper(II) to copper(I) after AFt disassembly and thus release MTIC.[8]

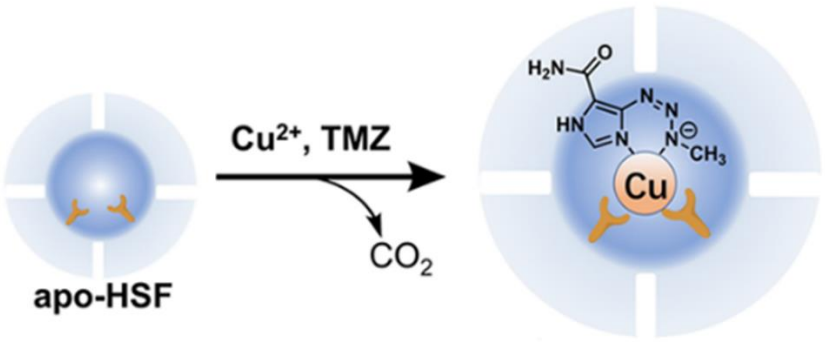

Figure 3.2. Mechanism of copper-enhanced TMZ hydrolysis to MTIC upon AFt encapsulation as reported by Li *et al.*

The work described in this chapter includes studies on the effects of the encapsulation of TMZ inside the HSAFt-Cu(phen) cages produced and characterised in Chapter 2. Following from the work of Li *et al.* it was decided to investigate if the presence of a copper(II)-phenanthroline complex would still induce the conversion of TMZ into MTIC otherwise observed in the presence of free copper (II).[8] The crystal structure of TMZ complex with divalent cations like cadmium (II) has been previously reported with no indication of prodrug degradation.[217] Furthermore, the deprotonated nitrogen on the imidazole ring of TMZ could offer a coordination site for the copper (II) loaded as its mono-phenanthroline complex inside AFt (Figure 3.3).[179] The formation inside AFt of copper (II) complexes with two ligands (one phenanthroline and one TMZ molecule) would provide greater cytotoxicity against resistant GBM cancer cells as copper(II)-phenanthroline complexes have anticancer activity (see Chapter 2, section 2.4). Besides, a Cu(phen)-TMZ complex loaded into AFt would result in a structure bulkier than TMZ with the potential of reducing the amount of drug diffusing out of the protein channels (Figure 3.3), thus providing an additional advantage over the potent AFt-TMZ formulation.[138]

To summarise, the purpose of the work presented here was to assess the impact of the formation of HSAFt-Cu(phen) in retaining and affecting the accumulation and the release of the anticancer agent TMZ. Upon the formation of the HSAFt-Cu(phen) adducts, TMZ was loaded via the nanoreactor route (Figure 3.3), encapsulation efficiency was assessed by UV-vis and copper content checked via ICP-MS. After confirming the cage integrity by HRTEM and DLS, the protein-metal-drug complexes were tested on three cancer cell lines (HCT-116, U373V, U373M) and normal cells (MRC5) by MTT and clonogenic assays. The rate of TMZ release from the AFt-Cu(phen)-TMZ complex was determined by UV-vis at different conditions and compared to literature findings for the AFt-TMZ systems.[138] This study could

contribute to the evaluation of the features of an HSAFt-Cu(phen)-TMZ formulation in comparison with metal-drug and drug only encapsulated systems already characterised, providing information on the use of AFt as drug delivery device for the metal-assisted controlled release of TMZ.

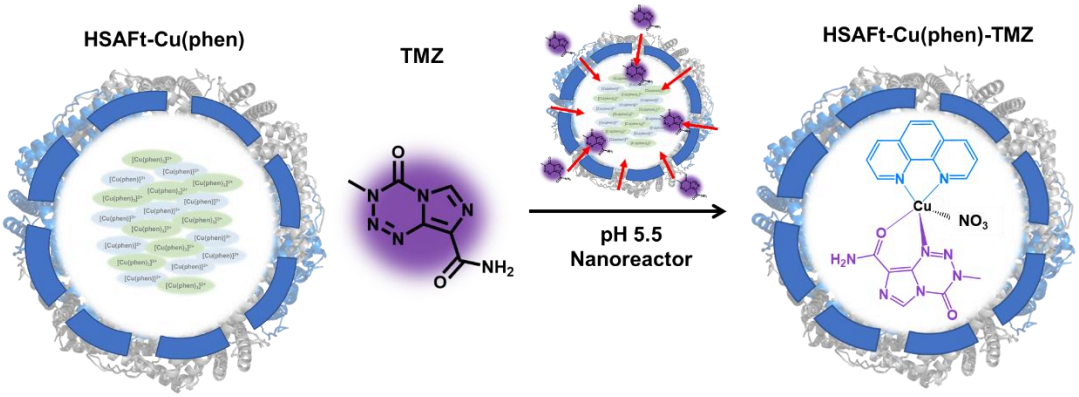

Figure 3.3. Encapsulation of HSAFt-Cu(phen) with the anticancer agent TMZ and proposed structure of HSAFt-Cu(phen)-TMZ complexes (only one Cu(phen)-TMZ complex is illustrated inside AFt for clarity).

3.2 Production of HSAFt-Cu(phen)-TMZ: characterisation and drug release studies

3.2.1 Encapsulation of TMZ into HSAFt-Cu(phen)

The encapsulation of TMZ followed the production and the formation of AFt-copper adducts as described in Chapter 2. To ensure consistency in results the TMZ loading was performed on HSAFt-Cu(phen) samples stored 1 month at -20 °C and with an average copper (II) content of 334 metal ions/AFt cage, at which point the formation of the crystalline metal adducts was confirmed by HRTEM (Chapter 2, Section 2.2.3). The TMZ encapsulation followed the protocol described by Bouzinab *et al.*[138] in which the AFt cages were incubated with TMZ in a 1:800 ratio for 3 h at 4 °C and pH 5.5, then purified by ultrafiltration using a 10000 MWCO VIVASPIN microfuge column.

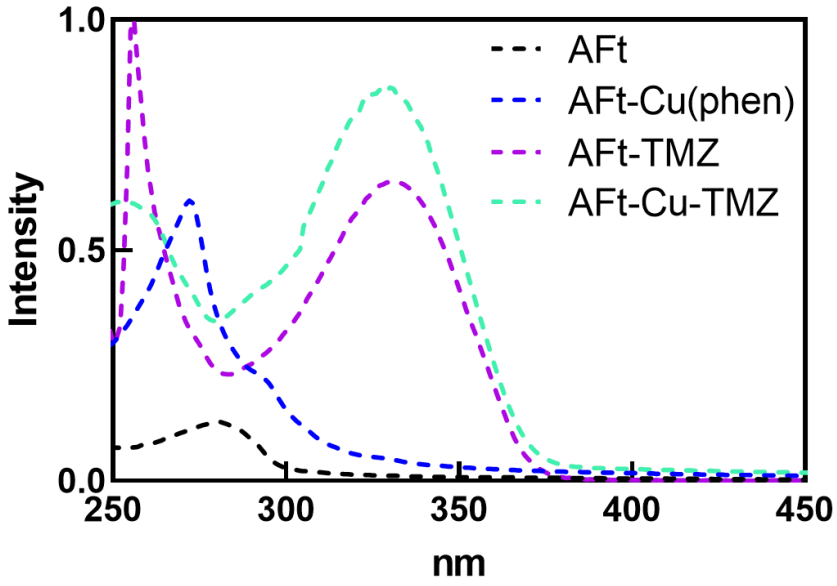

Figure 3.4: UV-vis spectrum of HSAFt-Cu(phen)-TMZ in NaOAc buffer pH 5.5.

After encapsulation, the sample was analysed by UV-vis to estimate the ratio of TMZ/AFt which was found to be 339 TMZ molecules per AFt cage (mean of 4 independent experiments, SD= 52). As shown in Figure 3.4 a TMZ has an absorbance maximum at 330 nm that can be used to estimate its concentration from the recorded intensity and its extinction coefficient of 9800 M^{-1} cm^{-1} using the Beer-Lambert equation (Appendix 3.B). The encapsulation efficiency (EE) and drug loading (DL) were 28.8 ± 4.0 % and 13.0 ± 2.8 % respectively (Appendix 3.C). Previous reports have shown that the AFt cage can accumulate up to 520 molecules of TMZ, with EE and DL higher than those reported in this study.[138] Instead, when the TMZ was loaded with free copper (II), the overall number of TMZ molecules encapsulated into AFt and converted into MTIC was much lower (Table 3.1).[8] Furthermore, is important to mention that the EE estimated for HSAFt-Cu(phen)-TMZ is higher if compared to liposomal formulations of TMZ.[216]

To validate the hypothesis that decreased TMZ encapsulation was due to the presence of copper(II)-phenanthroline and to compare the copper content to that reported by Li *et al.*, ICP-MS measurements were performed on the HSAFt-Cu(phen)-TMZ samples after encapsulation. As reported in table 3.1 there was a decrease in the metal ion content from 334 to 126 (SD= 48) copper/AFt upon TMZ encapsulation, which suggests that some of the copper is likely to be displaced from the AFt core to favour TMZ accumulation. The extremely low absorbance of the copper(II)-phenanthroline complex by UV-vis (ʎ= 697 nm) did not allow for the direct detection and estimation of the encapsulated complex. Therefore, ICP-MS demonstrated that

the copper content of HSAFt-Cu(phen)-TMZ was lower than reported for AFt-Cu-MTIC systems, in which the metal to complex ratio was consistent with the successful immobilisation of MTIC.[8] Distinct from the report by Li *et al.*, it is reasonable to infer that no interaction between the AFt-encapsulated copper (II) and MTIC was observed in the experiments reported here, as no change in the TMZ peak was visible by UV-vis. After the addition of copper (II), *Li et al.* reported a shift in the absorbance of aqueous TMZ solutions in PBS at pH 7.4 from 330 nm to 355 nm, suggesting the formation of a stable Cu-MTIC species also in presence of AFt.[8] Although there is no visible shift between the spectrum of TMZ and that of copper-TMZ (Appendix 3.A), the UV spectrum illustrated in Figure 3.4 of HSAFt-Cu(phen)-TMZ showed only a peak at 330 nm with no other peaks belonging to the prodrug metabolites. These results confirmed the presence of TMZ as the only species inside the protein cage (Appendix 3.A).

Formulation	Cu/AFt ratio	TMZ/AFt ratio
AFt-TMZ (Bouzinab *et al.*)	-	520
AFt-Cu-MTIC (Li *et al.*)	334	184
HSAFt-Cu(phen)-TMZ	126	339

Table 3.1. Table summarising the average metal and drug encapsulation per AFt cage recorded in this study (HSAFt-Cu(phen)-TMZ) and reported by Bouzinab *et al.* (AFt-TMZ) and by Li *et al.* (AFt-Cu-MTIC).

3.2.2 Evaluation of the structural integrity of HSAFt-Cu(phen)-TMZ

Once the preliminary characterisation of the HSAFt-Cu(phen)-TMZ was completed the formulation was analysed by HRTEM to investigate the effect of drug loading on the crystalline copper (II) adducts. In this case, the same sample was analysed by bright-field HRTEM with uranyl acetate staining (Figure 3.5). By using the staining on the sample, it was possible to achieve a better definition of the distribution of the copper adducts inside the AFt cages upon TMZ addition. As can be observed in Figure 3.5, there were visible dark circular structures corresponding to the copper adducts formed in HSAFt-Cu(phen)-TMZ samples aged 1 month as already described in Chapter 2. However, the image denoted non-homogeneous distribution

of the metal cores in a highly concentrated AFt sample. The density of copper cores observed compared to protein cages agrees with the ICP-MS results reported previously (Figure 3.5), which suggested a loss of copper upon encapsulation with TMZ. Therefore, even though the TMZ and the copper(II)-phenanthroline encapsulation ratios positively compare to similar literature studies, [138,8] these images show that the actual distribution of each agent and the metal adducts was variable among the AFt cages present in the sample.

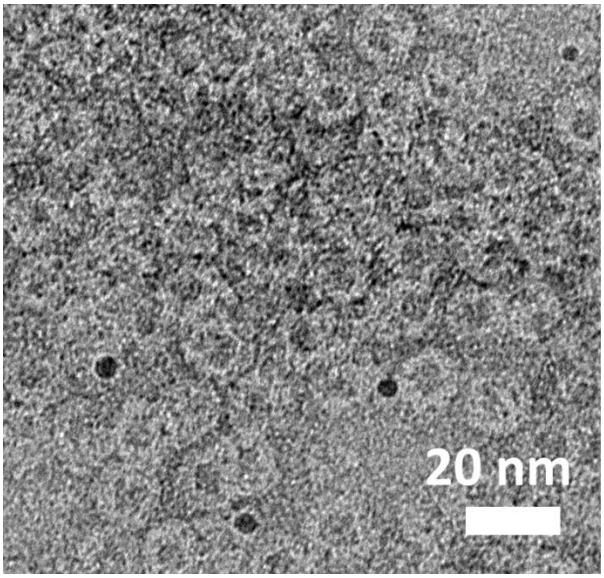

Figure 3.5. HRTEM on stained HSAFt-Cu(phen)-TMZ.

As reported in the previous HRTEM analysis of HSAFt-Cu(phen) samples exposed to different conditions, the presence of copper(II) detected by ICP-MS could not be corroborated by HRTEM, due to the low copper content (Chapter 2). In this case the low concentration of the metal has led to the formation of fewer visible cores inside the AFt cage with the remaining copper dissolved in solution and inside the protein without forming organised lattices (Chapter 2, section 2.2.6). For this reason, it is important to stress that the estimates that were provided on the encapsulation experiments referred to the whole sample and were not an exact measure describing the content of a single AFt cage. Literature examples of drug co-encapsulation into AFt with copper illustrated that the presence of the metal, although detected by UV or ICP-MS data is not always visible by HRTEM even when coordinated by the loaded organic compounds.[124,218]

Figure 3.6-a shows the DLS profile from which the hydrodynamic radius of the HSAFt-Cu(phen)-TMZ was estimated to be 14.7 ± 2.2 nm. The value recorded suggests no significant difference to the empty AFt cage (17.2 ± 1.3 nm) and from the HSAFt-

Cu(phen) precursor (15.4 ± 2.8 nm). However, the DLS profile for HSAFt-Cu(phen)-TMZ (Figure 3.6-a) could suggest the presence of particles with a larger size within the distribution. However, as reported for other anticancer formulations using AFt: having a large number of (charged) molecules loaded inside the cage can produce a small enhancement of its size.[120] The zeta potential measurement and the native PAGE (Figure 3.3-b) also confirmed the stability of the external charge of HSAFt-Cu(phen)-TMZ measured (-7.49 ± 0.63 mV) compared to that of AFt (-7.79 ± 1.97 mV) and so of its structural integrity.

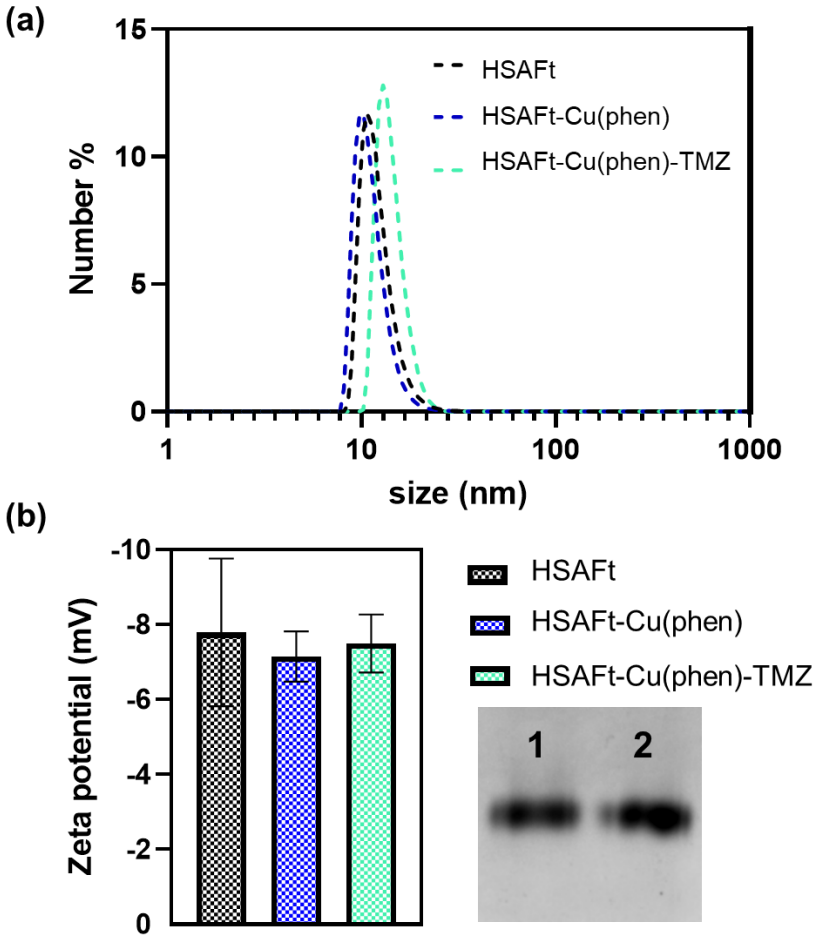

Figure 3.6 (a) Hydrodynamic size distribution of HSAFt, HSAFt-Cu-phen and HSAFt-Cu(phen)-TMZ measured by dynamic light scattering. (b) Zeta potential values of HSAFt, HSAFt-Cu-phen and HSAFt-Cu(phen)-TMZ (left) and native PAGE of HSAFt-Cu(phen) (lane 1) and HSAFt-Cu(phen)-TMZ (lane 2).

When compared to similar analyses there is no major deviation between the average hydrodynamic size reported in the literature. Both Bouzinab and Li *et al.* observed a protein diameter of 13 and 12 nm respectively after encapsulation. [8,138] However, significant differences are present when comparing the zeta potential measurements

to those reported for AFt-TMZ cages (-12.7 ± 0.3 mV).[138] The reason for this difference can be explained by the use of different media and pH values to perform the zeta potential measurement, compared to other literature reports.[138,215] The zeta potential measurements of HSAFt-Cu(phen)-TMZ and the control AFt reported in this section were performed in NaOAc buffer at pH 5.5 a value close to the HSAFt pI.[219] Given that the AFt-TMZ cages produced by Bouzinab *et al.* were analysed in water[138] this phenomenon can explain the less negative potential observed for the AFt cages analysed in this study. Recent reports of AFt-gold NPs formulation also introduced the hypothesis of protein oligomers forming in AFt loaded cages, leading to a change in the protein charge upon encapsulation of organic and inorganic compounds.[200] Although these results did not provide more insights into the variability of the core composition of the HSAFt-Cu(phen)-TMZ cages, there is enough evidence to infer that the copper(II)-phenanthroline and TMZ are localised inside AFt and did not affect the subunits assembly into its quaternary structure.

3.2.3 Drug release studies

The purpose of the encapsulation of a copper complex with an anticancer agent bearing potential metal coordinating functionalities like TMZ (Figure 3.1) was to prevent uncontrolled leakage of the drug and ensure tumour-specific delivery. The case of AFt and TMZ is especially interesting due to the pH-dependent features of the prodrug and the vehicle. TMZ lacks sufficient stability at pH > 7 to achieve tumour accumulation without damaging normal tissues and AFt has a structure able to favour drug delivery under acidic conditions (pH < 7).[213,138] The integrity of the AFt cage at pH > 7 could shield TMZ from premature activation and ensure its release only after internalisation in the tumour cell where the pH is more acidic.[134] In addition to the protective role of AFt, it was hypothesised that the encapsulation of a metal complex like copper(II)-phenanthroline with TMZ could favour the non-covalent immobilisation of the prodrug into AFt, preventing its leakage through the protein channels.[8,124,217] For this reason, it was crucial to test the ability of the HSAFt-Cu(phen)-TMZ formulation in stabilising the TMZ cargo when exposed to different conditions. As performed for HSAFt-Cu(phen) in Chapter 2, the HSAFt-Cu(phen)-TMZ sample was also exposed to pH 5.5 and 7.4 at 37 °C for 24 h, by dialysis. The acidic pH mimicked the endosomal environment upon internalisation into cancer cells, and the physiological pH was useful to identify any drug leakage in the bloodstream before reaching the tumour site. Given its absorbance at 330 nm, TMZ release was detected and quantified recording the UV-vis spectra of the dialysis buffers at different time points (0, 1, 3, 5, 7, 24 h) according to the method illustrated in Appendix 3.F. Also,

the total amount of copper released in the dialysis solutions after 24 h was measured by ICP-MS.

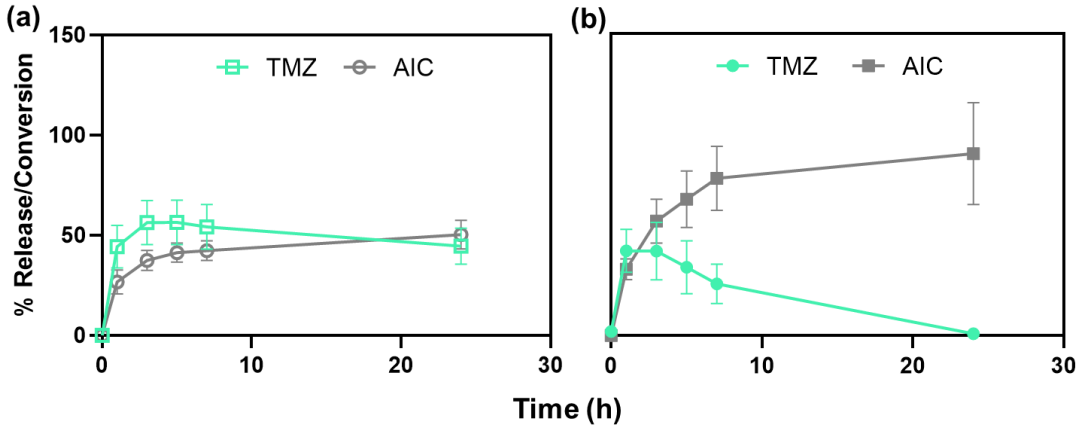

Figure 3.7. TMZ release from HSAFt-Cu(phen)-TMZ and degradation into AIC at pH 5.5 (a) and 7.4 (b).

The data collected show that the HSAFt-Cu(phen)-TMZ formulation released TMZ under both pH conditions (Figure 3.7). However, at pH 7.4 the overall TMZ leakage was only 42 % (Figure 3.7-a) compared to 56 % observed at pH 5.5 (Figure 3.7-b). Given that the half-life of TMZ at pH 7.4 is 2 h, the presence of the prodrug peak at 330 nm after more than 5 h of incubation suggested that no significant conversion into MTIC and AIC occurred while TMZ was loaded inside AFt (Appendix 3.D). On the contrary, the TMZ released into the dialysis buffer (PBS pH 7.4) started to degrade after 3 h of incubation, as shown by the second peak at 265 nm corresponding to AIC (Appendices 3.A, 3.D). The estimation of % drug released was based on the concentration of TMZ estimated into the sample dialysed (corresponding to 100 %, Appendix 3.F).

These results were very similar to the release profile of TMZ observed for AFt-TMZ cages exposed to the same conditions.[138] At physiological pH a slower diffusion of the anticancer agent from HSAFt-Cu(phen)-TMZ was observed, which stabilised between 1-3 h and then showed a marked degradation of TMZ into AIC. At pH 5.5 the release was quick, and more drug molecules leaked in the first 3 h before reaching a plateau. In this case, the degradation of TMZ was only detectable after 5 h. This release profile could be explained by the flexibility of the AFt cage, whose structure is more ‘relaxed’ at acidic pH leading to the progressive swelling of the subunits and the consequent widening of the channels which accelerates the leakage of its cargo.[122,145,220]

As expected, the conversion of the released TMZ into AIC after 24 h was complete at pH 7.4 and only partial at pH 5.5.[216] As mentioned in section 3.1, alkaline environments favour the conversion of TMZ into its active compound MTIC, which is extremely unstable and then degrades into AIC.[216] This pH sensitivity is attributed to the protonation of TMZ, at acidic pH the drug is protonated and undergoes a slower degradation.[221] These data are very similar to those of AFt-TMZ formulations[138] suggesting that the presence of copper (II) as copper(II)-phenanthroline did not improve significantly the retention of TMZ, with respect to AFt alone.

Interestingly, the metal release measured on the samples after 24 h of incubation by ICP-MS showed that almost twice as much copper was released at pH 7.4 compared to the lower pH (Figure 3.8). This behaviour observed for HSAFt-Cu(phen)-TMZ was the opposite of that described for HSAFt-Cu(phen) in Chapter 2, section 2.2.5. In the HSAFt-Cu(phen)-TMZ more copper was released at pH 7.4 compared to pH 5.5, a phenomenon that cannot be explained by the flexibility of the AFt quaternary structures at different pH conditions. However, if the coordination of some of the copper(II)-phenanthroline with TMZ occurred during the encapsulation, the release of part of the TMZ from AFt could have destabilised the bulk formed by Cu(phen)-TMZ, thus favouring metal discharge. Overall the ICP-MS data confirmed that at both pH conditions AFt was still able to retain most of the metal present after TMZ encapsulation.

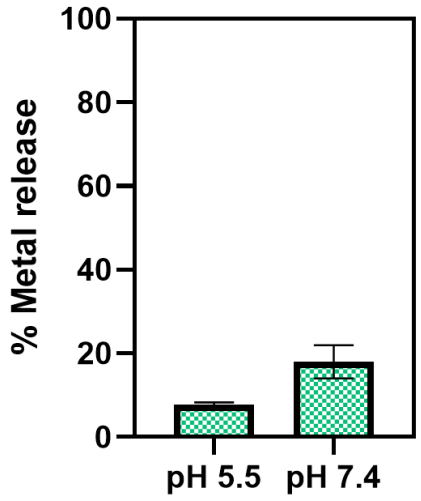

Figure 3.8. Copper release from HSAFt-Cu(phen)-TMZ after 24 h exposure to pH 5.5 and 7.4 at 37 °C (100 %= Cu concentration in the sample after encapsulation).

When the HSAFt-Cu(phen)-TMZ particles are compared to similar systems like the one described by *Li et al.* it is possible to observe the effect of the copper complex,

rather than just the metal, on the encapsulation and the stability of TMZ inside AFt. *Li et al.* reported the rapid conversion of TMZ into MTIC and the formation of stable Cu-MTIC complex upon encapsulation into AFt.[8] This stability was reflected by their experimental results, where > 90 % of MTIC was retained into AFt at pH 7.4 and 5.0.[8] Instead, from the data presented in this section, there was no evidence of MTIC forming upon co-encapsulation of AFt with $[Cu(phen)]^{2+}$ on the UV-vis spectrum recorded after TMZ encapsulation (Figure 3.4). This evidence was further substantiated by the drug release experiments (Appendix 3.C, 3.D) in which the compound visible in the dialysis buffer was TMZ as outlined by the peak at 330 nm, which degraded over time into AIC (Figure 3.7). More recent work from the same group reported that encapsulation of a TMZ-doxorubicin covalent complex with copper also led to the conversion of TMZ into MTIC.[215] Again, the copper-MTIC complex showed greater stability under physiologically relevant conditions.[215] This difference supports the hypothesis that all or most of the copper present into the HSAFt-Cu(phen)-TMZ formulation is coordinated either by 1,10-phenanthroline or by amino acid residues (as suggested in Chapter 2) and that formation of Cu-MTIC does not occur in the absence of free copper (II). Furthermore, the AFt-Cu-MTIC particles produced by Li *et al.* when tested for their stability demonstrated that MTIC release was dependent on the presence of millimolar concentrations of glutathione (GSH) which favours both redox and coordination interactions with copper(II).[215] A similar GSH-dependent drug release was reported also for copper-stabilised doxorubicin AFt formulations.[218] The data collected for HSAFt-Cu(phen)-TMZ show that TMZ diffused out of the AFt cage in the absence of intracellular components like GSH, in a way similar to that reported by Bouzinab *et al.* for AFt-TMZ.[138]

The AFt-Cu(phen)-TMZ formulation produced in this section successfully demonstrated that it is possible to prevent TMZ conversion into MTIC for encapsulation into AFt when using copper (II) coordinated by 1,10-phenanthroline instead of the free metal. This would favour pH-dependent drug release into tumour cells where TMZ would spontaneously produce its cytotoxic metabolites with no need for GSH-dependent activation. However, drug release experiments showed that the rate and the fraction of TMZ released from AFt were very similar between HSAFt-Cu(phen)-TMZ and AFt-TMZ[138] systems. Thus confirming the potent shielding effect that the protein cage can exert on TMZ stability at pH 7.4 and that the presence (and possible coordination) by a metal complex does not improve its retention. This protective effect of AFt is superior to that of liposomal formulations of TMZ.[216] Yet the $[Cu(phen)]^{2+}$ loaded into the HSAFt-Cu(phen)-TMZ formulation also showed its

potential antitumour effect on GBM cell lines (Chapter 2, Section 2.4). For this reason, the assessment of the *in vitro* activity of this formulation was considered essential in the evaluation of the anticancer effect of HSAFt-Cu(phen)-TMZ compared to AFt-TMZ.

3.3 *In vitro* anticancer activity of HSAFt-Cu(phen)-TMZ

HSAFt-Cu(phen)-TMZ showed behaviour similar to that already reported for AFt-TMZ[138] when tested for drug release and stability. The data collected by UV-vis suggest that the TMZ was not altered upon encapsulation into HSAFt-Cu(phen) and that the cage might have a role in prolonging the stability of the prodrug at pH 7.4. However, a portion of the encapsulated drug still leaked out under all tested conditions, leaving more than > 50 % of the drug molecules within AFt cages. At this point *in vitro* assays were required to assess the impact of TMZ leakage on the activity of the HSAFt-Cu(phen)-TMZ formulation. Cell culture studies were also needed to compare the growth inhibitory activity of the formulation in cancer and normal cells.

HSAFt-Cu(phen)-TMZ was tested against human fibroblasts (MRC5), colorectal cancer cells (HCT-116) and the isogenic GBM cells U373V (MGMT negative) and U373M (expressing high levels of MGMT). The first set of experiments performed were MTT assays, useful to identify the effect of the formulation on the GI_{50} value of TMZ. In this case, the exposure time to test agents was of 6 days for all cell lines. This extended incubation was essential to observe the pharmacological action of TMZ: the prodrug needs to hydrolyse into MTIC to then generate the methyl-diazonium ion that methylates the guanine on DNA to generate O^6-methylguanine.[1] At this point, O^6-methylguanine mispairs with thymine alerting the DNA mismatch repair machinery (MMR). However, the mismatch repair system does not remove the methylated guanine, instead removing and replacing thymine in futile cycles of attempted repair, ultimately causing lethal DNA damage during the S phase of the cell cycle, caused by the blockage of the replication fork (Figure 3.9).[1,222] While HCT-116 resistance to TMZ derives from their absence of MMR system, U373M cells are transfected with O^6-methylguanine-DNA methyltransferase (MGMT). Control experiments were performed on all cell lines with AFt and TMZ alone. No cytotoxicity was observed with the concentrations used of AFt. Instead, the anticancer effect of TMZ on GBM cells was denoted by a GI_{50} > 400 µM for U373M and ~50 µM for U373V (Figure 3.10, 3.11, Table 3.2).

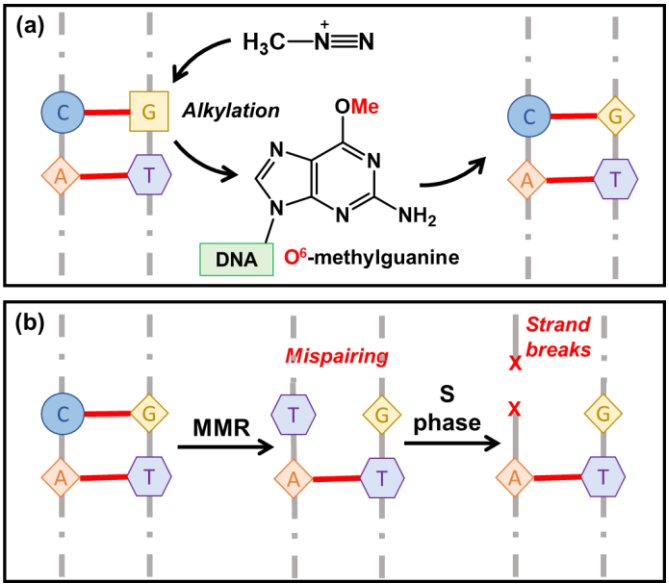

Figure 3.9. Mechanism of TMZ-driven DNA alkylation (a) and cell cycle arrest ultimately leading to tumour cell death (b).

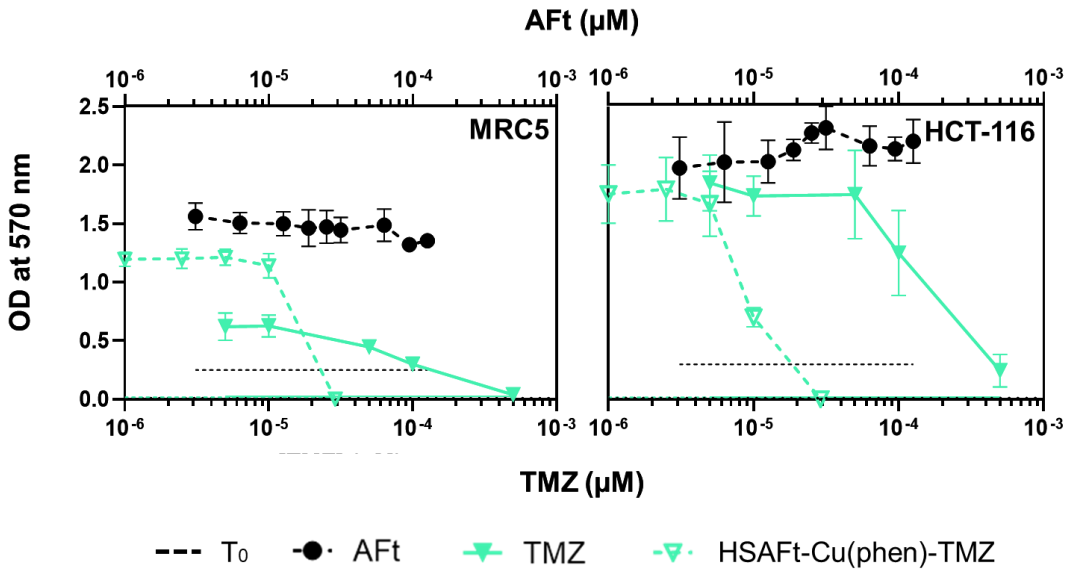

Figure 3.10. Effect of HSAFt, TMZ and HSAFt-Cu(phen)-TMZ on growth of MRC5 foetal fibroblasts and HCT 116 colorectal carcinoma cells. MTT assays were performed at time of test agent addition (T_0) and following 6 days treatment of cells with test agents. Representative dose-response curves are shown. Data points are mean ± SD (n=4); 3 independent trials were conducted.

There are several mechanisms of resistance that glioma cells can develop to survive the damage produced by TMZ, the main one being the expression of MGMT.[214] This enzyme can remove the methylation introduced by TMZ and allow for proper DNA replication.[214] MGMT expression is present in the U373M cells used for this study,

and the difference in sensitivity to TMZ was evident in the GI_{50} results (Table 3.2). Remarkably, HSAFt-Cu(phen)-TMZ was able to overcome the resistance and significantly increase the cytotoxicity exerted by the drug also on MGMT expressing cells. These data confirmed the effect of AFt on intracellular drug accumulation that was also observed for AFt-TMZ, which produced a 532-fold enhanced activity against TMZ-resistant U373M GBM cells (Table 3.2).[138]

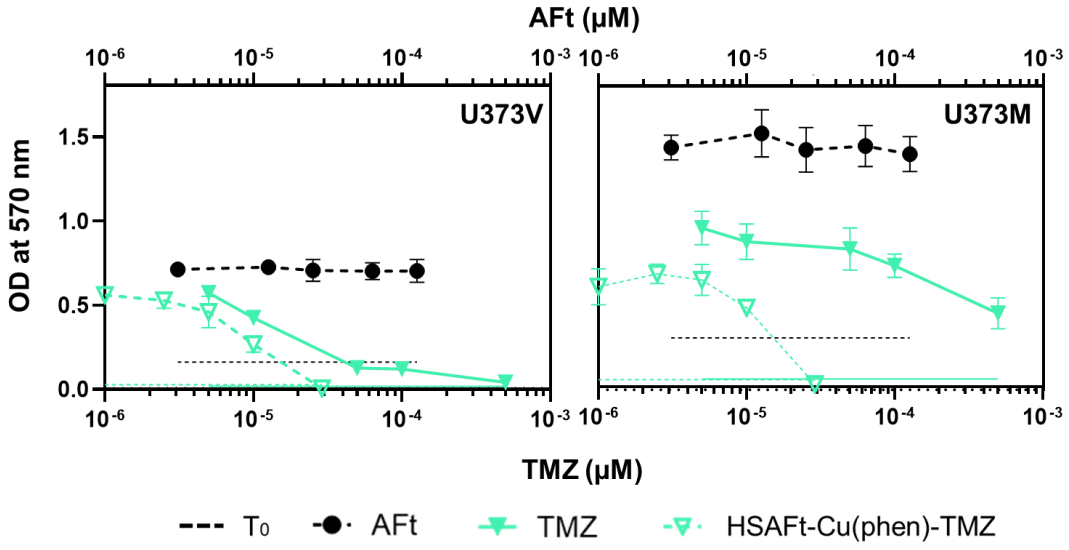

Figure 3.11. Effect of HSAFt, TMZ and HSAFt-Cu(phen)-TMZ on growth of TMZ-sensitive U373V and resistant U373M GBM cells. MTT assays were performed at time of test agent addition (T_0) and following 6 days treatment of cells with test agents. Representative dose-response curves are shown. Data points are mean ± SD (n=4); 3 independent trials were conducted.

The MTT assays showed the promising effects of HSAFt-Cu(phen)-TMZ against GBM cell lines tested. The results from the MTT assays were in line with that reported for AFt-TMZ.[138] To corroborate these results, clonogenic assays were performed on U373V and U373M. In this case, the concentrations tested were selected according to the GI_{50} values estimated from the MTT assays, being 0.05 μM for AFt and 20 μM for TMZ and HSAFt-Cu(phen)-TMZ and the exposure time was of 6 days (Figure 3.12, 3.13). Also, in this case exposure to AFt cages only led to no decrease in cell viability whilst HSAFt-Cu(phen)-TMZ caused a dramatic decrease in colony formation, more pronounced than with the TMZ only treatments (Figure 3.12, 3.13). Almost no colonies were stained after 13 days of incubation for both sensitive (U373V) and resistant (U373M) GBM cells.

	Cell line	TMZ	HSAFt-Cu(phen)-TMZ	AFt-TMZ
GI_{50} ± SEM (μM)	MRC5	140.5 ± 52.8	14.9 ± 6.7	<100
	HCT-116	198 ± 3.9	39.8 ± 24.5	<100
	U373V	23.2 ± 1.02	3.9 ± 0.93	< 1.5
	U373M	413 ± 48.1	13.3 ± 7.02	< 1.5

Table 3.2. Table summarising the GI_{50} values of TMZ (blue), AFt-TMZ (grey, from Bouzinab *et al.*) and AFt-Cu-TMZ (blue) in μM concentration estimated for the cell lines tested. GI_{50} is expressed as Mean ± SEM from Three Independent Trials, Where N = 8.

The ability to reduce cell viability of HSAFt-Cu(phen)-TMZ was especially important when observed for resistant U373M cells (Figure 3.13). This showed that the formulation can improve the efficiency of drug delivery to the point of overcoming the MGMT resistance mechanism, a result recently reported also by K. Bouzinab *et al* for AFt-TMZ cages.[138] However, if looking back at the MTT assays it is evident that the encapsulation that produced HSAFt-Cu(phen)-TMZ increased the toxicity also to MRC5 non-tumour cells (Table 3.1, Figure 3.10). Although this correlated with an acceptable GI_{50} difference with U373V cells, it did not for U373M cells with which the GI_{50} values of the HSAFt-Cu(phen)-TMZ formulation are very close (Table 3.2). This enhanced toxicity to normal cells was not observed when AFt-TMZ formulation was tested,[138] suggesting that the presence of copper(II)-phenanthroline in the HSAFt-Cu(phen)-TMZ could contribute to this effect. As this can be a major issue envisaging the clinical application of this system, another clonogenic assay was performed on U373M cells in which the incubation with the test agent was reduced to 24 h (Figure 3.13). Even though the decrease in colony number is not as dramatic it is still possible to observe a greater effect of HSAFt-Cu(phen)-TMZ (42 % cell viability reduction) after 24 h of exposure compared to TMZ only (35 % cell viability reduction). When treated with AFt-TMZ only, the U373M resistant cells colony formation was inhibited by 47 %.[214]

The cytotoxicity profile of HSAFt-Cu(phen)-TMZ showed greater activity compared to TMZ especially against TMZ-resistant U373M cells, which was consistent with the cytotoxicity reported for AFt-TMZ cages. However, this increased toxicity was also observed in normal fibroblasts, an effect that can constitute a challenge in the clinical application of the HSAFt-Cu(phen)-TMZ formulation. When compared to previous data on AFt-TMZ formulations an increase in cytotoxicity to MRC5 cells compared to TMZ was also observed.[214] However, in the case of AFt-TMZ the GI_{50} of the protein-

drug formulation for healthy MRC5 cells was reported to be almost 100 greater than that of GBM cells. This difference is enough to ensure selective cytotoxicity also against MGMT-positive U373M cells. The increased toxicity of HSAFt-Cu(phen)-TMZ against MRC5 cells can be explained by the presence of $[Cu(phen)]^{2+}$ complexes in the bulk of the AFt cargo with TMZ. As reported in Chapter 2, section 2.4, $[Cu(phen)]^{2+}$ and HSAFt-Cu(phen) the GI_{50} for this cell line was < 2 µM.

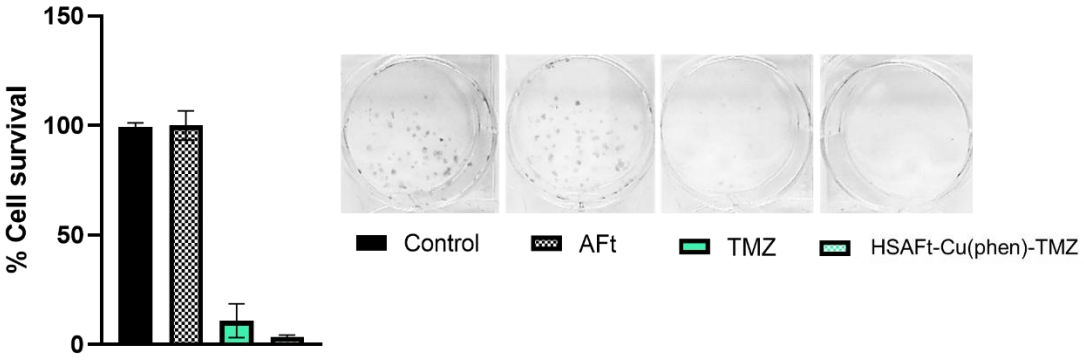

Figure 3.12. Effect of AFt, TMZ and HSAFt-Cu(phen)-TMZ on U373V cells (6 days exposure). Representative cell survival data are shown. Data points are mean ± SD (n=2); 3 independent trials were conducted.

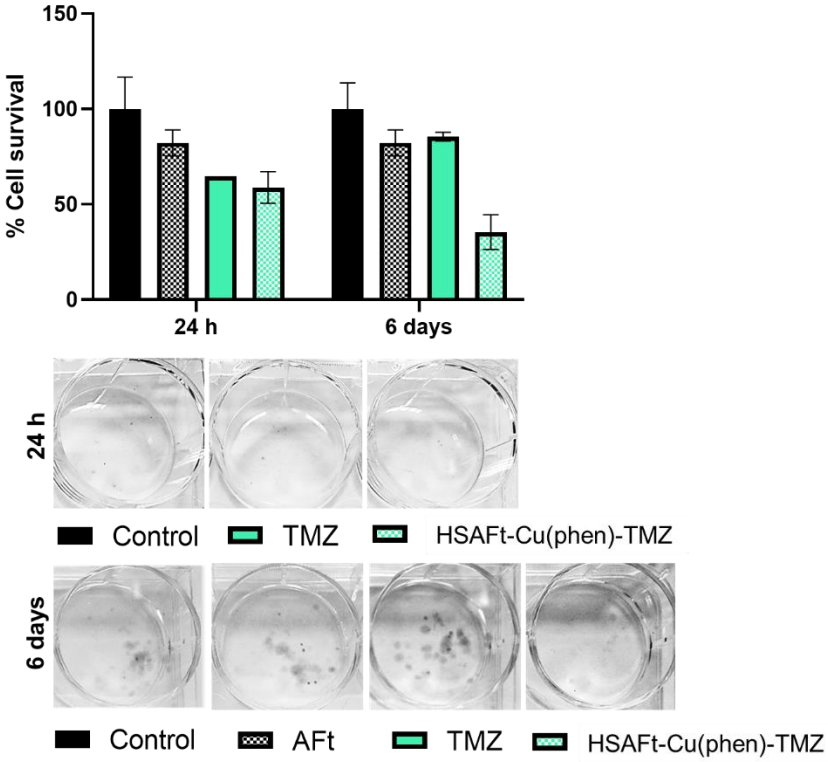

Figure 3.13. Effect of AFt, TMZ and HSAFt-Cu(phen)-TMZ on U373M cells (24 h and 6 days exposure). Representative cell survival data are shown. Data points are mean ± SD (n=2); 3 independent trials were conducted.

Overall, the *in vitro* studies of the effects of HSAFt-Cu(phen)-TMZ formulation showed that there is a greater anticancer effect compared to TMZ, which became particularly evident in TMZ-resistant cells. These data confirmed that although some drug was released from the cage at physiological conditions, the proportion of TMZ stabilised and retained by HSAFt-Cu(phen) was enough to decrease the viability of tumour cells. The greater anticancer effect exerted by AFt encapsulated TMZ formulation was observed both in the presence and in the absence of copper(II)-phenanthroline, thus suggesting a marginal role of the metal complex in enhancing pharmacological activity. The main difference emerging from the results presented in this section between HSAFt-Cu(phen)-TMZ and AFt-TMZ was the increase in toxicity observed on MRC5 non-tumour cells, which couldn't ensure selectivity over the TMZ resistant strain. Further evaluation of the toxicity exerted on U373M and MRC5 cells is required to better understand how to improve the risk-benefit ratio of HSAFt-Cu(phen)-TMZ for the treatment of resistant GBM. One way to do this would be by reducing the exposure time to detect an increase in the difference in the cytotoxicity observed. On this point, encouraging results were provided by the clonogenic assay testing HSAFt-Cu(phen)-TMZ on U373M cells over a 24 h exposure time. The same set of experiments could be performed on MRC5 cells in an attempt to optimise the ability of HSAFt-Cu(phen)-TMZ in overcoming GBM resistance without causing harm to healthy cells.

3.4 Summary and conclusions

The work described in this chapter reports the production of an AFt cage co-encapsulated with different copper(II)-phenanthroline species and the prodrug TMZ. The HSAFt-Cu(phen)-TMZ cages formed were able to load up to 339 TMZ molecules, with an EE and DL slightly lower than those reported for AFt-TMZ formulations.[138] An effect likely to have been caused by the presence of a copper(II)-phenanthroline bulk which limited the void space available for the TMZ molecules to accumulate. ICP-MS measurements showed that about 36 % of copper was released after the encapsulation of the HSAFt-Cu(phen) produced in Chapter 2 with TMZ. Although it was not possible to directly determine whether the copper measured was free or coordinated by 1,10-phenanthroline it is plausible to hypothesise that the observed release was a consequence of the low pH (5.5) at which the encapsulation was performed.

Recent literature reports showed that the interaction of copper with TMZ accelerates its degradation into MTIC to form a stable metal complex visible by UV (λ_{max}= 355

nm) both in solution and inside AFt. [8,215] However, no evidence of MTIC formation was observed by UV neither after the encapsulation nor during the drug release tests performed at different pH conditions. This evidence suggested that there was not enough free copper(II) to promote the conversion of TMZ into its metabolites and that most of the metal still present was coordinated by 1,10-phenanthroline. Therefore, the coordination exerted by the phenanthroline ligand on copper was able to prevent the degradation of TMZ into MTIC. The HSAFt-Cu(phen)-TMZ cages were imaged by HRTEM, which confirmed (along with DLS and native PAGE) the integrity of the AFt quaternary structure and showed the distribution of TMZ and the copper adducts in the sample to be highly variable between the protein cages.

When tested for drug release, the HSAFt-Cu(phen)-TMZ formulation showed a behaviour similar to that previously reported for AFt-TMZ, with slower drug release at pH 7.4 than 5.5.[138] The UV-vis data resulted in the release of intact TMZ (as evidenced by the peak at 330 nm) suggesting the ability of the cage to shield the prodrug from activation at physiological conditions (pH 7.4). A different release profile at pH 5.5 demonstrated that the flexibility of the AFt cage at lower pH favours a quicker and a larger discharge of its cargo, a feature that has the potential to favour selective drug delivery into cancer cells. Instead at pH 7.4, no significant TMZ leakage was observed after 1 h of incubation at 37 °C and the overall prodrug released and then degraded into AIC was 42 %. ICP-MS data revealed that more copper was released at pH 7.4 than at pH 5.5, a result opposite to what was observed for HSAFt-Cu(phen) (Chapter 2). These data illustrate that HSAFt-Cu(phen)-TMZ as AFt-TMZ can potentially reduce the amount of TMZ which gets degraded before reaching the BBB and the tumour site,[216] hence increasing the drug half-life and its efficacy at lower dosages. Therefore, the presence of copper(II)-phenanthroline did not produce any additional advantage over the control of TMZ release from AFt.

To evaluate the possibility of greater growth inhibitory activity exerted by the co-encapsulated anticancer agents Cu(phen) and TMZ, *in vitro* assays on GBM tumour cell lines were performed demonstrating the ability of the HSAFt-Cu(phen)-TMZ cage to increase the activity not only in MGMT(-) cells but also against MGMT(+) cells which are resistant to TMZ therapy. The GI_{50} value decreased by 30 times for U373M resistant cells when exposed to HSAFt-Cu(phen)-TMZ. These results were corroborated by clonogenic assays and also highlighted the increase in toxicity to non-tumour MRC5 cells as well. The potency of HSAFt-Cu(phen)-TMZ reduced the GI_{50} of TMZ for healthy fibroblasts by 10 times, which produced little difference from the average toxicity exerted against GBM resistant cells. This result was in contrast

with what was observed by Bouzinab *et al.* for AFt-TMZ cages,[138] conferring to the copper(II)-phenanthroline present into HSAFt-Cu(phen)-TMZ a role in the enhanced toxicity recorded on non-tumour cells. By reducing the exposure time of U373M cells to HSAFt-Cu(phen)-TMZ to 24 h it was still possible to observe a greater decrease in cell viability compared to TMZ alone. This result was useful in suggesting the possibility of optimising the selectivity of HSAFt-Cu(phen)-TMZ to resistant GBM cells by reducing the exposure time to the agent. However, further *in vitro* assays (such as apoptosis and cell count assays) are required to confirm the viability of this approach. Alternatively, the AFt outer surface can be modified for example with EGFR-targeting affibodies,[223] to increase the selectivity to GBM cells and avoid toxicity to healthy cells, thus improving the risk-benefit profile of the HSAFt-Cu(phen)-TMZ formulation.

To conclude the work herein reported illustrates the potential of a designed nanoformulation of AFt encapsulated with a copper(II)-phenanthroline and the prodrug TMZ for anticancer chemotherapy. The data displayed in this chapter fill the gap in the characterisation of AFt with a cargo combining the metal coordinating prodrug TMZ and a copper complex. These data can help in the optimisation and development of a system that could be tested for use in clinical settings for the site-specific delivery of pH-labile prodrugs like TMZ.[224]

4. Production of human AFt conjugated to copper(II)-phenanthroline and its effect on temozolomide encapsulation and release

4.1 Background

The previous chapters reported the study of the interaction between HSAFt and the metal complex copper(II)-phenanthroline before and after the encapsulation of the anticancer agent TMZ (Chapters 2 and 3). The protein-metal system was prepared using the nanoreactor method, then the effects on the release and stability of the co-encapsulated drug TMZ were explored (Chapter 3). HSAFt is the protein isoform most commonly used for drug delivery studies,[225] given its ease of preparation from the commercially available HSFt (see Chapter 7, section 7.4.1)[226] and the translatability of the *in vitro* results to the human protein.[68] However, as outlined in the literature review (Chapter 1) the use of HSAFt is more likely to cause immunogenicity upon clinical administration.[225,68,136] For this reason, the development of DDSs based on the use of human AFt is preferred. Furthermore, several *in vivo* studies performed on human H-chain AFt (HuHAFt) without additional targeting, reported a favourable pharmacokinetic profile characterized by enhanced accumulation into tumour tissue and efficient clearance from healthy organs.[227,228] The nuclear translocation ability of HuHAFt has been exploited for the delivery of siRNA, miRNA and the anthracycline antibiotic doxorubicin.[229,230] In addition to this, a recent study showed that HuHAFt uptake by cancer cells is enhanced and positively affected when the protein is loaded with inorganic compounds.[200]

However, the number of metal ions that can be stabilised into HuHAFt is < 1000 Fe(III) ions per cage compared to the 4500 Fe(III) ions for the light chain 24-mer.[180] This difference is related to the functions of each subunit. As described in Chapter 1 (section 1.3.1), the L-chain possesses amino acid side chains that can chelate metals and act as nucleation sites.[117] This was supported by the resolved X-ray crystal structures of both AFt subunits loaded with the platinum (II) drug cisplatin.[135] The different metal loading capacity of the AFt subunits was also reflected in the results of the preliminary work performed on HuHAFt before bioconjugation. The nanoreactor encapsulation of copper(II)-phenanthroline into HSAFt (Chapter 2) was replicated for HuHAFt. Under the same encapsulation conditions, the ICP-MS analysis of the sample detected < 1 copper ion per HuHAFt protein cage. The experiment was performed at pH 5.5 and pH 7.4 and both conditions gave the same copper content.

Lower metal complex loading with respect to HSAFt (Chapter 2) was also confirmed by the UV-vis spectra taken on the protein sample purified after encapsulation. The lower intensity of the HuHAFt-Cu(phen) protein compared to HSAFt-Cu(phen) from Chapter 2 at the same concentration suggested reduced phenanthroline retention (Appendix 4.A). The difference observed between the two formulations is linked to the different subunit ratios of each cage: HSAFt is > 80 % L-chain, instead, HuHAFt is 100 % H-chain.

The incorporation of metal complexes inside proteins can occur through different strategies[108] such as covalent anchoring, which was the method preferred for the work described in this chapter. The stability and the inert character provided by non-cleavable organometallic protein conjugates can afford a significant benefit for the targeted delivery of pharmacologically active molecules.[19] To achieve this objective, the decreased metal affinity of HuHAFt could be improved by the immobilisation of copper by covalent conjugation of the ligand (2-bromo-*N*-(1,10-phenanthrolin-5-yl)acetamide) to the interior surface of the protein. In this way, up to 24 copper (II) per /AFt cage could be introduced and their effect on drug accumulation and controlled release evaluated. The work reported by Zhang *et al.* showed the AFt size flexibility as a consequence of the electrostatic interactions between the protein and the species present in its core.[141] The binding of positively charged metal ions such as iron (II) or copper (II) to the negatively charged amino acids lining the internal surface of AFt can cause a contraction of its structure and the interprotein subunit channels.[141] It is reasonable to hypothesize that the modification of the AFt internal surface by introducing positively charged compounds could promote the entrapment of anticancer agents like TMZ and reduce their leakage. Modification of the AFt surface has already been employed for the loading of multiple agents with different levels of hydrophilicity/hydrophobicity.[149] Also the use of charged species to help the loading and retention of organic molecules has been described and documented in the literature.[119,145,150,8,151] The use of a HuHAFt copper bioconjugate for the encapsulation of TMZ would potentially immobilize part of the drug molecules by direct non-covalent interaction with the metal and physically entrap the remaining TMZ in the bulk formed inside the cavity. The combination of the protein-metal and metal-TMZ electrostatic interactions has the potential to reduce the leakage of TMZ from the protein cage (observed in Chapter 3) during drug delivery. For this reason, it was envisaged that labelling a recombinant cysteine mutant of HuHAFt with 2-bromo-*N*-(1,10-phenanthrolin-5-yl)acetamide would provide the advantage of greater

control over the localization of the metal and the composition of the labelled HuHAFt cages upon further encapsulation of TMZ (Figure 4.1).

The work reported in this chapter is aimed at the production of a HuHAFt cysteine mutant, modified by covalent conjugation with a copper(II)-phenanthroline complex, and loaded with the anticancer agent TMZ. The covalent conjugation could help to understand the effect of the copper coordinating phenanthroline on the metal binding capacity of the human H-chain homopolymer. The encapsulation with TMZ to produce a new formulation of recombinant human AFt can be assessed for controlled drug release and compared to the HSAFt-Cu(phen)-TMZ formulation produced by nanoreactor encapsulation in Chapter 3 and to similar AFt-TMZ systems reported in the literature.

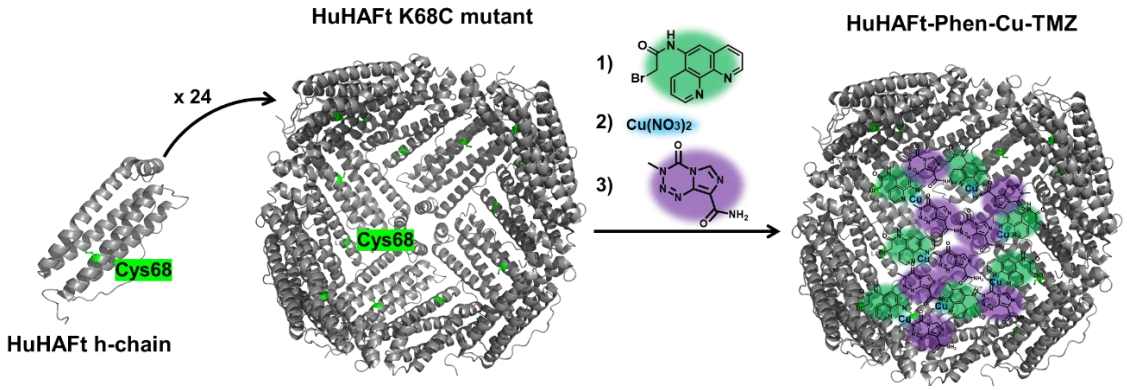

Figure 4.1 Design of the AFt_K68C-Phen(Cu) conjugate and encapsulation with TMZ. Site-specific mutagenesis of Lys68 to Cys68 gives the mutant AF_ K68C cage which is then used for covalent conjugation with bromoacetyl-phenanthroline (1), titration with copper (2) and encapsulation with the drug TMZ (3).

4.2 Production of the K68C cysteine mutant human AFt heavy chain

The HuHAFt used in this study was a recombinant mutant (AFt_WT His). The gene encoding for this mutant, cloned between the restriction sites *NdeI* and *XhoI* of pjexpress414 plasmid, was kindly provided by Isobel Holden, a PhD student working in Prof. Neil Thomas's group (Appendix 4.B). The heavy chain subunit sequence contained no cysteines. To provide the protein with a functional group reactive in nucleophilic attack the substitution of Lys68 into Cys68 was performed by site-directed mutagenesis. This mutation provided a cysteine whose side chain was exposed on the inner surface of the AFt cage, ensuring covalent binding of the

phenanthroline ligand exclusively inside the protein without affecting cage assembly (Figure 4.2). The site-directed mutagenesis was performed using the Q5® High Fidelity DNA polymerase from NEB and non-overlapping back-to-back primers, with mutation codon in the forward direction (Chapter 7, Materials and Methods, section 7.5.1). Troubleshooting of the PCR amplification reaction was required to adjust the annealing temperature of the primers to optimal values. After extensive optimisation, a touchdown PCR produced the mutated plasmid (Chapter 7, section 7.5.1). This technique exposed the reaction mix to different annealing temperatures, starting from T_m + 10 °C with a decrease of 1-2 °C at each cycle until the annealing temperature of the primers is reached. [55] The success of the site-directed mutagenesis was then checked by sequencing upon transformation into chemically competent *E. coli* DH5α cells and subsequent plasmid extraction.

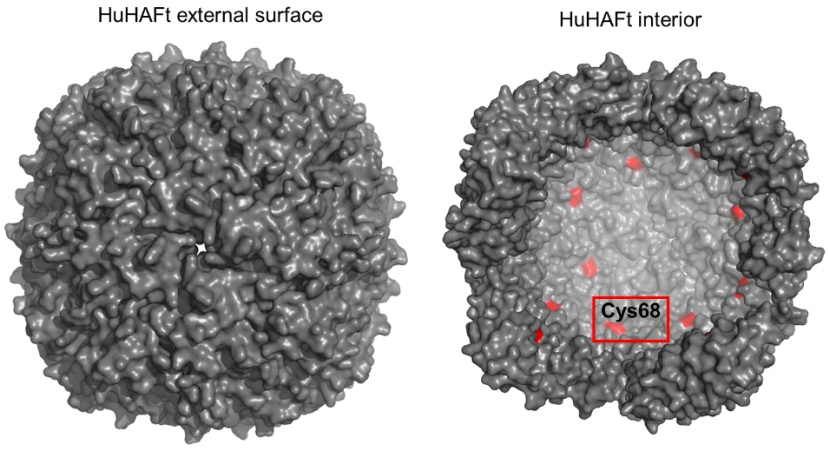

Figure 4.2. Structure of the HuHAFt cage (grey) with the K68C mutation visible on the inside of the protein shell (red). Figure produced with The PyMOL Molecular Graphics System, Version 2.5.2 Schrödinger, LLC.

4.2.1 Expression and purification of the HuAFt wild type and K68C protein mutant

Once the K68C mutant of HuHAFt (AFt_K68C His) was confirmed by sequencing analysis, the plasmid DNA of the wild type protein (AFt_WT His) and the mutant were (separately) transformed into *E. coli* Rosetta™ 2 (DE3) competent cells for protein expression. This cell strain was chosen due to its enhanced ability in expressing eukaryotic proteins compared to other bacterial cells.[231] Optimization was required both for the expression and the purification methods. Overnight expression at 20 °C was found to improve the overall protein yield compared to higher temperatures and shorter incubation after induction (Figure 4.3-a). No increase in the amount of soluble

protein in the cell lysate could be achieved at lower expression temperatures. Purification from inclusion bodies was also attempted, but no significant protein recovery was possible.

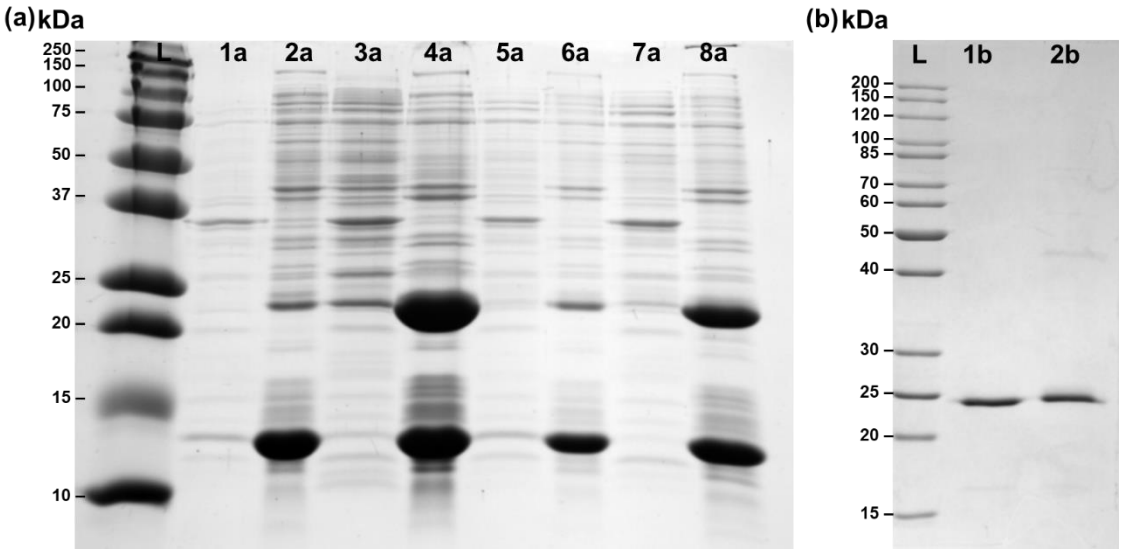

Figure 4.3. SDS-PAGE of the expression test for AFt_K68C His (a) and of the purified AFt_WT His and AFt_K68C His mutant (b). (a) SDS-PAGE of AFt_K68C His expression test with sonication degradation products (12 kDa): L= ladder, 1a, 2a= soluble and insoluble cell lysate with no IPTG at 20 °C; 3a, 4a= soluble and insoluble cell lysate with 1 mM IPTG at 20 °C; 5a, 6a= soluble and insoluble cell lysate with no IPTG at 37 °C; 7a, 8a= soluble and insoluble cell lysate with 1 mM IPTG at 37 °C. (b) SDS-PAGE of purified HuHAFt proteins (24 kDa): L= ladder, 1b= AFt_WT His, 2b= AFt_K68C His.

The purification was performed by affinity chromatography using a Ni^{2+} column, as both HuHAFt genes were designed with a His-tag on their N-termini. The protein was eluted at 60 % concentration of 0.8 M imidazole buffer (Appendix 4.C). The preparation of the soluble fraction was crucial to achieving successful purification. Particular attention was required for the sonication step performed to ensure cell membrane rupture and protein release. In this case, excessive pulse amplitude and exposure time led to protein degradation in smaller fragments that eluted with the AFt_K68C His mutant. This markedly reduced the yield of functional protein and contaminated the purified sample (Appendix 4.D).

After purification, dialysis in storage buffer (20 mM Tris, pH 8.0) and concentration, the protein content was estimated by the Bradford assay. The pure AFt_WT His and AFt_K68C His proteins (Figure 4.3-b) were produced with average yields of 127 and 37 mg/1 L cell culture respectively. The yield for the recombinant AFt_K68C His

protein was lower than that of the AFt_WT His. In some cases, the introduction of the thiol groups of cysteine favours the formation of disulphide bridges causing precipitation of protein aggregates in the insoluble cell fraction.[232] Mindful of this, the purification of the AFt_K68C His using 1 mM DTT as reducing agent was attempted, without any improvement in the purification yield.

To increase the yield of AFt_K68C His mutant produced per expression round, batch fermentation in a 10 L cell culture volume was attempted.[233] The fermentation was set up using LB media supplemented with carbenicillin and chloramphenicol as for the small scale expression, and the 1 L inoculum was prepared from a 1 mL glycerol stock of *E. coli* Rosetta™ 2 (DE3) carrying the AFt_K68C His plasmid. The cell growth and protein expression were carried out using the same conditions as previously described with the addition of pH and O_2 monitoring (see Chapter 7, section 7.5.3). The growth of the bacterial culture was monitored by OD measurements and induction at 20 °C was found to be challenging. Due to the slow cooling process of the reactor combined with the fast growth of the bacteria between the inoculation and induction time point (doubling time = 45 min) the addition of IPTG was performed before the reactor temperature reached 20 °C. Two fermentation experiments were performed where optimization of temperature and pH control allowed for a protein yield of 20 mg/ 10 L. The 10 L expression produced a significantly lower amount of recombinant protein compared to the expression in 1 L culture. There are a few reasons to explain this issue, the first being the need for better control over induction time and temperature by using a lower inoculum volume and starting the fermentation with OD ≤ 0.1. The second reason could be the overflow metabolism which has been reported for *E. coli* cultured in large volumes.[234,235] This phenomenon consists of a switch of the bacterial metabolism from aerobic to anaerobic even in the presence of high amount of oxygen because of regulatory triggers activated by membrane surface limitation and high [NADH]/[NAD+] ratio.[236] This switch was reported to contribute to a decrease in cell density and recombinant protein production.[234,235]

In addition to the issues related to the use of *E. coli* for fermentation, also during the expression of AFt_K68C His in 1 L batches, it was observed that the protein yield substantially decreased with glycerol storage time. This problem was detected regardless of the storage time of the glycerol stocks used to prepare the plates for picking the colonies for inoculation. This problem could be also included in the explanation of the low yield fermentation experiments. Although it was not possible to address this issue at the time it is reasonable to hypothesise a decrease in the

expression efficiency of the bacterial cells upon storage. A possible solution would be to perform the expression from single colonies picked from a plate prepared from freshly transformed cells, not glycerol stocks. Although the production of recombinant AFt_K68C His was sub-optimal, it was still sufficient to proceed to the His-tag removal procedure and then the bioconjugation to 2-bromo-*N*-(1,10-phenanthrolin-5-yl)acetamide.

4.2.2 Removal of the His-tag from HuHAFt variants through TEV protease cleavage

The sequences used to produce the AFt_WT His and AFt_K68C His recombinant proteins were provided with a hexahistidine tag on the N-terminus of the subunit to allow purification by affinity chromatography (IMAC). The design of the protein gene included the first methionine starting codon (ATG), followed by the tag and the TEV protease cleavage site for removal of the His residues after protein purification.[237] The effect of the hexahistidine tag on the folding and stability of recombinant proteins is highly dependent on the single protein.[238] However, its removal is required to produce biological proteins envisaged for clinical applications as it is an immunogenic sequence.[239] In addition to this it is important to highlight that the tag has high affinity for metal ions including nickel (II), cobalt (II), copper (II), and zinc (II).[237] Although this property makes it extremely valuable for protein purification, the presence of the tag can impact the data collected when studying quantitative metal-protein interactions like in the case of AFt.

The TEV protease required to remove the His-tag from AFt_K68C His was the mutated form of the tobacco etch virus enzyme that can be expressed by *E. coli*, purified by IMAC affinity chromatography and has enhanced catalytic activity.[240] The presence of the hexahistidine tag on its sequence allowed for its purification and efficient separation from the cleaved HuHAFt (AFt_K68C, AFt_WT) after the reaction.[240] Among the other enzymes used for fusion tags removal, the TEV protease showed greater specificity.[241] TEV recognizes the sequence ENLYFQG/S and cuts between the amino acids Q and G/S (Figure 4.4).[240] The TEV protease used in this work was expressed in *E. coli* BL21 (DE3) CodonPlus-RIL and subsequently purified by affinity chromatography.[240] Upon protein purification it was possible to observe the presence of the maltose-binding protein (MBP) band at 50 kDa, which was fused with the TEV gene to reduce the formation of inclusion bodies in the insoluble cell fraction (Appendix 4.E).[240] After purification the fractions containing pure TEV were pooled,

concentrated and the yield estimated by UV-vis (13 mg/ 1L culture) and stored at -80 °C for a maximum of 6 months.

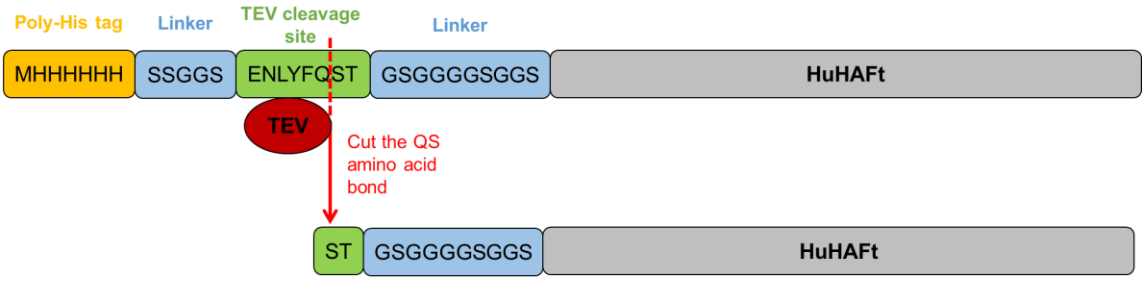

Figure 4.4. TEV recognition sequence and cutting site on HuHAFt.

The optimal digestion conditions for the His-tag cleavage were identified using the WT_AFt over different incubation temperatures (30 and 37 °C) and reaction times (1 h, 3 h, overnight), using a 1:20 protease to AFt ratio. The results of this test showed that there were no substantial differences between incubation at 37 or 30 °C, with the latter providing a slightly better cleavage ratio at the same incubation time (Figure 4.5-a). This was visible in both samples loaded on the SDS-PAGE that showed the presence of the TEV protease (28 kDa), the AFt_WT His (24 kDa) and AFt_WT (22 kDa) at different incubation times (Figure 4.5-a). It was also observed that after 3 h of incubation the reaction produced a precipitate whose composition was checked by SDS-PAGE and revealed that it was mainly aggregated AFt (Appendix 4.F). The aggregated protein could not be solubilized and thus was lost due to the TEV cleavage reaction. Up to 60 % of protein loss was observed even upon reduction of the incubation time to 1.5 h and after decreasing the protein concentration in the reaction. The reaction mixture was purified by affinity chromatography using a His-Trap column and the flow-through fractions containing only the digested protein were collected (Appendix 4.F). The flow-through fraction was then dialyzed to remove imidazole and concentrated using Vivaspin® (3000 MWCO). Protein recovery was quantified by Bradford giving 40 % of cleaved AFt_WT and AFt_K68C. The ability of the protein to form intact cages was assessed by native PAGE, which also showed the different molecular weights of the cleaved protein (Figure 4.5-b).

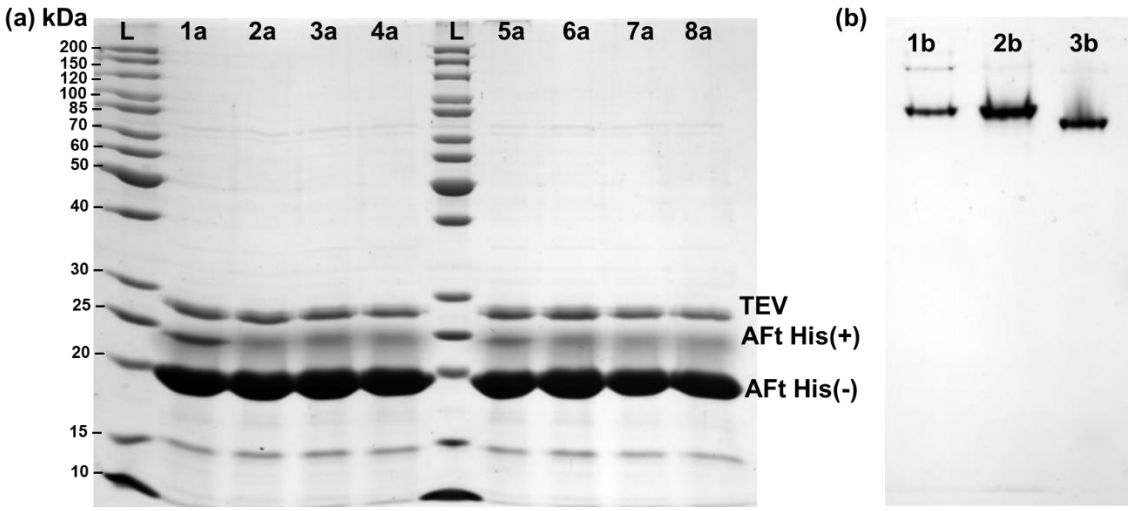

Figure 4.5. SDS-PAGE of the TEV digestion optimisation test (a) and native PAGE of the AFt_WT His, AFt_K68C His and AFt_K68C (b). SDS-PAGE of TEV protease (28 kDa) cleavage of AFt_WT His: L= ladder, 1a, 5a= reaction at time zero (37 and 30°C), 2a, 6a= reaction at 1 h (37 and 30°C), 3a, 7a= reaction at 3 h (37 and 30°C), 4a, 8a= overnight reaction (37 and 30°C). (b) Native PAGE of HuHAFt: 1b= AFt_WT His (MW= 24 kDa, pI= 5.76), 2b= AFt_K68C His (MW= 24 kDa, pI= 5.67), 3b= AFt_K68C (MW= 22 kDa, pI= 5.31).

4.3 Production of AFt_K68C-Phen(Cu)

The covalent anchoring of metal ligands to proteins is based on the nucleophilic attack between a specific cysteine residue in the protein and an activated group on the metal-ligand. This method permits the control of the metal localization inside the protein scaffold.[242] The low natural abundance of cysteine, its unique nucleophilicity and reactivity at neutral pH, made it a useful tool in the production of protein-engineered bioconjugates.[243] The use of a genetically engineered HuHAFt protein with only one cysteine in its peptide sequence can significantly reduce the probability of nonspecific labelling and ensure the binding of the phenanthroline ligand exclusively on the interior surface of the protein, where metal accumulation is preferred for the stabilization of TMZ upon encapsulation.

The acidity of the thiol group (pKa= 8-9) with the ability of sulfur to be easily polarizable make cysteine particularly reactive toward electrophiles like maleimides and alkyl halides.[243] Maleimides have been widely exploited to produce macromolecules for therapeutic use.[80] However, recently it was found that these bioconjugates can undergo disruptive cleavage by thiol exchange, ring hydrolysis and retro-Michael addition in the organism, compromising their therapeutic efficacy and

causing undesired toxicities.[80,78,79] Furthermore, the heterogenicity of these drug-to-antibody mixtures combined with uncontrolled maleimide conjugation site occupancy can lead to issues in batch reproducibility for clinical applications.[244] Iodoacetyl groups have been employed to produce more stable thiol-conjugates in particular in the production of ADCs.[244,245] Alley *et al.* reported the improved plasma stability of 14 days for ADCs prepared with a bromoacetamidecaproyl (bac) in place of the maleimidocaproyl (mc) linker, with higher intratumoral drug exposure and similar tolerability.[82] Camacho *et al.* used the bromoacetamide group to conjugate a G-protein-coupled-receptor agonist used in the treatment of obesity and hyperglicemia to a cysteine bearing immunoglobulin (IgG), resulting in a long-acting formulation with enhanced plasma half-life.[246]

Thiol conjugation with halogen-substituted ligands can be achieved with higher specificity in buffers whose pH ensures the stability of AFt.[244, 245] In fact, the reactivity of the cysteine is highly dependent on the environmental pH, determined by the pKa of the amino acid residue ≈ 8.5.[247] The deprotonation of the thiolate ion at alkaline pH (> 8.5) favours the nucleophilic attack to the halogen-substituted electrophile and the expulsion of the halogen atom by an S_N2 mechanism (Figure 4.6).[247]

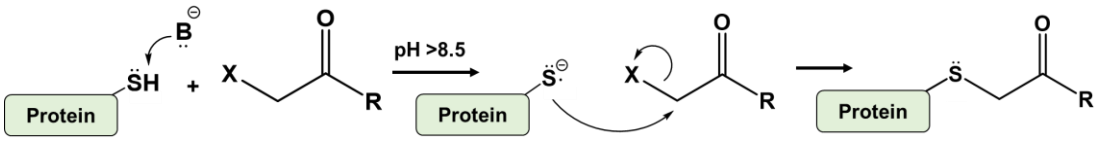

Figure 4.6. Cysteine alkylation mechanism by halogen-substituted electrophilic ligands.

4.3.1 Covalent conjugation of phenanthroline to AFt_K68C

With the hexahistidine removed, the AFt_K68C protein was used for covalent conjugation of the ligand 2-bromo-*N*-(1,10-phenanthrolin-5-yl)acetamide as illustrated in Figure 4.7 (see Chapter 7, section 7.2.2). As mentioned in the previous section, the use of haloalkyl reagents provides a valid alternative to maleimides for protein conjugation due to the ease and reliability of the reaction.[78] Control over the bioconjugation pH was essential to avoid the non-specific labelling of other nucleophilic side chains of lysines and histidines as the specificity towards cysteines is favoured at pH > 8.[78] For this reason the bioconjugation reaction was performed in 20 mM Tris at pH 8.5 (see Chapter 7, section 7.5.6).

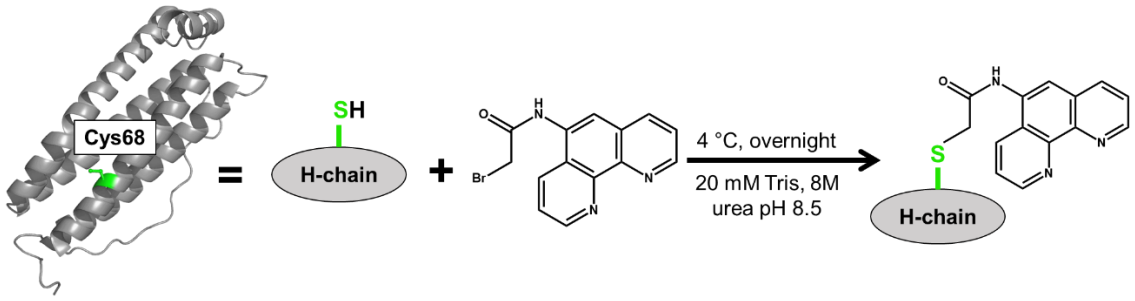

Figure 4.7. Bioconjugation of bromoacetyl-1,10-phenanthroline to AFt_K68C.

In addition to the pH, it was necessary to tune the best reaction conditions that would ensure thiol availability to the ligand. This aspect was of particular importance for the completion of the labelling reaction as the SH groups were localized exclusively on the inside of the AFt cage. It was decided to avoid the use of pH-dependent disassembly of AFt due to concerns reported by the literature on the reversibility of the procedure, and to reduce the risk of aggregation.[122] Instead the availability of the thiol groups was evaluated by dissociating the AFt subunits by introducing urea in the reaction buffer. Two test concentrations were evaluated (4 and 8 M urea) using Ellman's assay for thiol quantification. The results of the Ellman showed that 8 M urea exposed 104 % of SH available compared to 47 % at 4 M urea (Figure 4.8-a), confirming that higher urea concentrations help exposing the inner-facing SH residues of AFt. Mindful of the potential denaturing conditions of 8 M urea to AFt, the protein tested was run on a native PAGE after purification (PD-10) to ensure proper reassembly, which was confirmed by the results outlined in Figure 4.8-b.

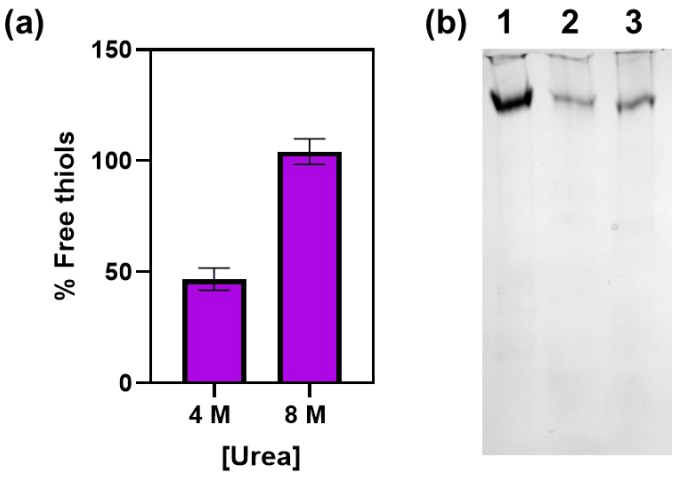

Figure 4.8. Ellman's assay of the AFt_K68C exposed to different urea concentrations (a) and native PAGE to check for cage integrity (b). (a) AFt_K68C treated with 4 M and 8 M urea, (b) native PAGE of reassembled cage 1= AFt_K68C untreated, 2-3= AFt_K68C reassembled after treatment with urea.

The effect of pre-treatment of the protein sample with reducing agents was also investigated. A first preliminary experiment was directed at testing the UV background signal that could be produced by contamination of the Ellman reaction by DTT, BME and TCEP reagents. The test was performed by incubating two 45 µL dilutions of each reagent within the detection range of the Ellman's assay (40-300 µM) with 10 µL of DTNB stock in 445 µL of Ellman's buffer. The absorbances at 412 nm were recorded and showed that DTT could produce the most significant background signal if not properly removed from the bioconjugation sample (Appendix 4.G). Although BME and TCEP reported the equivalent reactivity with DTNB, the latter was preferred being less volatile and therefore safer. After this preliminary evaluation, cysteine exposure in AFt_K68C was assessed by Ellman's assay with and without pre-treatment using TCEP (Figure 4.9). The AFt_K68C protein was incubated with 20 mM TCEP in urea-Tris buffer at pH 8.5 for 1 h at 37 °C under inert atmosphere. The reaction was then purified by PD-10 and dialysis and analyzed by Ellman's assay (Figure 4.9). The results from the assay demonstrated that there was no significant improvement in the thiol availability after treatment of AFt_K68C with TCEP. The results illustrated in Figure 4.9 did not exclude some background signal generated by low quantities of the TCEP reagent contaminating the reaction. As reported in Appendix 4.G TCEP can react with DTNB and it was still present in the protein solution after PD-10, hence requiring purification by dialysis. For these reasons, it was evaluated that the potential disadvantages of using and then removing TCEP from the protein for bioconjugation overcame the minimal increase in thiol availability produced by pre-treatment.

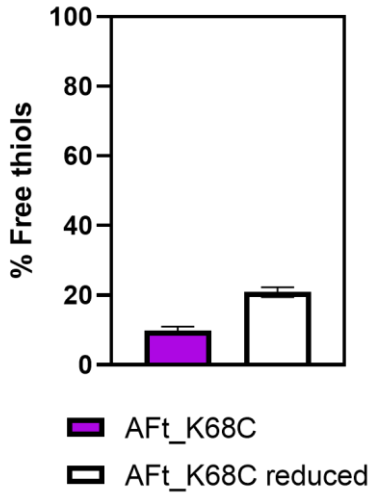

Figure 4.9. Ellman's assay testing the effect of pre-treatment of AFt_K68C with TCEP on free thiols availability.

The conjugation reaction was carried out in degassed Tris-urea buffer (20 mM and 8 M respectively) at pH 8.5. The AFt cysteine mutant was incubated with up to 50 equivalents of ligand, diluted from a DMSO stock, at 4°C overnight under nitrogen atmosphere. No substantial difference was observed by incubating the reaction at 37 °C. Purification of the protein bioconjugate was performed with two successive rounds of dialysis (1000 dilution) using freshly prepared 20 mM Tris buffer pH 8.5. Effective removal of excess ligand was checked by recording the UV-vis spectrum of the dialysis buffer. The measurement of the UV-vis absorbance intensity of a range of concentrations of 2-bromo-*N*-(1,10-phenanthrolin-5-yl)acetamide in Tris buffer showed that ligand peak was detected down to 0.1 µM concentration (Appendix 4.H).

4.3.1.1 Evaluation of AFt_K68C His conjugation reaction by UV-vis, Ellman's assay and MALDI-TOF

The first attempts at protein labelling were performed using the AFt_K68C His cage. This approach was chosen considering the significant protein loss caused by the TEV protease cleavage, which considerably reduced the amount of cleaved protein available for the conjugation reaction (see section 4.2.2). The first bioconjugation reaction was performed using only 20 equivalents of the phenanthroline ligand. The lower concentration of phenanthroline was supposed to minimize the probability of protein aggregation during the reaction. The other reaction conditions were kept as described above (degassed Tris-Urea buffer pH 8.5, incubation at 4°C overnight under nitrogen atmosphere). The reaction was purified by dialysis, concentrated by Vivaspin® (3000 MWCO) and the protein recovered was quantified by Bradford assay. The initial evaluation of the purified bioconjugation reaction was performed by UV-vis and Ellman's assay (Figure 4.10).

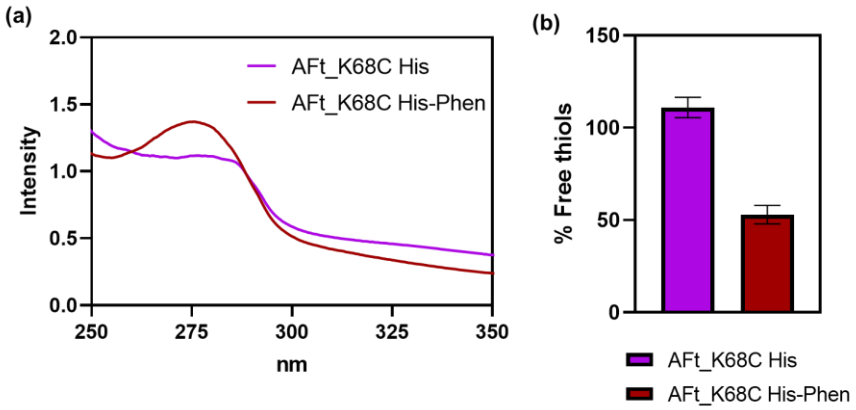

Figure 4.10. Results of the AFt_K68C His bioconjugation using 20 equivalents to bromoacetyl-1,10-phenanthroline: UV-vis (a) and Ellman's assay (b).

The Ellman's assay recorded a 47 % decrease in free thiols (Figure 4.10-b), thus suggesting labelling of almost half of the cysteine residues inserted per AFt cage. This result could be partially corroborated by the UV-vis spectrum which showed an increase in the intensity at 280 of the protein cage, which could be linked to the presence of phenanthroline (Figure 4.10-a). The analysis of the protein concentration by Bradford assay before and after the bioconjugation confirmed that 58 % of the AFt_K68C His was recovered. Protein loss could be caused by aggregation due to the high concentration of urea required to allow cysteine exposure.

To directly visualize the extent of the bioconjugation on the AFt_K68C His-Phen protein, the analysis of the sample with Matrix-Assisted Laser Desorption/Ionization Time-of-Flight Mass Spectrometry (MALDI-TOF) was attempted (Figure 4.11). The protein sample was desalted and spotted on a stainless plate using a saturated solution of sinapic acid in 30:70 (v/v) acetonitrile: TFA 0.1% in water. Once dried, the spots were analysed in the mass range of 13000-28200 Da using a myoglobin standard for calibration (see the example provided in Appendix 4.I).

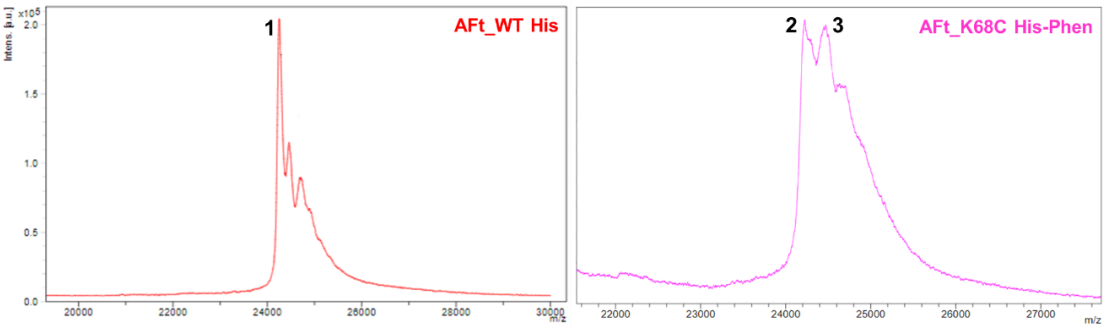

Figure 4.11. MALDI-TOF results of the AFt_K68C His bioconjugation using 20 equivalents to bromoacetyl-1,10-phenanthroline. Peak 1= 24256.2 Da, AFt_WT His sample at 1.5 mg/mL; Peak 2= 24224.3 Da, AFt_K68C His-Phen sample at 1 mg/mL; Peak 3= 24449.3 Da AFt_K68C His-Phen at 1 mg/mL.

The spectra produced by the unlabelled protein (AFt_WT His) and the bioconjugation product AFt_K68C His-Phen seemed to support Ellman's assay findings even though UV-vis could not discriminate between covalently bound phenanthroline and encapsulated phenanthroline. While the AFt_WT His sample showed a sharp peak at 24256 Da (expected 24204 Da), the AFt_K68C His-Phen sample presented two peaks (2,3) with a mass difference of 225 Da, which was about 12 Da less than the shift of 237 Da expected for the protein bioconjugate with phenanthroline (Figure 4.11). This evidence was encouraging in suggesting the possible presence of two

protein species in the sample: the AFt_K68C His (peak 2, 24224 Da) and the AFt_K68C His-Phen conjugate (peak 3, 24449 Da).

The data reported for the AFt_K68C His-Phen bioconjugation performed using 20 equivalents of phenanthroline ligand suggested labelling of about half of the recombinant AFt subunits. Encouraged by these results, another experiment was performed aimed to achieve a larger percentage of subunits labelling by using 50 equivalents of 2-bromo-*N*-(1,10-phenanthrolin-5-yl)acetamide. The covalent conjugation was performed again on AFt_K68C His in urea-Tris buffer at pH 8.5, 4 °C overnight under inert atmosphere. The reaction was dialyzed to remove excess phenanthroline and the purified sample was analyzed by UV-vis, Ellman's assay and MALDI-TOF (results of two independent replicates).

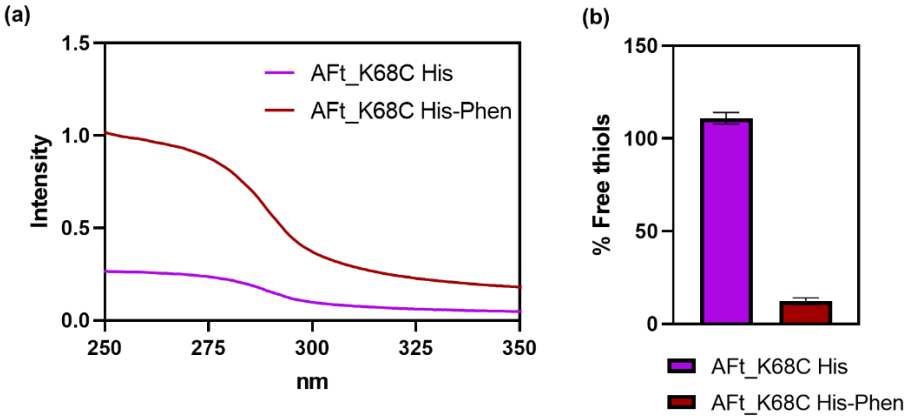

Figure 4.12. Results of the AFt_K68C His bioconjugation using 50 equivalents to bromoacetyl-1,10-phenanthroline: UV-vis (a), Ellman's assay (b).

In this case, up to 64 % of AFt_K68C His-Phen was lost due to aggregation after the bioconjugation reaction as measured by Bradford assay. However, the data from Ellman's assay suggest labelling of 88 % of the free cysteine residues in the protein. These encouraging data were supported by the UV-vis spectra that showed a significant increase in absorbance for the AFt_K68C His-Phen compared to that of AFt_K68C His. The AFt_K68C His-Phen was also analysed by MALDI-TOF as for the previous conjugation (Figure 4.13). The results of the analysis on AFt_WT His and AFt_K68C His produced masses of 24189 Da and 24287 Da respectively, with shifts of 14 Da and 111 Da (TFA) from the expected values (Figure 4.13). Furthermore a broadening of the peak was visible in the AFt_K68C His spectrum, possibly related to the presence of a larger quantity of sinapic acid on the sample spot and the prolonged exposure of the protein to alkaline buffer before desalting.[248]

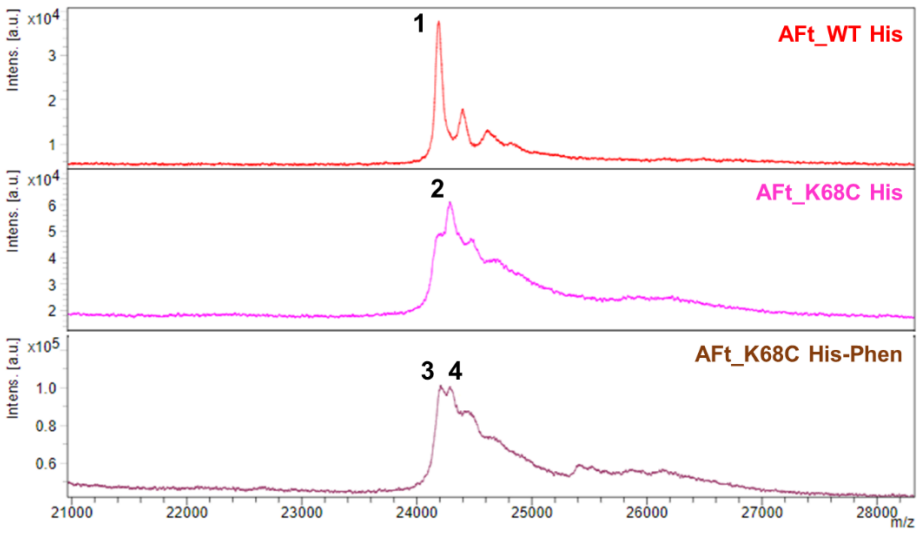

Figure 4.13. MALDI-TOF spectrum of HuHAFt species. Peak 1= 24189 Da, AFt_WT His sample at 1.7 mg/mL; Peak 2= 24287 Da, AFt_K68C His sample at 1 mg/mL; Peak 3= 24207 Da and peak 4= 24287 Da AFt_K68C His-Phen sample at 1 mg/mL.

The mass spectrum recorded for the AFt_K68C-Phen His mutant used for the bioconjugation illustrated in Figure 4.13 showed a broad signal with two peaks at 24207 Da and 24287 Da. Although the AFt_K68C His-Phen protein had a spectrum like the one observed in Figure 4.11, neither of the two peaks (3,4) corresponds to the mass shift expected for the labelled protein (237 Da). Peak 2 and 4 reported the same mass of 24287 Da that could be associated with the unlabelled protein. In this case, the MALDI-TOF spectrum of AFt_K68C His-Phen suggested a heterogeneous composition of the sample, likely formed by a mixture of several protein forms including labelled and unlabelled subunits, some aggregated subunits or the presence of non-covalently associated phenanthroline ligand. The heterogeneity of the sample was also supported by the UV-vis profile of AFt_K68C His-Phen in which the peak at 280 nm was significantly broadened (Figure 4.12-a).

MALDI-TOF was not able to provide further evidence of successful conjugation due to heterogeneity of the bioconjugation reaction sample, which made the resolution of protein peaks difficult. However, Ellman's assay suggested the labelling of 88 % of the cysteine residues upon incubation of AFt_K68C His with 50 equivalents of the phenanthroline ligand. Even though the mass spectra could not corroborate the results from the Ellman reagent, the experiments of conjugation with AFt_K68C His mutant provided positive evidence of possible labelling occurring at the protein subunits.

4.3.1.2 Evaluation of AFt_K68C conjugation reaction by UV-vis and Ellman's assay

Encouraged by the results observed for the bioconjugation of the HuHAFt with the hexahistidine tag, the same reaction was reproduced using the AFt_K68C digested by the TEV protease. Along with the AFt_K68C, also AFt_WT with no cysteine residues were used in parallel as a control experiment. The proteins were incubated in degassed urea-Tris buffer at pH 8.5 under a nitrogen atmosphere at 4° C, overnight. Also in this case protein recovery was measured by Bradford assay after reaction purification by dialysis and concentration by Vivaspin® (MWCO 3000 Da) to its initial volume. The final protein recovery was improved up to 67 % and 78 % for AFt_K68C-Phen and AFt_WT-Phen respectively (results of two independent experiments) compared to the previous experiments (Section 4.3.1.1). The bioconjugate and the control were characterized by UV-vis and Ellman's assay (Figure 4.14).

As reported in the previous section, the increase in the 280 nm intensity can be associated with the presence of the phenanthroline ligand in the sample with AFt. However, the UV-vis spectrum is not able to differentiate between covalent conjugation of the ligand to the protein or physical entrapment into its hollow core. The spectrum of AFt_K68C-Phen reported an increase in absorbance at 280 nm compared to the protein stock at an equal concentration (Figure 4.14-a). Although this seemed encouraging, a similar increase in intensity was also observed for the AFt_WT-Phen control which had no cysteines in its peptide sequence (Figure 4.14-a). This phenomenon could be a consequence of the entrapment of some 2-bromo-*N*-(1,10-phenanthrolin-5-yl)acetamide molecules into the protein cage reassembled during the dialysis steps performed to remove urea. Therefore, it is possible to hypothesize that not all the phenanthroline molecules retained in the AFt_K68C-Phen sample resulted from the covalent bond with cysteine residues. It was possible to expect the AFt_K68C-Phen cages to be composed of a mixture of labelled and unlabelled subunits and some free 2-bromo-*N*-(1,10-phenanthrolin-5-yl)acetamide molecules occupying the protein core.

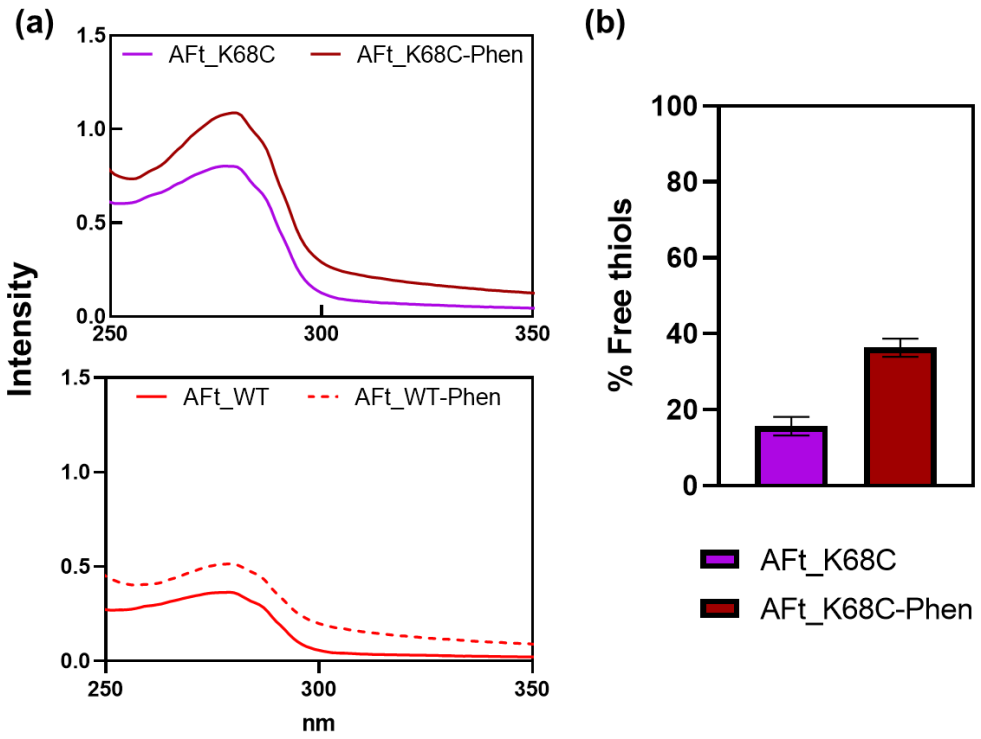

Figure 4.14. Results of the AFt_K68C bioconjugation to bromoacetyl-1,10-phenanthroline: UV-vis (a), Ellman's assay (b).

The UV-vis spectrum was used to estimate the concentration of ligand present in the sample from the increase in absorbance at 266 nm and the extinction coefficient calculated for 2-bromo-*N*-(1,10-phenanthrolin-5-yl)acetamide (21700 M^{-1} cm^{-1}) using the Beer-Lambert Law (Appendix 4.L). The concentrations of ligand present in the AFt_K68C-Phen sample and that of the AFt_WT-Phen accounted for 8 and 9 ligand molecules per AFt cage respectively. Although the UV-vis data suggested a similarity to the results reported for AFt_K68C His-Phen, Ellman's assay outcome was substantially different (Figure 4.14-b). In this case, Ellman's assay consistently showed a low availability of the free thiols in the protein even before the conjugation reaction (Figure 4.14-b). The available thiols concentration seemed to increase after the bioconjugation and therefore it was not possible to properly evaluate such results. The results from different batches of pure AFt_K68C showed high variability in the number of free thiol groups. A problem that could be explained by the irreversible oxidation of the cysteine thiol in AFt_K68C occurring during the protein storage and hampering proper labelling.

As mentioned previously the effect of reducing agents on the thiol availability of cysteines was evaluated and no significant improvement was detected when AFt_K68C was pre-treated with TCEP (Figure 4.9). Such preliminary tests ruled out

the possibility of disulfide bond formation between AFt_K68C subunits, the possibility of aerobic oxidation of the cysteines should be considered instead. As represented in Figure 4.15 some products can be generated by cysteine oxidation, in some cases irreversibly. By excluding the disulfide cysteine interaction, which is normally reversed using reducing agents like TCEP, progressive oxidation of the sulfur atom can lead to the irreversible conversion to cysteine sulfonic acid (Figure 4.15).[249] It is possible that the thiols exposed on the AFt_K68C subunits progressively underwent overoxidation into sulfonic acid between the protein purification and the bioconjugation reaction which irreversibly reduced cysteine accessibility for conjugation. Such an issue could be prevented by performing the protein purification and TEV cleavage under an inert atmosphere and storing the protein aliquots under nitrogen for a minimal amount of time before the conjugation.

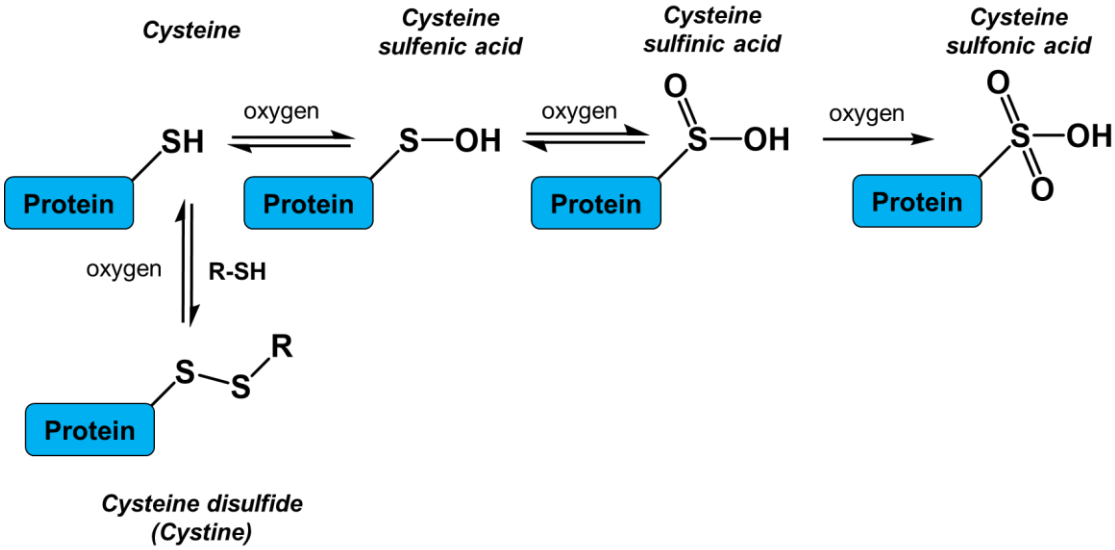

Figure 4.15. Possible cysteine oxidation products under aerobic conditions.

Due to the lack of sufficient sample and pure protein available it was not possible to further test the bioconjugation products or repeat the reaction to further investigate the AFt_K68C-Phen by mass spectrometry. Another analysis that would be useful to confirm the cysteine conjugation and determine its efficiency is the MALDI-TOF analysis on a trypsin digest of the AFt_K68C-Phen. In this case, the degradation of the protein in small peptide fragments would provide peaks with better resolution and the shift due to cysteine labelling would be more significant and therefore easier to detect. The presence of ligand retained into the AFt_K68C-Phen sample as estimated by UV-Vis (8.6 ligand/ AFt cage) allowed for the metalation with $Cu(NO_3)_{2+}$ to be performed as indirect analysis to further support the hypothesis that some of the cysteines were conjugated to 2-bromo-*N*-(1,10-phenanthrolin-5-yl)acetamide.

4.3.2 Metalation of AFt_K68C-Phen with $Cu(NO_3)_2$

The data from the bioconjugation reaction of AFt_K68C with 2-bromo-*N*-(1,10-phenanthrolin-5-yl)acetamide to produce AFt_K68C-Phen did not provide definitive evidence of covalent labelling of the cysteine residues. Furthermore, the presence of the phenanthroline ligand was also suggested by the UV-vis of the AFt_WT protein used as the control for the bioconjugation reaction. This could indicate the covalent binding of a small portion of the phenanthroline, making the complex less likely to leak out of the AFt cage during subsequent experiments. In this context, it was envisaged that progressing through the metalation step could help in the clarification of this hypothesis and allow observing the effects of the AFt_K68C-Phen(Cu) conjugate.

The introduction of copper into the AFt_K68C-Phen cages was performed by incubating 100 equivalents of $Cu(NO_3)_2$ with the protein in 20 mM Tris buffer at pH 8.5 for 3 h at room temperature. The excess copper was then removed by dialysis in fresh buffer (2 rounds x 2000 volumes). The final protein concentration was estimated by Bradford assay and the metal content was measured by ICP-MS. Two control reactions were performed, where two additional samples were incubated with the copper salt: the sample used as a control for the conjugation reaction, AFt_WT-Phen, where phenanthroline was likely to be retained in the cage by encapsulation, as well as a fresh aliquot of AFt_WT without phenanthroline.

The results from the ICP-MS showed no significant difference in the metal accumulation observed between the bioconjugation samples and the controls (Table 4.1). Most importantly, it was not possible to evaluate whether if the presence of the phenanthroline ligand influenced the amount of copper retained compared to the native protein (Table 4.1).

Overall, the metalation did not provide any evidence of an increased copper accumulation in the AFt_K68C-Phen(Cu) sample compared to the controls, thus suggesting that the presence of the ligand as < 10 molecules per protein cage did not affect the metal retention regardless of its state (covalently bound or encapsulated). X-ray crystallography reported for heavy chain AFt cages loaded with the anticancer metal complex cisplatin showed that the amino acid residues interacting with the metal are not conserved between the L-chain and the H-chain protein subunits.[135] Such difference was reported to affect the metal recruiting ability and the type of metal-binding between AFt cages from different organisms, such as HuHAFt and

HSAFt.[135] This work was in part aimed at investigating the effect of the introduction of one additional Cys68 by engineering the HuHAFt protein, thus increasing the number of metal-binding sites by 24/cage. The ICP-MS results of the metallated protein suggest that covalent conjugation of metal-coordinating complexes requires a very high labelling yield for it to impact the metal accumulation capacity of the HuHAFt cage. At the same time, it could explain why almost no difference could be seen in metal binding for the AFt_K68C-Phen(Cu) sample, as the concentration of labelled cysteine residues was not high enough to affect the copper binding. However, some copper retention was confirmed by ICP-MS by the AFt_K68C-Phen(Cu) cages, so the conjugation product was used to encapsulate TMZ.

Sample	Cu/AFt subunit (Average ± SEM)		Cu/AFt cage (Average ± SEM)	
	Exp 1	Exp 2	Exp 1	Exp 2
AFt_K68C-Phen(Cu)	0.78 ± 0.11	0.85 ± 0.05	19 ± 3.2	20 ± 1.1
AFt_WT-Phen(Cu)	1.2 ± 0.03	0.68 ± 0.02	28 ± 0.99	16 ± 0.46
AFt_WT(Cu)	0.34 ± 0.04	1.2 ± 0.10	8.3 ± 1.3	30 ± 2.5

Table 4.1. Copper content into AFt_K68C bioconjugates with AFt_WT controls. The results of each experiment are reported as the number of copper ions per AFt subunit and protein cage. No significant increase in metal accumulation was observed regardless of the presence and loading method of the phenanthroline ligand. The results are presented as an average of 3 analytical measurements and errors are calculated as the standard error of the mean (SEM).

4.4 Encapsulation of TMZ into AFt_K68C-Phen(Cu) cages and drug release study

This study aimed to understand and characterize the potential of the AFt_K68C-Phen(Cu) bioconjugate as a drug delivery system for TMZ. As reported in Chapter 3 and the literature, *in vitro* activity of AFt-encapsulated TMZ was characterized by a striking increase in cancer cell growth inhibitory activity. However, TMZ can still exert damage also to non-cancer cells such as MRC5 (Chapter 3, section 3.3) especially when combined with copper(II)-phenanthroline. For this reason, the evaluation of the ability of the AFt_K68C-Phen(Cu) in retaining the drug under physiological conditions

(pH 7.4, 37 °C) was fundamental to evaluate the viability of this formulation for targeted delivery.

4.4.1 Production of AFt_K68C-Phen(Cu)-TMZ

In the case of AFt_K68C-Phen(Cu) the encapsulation with TMZ was performed directly after metalation. The method for TMZ loading was the nanoreactor route, which followed the same procedure described in Chapters 3-7. However, as the protein bioconjugate was stored in Tris buffer at pH 8.5, the protein solution was dialyzed overnight in 0.1 NaOAc buffer at pH 5.5 before the encapsulation to prevent TMZ degradation. The encapsulation ratio was kept as 1:800 protein to drug molecules and the product solution was purified by ultrafiltration using 3000 MWCO Vivaspin®. The protein content was quantified by Bradford assay and the TMZ encapsulated was estimated by UV-vis (refer to Appendix 3.B). The UV-Vis confirmed successful encapsulation of TMZ by showing the drug peak at 330 nm (Figure 4.16).

The average drug content was estimated to be 335 TMZ molecules per protein cage (average of two replicates, SD= 18), with DL and EE of 42.9 % and 12.9 % respectively (Appendix 3.C). Overall these results did not differ from those obtained with HSAFt-Cu(phen)-TMZ reported in Chapter 3, supporting the hypothesis that the presence of even low amounts of phenanthroline molecules can have an impact on the TMZ loading compared to AFt-TMZ cages.[138] As mentioned previously, the use of HuHAFt for the encapsulation of therapeutic agents such as TMZ is not as common as that of HSAFt, which provides the main literature reference for drug encapsulation studies.[225] Successful encapsulation of the anticancer agent TMZ was also confirmed by the DLS spectrum recorded for the AFt_K68C-Phen(Cu)-TMZ sample which was very similar to that produced by the AFt_K68C control (Figure 4.16). Furthermore, the average hydrodynamic radius measured was 17.6 ± 1.2 nm for the empty AFt_K68C and 16.8 ± 0.2 nm for AFt_K68C-Phen(Cu)-TMZ. These results confirmed that the AFt_K68C-Phen(Cu)-TMZ cages produced are comparable to those described in Chapter 3 and derived from HSAFt and that modified HuHAFt is suitable for drug encapsulation.

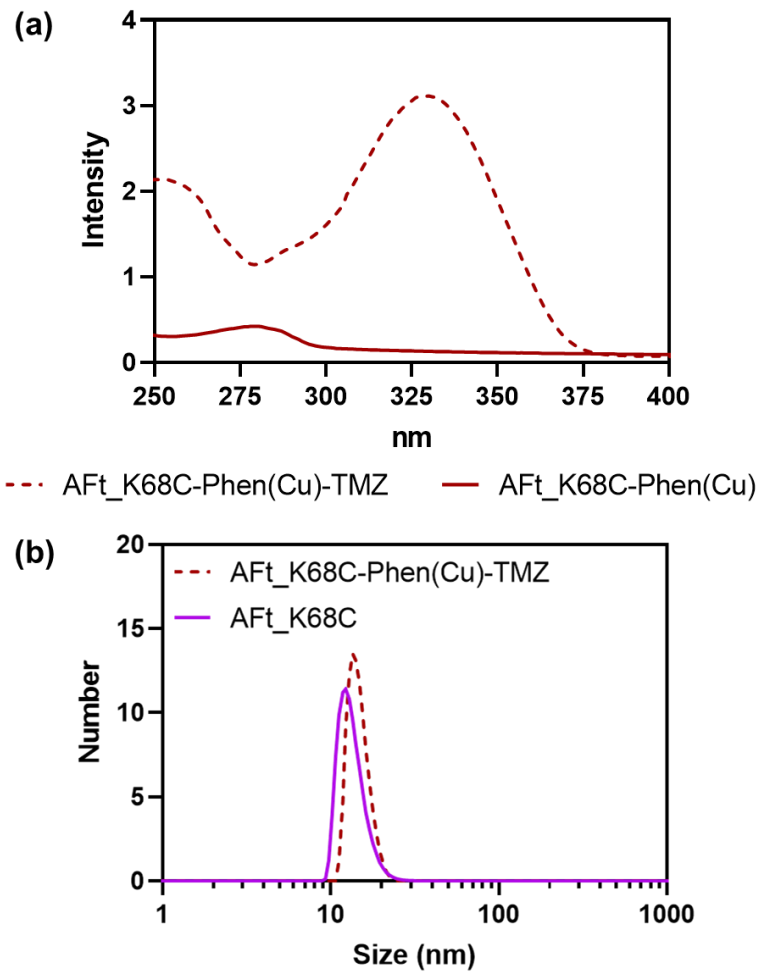

Figure 4.16. UV-vis (a) and DLS (b) spectra of AFt_K68C-Phen(Cu)-TMZ in 20 mM Tris buffer at pH 8.5.

4.4.2 TMZ release from AFt_K68C-Phen(Cu)-TMZ

The evaluation of the ability of the AFt_K68C-Phen(Cu)-TMZ bioconjugate to retain the drug TMZ under different environmental conditions was a crucial analysis to elucidate the potential role of this system for therapeutic applications. As for HSAFt-Cu(phen)-TMZ also the AFt_K68C-Phen(Cu)-TMZ bioconjugate was exposed to two different pH conditions (pH 7.4 and 5.5) relevant to the physiological and endosomal environment. The UV measurement of drug release was performed on the dialysis solution in which the protein sample was incubated (pH 7.4 or 5.5) for up to 24 h at 37 °C. As previously described in Chapter 3 (Section 3.2.2) the UV-vis data were used to estimate the percentage release of TMZ over time and its conversion to AIC (Figure 4.17).

From Figure 4.17-a it is possible to observe a marked difference between the TMZ release rate observed for AFt_K68C-Phen(Cu)-TMZ compared to the HSAFt-

Cu(phen)-TMZ produced in Chapter 3. The bioconjugate sample released ~ 62 % of TMZ when exposed to pH 7.4 within 3 h and 100 % of the drug when exposed to pH 5.5. No cloudiness or precipitation in the sample solution was observed at pH 5.5 to suggest loss of the protein cage structure. As expected from previous experiments (Chapter 3, section 3.2.3) almost all of the released TMZ was degraded into AIC at pH 7.4 within 24 h, only 50 % of AIC formed instead at pH 5.5 (Figure 4.17).

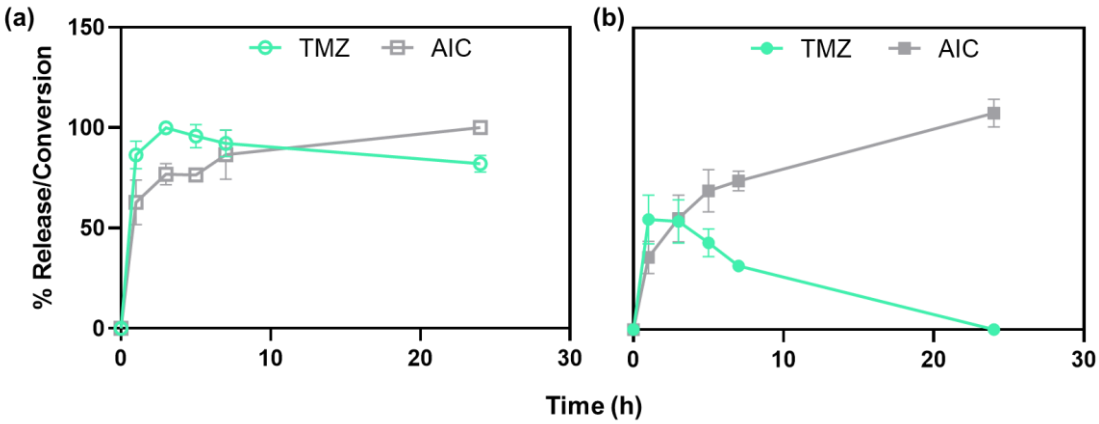

Figure 4.17. TMZ release from AFt_K68C-Phen(Cu)-TMZ and degradation into AIC at pH 5.5 (a) and 7.4 (b) measured by UV-vis (TMZ encapsulated= 100%).

When compared to previous data reported for HSAFt-Cu(phen)-TMZ (Chapter 3) it was possible to notice the difference of the two formulations in their ability to slow down TMZ release at both pH 7.4 and 5.5 (Table 4.2). Faster leakage of TMZ from AFt_K68C-Phen(Cu)-TMZ could be explained by the different metal loading of HuHAFt from HSAFt. By comparing the data illustrated in this chapter with the results reported for HSAFt-TMZ[138] it is evident that the release profile of TMZ from AFt_K68C-Phen(Cu)-TMZ is very similar at both pH conditions. In both cases, the release of TMZ at pH 7.4 is slower compared to more acidic pH at which the protein channels enlarge, but quicker than that observed for HSAFt-Cu(phen) in presence of the metal (Chapter 3). If these findings in some respect support the positive effect of the copper ion on the retention of TMZ into HSAFt, they also confirm the ICP-MS data reported previously for AFt_K68C-Phen(Cu). The lack of an effect on TMZ retention by AFt_K68C-Phen(Cu)-TMZ supported that no significant increase in copper binding could be achieved by the protein bioconjugate.

Formulation	% TMZ release pH 5.5	% TMZ release pH 7.4
AFt_K68C-Phen(Cu)-TMZ	100	73
HSAFt-Cu(phen)-TMZ	56	42

Table 4.2. Percentage of TMZ released at pH 5.5 and 7.4 from AFt_K68C-Phen(Cu)-TMZ, HSAFt-Cu(phen)-TMZ.

4.5 Summary and conclusions

The work reported in this chapter described the attempt to design a human heavy chain apoferritin bioconjugate with copper-phenanthroline for the encapsulation and the controlled release of the anticancer agent temozolomide. The use of HuHAFt instead of protein isoforms from other organisms bears the advantage of a lower risk of immunological reactions.[68] Furthermore homopolymers of heavy chain AFt subunits showed greater uptake by tumour cells compared to protein cages composed mostly of light chain subunits (like in the case of HSAFt).[200] These two facts provide a significant advantage when developing drug delivery systems envisaged for therapeutic applications. In addition, the ferroxidase function of heavy chain AFt is linked to its reduced metal storage capability compared to the light chain subunit.[180] Consequently the introduction of a metal coordinating ligand by covalent binding had the potential to improve the metal accumulation into heavy chain AFt homopolymers too. For these reasons, the development of the AFt_K68C-Phen(Cu)-TMZ was considered valuable to allow for direct comparison with a similar system produced from HSAFt-Cu(phen)-TMZ. In this case, the immobilization of the copper-phenanthroline complex by covalent conjugation was also considered a valid approach to promote metal accumulation into the HuHAFt structure.[180]

The results reported in this chapter showed that a K68C mutation was successfully introduced into the HuHAFt peptide sequence with no other cysteines. The recombinant AFt_K68C His cage had one cysteine residue per heavy chain subunit, positioned on the internal surface of the protein shell. Expression in *E. coli* and purification by affinity chromatography highlighted the lower protein yield obtained for the AFt_K68C His mutant over the AFt_WT His, even after protein expression in 10 L bioreactor. The progressive decrease in AFt_K68C His expressed over time from glycerol stocks led to the conclusion that the use of freshly transformed colonies would significantly improve the protein yield. The use of a metal complex for AFt_K68C His conjugation required the removal of the poly-His tag by TEV protease cleavage. Although extensive reaction optimization was carried out, up to 50 % of the HuHAFt protein was lost due to aggregation during the TEV digestion and could not be recovered. This issue led to a limited amount of AFt_K68C pure sample available for bioconjugation experiments.

The covalent conjugation reaction with 2-bromo-*N*-(1,10-phenanthrolin-5-yl)acetamide produced encouraging results which require validation after extensive optimization of the bioconjugation conditions. The covalent binding was carried on AFt_K68C His first, then on AFt_K68C and AFt_WT as a negative control. The UV-vis data reported an overall increase in the 280 nm peak correlated to the retention of < 10 ligand molecules per AFt cage for both sample and control. The reduction in available thiol concentration was observed only in AFt_K68C His-Phen suggesting conjugation. The same could not be assessed for the AFt_K68C-Phen reaction possibly because of overoxidation of the protein cysteines. MALDI-TOF analysis on the native protein subunits could not provide conclusive evidence of conjugation due to the presence of different protein variants in the samples analysed. ICP-MS data were collected after the metalation of AFt_K68C-Phe(Cu). The average copper content was estimated to be < 22 ions per cage, in the sample and the AFt_WT controls. The accumulation of similar quantities of copper ions in both sample and control suggested a lack of influence of the phenanthroline ligand on metal retention in the AFt_K68C-Phen(Cu) sample.

Although no significant differences in the copper content of AFt_K68C-Phen(Cu) and the controls were observed, the presence of the metal was still evaluated for its effect on TMZ retention. Drug encapsulation into AFt_K68C-Phen(Cu)-TMZ produced a protein to TMZ ratio, EE and DL similar to those recorded for HSAFt-Cu(phen)-TMZ. This evidence provided indirect confirmation of phenanthroline presence in the protein cage and suggested that AFt_K68C-Phen(Cu) could be a suitable vehicle for drug delivery. However, the drug release experiments showed that AFt_K68C-Phen(Cu)-TMZ was less efficient in retaining TMZ than HSAFt-Cu(phen)-TMZ both at pH 7.4 and pH 5.5. Under both conditions, more drug was released within the first 3 h of incubation than with HSAFt-Cu(phen)-TMZ. However, the AFt_K68C-Phen(Cu)-TMZ showed a drug release behaviour similar to that reported by Bouzinab *et al.* for HSAFt-TMZ,[138] thus providing further evidence that no significant copper accumulation occurred in the recombinant AFt cage.

The data reported in this chapter did not provide substantial evidence of AFt labelling with phenanthroline, but still showed encouraging results that can't exclude the potential presence of bioconjugation like in the case of Ellman's assay. Most of the techniques used suggested the presence of heterogeneous protein mixtures in the AFt_K68C samples which likely had an impact on copper accumulation and TMZ retention. The main issue outlined by these results is related to the potential

overoxidation of the cysteine residues in AFt_K68C which caused inefficient conjugation with phenanthroline and the inability to generate replicable data for interpretation. Tests performed using TCEP as a reducing agent did not show any improvement making advisable the storage of the recombinant HuHAFt under nitrogen for a short time between the purification and the bioconjugation. The use of degassed solutions for all experimental procedures following AFt purification should also be considered along with performing the histidine tag removal and the purification itself under inert atmosphere. Such corrections should be able to reduce the risk of irreversible thiol oxidation and ensure replicability and ease of sample analysis.

Although promising, these results require further validation. The optimization of recombinant AFt storage and handling is needed to achieve consistent conjugation, which would provide a ligand concentration quantitatively detectable by MALDI-TOF and that could affect the accumulation of metal ions into the engineered AFt cage. An HuHAFt bioconjugate characterized by high metal complex concentration would also help in increasing its effect on the efficiency of TMZ retention and delivery as well as providing clear sites for optimization of this formulation.

5. Discussion

The research described in the previous chapters was aimed at the characterisation of two apoferritin protein cages loaded with the metal complex copper(II)-1,10-phenanthroline (Cu(phen)) by nanoreactor and covalent conjugation methods and on their efficiency at preventing the leakage of the anticancer agent temozolomide in solution. The first part of this work focused on the encapsulation of Cu(phen) into horse spleen AFt (HSAFt) by the nanoreactor route, which consisted in the diffusion of the metal into the protein core through the AFt hydrophilic channels. Encapsulation in sodium acetate buffer at pH 5.5 was identified as the optimal method to produce the protein-metal complex HSAFt-Cu(phen) also according to previous literature.[135] The metal content of HSAFt-Cu(phen) cages was within the values reported for other metal complexes like the Au_2Phen complex (432 gold ions/ AFt cage) and the platinum (II) anticancer agent cisplatin (45 platinum ions/AFt cage).[163,8,133] The Cu(II) content measured through different experiments was between 70 to 337 metal ions/ AFt cage. DLS, zeta potential and native PAGE confirmed the integrity of the HSAFt cage after its loading with Cu(phen). The UV-vis, HRTEM and EELs provided valuable information to hypothesise the composition of the HSAFt-Cu(phen) cores, the fate of the Cu(phen) and the likely coordination state(s) of copper (II) as a consequence of the encapsulation into the protein.

The presence of 1,10-phenanthroline confirmed by UV-vis suggested the presence of the intact Cu(phen) complex inside the AFt core. Ozutsumi *et al.* identified two predominant copper (II) species in aqueous solution: the hexacoordinated copper-1,10-phenanthroline $[Cu(phen)]^{2+}$ and the ternary complex $[Cu(phen)_3]^{2+}$ (Section 2.2.4).[190] Similar studies also supported that the copper (II) coordination by the nitrate groups and phenanthroline is usually preferred over water.[193,194,195] Furthermore, the X-ray crystallography study performed by Monti *et al.* on the Au_2Phen complex and on the parent Auoxo metallodrugs showed that decomposition occurred during encapsulation into HSAFt, leading to the loss of the ligand by the metal and its interaction with the protein amino acid residues.[163] It is therefore plausible to expect an abundance of the more stable ternary copper (II) complex with phenanthroline,[191] some mono-phenanthroline complexes and some free copper (II). The evidence from the HRTEM images collected using the HSAFt-Cu(phen) samples showed the presence of copper cores that grew over 4 months from d= 2.5 ± 0.8 nm (n= 805) at 1 week to d= 5.6 ± 1.1 nm (n= 83). The analysis of the crystal lattice observed, and the EELs data suggested the presence of oxygen atoms in the environment

surrounding the free copper forming the electron dense cores visible by HRTEM. This supported the hypothesis of the decomposition of part of the Cu(phen) used for the encapsulation leading to the release of free copper (II) able to interact with the acidic amino acid residues lining the interior of the AFt cage that provided coordination sites for the free metal. This interaction could have resulted in an organised arrangement visible in the lattice structure observed by HRTEM. When the encapsulation was performed at neutral pH, those structures were not visible in the HSAFt-Cu(phen) sample. When HSAFt-Cu(phen) was exposed to pH 7.4 at 37 ºC for 24 h, the protein cage provided improved stability and reduced leakage of the metal complex over lipid nano-formulations.[201]

The pronounced activity of the Cu(phen) complex against cancer and non-tumour cells was not affected by encapsulation into AFt. HSAFt-Cu(phen) was still very toxic to colorectal cancer cells, glioblastoma (GBM) cells and healthy fibroblasts. The release of 1,10-phenanthroline from HSAFt observed by UV upon incubation of HSAFt-Cu(phen) at pH 5.5, 37 °C suggested the discharge of the intercalating agent in the tumour microenvironment before internalisation, thus leading to anticancer activity like that of the free Cu(phen).

The full characterisation of the HSAFt-Cu(phen) allowed for the progression of the experimental work and its use for the encapsulation of the prodrug temozolomide (TMZ) by nanoreactor route. The drug loading and encapsulation efficiency of HSAFt-Cu(phen)-TMZ were lower than those reported previously for AFt-TMZ studies.[138] This could be explained by the presence of the Cu(phen) already filling some of the protein internal volume. About 36 % of copper was released during the encapsulation of TMZ because of the acidic pH 5.5 that favoured the swelling of the protein channels and the leakage of its content. The UV-vis data showed that (differently from other reports) the encapsulated TMZ was stable and did not degrade in the presence of Cu(phen). Therefore, it is feasible that the presence of Cu(phen) favoured the formation of a Cu(phen)-TMZ complex through the deprotonated nitrogen on the imidazole ring, rather than a Cu-MTIC one.[8,215,179] Structural integrity of the HSAFt-Cu(phen)-TMZ cage was assessed, with no evidence of TMZ accumulation on the outer surface. The HRTEM (stained and unstained) images of the HSAFt-Cu(phen)-TMZ sample showed the heterogeneous accumulation of the copper adducts between the protein cages and the reduced copper (II) content following, TMZ encapsulation at pH 5.5.

When tested for drug release, the HSAFt-Cu(phen)-TMZ formulation showed a behaviour similar to that previously reported for AFt-TMZ.[138] The UV-vis data at pH 7.4 reported the release of up to 42 % of intact TMZ which supported that the prodrug remained stable under physiological conditions as long as loaded inside the HSAFt capsule. Degradation of the released TMZ in solution was then progressively observed over time. At pH 5.5 instead the flexibility of the AFt cage favoured the discharge of larger amounts of TMZ, demonstrating the ability of AFt to favour selective drug delivery into cancer cells. Such results were also reported for AFt-TMZ.[216] Although this evidence demonstrated that AFt could increase the amount of TMZ delivered only into the BBB and reduce toxicities due to non-specific prodrug activation and degradation, it also illustrated that the presence of Cu(phen) was not able to produce any additional advantage over the control of TMZ release from AFt. It is possible to infer that the AFt protein cage plays a crucial role in the controlled delivery of the anticancer agent and its protection from degradation.

The HSAFt-Cu(phen)-TMZ was tested *in vitro* to evaluate the combined anticancer effect of Cu(phen) and TMZ by MTT and clonogenic assays. The formulation was tested on colorectal cancer, GBM MGMT(+) and MGMT(-) cancer cells and healthy fibroblasts. The enhanced intracellular accumulation favoured by encapsulation into AFt was evident by the 30-fold decrease in the GI_{50} for MGMT(+) GBM cells exerted by HSAFt-Cu(phen)-TMZ compared to non-encapsulated TMZ. However, this enhanced anticancer effect was also reflected into an increase in the toxicity to healthy fibroblasts, quantified into a 10-fold decrease in the GI_{50} value of the HSAFt-Cu(phen)-TMZ. Such data suggested that the increase in anticancer effect against GBM cells is coupled to a decrease in selectivity of the cytotoxicity. Although selectivity could be achieved between TMZ susceptible MGMT(-) GBM cells and fibroblasts, the difference to the GI_{50} value estimated for TMZ-resistant MGMT(+) cells was smaller. This effect could significantly decrease the advantage provided by AFt delivery in the treatment of TMZ-resistant GBM. This phenomenon was not reported for the AFt-TMZ formulation produced by Bouzinab *et al.*, the selective anticancer activity was preserved for both TMZ-susceptible and resistant cells.[138] This evidence suggested that the enhanced toxicity detected from HSAFt-Cu(phen)-TMZ with respect to AFt-TMZ on non-tumour cells was related to the presence of Cu(phen), able to exert anticancer activity as reported in this work and in the literature.[250,251] Interestingly, when the MGMT(+) cells were exposed to HSAFt-Cu(phen)-TMZ for a reduced time (24 h), enhanced anticancer activity was still observed for the AFt formulation over non-encapsulated TMZ. This result could suggest that the issue of

lower selectivity toward non-tumour cells could be optimised by reducing the treatment exposure time or by promoting quicker accumulation at the tumour site by AFt surface functionalisation.

Another way to decrease the cytotoxic effect of the encapsulated Cu(phen) to non-tumour cells could be to immobilise the 1,10-phenanthroline complex by covalent conjugation to the internal surface of AFt, thus reducing its ability to diffuse out of AFt and interact with cellular components. It was envisaged that this approach would be feasible by producing an AFt recombinant mutant with a cysteine amino acid substitution to provide for an anchor for covalent immobilisation of 1,10-phenanthroline. The possibility to produce human heavy chain AFt (HuHAFt) in-house along with its favourable features over HSAFt for clinical applications led to the design of a mutant (HuHAFt_K68C) with one cysteine per subunit, exposed on the internal surface of the AFt cage. The cysteines provided the reactive nucleophilic center for the thiol-conjugation of 1,10-phenanthroline. In addition to the potential decrease in non-specific toxicity produced by the immobilisation of the copper (II) ligand, the design of the HuHAFt_K68C His bioconjugate was aimed at the encapsulation and controlled release of TMZ. HuHAFt provides some advantages over HSAFt for clinical applications: lower risk of immunological reactions[68] and better innate uptake by tumour cells due to the expression of TfR1 reaceptor.[200] However, differently from the light chain AFt (mostly expressed in HSAFt), HuHAFt has a reduced accumulation capacity for metal ions.[180] In this context the introduction of an additional metal coordinating functionality by covalent conjugation was also useful in the evaluation of its impact on the metal binding ability of the recombinant HuHAFt_K68C.[180]

A single cysteine per AFt subunit was introduced through a K68C mutation of the HuHAFt peptide sequence. The cysteine expressed was exposed on the internal surface of the protein shell. The mutation induced a reduced protein yield upon expression and purification compared to the wild type HuHAFt even when a 10 L bioreactor was used. One of the causes identified for the reduced expression was the progressive decrease in the expression efficiency of the bacterial glycerol stocks over time, which required the expression to be carried out from freshly transformed colonies every time. The amount of pure recombinant HuHAFt_K68C available for bioconjugation was further reduced by the TEV removal of the hexa-histidine tag, that led to 50 % of protein aggregation into insoluble precipitated during the reaction. This step was required to reduce the sites for non-specific copper (II) coordination. However, due to the low amount of pure HuHAFt_K68C recovered, the covalent

conjugation experiments were carried first on HuHAFt_K68C with the hexa-histidine tag and then on the protein digested by TEV protease.

A general increase in the UV intensity of the HuHAFt_K68C protein was detected after covalent conjugation reaction to the phenanthroline ligand, that was estimated to correspond to < 10 ligand molecules per protein cage. However, the same UV results were observed also when the reaction was carried out on the wild type HuHAFt protein expressing no cysteines, suggesting that some physical entrapment might occur during the protein reassembly during the purification step. On some of the HuHAFt_K68C reactions, the UV was correlated to a decrease in the thiols available detected by Ellman's which suggested covalent labelling. Although a significant reduction in thiols available could be detected in some of the conjugation experiments on HuHAFt_K68C, such results were not replicable. This was likely due to cysteines overoxidation which irreversibly caused a significant reduction in the number of thiols available in the HuHAFt_K68C sample before the conjugation. No improvement could be observed upon protein treatment with reducing agents like TCEP. Also in biological environments the generation of the sulfonic acid oxidation product of cysteine (Section 4.3.1) cannot be reversed by glutaredoxin or sulfiredoxin, leading the affected protein to proteasomal degradation.[249] For this reason, it was envisaged that the storage of the purified recombinant HuHAFt_K68C and its handling under inert atmosphere would be a potential solution to this issue. MALDI-TOF was performed on the HuHAFt_K68C bioconjugation reaction (HuHAFt_K68C-Phen) and on wild type HuHAFt to corroborate the possible labelling when detected by Ellman's assay. However, no conclusive data could be collected due to the heterogeneity of the reaction mixtures. Although these results were not able to confirm conjugation of 1,10-phenanthroline to recombinant HuHAFt_K68C, at the same time they did not provide enough evidence to exclude the presence of labelled HuHAFt_K68C subunits.

Metalation of the wild type HuHAFt and HuHAFt_K68C-Phen with $Cu(NO_3)_2$ reported an average of < 22 ions per AFt cage, with no significant differences observed between the two proteins. The collected data suggested that the presence of 1,10-phenanthroline (either encapsulated or covalently linked) did not influence or improve metal retention in the HuHAFt_K68C-Phen with respect to the HuHAFt wild type. Although characterised by a low metal content, the encapsulation of TMZ into HuHAFt_K68C-Phen with copper (II) was performed, and the formulation tested for drug leakage at pH 7.4 and 5.5. The protein to TMZ ratio, the encapsulation efficiency and the drug loading estimated were similar to those recorded for HSAFt-Cu(phen)-

TMZ, confirming the potential of the HuHAFt K68C conjugate system as a suitable vehicle for drug delivery. However, it was less efficient in retaining TMZ than HSAFt-Cu(phen)-TMZ both at pH 7.4 and pH 5.5, with a larger amount of drug released within 3 h. This provided further confirmation that no significant copper (II) accumulation occurred in the HuHAFt_K68C-Phen cage. These results illustrated the challenges emerging for the design of an engineered HuHAFt cage by covalent conjugation for drug delivery. More work will be required to optimise the experimental protocols and identify suitable techniques for the robust and replicable characterisation of the HuHAFt_K68C-Phen bioconjugate, whose synthesis constitutes the crucial step in the design of this novel drug delivery strategy.

6. Conclusions and future work

This work represented an attempt to improve the delivery of the anticancer agent temozolomide for the treatment of glioblastoma multiforme. The encapsulation within the nano-cage AFt could shield the drug from degradation and favour intracellular accumulation. The concomitant encapsulation of the copper(II)-phenanthroline complex with temozolomide would prevent its premature leakage and its non-specific activation. The preparation of these metal-stabilised formulations of temozolomide was done using HSAFt and HuHAFt, that provided different methods to produce AFt-Cu(phen) cages for temozolomide encapsulation. This approach helped in the definition of the challenges related the use of different AFt homopolymers for metal-drug incorporation and delivery. It was also possible to elucidate the interaction between the copper (II) complex with AFt, and the potential of AFt-Cu(phen) for anticancer chemotherapy.

The first part of this work focused on the synthesis of HSAFt-Cu(phen) through the encapsulation of copper(II)-phenanthroline using the nanoreactor method (Chapter 2). The successful encapsulation of copper(II)-phenanthroline and the characterisation of the HSAFt-Cu(phen) system led to the identification of organised structures formed by copper (II) upon storage at pH 5.5 and stable for up to 4 months. Further investigation into the composition of these copper (II) cores by EELs and UV-vis showed no evidence of metal NPs formation or of an alteration in the copper oxidation state. It was possible to hypothesise that the encapsulation of copper(II)-phenanthroline into HSAFt was followed by the decomposition of part of the metal complex into free copper (II). The excess phenanthroline produced tris-phenanthroline complexes and the free copper (II) was coordinated by the amino acid residues lining the interior of the protein core. It is reasonable to postulate that such interactions would be favoured in the HSAFt cage due to the predominance of L-chain subunits, rich in amino acid residues able to act as nucleation sites.[117] These observations led to the conclusion that the composition of the HSAFt-Cu(phen) core was formed by a mixture of copper species: mono and tris-copper(II)-phenanthroline trapped in the central bulk and the free copper (II) coating the internal surface of AFt as a consequence of side chains coordination. X-ray photoelectron spectroscopy (XPS) would be a useful technique to apply on the HSAFt-Cu(phen) preparation to corroborate this hypothesis and to determine the elemental composition and the oxidation states of the copper species present within AFt.

The *in vitro* cytotoxicity of copper(II)-phenanthroline was not affected by encapsulation into HSAFt. The metal complex showed promising activity against glioblastoma cell lines, both TMZ-sensitive and TMZ-resistant. However, this anticancer effect was also associated to a significant toxicity toward non-tumour fibroblast. The toxicity exerted by HSAFt-Cu(phen) on both cancer and healthy cells poses a challenge for *in vivo* studies and clinical translation of this system. For this reason, the evaluation of a HSAFt cage with surface functionalisation to improve the specificity of tumour targeting should be considered for future work.

The HSAFt-Cu(phen) cages successfully encapsulated high quantities of temozolomide, without affecting the protein cage integrity and the prodrug structure (Chapter 3). The low pH required for drug encapsulation, causing the expansion of the AFt cage, contributed to the release of part of the copper(II)-phenanthroline. Consequently, the HSAFt-Cu(phen)-TMZ showed a lower metal content and a heterogeneous distribution of the metal-drug cargo across the nano-cages. When subjected to drug release experiments, the AFt cage demonstrated its ability to shield the temozolomide from degradation and to retain up to 58 % of the loaded drug at pH 7.4 over 24 h. The ability of HSAFt-Cu(phen) to retain temozolomide was not different from that reported for AFt-TMZ formulations without the metal complex.[138] This confirmed that the introduction of the copper(II)-phenanthroline complex did not improve temozolomide retention. Although copper(II)-phenanthroline did not affect the controlled release of temozolomide from AFt, it could have contributed to the increased toxicity observed for HSAFt-Cu(phen)-TMZ in the *in vitro* experiments against cancer cells and normal cells. When compared to AFt-TMZ,[138] the formulation with copper(II)-phenanthroline showed increased anticancer activity against resistant glioblastoma cells over short-term exposure (24 h), correlated to a greater toxicity to healthy fibroblasts. This results in a lower specificity of the anticancer activity of HSAFt-Cu(phen)-TMZ with respect to AFt-TMZ.[138] Future use of flow-cytometry and enzyme-linked immunosorbent assay (ELISA) on cancer and normal cells treated with HSAFt-Cu(phen)-TMZ, would help in understanding the cell cycle progression and level of DNA damage induced by the combined administration of copper(II)-phenanthroline and temozolomide. This information would be valuable in reducing the toxicity observed on normal cells.

The preparation of a HuHAFt-based metal-drug formulation using copper(II)-phenanthroline was deemed preferable by covalent immobilisation of the metal complex to a mutated cysteine residue expressed on the H-chain sequence (Chapter 4). The K68C substitution was successfully inserted into the HuHAFt sequence, which

showed proper protein folding and cage assembly upon expression and purification. However, no substantial evidence to confirm bioconjugation with the phenanthroline ligand could be collected, even though in some cases thiol availability was markedly reduced upon incubation with phenanthroline. The techniques used for the bioconjugate characterisation revealed the presence of heterogeneous protein mixtures in the purified reaction solution which negatively affected the quality of the data produced. The cause of these problems was identified in the potential overoxidation of the cysteine residues in the K68C mutant which prevented efficient and replicable conjugation with phenanthroline. The challenges in the bioconjugation affected and were reflected in the protein ability to accumulate copper (II) and to prevent drug leakage. No enhancement in copper (II) binding was detected for the K68C mutant incubated with phenanthroline. Any future attempts at producing a HuHAFt K68C bioconjugate would require the handling and storage of the protein under inert atmosphere. Furthermore, it would be preferable to perform the bioconjugation reaction shortly after protein purification, to minimise the risk of irreversible thiol oxidation. The analysis of the protein bioconjugation reaction by protein digest MALDI-TOF rather than native MALDI-TOF should also be considered, as smaller protein fragments would allow for better resolution of the protein peaks and an easier interpretation of the bioconjugation outcome.

Although the HuHAFt protein conjugation step was characterised by unexpected challenges, the encapsulation of temozolomide was performed successfully and without affecting the assembly of the protein cage. In this case drug release experiments, revealed the inability of the HuHAFt in retaining temozolomide, with up to 62 % of the drug released at pH 7.4 and almost none left inside AFt after 24 h at pH 5.5. These findings confirmed the need to concentrate on the improvement of the bioconjugate synthesis and characterisation for the proper evaluation of its potential as delivery system for temozolomide. The production of the HuHAFt copper(II)-phenanthroline conjugate would require a systematic analysis of its ability to encapsulate and retain temozolomide compared to HuHAFt-temozolomide systems synthesised using the wild type and the K68C mutant. If successful, this work should be followed by the evaluation of the *in vitro* anticancer activity of HuHAFt K68C mutant, of its bioconjugate and of the final formulations with encapsulated temozolomide.

7. Materials and Methods

7.1 Materials

All the reagents commercially available were purchased from Sigma-Aldrich (now Merck) and all enzymes used for molecular biology experiments were purchased from New England Biolabs unless otherwise stated in the text. Buffers and aqueous solutions were prepared using milli-Q grade water. Commercially available reagents for chemical syntheses were used throughout, without purification unless otherwise stated. In cell culture experiments, media components were sterilised by autoclaving (121 °C, 20 min, 15 psi), or were stated in the text by filtration (0.2 µm filter), and mixed when cooled. Media solutions were prepared in deionised water (dH2O) and stored at room temperature unless otherwise stated. Where solid medium was required, agar (Melford; 15 g/L) was added to the medium before autoclaving. Carbenicillin (100 mg/mL), chloramphenicol (25 mg/mL) and IPTG (1 M) stock solutions were filter sterilised and stored at -20 °C as 1000 concentrated stocks, prior addition to the media. Expressed proteins were purified using a 5 mL HisTrap FF crude pre-charged nickel column (GE Healthcare) installed on an AKTA purifier 10 (GE Healthcare).

Protein concentrations were determined by Bradford assay on a Fluostar OPTIMA plate reader (BMG Labtech) using BSA as standard. Protein mass spectra were acquired using a Bruker Ultraflex III MALDI-TOF analyser. UV-Vis spectra were acquired on a UV-2600 with a CPS-100 cell positioner (Shimadzu) and with Agilent Cary 8454 UV-Vis spectrometer. The multi-elemental analysis was undertaken using ICP-MS iCAP-Q (Thermo Fisher Scientific). Absorbances for cell viability assays were measured using a Perkin Elmer plate reader. High-resolution transmission electron microscopy (HRTEM) images were acquired using a JEOL 2100F TEM microscope.

Analytical thin-layer chromatography was carried out on aluminium backed plates coated with Merck Kieselgel 60 GF254 and visualised under UV light at 254 and/or 360 nm. Chemical staining was also routinely used, with aqueous basic potassium permanganate. Flash chromatography was carried out using Davisil silica 60 Å, with the eluent specified. H^1 NMR spectra were recorded at 298 K using a Bruker AV(III)400, AV400 (400 MHz). Mass spectra analyses of the chemicals synthesised were obtained from a Bruker microTOFII with ElectroSpray Ionisation (ESI) sample injection method.

7.2 Syntheses

7.2.1 Preparation of the copper-1,10-phenanthroline complex $[Cu(phen)]^{2+}$ [211]

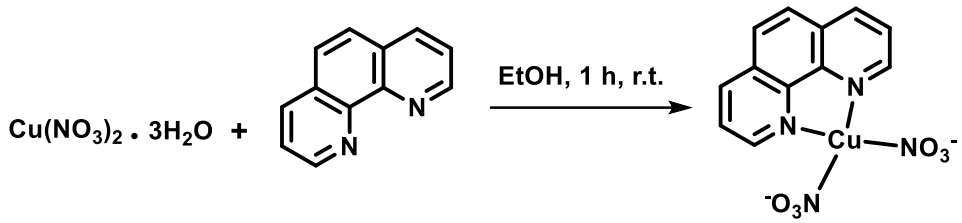

To a solution of 1, 10-phenanthroline (270.3 mg, 1.5 mmol) in ethanol (80 mL) was added $Cu(NO_3)_2.3H_2O$ (398.6 mg, 1.5 mmol). The blue solution was stirred for 1 hour at room temperature giving a blue precipitate. The precipitate was filtered under vacuum and washed with isopropanol (≈ 10 mL). The crude powder was then dried under nitrogen overnight. The final product (464.2 mg, 84 %) was characterised by ESI mass spectrometry (calculated mass 367.8 Da ($2NO_3^-$) and 304.9 Da (NO_3^-)) *m/z* 304.9 (M^+ 100 %), 271.0 (67), 244.0 (25), elemental analysis (found: C 38.45, H 2.06, N 14.89, $C_{12}H_8CuN_4O_6$ expected C 39.19, H 2.19, N 15.23), UV-Vis analysis (λ_{max} = 679 nm, Appendix 7.B) and ICP-MS (Cu/ligand= 0.90 ± 0.01).

7.2.2 Preparation of 2-bromo-*N*-(1,10-phenanthrolin-5-yl)acetamide

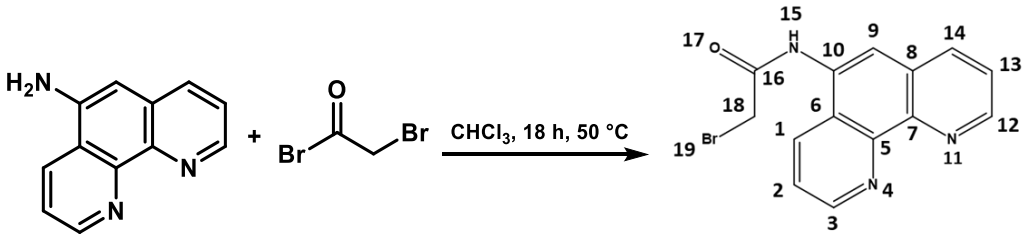

To a 50 mL two necked flask filled with 30 mL of anhydrous $CHCl_3$ at 50 °C was added 624.7 mg (3.2 mmol, 1 eq) 1,10-phenantroline-5-amine under a nitrogen atmosphere. To this solution was added slowly half of 0.42 mL (968.9 mg, 4.8 mmol, 1.5 eq) bromo acetyl bromide. After 1 h of incubation the remaining volume of bromo acetyl bromide was added. The reaction mixture was heated under reflux overnight and the resulting suspension was filtered. The solid was recrystallized from hot MeOH, yielding the HBr salt of the desired compound as a yellow/orange solid. The final product (692.3 mg, 69 %) was characterised by ESI mass spectrometry (calculated mass 316.2) *m/z* 316.2 (M^+ 100 %) and ^1H NMR (400 MHz, DMSO) δ (ppm) 10.87 (s, 1H, H^{15}), 9.34 (dd, 1H, H^{12}, J_1= 4.76, J_2= 1.64 Hz), 9.22 (dd, 1H, H^3, J_1= 5.04, J_2= 1.64 Hz), 9.13

(dd, 1H, H^{14}, J_1= 8.28, J_2= 1.04 Hz), 9.03 (dd, 1H, H^1, J_1= 8.64, J_2= 1.64 Hz), 8.23 (, 3H, $H^{2,9,13}$, J_1= 3.60 Hz).

7.2.3 Synthesis of *N*-methyl-*N*-phenylpicolinamide

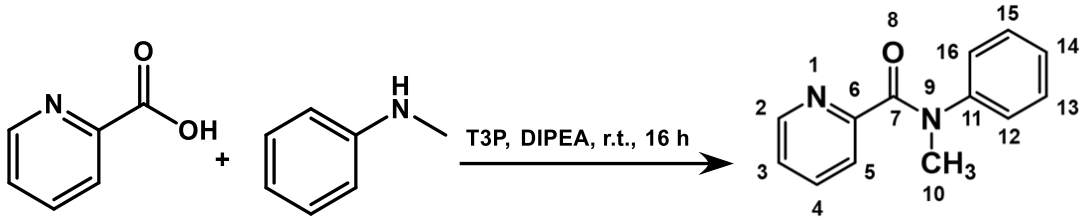

The picolinic acid (393.9 mg, 3.2 mmol) was dissolved in 5 ml of heated THF (61°C) under reflux conditions. Upon complete dissolution of the picolinic acid, T3P (0.93 ml, 1018.2 mg, 3.2 mmol), DIPEA (1.12 ml, 830.3 mg, 6.4 mmol) and the monomethylaniline (0.33 ml, 342.9 mg, 3.2 mmol) were added to the mixture which was kept heated under reflux overnight. A yellow solution formed the organic phase which is washed with water acidified with HCl (1/20, v/v, 5 ml, 2 washes) and then with water only (5 ml). The organic phase was then washed with brine (5 ml, 3 washes). The organic phase was dried by addition of $MgSO_4$ and filtered under gravity. The solvent was evaporated from the filtrate under reduced pressure to give a brown oil. The product (242.4 mg, 35,6 %) was characterised by ESI-MS in acetonitrile (calculated mass 212.25 Da) *m/z* 213.10 (M^+ 100 %) and H^1NMR (400 MHz, $CDCl_3$) δ (ppm) 8.34 (s,1H, H^2), 7.62 (t, 1H, H^5, J = 11.36 Hz), 7.45 (d, 1H, H^4, J= 6.0 Hz), 7.23 (m, 4H, $H^{3,13,14,15}$), 7.06 (s, 2H, $H^{12,16}$), 3.52 (s, 3H, H^{10}).

7.2.4 Synthesis of ethyl-*N*-phenylcarbamate

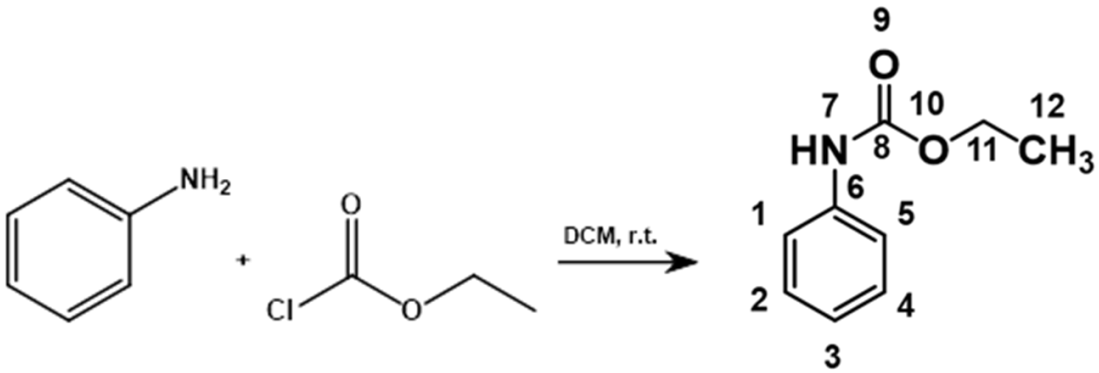

To a solution of aniline (0.3 ml, 306.6 mg, 3.3 mmol) in DCM (12 ml) was added ethylchloroformate (0.29 ml, 325.6 mg, 3.0 mmol) dropwise, the mixture was kept in

ice-water bath for 1 hour. After 1 h, water (20 ml) was slowly added to the reaction mixture which was left stirring for 30 minutes. The organic phase was then extracted with DCM (10 ml, 2 washes) and then dried with $MgSO_4$. The solvent was removed under reduced pressure to give the final product (312.0 mg, 63 %). The product was characterised by H^1 NMR (400 MHz, acetone) δ (ppm) 7.39 (d, 2H, $H^{1,5}$ J= 8.0 Hz), 7.32 (t, 2H, $H^{2,4}$, J= 8.0 Hz), 7.07 (t, 1H, H^3, J= 8.0 Hz), 4.25 (q, 2H, H^7, J= 8.0 Hz), 1.33 (t, 3H, H^8, J= 8.0 Hz).

7.3 Assessment of the catalytic activity of copper(II)-phenanthroline

The catalytic assay testing the copper catalyst for the hydrolysis of 4-nitrophenyl acetate was performed by keeping the substrate concentration fixed while varying the catalyst to substrate ratios (0.05, 0.1, 0.15). The reactions were prepared in 1 mL of 50 mM phosphate buffer at pH 7.4 with 500 µM *para*-nitrophenyl acetate and respectively 25, 50 and 75 µM of the AFt encapsulated with Cu-phen. The protein concentration was measured by Bradford after encapsulation. The reaction controls were prepared as 1 mL buffer with 500 µM *para*-nitrophenyl acetate. Product formation was followed by monitoring the absorbance at 405 nm (λ_{max} of 4-nitrophenol) at a constant temperature of 37 °C for up to 24 h.

The catalytic assay using the carbamate and amide substrates were instead prepared by dissolving the substrate in 50 mM phosphate buffer at pH 8 at 37°C. A solution of the catalyst in the same buffer was then added to start the reaction that was then incubated under constant stirring at 37°C for 24 hours. The final reaction volume was 2.5 ml containing 20 mM substrate and 1 mM catalyst concentrations. Two controls were prepared for each experiment, one containing only the substrate and the other being a reaction mixture with $Cu(NO_3)_2$ instead of the catalyst. After 24 hours the organic phase was the extracted from the reaction mixture using deuterated chloroform and product formation was analysed by H^1 NMR.

7.4 Horse spleen Apoferritin

7.4.1 Preparation of AFt from horse spleen Ferritin

The AFt protein cage used for this work was prepared from 3 batches of HSFt purchased from Sigma-Aldrich as a saline solution.

A sample of the stock HSFt protein was diluted 10 times into sodium acetate buffer (0.1 M NaOAc, pH 5.5) and transferred into a dialysis bag (MWCO 14000). The protein solution was then immersed in acetate buffer (0.1 M NaOAc, pH 5.5, 1.5 L) and purged with nitrogen for 15 min before the addition of 0.03 M of thioglycolic acid (2 mL). The protein was dialysed for 2 hrs under constant purge with N_2 and then 1 mL of thioglycolic acid (0.03 M) was added. After one hour the protein was transferred into a fresh sodium acetate buffer (0.1 M NaOAc, pH 5.5, 1.5 L) and the procedure was repeated 6 times keeping the solution at room temperature. After that, the protein was finally transferred into 1.5 L of fresh sodium acetate buffer and dialysed for another 24 h to remove any thioglycolic acid residue. The protein was then split into 1 mL aliquots and stored at -20 °C. The residual iron content was assessed by ICP-MS.

7.4.2 Encapsulation of copper-1,10-phenanthroline within HSAFt

The $[Cu(phen)]^{2+}$ complex was loaded into the AFt cage by passive diffusion through the protein channels. The metal complex and the protein cage (24 mer) were mixed in different ratios up to a maximum of 22000 to 1 ratio in 0.1 M sodium acetate buffer (pH 5.5) or 50 mM glycine buffer (pH 7.4) for a total incubation time of 3 h. The AFt solution (3 mL, 3.5 µM) was kept stirring at room temperature while 0.5 mL of the copper-phenanthroline solution (4 mL, 57.2 mM) was added every 30 min to avoid AFt precipitation. After incubation, the free copper-phenanthroline was removed by overnight dialysis against at least 500 volumes of 0.1 M NaOAc pH 5.5 or 50 mM glycine pH 7.4 buffer. The samples were stored at -20 °C for further analysis. Copper content was assessed by ICP-MS analysis and UV-vis spectrometry. The integrity of the protein cage was confirmed by native PAGE, DLS and HRTEM. Sample dilutions were prepared for UV-vis at protein concentration of 0.30-0.50 mg/mL for UV-vis (except for the HS-Ft control which was at 0.05 mg/ml due to the high intensity absorbance produced by the iron), 0.05 mg/mL for DLS, 1.0 µM for HRTEM using freshly prepared encapsulation buffer (0.1 M NaOAc pH 5.5 or 20 mM glycine pH 7.4).

7.4.3 Effect on environmental conditions on HSAFt-Cu(phen) adducts formation

The AFt cages with encapsulated $[Cu(phen)]^{2+}$ were subjected to different temperature and pH conditions and the formation of metal nanoparticles inside the protein was followed by TEM imaging. In the first experiment, three sample aliquots (0.5 mL) originally stored in 50 mM glycine buffer at pH 7.4 were incubated for 18 hrs

at -20, 37 and 50 °C respectively before TEM imaging. In the second experiment, three sample aliquots (0.5 mL) were dialysed against pH 7.4, 6.0, and 2.0 for 6 hrs. Different buffers were employed to achieve different pH conditions: 20 mM Glycine was used for pH 7.4 and 6.0, 0.1 M sodium acetate was used for pH 5.5 and 2.0. All the buffers were supplemented with CHELEX (10.0 mg/L) to ensure removal of external metal ions. After dialysis, all the samples were incubated at 37 °C overnight.

7.4.4 Catalytic activity of copper(II)-phenanthroline loaded inside HSAFt

The catalytic assay testing the copper catalyst for the hydrolysis of 4-nitrophenyl acetate was performed by keeping the substrate concentration fixed while varying the catalyst to substrate ratios (0.05, 0.1, 0.15). The reactions were prepared in 1 mL of 50 mM phosphate buffer at pH 7.4 with 500 µM *para*-nitrophenyl acetate and respectively 25, 50 and 75 µM of the AFt encapsulated with $[Cu(phen)]^{2+}$. The reaction controls were prepared as 1 mL buffer with 500 µM *para*-nitrophenyl acetate. Product formation was followed by monitoring the absorbance at 405 nm (λ_{max} of 4-nitrophenol) at a constant temperature of 37 °C for up to 24 h.

7.4.5 Encapsulation of temozolomide within the HSAFt-Cu(phen) structures

The anticancer agent temozolomide (TMZ) was loaded into the HSAFt-Cu(phen) cages by passive diffusion through the protein channels. The nanoreactor procedure was performed at 2 weeks after the encapsulation of the AFt protein with $[Cu(phen)]^{2+}$ to allow enough time for the formation of crystal copper structures. The drug and the protein cage (24mer) were mixed in 800 to 1 ratio in 0.1 M sodium acetate buffer (pH 5.5) for a total incubation time of 3 h. The TMZ solution (TMZ: 10 mM, 7.2 µmol) was prepared in DMSO and was added every 30 min, to the AFt solution with constant stirring at 4 °C to prevent precipitation of the test agent. The solution was then ultra-filtered through an Amicon ultra-4 centrifugal filter (MWCO 10000 Da) at 4000 *xg* for 4 min. The final TMZ concentration was estimated by UV-vis, and AFt concentration was confirmed by Bradford assay. The integrity of the cage was confirmed by native PAGE, DLS and HRTEM. Samples were stored at -20 °C for further analyses.

7.4.6 Drug release studies on HSAFt-Cu(phen) and HSAFt-Cu(phen)-TMZ

Drug release studies were performed by adding 250 µL of AFt nanoformulation into a D-Tube Dialyzer Mini 12-14 kDa MWCO (Novagen), and samples were dialyzed at 37 °C and mixed at 150 rpm against 1 mL of either pH 5.5 NaOAc buffer (0.1 M) or pH 7.4 phosphate-buffered saline (PBS). After 1, 3, 5, 7, and 24 h of dialysis, drug

leakage in the dialysis solution was monitored by UV−vis spectroscopy (AIC λ= 265 nm, 1,10-phenanthroline λ= 268 nm, TMZ λ = 330 nm).

The Beer-Lambert law states the proportional relation between the absorbance of a compound in solution and its concentration. Given that only the extinction coefficient of TMZ is known (9800 M^{-1} cm^{-1}) the absorbance values of TMZ (330 nm) and that of its degradation product AIC (265 nm) were used as representative of the amount of agent released in the experiment. The estimation of percentage release was determined by assuming as absolute maxima the absorbance value of TMZ in the initial AFT-Cu-TMZ sample. The estimation of percentage release at each time point was calculated as follows:

$$\frac{Abs\ max\ from\ dialysis\ solution}{Abs\ max\ from\ sample}\ X\ 100$$

To solidify the reliability of the estimation method described above, the integrated peak intensities were extrapolated using the software Origin from the maxima of the Gaussian curve fitted using the original spectra with the software GraphPad Prism.

7.4.7 High-resolution transmission electron microscopy (HRTEM) studies

The unstained samples HRTEM analysis were diluted to an AFt concentration of 1.0 μM in sodium acetate buffer, deposited on a graphene oxide grid on holey carbon film, left to dry for 10 minutes, washed with one droplet of deionised water and dried under vacuum overnight before analysis. An aliquot from the same sample was applied on a separate carbon grid, stained with 2 % uranyl acetate and dried at room temperature overnight before imaging.

7.5 Human Apoferritin

7.5.1 Preparation of the HuHAFt cysteine mutant

Plasmid pJexpress414 containing the wild type gene of the Hu-HAFt (Appendix II) was kindly provided by prof. Thomas' group. All primers (Table 1) were synthesised by Integrated DNA Technologies Inc. (IDT).

Primer	Sequence (5’ to 3’)
Hu-HFt-K68C_F	CACGCCGAG**TGC**CTGATGAAACTG
Hu-HFt-K68C_R	CTCGCGTTCTTCATGG

Table 1. Primers used to introduce a K68C mutation (codon in bold) in the Hu-HAFt gene to provide a cysteine residue per subunit.

The polymerase polymerase chain reaction (PCR) to amplify and mutate the plasmid was perfomed using the Q5 high fidelity DNA polymerase enzyme from purchased from New England Biolabs. PCR reaction mixes (25 µL) contained: 5x master mix buffer for Q5 polymerase (5 µL), dNTPs (10.0 mM each; 0.5 µL), 5’ primer (10.0 µM; 1.25 µL), 3’ primer (10.0 µM; 1.25 µL), template DNA (25 ng), Q5 high fidelity DNA polymerase (1 U) and PCR grade water. The thermocycler conditions used are shown in (Table 2). Digestion of the DNA template was done by adding 1 µL of the DpN I enzyme to the reaction tube which was incubated for 5 minutes at 37 °C. The digestion reaction was then mixed with 5 x loading dye (New England Biolabs) and analysed by agarose (1%) gel electrophoresis.

Initial denaturation	98 °C, 30 s	
Denaturation	98 °C, 10 s	Repeated for 30 cycles
Primer annealing	45-65 °C, 30 s	
Elongation	72 °C, 3 min	
Final elongation	72 °C, 2 min	

Table 2. Thermocycler conditions used for the Q5 mutagenesis on Hu-HAFt.

DNA gel extraction and purification were performed on the electrophoresis sample using the Monarch DNA Gel Extraction Kit giving a final solution of 6 µL. The purified DNA was then subjected to 5-OH’ ends phosphorylation and ligation using T4 PNK and ligase enzymes (New England Biolabs). The phosphorylation reaction mix was made by adding 1 µL of 5 x T4 buffer and 1 uL of T4 PNK to the purified DNA solution,

which was incubated at 37 °C for 30 minutes. The further addition of 1 µL of 5 x T4 buffer and 1 µL of the T4 ligase allowed for the circularisation of the plasmid DNA. The ligation reaction mix was allowed to react for 2 h at room temperature.

The Q5 mutagenesis product was then transformed into chemically competent *E. coli* DH5α cells by heat shock. Heat shock transformation was performed by transferring plasmid DNA (200.0 ng) to sterile microfuge tubes and chilling them on ice (10 min). Chemically competent cells (50 µL) were defrosted on ice and transferred to the tube containing DNA. The suspension was mixed by gently swirling and stored on ice (30 min). Cell suspensions were heat-shocked in a water bath (42 °C, 45 s) and immediately transferred to ice (2 min). SOC medium (800 µL) was added to the cells and the culture incubated (1 h). Transformants were selected by plating the culture (200 µL) on LB supplemented with carbenicillin (50 µg/mL) and incubated overnight at 37 °C. Plates were stored at 4°C for a maximum of two weeks.

Single colonies were picked and inoculated in LB media supplemented with carbenicillin and incubated overnight at 37 °C, 250 rpm. The cell solution was used to prepare 25 % glycerol stocks which were stored at -80 °C and to verify plasmid internalisation via sequencing after DNA extraction and purification. After verification of successful mutation, the genetic material was stored at -20 °C. Restriction digests were performed to confirm plasmids had been correctly assembled by extracting the DNA using a miniprep kit (Monarch). The restriction enzyme digestion was performed using the NdeI kit from Thermo Fisher Scientific on the Q5 mutagenesis product and the template. The reaction was prepared by mixing 2 µL of 10 x kit buffer, 1 µL of NdeI, 200 ng of plasmid DNA and PCR grade water. A first incubation step at 37 °C for 10 minutes allowed for the digestion and then 5 minutes at 65 °C ensured inactivation of the restriction enzyme. Following the reaction, samples were loaded directly into agarose gels for analysis.

7.5.2 Expression and purification of AFt_WT His and AFt_K68C His mutant

After transformation of the mutated plasmid into *E. coli* Rosetta™ 2 (DE3) competent cells from Novagen according to the manufacturer protocol single colonies were inoculated into 100 mL of LB-carbenicillin (50 µg/ml) medium which was then incubated for 18 h at 37°C, 250 rpm shaking. The OD_{600} of the preculture was measured and a suitable volume of the preculture was added into 1 L of LB-carbenicillin (50 µg/ml) to have a starting OD_{600}= 0.1. The 1L culture was then incubated at 37°C and shaking at 250 rpm until the OD_{600}= 0.6. At that point, protein

expression was induced by adding IPTG to reach a final concentration of 1 mM followed by incubation at 37°C, 250 rpm for 4 h for the Hu-HAFt wild type and at 20°C with shaking at 180 rpm, for 18 h for the Hu-HAFt K68C mutant. After induction, cells were harvested at 5000 *xg* at 4°C for 20 minutes, pellets were stored at -80°C and the supernatant was discarded.

To prepare the protein sample for purification, the pellet was suspended in a cell lysis solution composed of a protease inhibitor cocktail tablet, lysozyme (1.0 mg/mL) 0.1 µg/mL of nuclease (benzonase) and stirred for 1 hour in ice. After that, the solution was sonicated (35 % amplitude, cycles 1-2: 30 seconds pulse on, 5 minutes pulse off, cycles 3-5: 15 seconds pulse on, 5 minutes pulse off) while kept on ice. Centrifugation at 35000 *xg*, 4°C, for 35 minutes allowed for the separation of the cell debris (insoluble cell fraction) from the supernatant (soluble cell fraction, 10 mL) which was then passed through a 0.45 µM filter and loaded on a 5 mL His-Trap FF Crude column. The soluble fraction was purified by IMAC affinity chromatography using 20 mM Tris, 300 mM NaCl, 30 mM imidazole, pH 8.0 as the binding buffer to initially equilibrate the column and 20 mM Tris, 300 mM NaCl, 0.8 M imidazole pH 8.0 as the elution buffer. Protein purification was assessed by SDS-PAGE gel (15 %) electrophoresis.

The purified K68C mutant AFt was dialysed at 4 °C overnight in dialysis buffer 1 (20 mM Tris, 1 mM EDTA, pH 8.0) then 4 h in dialysis buffer 2 (20 mM Tris, pH 8.0), which allowed for the removal of the residual iron ions bound to the subunits. After dialysis, the amount of protein was quantified by Bradford assay before concentration (VIVASPIN, 10000 MWCO) and storage at -80 °C.

7.5.3 Fermentation for 10 L expression of AFt_K68C His

The preculture for the large-scale human apoferritin expression was prepared by inoculating a 1 mL glycerol stock of *E. coli* Rosetta™ 2 (DE3) competent cells containing the plasmid encoding for the HuHFt K68C protein in 1 L of sterile LB media supplied with carbenicillin (50 µg/ml) and chloramphenicol (25 µg/ml). The preculture was incubated for 18 h at 37°C, 250 rpm shaking.

The 10 L reactor (Electrolab 10 L SIP) was prepared by pouring 9 L of LB solution (250 g) supplied with 5 mL of antifoaming agent (propylene glycol 2000) which was sterilised by bringing it to 121 °C for 15 minutes. The media was let to cool down to 37 °C and then supplied with sterile carbenicillin (50 µg/ml) and chloramphenicol (25

µg/ml). The volume of preculture pumped into the reactor was determined from its OD_{600} (1 L for $OD_{600} < 2$, 0.5 L for $OD_{600} \geq 2$). The culture was incubated at 37 °C, 800 rpm agitation, 1 vvm oxygen, pH 7.0. The initial OD_{600} of the 10 L culture was measured and was checked every 30 minutes until reaching 0.6. At $OD_{600} \approx 0.6$ the temperature was reduced to 20 °C and when stabilised IPTG was added to a final concentration of 1 mM to start protein induction for 18 h. After induction, cells were harvested at 8000 *xg* at 4°C for 10 minutes, pellets were stored at -80°C and the supernatant was discarded. Pellets were treated for AFt_K68C His protein purification as described in section 3.5.2.

7.5.4 Expression and purification of the TEV protease[240]

After transformation of the TEV protease expression vector pRK793 into *E. coli* BL21(DE3) CodonPlus-RIL according to the manufacturer protocol single colonies were inoculated into 15 mL of LB medium supplied with carbenicillin (100 µg/mL) and chloramphenicol (30 µg/mL). The inoculum was then incubated for 18 h at 37 °C, 250 rpm shaking. After overnight incubation the preculture was added into 0.6 L of LB with carbenicillin (100 µg/ml) and chloramphenicol (30 µg/mL) and its starting OD_{600} measured. The 0.6 L culture was then incubated at 37 °C and shaking at 250 rpm until the $OD_{600} \geq 0.6$. At that point, protein expression was induced by adding IPTG to reach a final concentration of 1 mM followed by incubation at 30 °C, 250 rpm for 4 h. After induction, cells were harvested at 8000 *xg* at 4 °C for 10 minutes, pellets were stored at -80 °C and the supernatant was discarded.

To prepare the protein sample for purification, the pellet was suspended in a cell lysis solution composed of a protease inhibitor cocktail tablet, lysozyme (1.0 mg/mL) 0.1 µg/mL of nuclease (benzonase) and stirred for 1 hour in ice. After that, the solution was sonicated (35 % amplitude, 30 seconds pulse on, 30 seconds for 5 minutes) while kept on ice. Centrifugation at 15000 *xg*, 4 °C, for 30 minutes allowed for the separation of the cell debris (insoluble cell fraction) from the supernatant (soluble cell fraction) which was then passed through a 0.45 µM filter and loaded on a 5 mL His-Trap FF Crude column. The soluble fraction was purified by IMAC affinity chromatography using 50 mM Na_2HPO_4-NaH_2PO_4, 200 mM NaCl, 10 % glycerol, 25 mM imidazole pH 8.0 as the binding buffer to initially equilibrate the column and 50 mM Na_2HPO_4-NaH_2PO_4, 200 mM NaCl, 10 % glycerol, 250 mM imidazole pH 8.0 as the elution buffer. Protein purification was assessed by SDS-PAGE gel (12 %) electrophoresis.

The relevant fractions were pooled together and EDTA (2 mM) and DTT (5 mM) were added before concentration with VIVASPIN (10000 MWCO). The concentrated protein solution was dialysed against 25 mM Na_2HPO_4-NaH_2PO_4, 100 mM NaCl, 10 % glycerol pH 7.5 overnight. Fresh storage buffer was used to dialyse the protein solution for other 2 h before determining its concentration by UV and storing the protein in aliquots at -80 °C.

7.5.5 TEV protease cleavage reaction on AFt_K68C His to produce AFt_K68C

The purified aliquots of TEV protease were used to remove the His-tag from the N-terminus of the HuHAFt K68C before bioconjugation with the 2-bromo-N-(1,10-phenanthrolin-5-yl)acetamide. The reaction was set up by mixing the HuHAFt (1 mg/mL, 45 µM) and TEV (0.05 mg/mL, 1.8 µM) in a 1:20 molar ratio in 50 mM Tris, 0.5 mM EDTA, 1 mM DTT pH 8.0. The mixture was incubated at 30 °C for 2 h and the reaction was then purified by IMAC affinity chromatography using 20 mM Tris, 300 mM NaCl, 30 mM imidazole, pH 8.0 as the binding buffer to initially equilibrate the column and 20 mM Tris, 300 mM NaCl, 1 M imidazole, pH 8.0 as the elution buffer. The reaction was loaded on a His-Trap FF crude 5 mL column and the fractions were run on a SDS-PAGE. The relevant fractions containing pure cleaved HuHAFt K68C His^- were pooled together, concentrated by VIVASPIN (3000 MWCO), analysed by Bradford assay and stored at – 80 °C for future experiments.

7.5.6 K68C mutant labelling with 2-bromo-*N*-(1,10-phenanthrolin-5-yl)acetamide

The protein K68C mutant (67.5 nmol, 1 mg/ mL) was exchanged in 20 mM Tris, 8 M urea pH 8.5 by dialysis (200 volumes) for 2 h at room temperature. After dialysis the protein solution was purged with nitrogen gas and mixed with 20 equivalents (1.35 µmoles) of 2-bromo-N-(1,10-phenanthrolin-5-yl)acetamide from a 10 mM stock solution in DMSO. The protein and the ligand were incubated at 4 °C, overnight under constant stirring and nitrogen atmosphere. Upon reaction completion the sample was purified through PD-10 desalting column, previously equilibrated with 20 mM Tris, 8 M urea pH 8.5. Fractions were analysed by UV-vis and Bradford assay. The fractions of interest were pooled and concentrated with VIVASPIN (MWCO 3000). The final concentration was estimated by Bradford and the ratio of free thiols available was determined by Ellman's assay. After this preliminary characterisation the protein conjugate was dialysed against 20 mM Tris pH 8.0 at 4 °C overnight. After dialysis the protein sample was stored at -20 °C for further analysis.

7.5.7 Ellman's assay

The protein control (1 mL) was dialysed in 200 mL of 20 mM Tris, 50 mM NaCl and 8 M urea at pH 7 for at least 2 h. After dialysis a 4.0 mg/ml solution of Ellman's reagent (5, 5'-dithiobis (2-nitrobenzoic acid), DTNB) was prepared in 100 mM sodium phosphate, 1 mM EDTA at pH 7.0. Free thiols estimation was achieved in accordance with the following reaction:

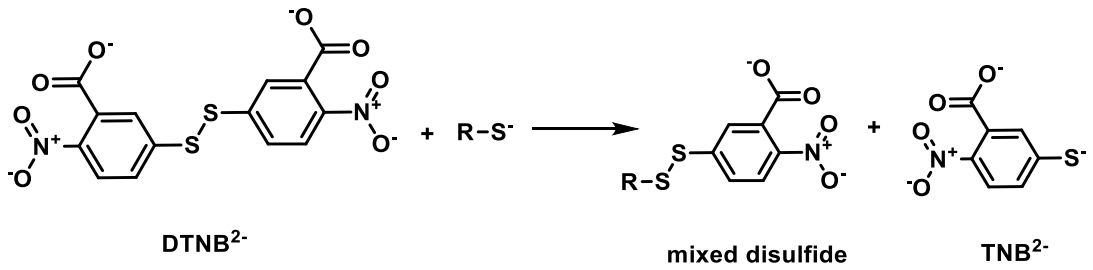

DTNB^{2-} mixed disulfide TNB^{2-}

Samples were prepared as follows: 445 µL of buffer, 45 µL of protein sample (or protein buffer for negative control) and 10 µL of Ellman's reagent solution. The reaction was left at room temperature for 15 minutes then absorbance was monitored at 412 nm. Concentration of free thiols were then calculated according to the following equation:

$$[free\ SH] = \frac{(Abs_{TEST} - Abs_{CONTROL}) \cdot 500 \cdot 1{,}000{,}000}{14{,}500 \cdot 45}$$

Where [free SH] correspond to the concentration of free thiol (in µM), Abs test is the absorbance of the protein sample at 412 nm, Abs control is the absorbance of the control cuvette at 412 nm, 500 and 45 are the dilution factors due to the assay protocol, 1,000,000 is the conversion factor from M to µM and 14500 M-1cm-1is the coefficient of molar extinction of $TNB2^-$ at 412 nm under the assay's conditions. A cuvette of path length 1 cm was used for each experiment.

7.5.8 MALDI-TOF

Protein samples for MALDI-TOF analysis were prepared as follows: 10 µL of protein solution at 1 mg/mL and above were desalted using C_4 ZipTips previously equilibrated with 0.1 % TFA. The protein was then eluted using a solution of saturated sinapic acid in 30:70 (v/v) Acetonitrile: TFA 0.1% in water. The plate was spotted with 0.5 µL of saturated sinapic acid in ethanol and allowed to dry, then 0.5 µL of sample were deposited on top of the first layer and allowed to dry. The analysis was performed on a MALDI-TOFMS Bruker Autoflex Max in linear mode, using a mass range of 1300-

28200 Da and laser intensity of up to 70 %. Myoglobin from equine skeletal muscle purchased from Merck was used as a standard for external calibration.

7.6 AFt cage integrity assessment

7.6.1 Native PAGE

Discontinuous native PAGE gels were prepared to assess the integrity of the horse spleen AFt cage upon Cu(phen) encapsulation. The 6 % (w/v) resolving gel and the 4 % (w/v) stacking gel were prepared according to the procedure described in Table 3 and allowed to polymerise for 30 minutes before sample loading. The protein samples were mixed with a 4 x loading buffer (50 mM Tris-HCl pH 6.8, 100 mM DTT, 50 % v/v glycerol, 0.1 % w/v bromophenol blue) and loaded on the gel. Horse spleen AFt control was also loaded along with the encapsulation samples as reference. The gel was run in 200 mM glycine, 25 mM Tris base at 125 V for 1.5 h. The gel was stained for 30 minutes with Coomassie brilliant blue buffer and then destained for 2 h before imaging.

	Stacking gel 4% (w/v)	**Resolving gel 6 % (w/v)**
Milli-Q H_2O	2.88 mL	6.66 mL
30% (w/v) acrylamide	0.5 mL	2.3 mL
1.5 M Tris	0.94 mL (pH 6.8)	3 mL (pH 8.8)
10 % (w/v) APS	60 µL	150 µL
TEMED	6 µL	15 µL

Table 3. Composition of the stacking and resolving gels prepared for the native PAGE of horse spleen AFt.

7.6.2 DLS and zeta potential

The analysis of DLS and zeta potential were carried out on samples at 0.0 5mg/mL protein concentration which was identified as the optimal condition to avoid excessive aggregation. Both analyses were performed on a Malvern Zetasizer Nano ZS using a quartz cell Zen-2112 for DLS measurements and a DTS1070 cell for zeta potential.

Before the analyses samples were filtered using a 0.22 µM filter to prevent protein aggregation and then stored at 4 °C.

7.7 Cytotoxicity studies

7.7.1 MTT assay[210]

HCT-116 human-derived colorectal carcinoma (CRC) cells, MRC-5 foetal fibroblasts, glioblastoma multiforme (GBM) U373V (MGMT-) and U373M (MGMT+) cells were seeded at a density of 5×10^3 cells per well into 96-well microtiter plates and allowed to adhere for 24 hr before treatment with test compounds AFt, $[Cu(phen)]^{2+}$, TMZ, HSAFt-Cu(phen), HSAFt-Cu(phen)-TMZ, solvent and buffer controls. The seeding density was 400 cells per well for HCT-116, MRC5 and 650 cells per well for GBM cell lines when tested with the anticancer agent TMZ. Serial dilutions were prepared in medium supplemented with 10 % FBS, before each assay. Viable cells at the time of drug addition (time-zero; T_0), following 72 hr drug exposure and 6 days drug exposure (for TMZ and HSAFt-Cu(phen)-TMZ only) were determined by adding MTT (2 mg/mL) in PBS solution to reach a final concentration of 400 µg mL-1). Incubation of the plates for an additional 2-3 h at 37 °C allowed reduction of MTT by viable cell dehydrogenases to insoluble formazan product. Supernatants were aspirated from the wells and formazan solubilised with 150 µL DMSO. Absorbance was read at 570 nm using a plate reader (Perkin Elmer). Absorbances were then corrected by subtraction of the solvent background and used to calculate the estimated concentration causing reduction of cell viability by 50% (GI_{50}) for both cell lines. Control cell growth was determined using the control groups at T_0 after 24 h incubation as references. The final GI_{50} values were estimated through the curve-fit analysis of GraphPad Prism, using the non-linear regression function.

7.7.2 Cell count assay

The cell lines of interest (MRC5 and HCT-116) were seeded at a density of 1×10^4 cells/ well in 0.5 mL medium in 12-well plates and incubated at 37 °C for 24 h. On day 2 each well was treated with 0.5 mL of the test agents diluted in medium. The treatments used for this assay were AFt, $[Cu(phen)]^{2+}$, HSAFt-Cu(phen) at the final concentrations 0.5 and 1.5 µM. After 72 h of exposure to the treatment the well content was aspirated, and the cells were resuspended with 0.25 mL of trypsin. Trypsin was inactivated by adding 0.25 mL of medium and a single cell suspension was produced by putting the content of each well through a syringe needle. The cells were then counted using a haemocytometer.

7.7.3 Clonogenic assay[201]

Clonogenic assays were set up in 6-well plates and U373V, U373M were seeded at 400 cells/well. The cells were incubated at 37 °C for 24 h before treatment with AFt (0.05 µM), $[Cu(phen)]^{2+}$ and HSAFt-Cu(phen) (2.5 µM), TMZ and HSAFt-Cu-TMZ (20 µM). The cells were exposed to the test compounds for 24 h and/or 6 days. The media was then removed, the cells were washed with ice cold PBS and fresh medium was added into the wells. Plates were incubated at 37 °C until colonies of ≥50 cells were observed in control wells. The medium was removed, colonies were washed in ice cold PBS, fixed with 100 % methanol, stained with 0.05 % methylene blue and counted. Duplicate repeats for each test agent were performed in at least three independent trials.

8. Appendices

Appendix 1.A: COVID-19 Impact statement

I started the Doctoral Training Programme (DTP) in October 2017. For most of my first year I worked on three different projects as part of three lab rotations from which I defined my PhD project, which started in May 2018. The initial idea for my PhD was to prepare a catalyst able to perform targeted prodrug activation by hydrolysis (the prodrug selected was the anticancer agent capecitabine). This project spanned different disciplines (synthesis of metal complexes, protein modification and characterisation and drug delivery in cells). Starting from the work of Distefano *et al.* the catalyst selected was copper(II)-phenanthroline, that was reported to promote the hydrolysis of non-activated esters and amides when inserted within the confined space of a protein shell (for which we selected apoferritin). According to this objective, the first few months of my PhD have been devoted to assess and improve the catalytic activity of copper(II)-phenanthroline and apoferritin copper(II)-phenanthroline. However, no significant hydrolytic activity was detected under the conditions tested. Instead copper(II)-phenanthroline demonstrated the accumulation of metal structures inside apoferritin; these complexes also have bioactivity towards cancer cells, evidence which is supported by the literature. Therefore, the following experimental phase pursued to investigate the effects of copper(II)-phenanthroline when loaded into apoferritin on its bioactivity and the interaction between the metal complex and the protein. In addition to encapsulation by diffusion, also the bioconjugation of copper(II)-phenanthroline to apoferritin was considered for study. In parallel, to address the initial vision of the PhD, I started synthesising alternative complexes for *in vivo* catalysis (based on Ru). That's when the pandemic started.

By the time the pandemic hit the experimental work performed for my PhD project was too advanced to adjust my research objectives to mitigate the lack of lab/equipment access. The experimental approach required for my research could not be reverted to computational, as the study of apoferritin requires years of training and specialist knowledge to produce doctoral-level computational data- myself or my supervisors did not have this training. I had no laboratory access from March 2020 until August 2020 which caused the loss of essential samples of apoferritin copper(II)-phenanthroline, which required 4 months of preparation for imaging. Such samples were vital to producing robust conclusions for the work described in Chapter 2 of the thesis. From August until December 2020 I could work in the lab only 50 % of the time

due to shifts to ensure a COVID-19 secure environment. I couldn't access Chemistry facilities until the beginning of September 2020 for chemical compounds characterisation, same for the nmRC (samples imaging) and I got access to BDI (for cell culture work) only in February 2021. Even then, although access was resumed the use of facilities was still restricted: direct access to instruments in Chemistry (NMR, MALDI-TOF) was only allowed to technical staff, who had stringent pressure on their time; and access to BDI was restricted by working shifts to ensure the respect of COVID safety requirements; and access to nmRC was also reduced. During this time some experimental work was performed to synthesise the ruthenium-based metal catalysts to provide an alternative to copper(II)-phenanthroline for prodrug activation, however the progress was too slow and this work was abandoned in spring 2021.

During my PhD regular travel has been essential for my personal life, because I am an international student and my partner and family live abroad (Italy). Before pandemic, I managed this situation with regular visits either from myself or from my partner. The pandemic meant that the travel disruptions prevented me from visiting my partner and family (and vice versa), so I found myself isolated at times and worried for them. This inability to travel and the uncertainty of the whole situation had therefore a non-negligible impact on my overall well-being during the last year and a half of my PhD, which affected some of my experimental progress.

Another significant disruption caused by the COVID-19 outbreak on my PhD was the cancellation of the compulsory placement (required by the BBSRC funder) that was planned to take place in a Research Institute in Basel in the summer of 2020. Extra time and resources had to be devoted to organising a new adapted placement compatible with the COVID-19 safety requirements which took place at the University of Nottingham between March and June 2021 and allowed me to spend some time working on my PhD, in parallel with the placement.

After careful evaluation with my supervisors once some experimental work could resume with certain regularity, we developed a revised experimental plan to complete the doctoral thesis which involved the significant scaling down of the original objectives to the understanding of the encapsulation of copper(II) complexes into apoferritin. The suspension of lab activities had a heavy impact on data collection for drawing robust conclusions for the thesis and meeting the minimum doctoral outcomes. To partially mitigate for the experimental inactivity caused by the lockdown I was granted a funded extension (3 months) of my BBSRC scholarship which I spent

in the lab to conclude the essential experiments to achieve the minimum doctoral objectives. This experimental work involved the optimisation of the protein bioconjugate synthesis and its tests for stability and drug release under relevant conditions for clinical application (Chapter 3). Despite the impact of the pandemic, isolation from family and partner, laboratory restrictions and experimental setbacks, with this revised experimental plan I managed to show the anticancer effect of copper(II)-phenanthroline, follow and characterise the formation of organised copper cores within apoferritin for up to 4 months under acidic conditions (pH 5.5), demonstrate the effect of apoferritin copper(II)-phenanthroline over temozolomide degradation and its anticancer effect, show that also human heavy chain apoferritin has the potential to be a valid drug delivery system for temozolomide and open to the possibility to conjugate copper(II)-phenanthroline to human apoferritin with tight control over cysteine oxidation.

Appendix 1.B: PIPS reflective statement

Note to examiners:

This statement is included as an appendix to the thesis in order that the thesis accurately captures the PhD training experienced by the candidate as a BBSRC Doctoral Training Partnership student.

The Professional Internship for PhD Students is a compulsory 3-month placement which must be undertaken by DTP students. It is usually centred on a specific project and must not be related to the PhD project. This reflective statement is designed to capture the skills development which has taken place during the student's placement and the impact on their career plans it has had.

PIPS Reflective Statement

The PIP was carried out within the Research and Innovation Department at the University of Nottingham under the supervision of Dr Maria Arruda, in the role of research officer trainee. The placement lasted from 3 months from March to June 2021 and was performed through remote working. The project I was responsible for aimed at improving the operational and strategic management of the University of Nottingham COVID-19 research asset through the promotion of internal and external communication of the University's research excellence in the COVID-19 arena. My role was to directly support the Research and Innovation team responsible for the strategic management of COVID-19 research projects lead and co-lead by the University of Nottingham and in the identification of new stakeholders. The work activities were carried out in collaboration with the office of the Pro-Vice Chancellor for Research and Knowledge Exchange, the Faculties concerned, the Global Research Themes, the Interdisciplinary Research Clusters, the University of Nottingham Beacons of Excellence, and the Executive Office.

The placement was very valuable in expanding my knowledge of the extent of the University of Nottingham research across different disciplines. This helped me in understanding and appreciating the importance of multidisciplinary collaboration between university groups, departments, faculties and with external partners. The possibility to interact with experts from all these categories has made me conscious of the importance of cultivating collaborations to promote high quality and high impact research. Even though the placement was done by remote working, the daily work was very dynamic and helped me in acquiring the ability to adapt to different challenges and to critically evaluate and look at the impact of the different research strategies adopted within the university.

The daily task performed during this placement involved: participation in meetings, comparative analyses and identification of potential research funding, preparation of Power Point presentations and reports. The experience I gained improved my collaboration skills with colleagues on tasks characterised by short-time deadlines which involved the management and the organisation of large amounts of data on research projects, funding and funding bodies. Often these data required to be collected and presented in a non-academic context. This tasks favoured the improvement of my presentation and writing skills for academic and non-academic audiences. I learned to adapt my presentation style to the different contexts which formed part of my day to day work. To conclude, this placement has given me the opportunity to have an insight on a different aspect of academia and the research work done within the University. In particular it has showed me how it is possible to (indirectly) contribute to high impact research outside the laboratory. The best part of this

Appendix 2.A: Images of HSAFt-Cu(phen) sample at pH 5.5 aged 6 months.

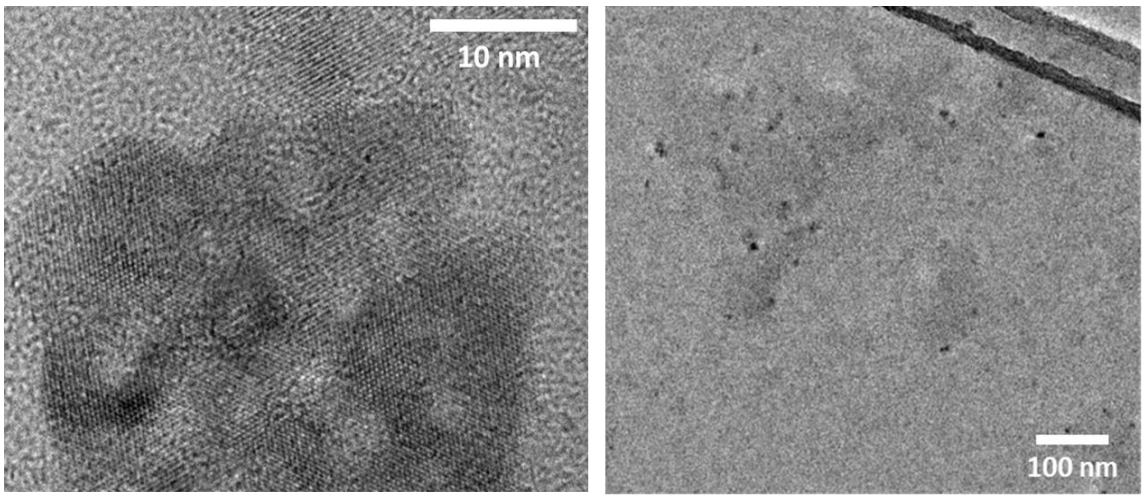

Appendix 2.B: Lattice fringes spacing estimation of the HSAFt-Cu(phen) adducts.

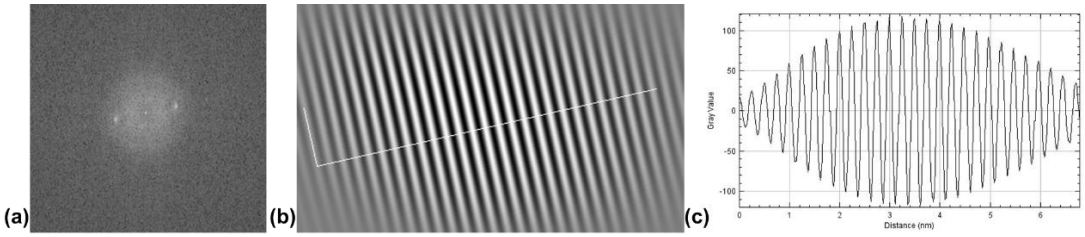

The measurement of the lattice fringes was performed using the image analysis tool ImageJ. The original image (Figure 2.9 a) was processed by Fourier transformation (a) from which a representation of the lattice fringes based on their intensity from the original image (b) was obtained. By drawing a section perpendicular to the fringes on image b it is possible to produce a plot with the intensity profile of the fringes (c). The number of peaks shown on the plot corresponds to the number of fringes present in the perpendicular segment drawn. The ratio between the line length (nm) and the number of peaks gives the nm estimate of the atoms spacing which can be used to determine the unit cell arrangement.

Appendix 2.C: UV-vis spectra of the HSAFt-Cu(phen) dialysis solutions of the release test at pH 7.4

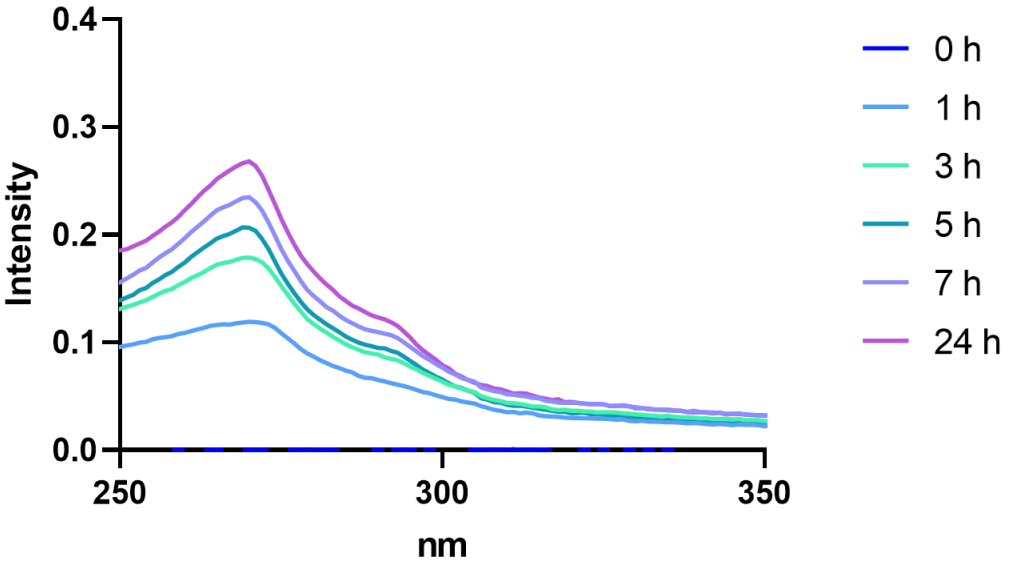

Appendix 2.D: UV-vis spectra of the HSAFt-Cu(phen) dialysis solutions of the release test at pH 5.5

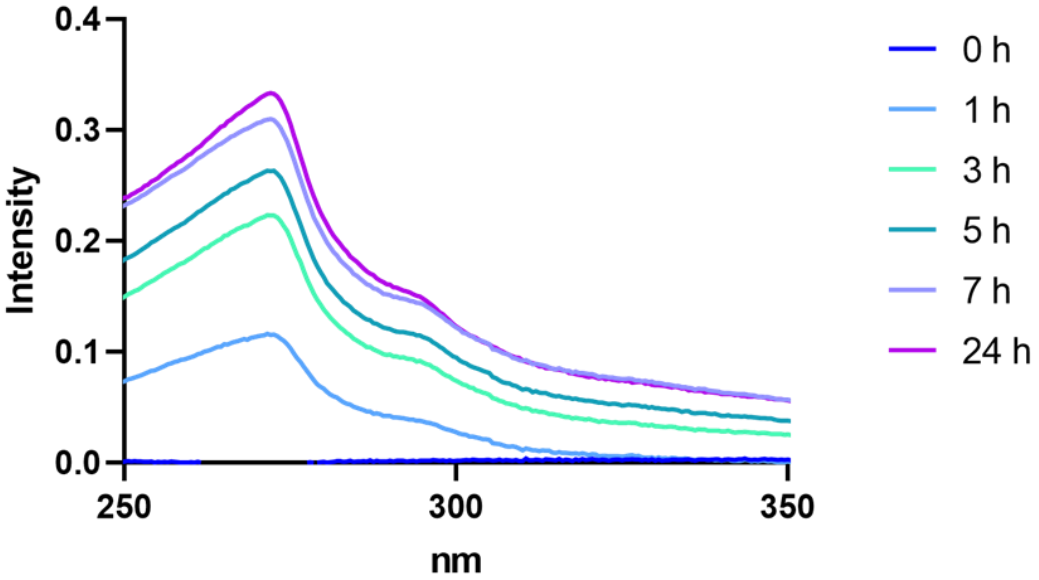

Appendix 3.A: Reference curve for TMZ, AFt-TMZ and table of the λ_{max} wavelengths for TMZ, Cu-MTIC and the metabolite AIC.

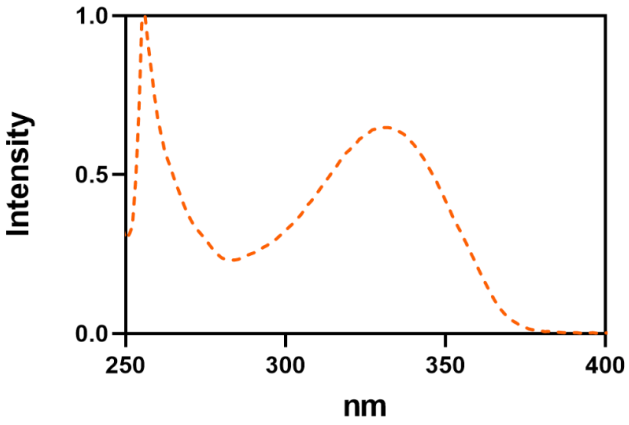

Name	Structure	λ_{max} (nm)
TMZ	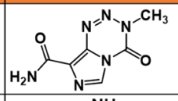	330
AIC	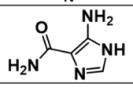	265
Cu-MTIC	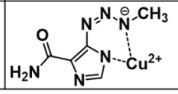	355

Appendix 3.B: Estimation of TMZ loaded in HSAFt-Cu(phen)-TMZ cages, encapsulation efficiency and drug loading

The estimation of the TMZ retained inside the AFt-Cu(phen)-TMZ performed using the intensity of the sample at 330 nm (TMZ λ_{max}) and the extinction coefficient of the loaded agent (9800 M^{-1} cm^{-1}) factored into the Beer-Lambert equation:

$$A = \varepsilon l c$$

Where *A* is the intensity at λ_{max}, ε is the extinction coefficient of TMZ, *l* is the cuvette path (1 cm) and *c* is the estimated TMZ concentration. For the estimate to be accurate the intensity used in the equation was the difference (grey line) between the intensity of the AFt-Cu(phen)-TMZ sample and that of the precursor AFt-Cu(phen) sample at equal concentration (0.5 mg/mL) and in NaOAc buffer (0.1 M, pH 5.5) as shown in the graph below:

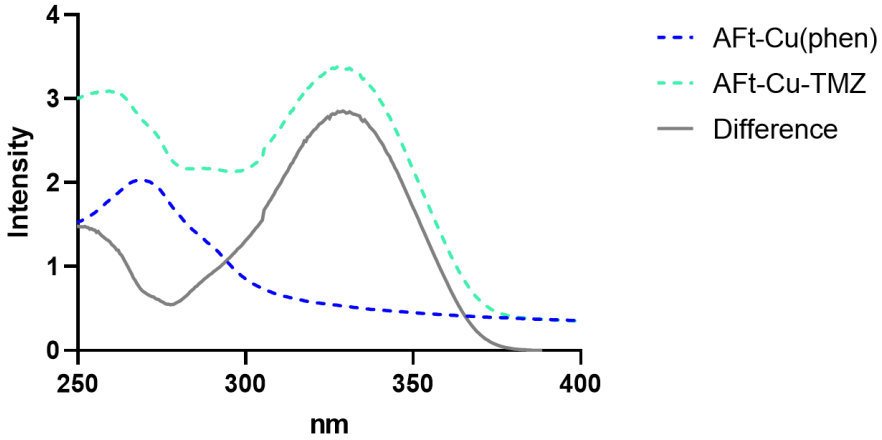

These calculations were performed for 4 independent encapsulation experiments. Once the concentration of TMZ into AFt-Cu(phen)-TMZ samples was estimated it was possible to calculate the TMZ: AFt ratio as follows:

$$TMZ{:}\,AFt = \frac{Final\ moles\ of\ TMZ\ in\ solution}{Final\ moles\ of\ AFt\ in\ solution}$$

Appendix 3.C: Encapsulation efficiency and drug loading of HSAFt-Cu(phen)-TMZ cages

The calculations for TMZ encapsulation efficiency (EE) and drug loading (DL) were performed using the following equations:[138]

$$EE\ (\%) = \frac{Final\ amount\ of\ drug\ (moles)}{Initial\ amount\ of\ drug\ (moles)} \times 100\%$$

$$DL\ (\%) = \frac{(Number\ of\ drugs\ encapsulated\ \times Drug\ MW)}{((Number\ of\ drugs\ encapsulated\ \times Drug\ MW) + AFt\ MW)} \times 100\%$$

Appendix 3.D: UV-vis spectra of the HSAFt-Cu(phen)-TMZ dialysis solutions of the release test at pH 7.4.

The experiments were performed as three independent replicates. AFt-Cu(phen)-TMZ samples with different AFt concentrations were used for each replicate, thus explaining the variability in the AUC observed between replicates tested for the two pH conditions.

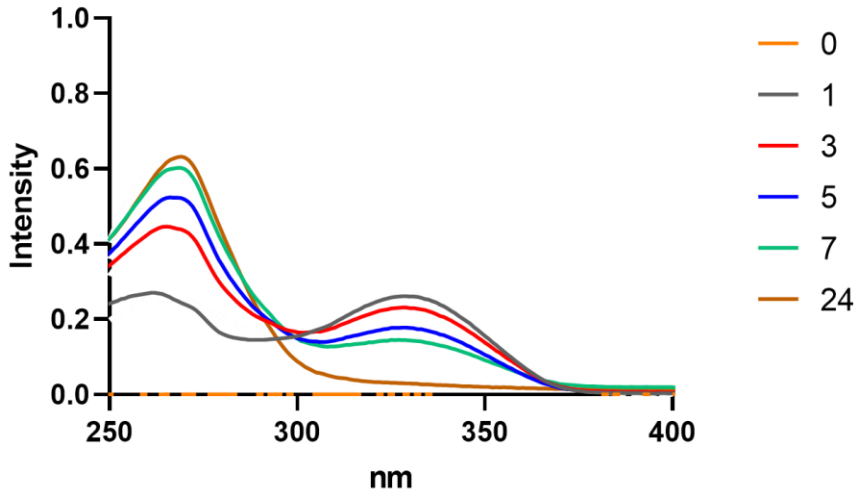

Appendix 3.E: UV-vis spectra of the HSAFt-Cu(phen)-TMZ dialysis solutions of the release test at pH 5.5.

The experiments were performed as three independent replicates. AFt-Cu(phen)-TMZ samples with different AFt concentrations were used for each replicate, thus explaining the variability in the AUC observed between replicates tested for the two pH conditions.

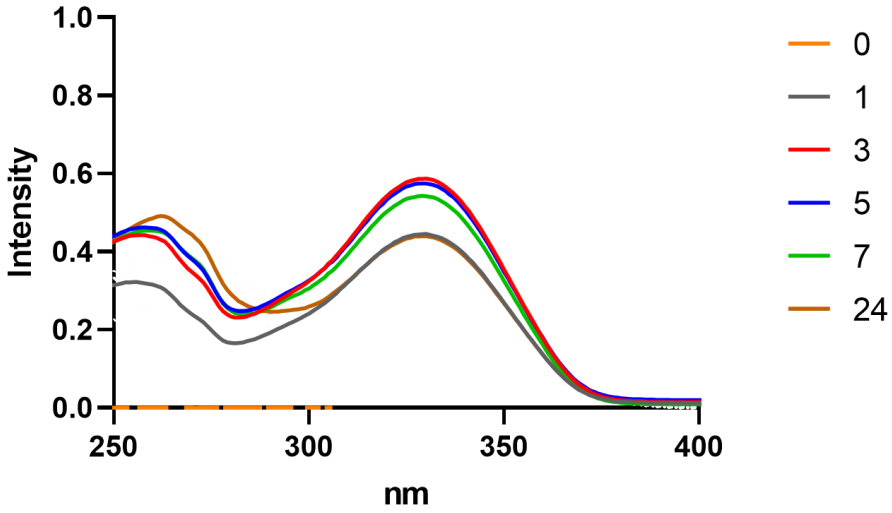

Appendix 3.F: HSAFt-Cu(phen)-TMZ stability test: curve fitting and peak integration analysis.

To estimate the release of TMZ from the AFt-Cu(phen)-TMZ exposed to pH 7.4 and pH 5.5 at 37 ºC for up to 24 h the integrated absorbances at the maximum of 330 nm were calculated. The estimation method was based on the direct correlation between

concentration and absorbance expressed in the Beer-Lambert law. The method was developed to produce the closest curve-fit with the software GraphPad Prism and then use those best-fit values on Origin for peak integration. The percentage of TMZ release in the dialysis buffer was calculated from the integration results, using the absorbance at 330 nm of the initial AFt-Cu(phen)-TMZ sample equivalent to 100 % TMZ. The same method was employed to quantify the ratio of released TMZ converted over time into AIC, using the absorbaces at 265 nm for peak integration. Each step of this method is shown below using the UV-vis spectrum of the dialysis sample taken after 3 h of incubation at pH 7.4 (Appendix 3.D, red line) as example.

The first step for the estimation of TMZ % release consisted in performing a non-linear regression analysis on the raw data (UV-vis spectrum collected at 3 h) using GraphPad Prism. The UV-vis measurements included to produce the model were between 250 to 400 nm and the absorbances at 265 nm and 330 nm were kept as fixed parameters. The GraphPad analysis produced a series of best-fit values which formed an ideal curve (Figure 1) which was used in the next step for peak integration in Origin.

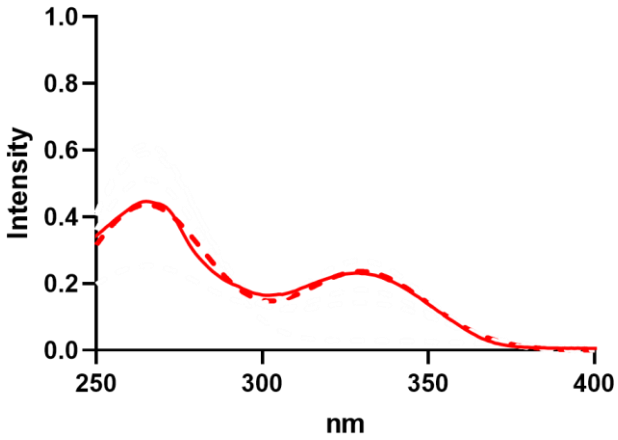

Figure 1. UV-vis spectrum (full red line) and curve-fit (red dashed line) of the absorbance measured on the dialysis buffer at 3 h of incubation of AFt-Cu(phen)-TMZ in PBS pH 7.4.

The XY data generated by the curve-fitting in GraphPad were exported into Origin to perform the peak integration using the Peak Analyzer function. The integration was automatically executed by the software upon definition of the 'Integrate Peaks' as the goal of the analysis. The peak baseline was identified using the minimum Y value and the graph was rescaled accordingly. Once the baseline was defined, the peaks were identified using the 'Local Maximum' method, which compared the neighbouring Y

values to find the maximum. In this case the maxima were always identified as 265 nm and 330 nm as expected. At this point the peak integration was performed by Origin using the set baseline and the peak width (which was determined automatically) with the drop perpendicular method to separate the areas of the two peaks (Figure 2).

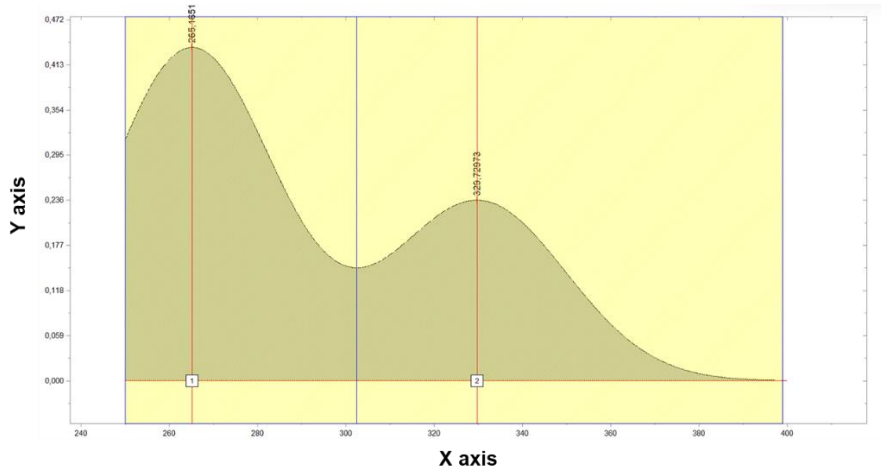

Figure 2. Peak integration on the curves produced by GraphPad using Origin.

When the Peak Analyzer function is employed in Origin, the output of the peak integration includes the area under the curve but also the full width at half maximum (FWHM) and the height (Table 1).

Long Name	Index	Area	AreaIntgP(%)	Row Index	Beginning X	Ending X	FWHM	Center	Height
Units									
Comments	Integral Result of C	Integral Result of C	Integral Result of C	Integral Result of C	Integral Result of C	Integral Result of C	Integral Result of C	Integral Result of C	Integral Result of C
F(x)=									
1	1	16,54845	59,82327	102	250	302,4024	39,04769	265,16517	0,43541
2	2	11,11373	40,17656	532	302,4024	398,94895	50,74685	329,72973	0,23564

Table 1. Output values generated by Origin for the peak integration analysis.

The height of the integrated peak was then used as the absorbance value for the estimation of the % of TMZ released in solution. As mentioned in the paragraph above, the direct correlation between absorbance and concentration established by the Beer-Lambert law allowed for the direct comparison of the integrated peak height and the absorbance of the AFt-Cu(phen)-TMZ sample analysed (100 %). The calculation of the % release was performed using the peak at 330 nm (center= 329.7) for TMZ and that at 265 nm (center= 265.1) for AIC as illustrated in the formula below:

$$\%\ Drug\ release = \frac{Integrated\ peak\ height}{Dyalised\ sample\ absorbance} \times 100$$

Appendix 4.A: UV-vis spectra of the HuHAFt after encapsulation with Cu(phen) at pH 5.5 and of HSAFt-Cu(phen) from Chapter 2 at 1 μM.

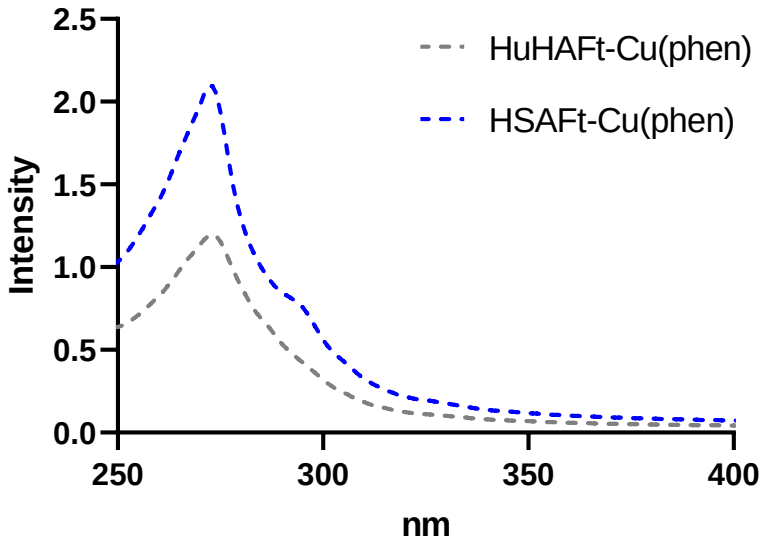

Appendix 4.B: AFt_K68C His plasmid and sequence.

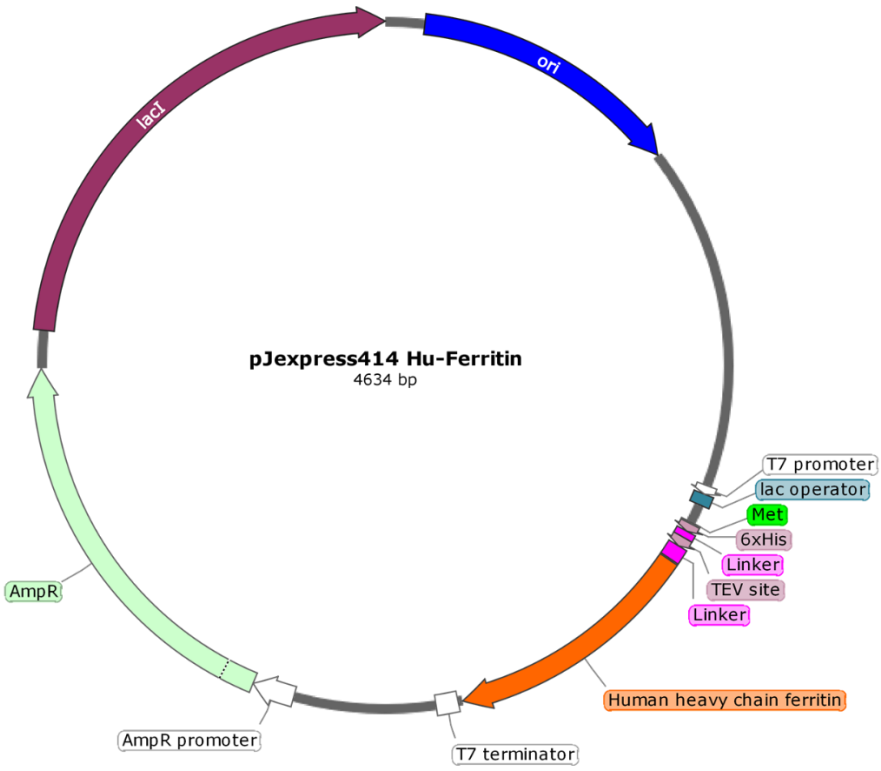

Nucleotide sequence

ATGCATCATCATCACCACCATAGCAGCGGTGGCTCTGAAAATCTGTATTTTCAGTCTAC
CGGTAGCGGCGGTGGTGGTTCTGGCGGATCCATGACCACTGCTAGCACCAGCCAAGT
CCGCCAAAACTATCACCAGGACAGCGAGGCGGCAATCAACCGTCAAATCAACTTGGAG
CTGTACGCGAGCTATGTTTACCTGAGCATGTCTTACTATTTCGACCGCGACGATGTCGC
ACTGAAGAACTTTGCGAAGTATTTCCTGCACCAGTCCCATGAAGAACGCGAGCACGCC
GAG**TGC**CTGATGAAACTGCAGAACCAGCGTGGCGGTCGTATCTTTCTGCAAGACATTA
AGAAACCGGATCGCGATGATTGGGAGTCGGGCCTGAATGCCATGGAAGCTGCCCTGC
ACTTGGAGAAGAATGTGAACCAAAGCTTGCTGGAGCTGCACAAACTGGCGACGGACAA
GAATGACCCGCACCTGAGCGATTTCATTGAAACCCATTACCTGAATGAGCAGGTTAAAG
CGATCAAAGAACTGGGCGACCATGTTACGAACCTGCGTAAGATGGGTGCGCCGGAGT
CCGGTCTGGCTGAGTACTTGTTCGATAAACATACCCTGGGCGACAGCGATAATGAGAG
CTAA

Peptide sequence

MHHHHHHSSGGSENLYFQSTGSGGGGSGGSMTTASTSQVRQNYHQDSEAAINRQINLEL
YASYVYLSMSYYFDRDDVALKNFAKYFLHQSHEEREHAE**C**LMKLQNQRGGRIFLQDIKKPD
RDDWESGLNAMEAALHLEKNVNQSLLELHKLATDKNDPHLSDFIETHYLNEQVKAIKELGD
HVTNLRKMGAPESGLAEYLFDKHTLGDSDNES

His-tag TEV protease cleavage site Amino acid linker **Mutation site**

Appendix 4.C: SDS-PAGE of AFt_K68C His elution of the purified soluble fraction.

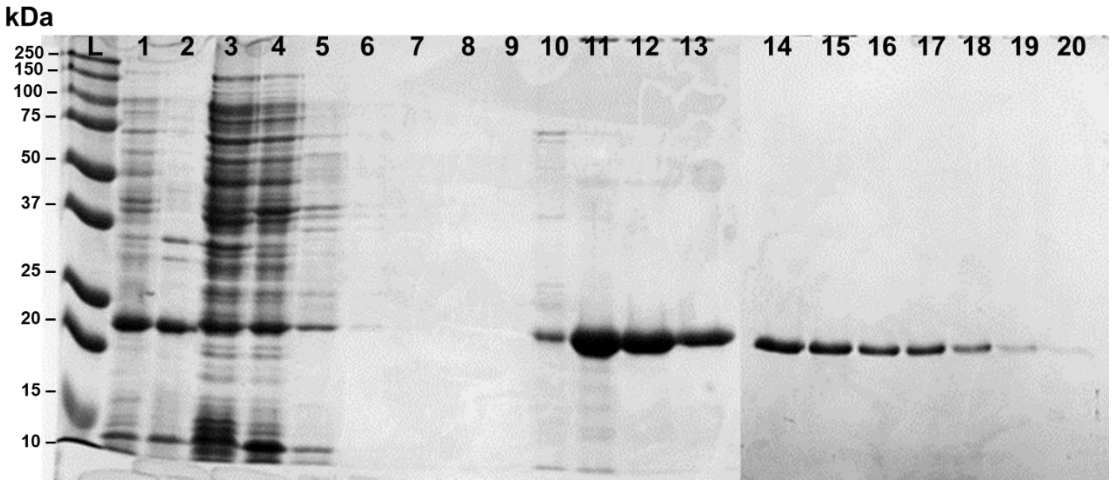

L= protein marker, 1= soluble fraction, 2= insoluble fraction, 3= flow-through, 4= column wash, 5-7= fractions eluted at 30 % imidazole, 8-16= fractions eluted at 60 % imidazole containing

24 kDa recombinant AFt_K68C His, 17-20= fractions eluted at 100 % imidazole (0.8 M) containing 24 kDa recombinant AFt_K68C His.

Appendix 4.D: Purified AFt_WT His and AFt_K68C His SDS-PAGE showing high concentration of degradation products.

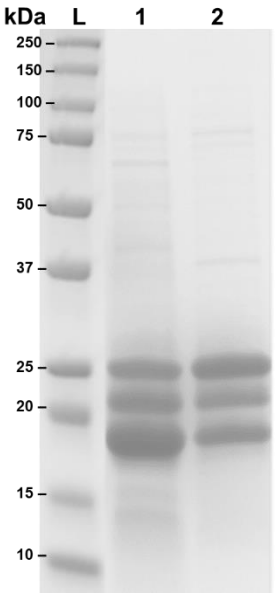

L= protein marker, 1= AFt_WT His, 2= AFt_K68C His.

Appendix 4.E: TEV elution of the purified soluble fraction and separation from the cleaved MBP.

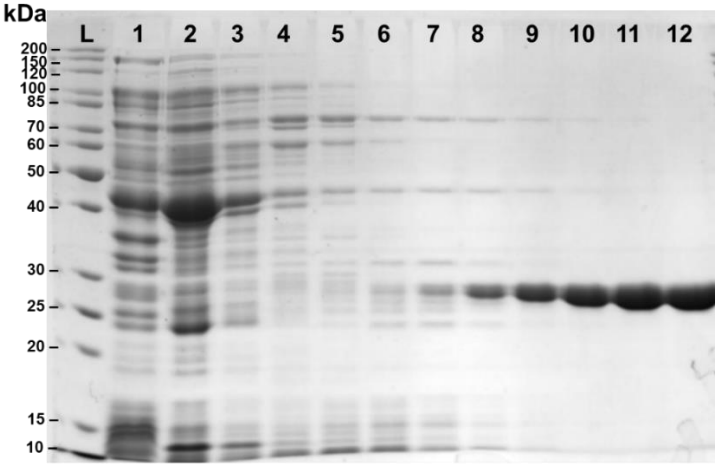

L= protein marker, 1= insoluble fraction, 2= soluble fraction, 3= flow-through, 1-14= fractions eluted by gradient to 100 % imidazole (250 mM) containing the MBP fusion protein (49 kDa) and/or TEV (28 kDa).

Appendix 4.F: AFt_K68C purification by affinity chromatography after reaction with the TEV protease.

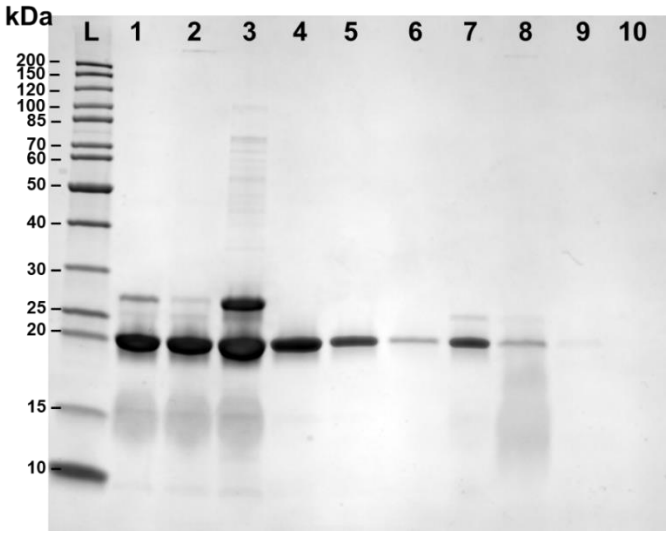

L= protein marker, 1= reaction at T_0 showing TEV (28 kDa), AFt_K68C His (24 kDa) and AFt_K68C (22 kDa), 2= reaction at T_{3h} showing TEV and AFt_K68C, 3= precipitate from reaction containing TEV and AFt_K68C, 4= flow-through containing AFt_K68C, 5= column wash containing AFt_K68C, 6-10= fractions eluted at 100 % imidazole (0.8 M) containing AFt_K68C His and AFt_K68C.

Appendix 4.G: Ellmann's assay to test the reactivity of reducing agents with DTNB.

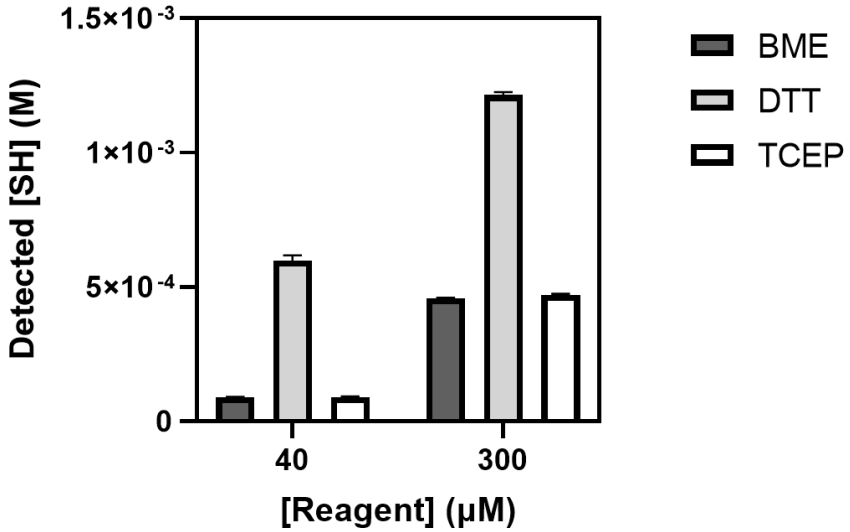

Appendix 4.H: UV-vis spectra of stock solutions 2-bromo-*N*-(1,10-phenanthrolin-5-yl)acetamide in 20 mM Tris pH 8.5.

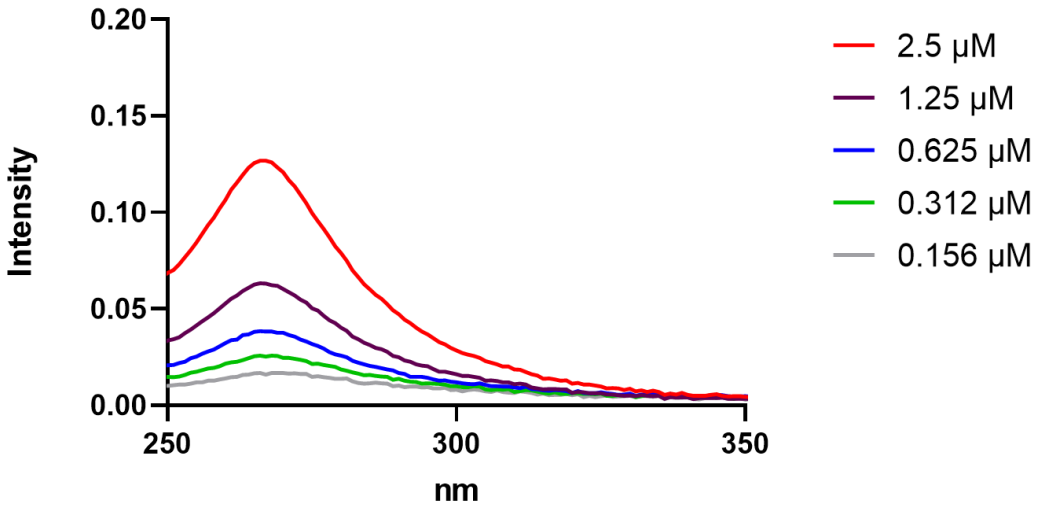

Appendix 4.I. MALDI-TOF spectra of HuHAFt species with Myoglobin calibrant.

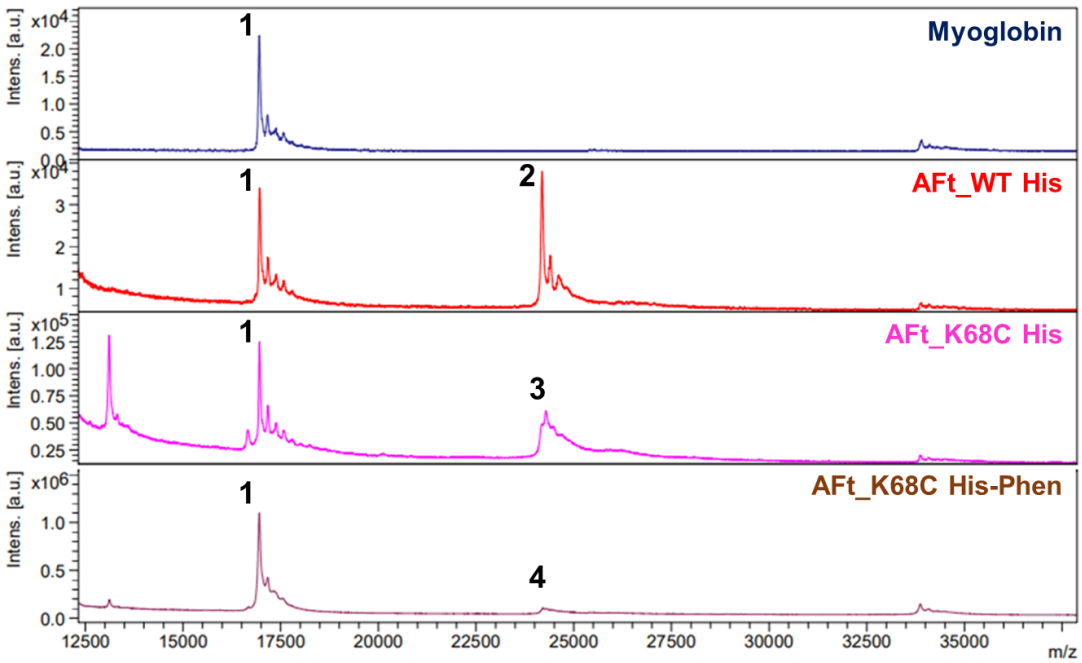

Peak 1= 16952.3 Da, Myoglobin standard 1 mg/mL; Peak 2= 24189.3 Da, AFt_WT His sample at 1.7 mg/mL; Peak 3= 24286.6 Da, AFt_K68C His sample at 1 mg/mL; Peak 4= 24206 Da, AFt_K68C His-Phen sample at 1 mg/mL.

Appendix 4.L. Calculation of the extinction coefficient of 2-bromo-*N*-(1,10-phenanthrolin-5-yl)acetamide and estimation of its concentration in solution

The estimation of the extinction coefficient of 2-bromo-*N*-(1,10-phenanthrolin-5-yl)acetamide was based on the absorbance at 266 nm measured on stock solutions at increasing concentrations of the compound (n= 3, media= milliQ-H_2O).

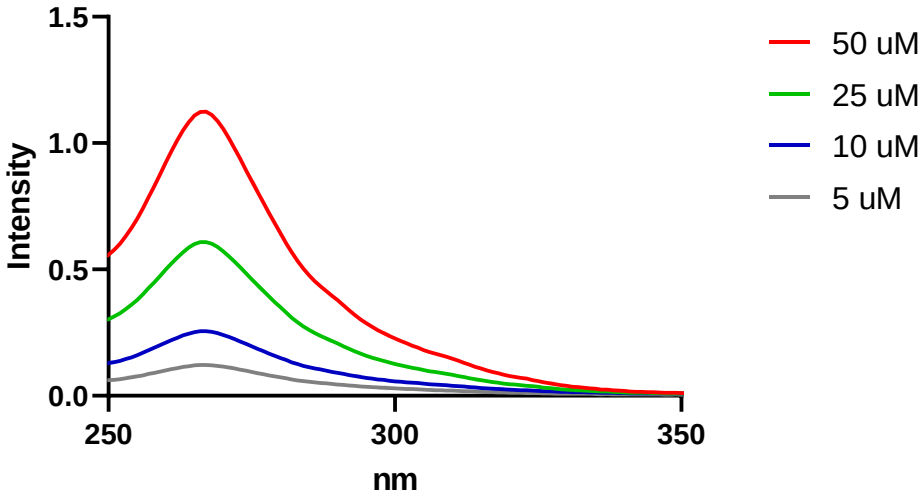

The mean on the intensity at each concentration was used to plot a curve to correlate intensity with concentration in a simple linear regression using the function from GraphPad Prism (Figure 1).

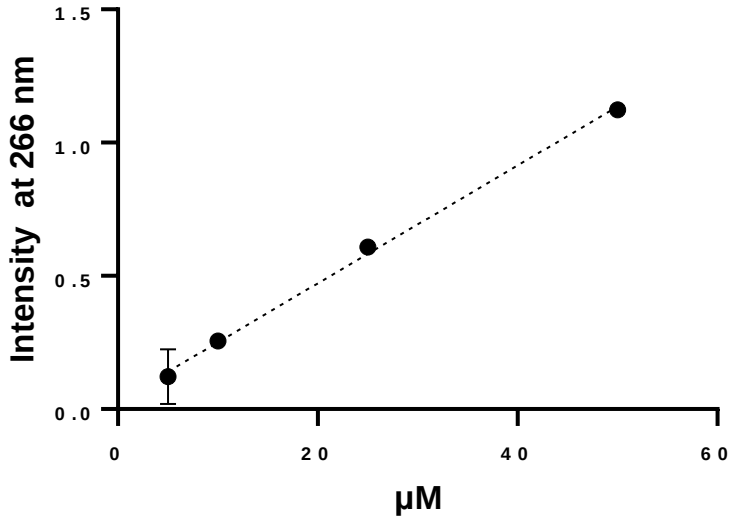

The linear regression confirmed the linear relationship between the intensity at 266 nm and the concentration of the ligand. To estimate the extinction coefficient the following equation was used on the intensity replicates:

$$\varepsilon_{ligand} = \frac{(Abs2 - Abs1)}{(Conc.2 - Conc.1)}$$

Where: Abs_2 = intensity at higher concentration, Abs_1 = intensity at lower concentration, $Conc._1$ = higher concentration, $Conc._2$ = lower concentration.

The calculation of the extinction coefficient allowed for the estimation of the phenanthroline ligand concentration in the AFt_K68C-Phen bioconjugation reaction. The UV intensity recorded for the AFt_K68C-Phen sample at 266 nm was subtracted with the intensity produced by the AFt_K68C spectrum at the same concentration (assessed by Bradford) and used in the Beer Lambert law as follows:

$$c = A/\varepsilon l$$

Where c = phenanthroline ligand molar concentration, A= $Abs_{AFt\_K68C\text{-}Phen} - Abs_{AFt\_K68C}$, Ɛ = extinction coefficient of phenanthroline ligand, l= cuvette path length.

Appendix 7.A: ESI spectrum of copper-1,10-phenanthroline

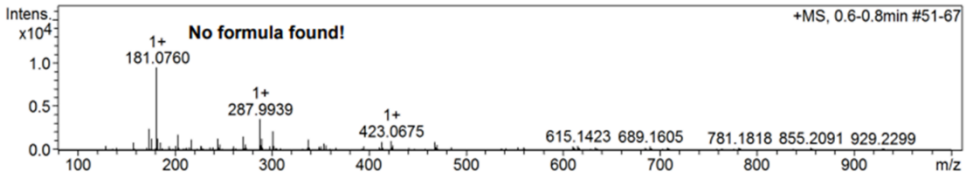

#	m/z	I %	
1	157.0826	9.5	
2	173.0778	25.7	
3	176.1285	13.9	
4	181.0760	100.0	← 1,10-phen ligand
5	182.0782	14.2	
6	185.1127	9.5	
7	203.0587	18.7	
8	217.1049	13.2	
9	244.0039	13.9	← M+H
10	246.0035	6.9	
11	271.0024	16.7	
12	273.0021	7.3	
13	287.9939	37.6	
14	289.9918	14.0	
15	301.1398	23.1	
16	338.1135	13.2	
17	353.9670	8.4	
18	413.2691	10.0	
19	423.0675	11.4	← M+ 2 DMSO+ Na
20	468.0649	10.2	

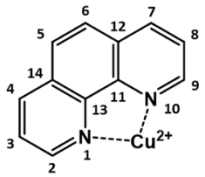

Appendix 7.B: UV-vis spectrum of copper-1,10-phenanthroline

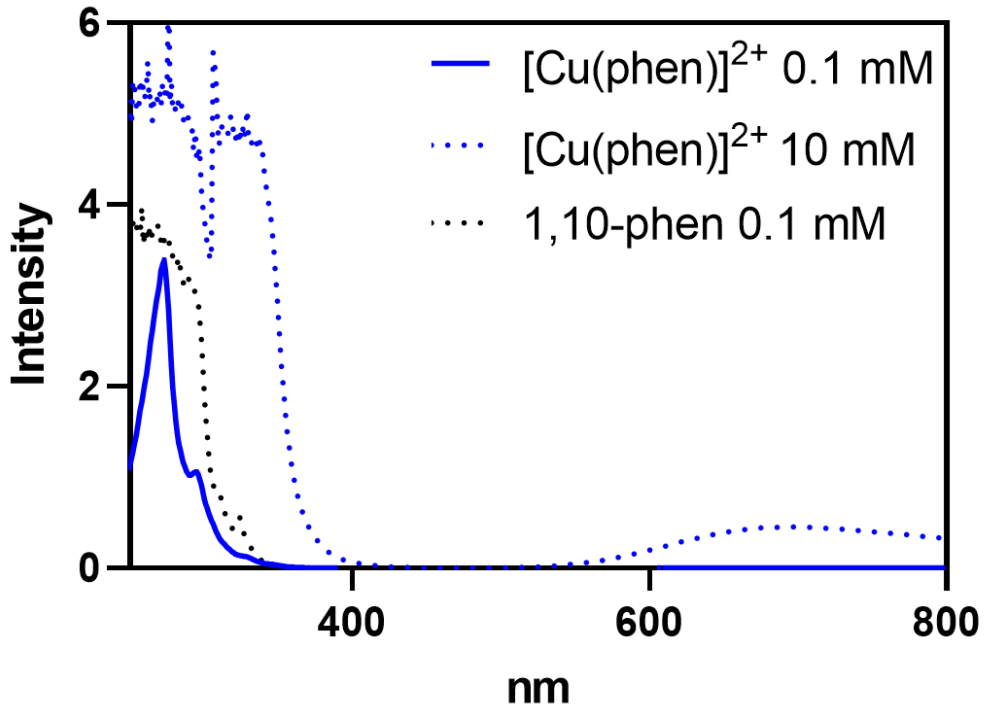

Appendix 7.C: ESI and ^{1}HNMR spectra of 2-bromo-*N*-(1,10-phenanthrolin-5-yl)acetamide

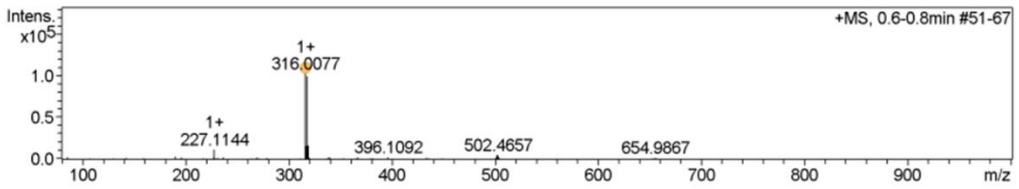

#	m/z	I %
1	85.0591	2.5
2	190.0893	3.2
3	227.1144	11.3
4	236.0815	2.3
5	316.0077	100.0
6	317.0107	15.5
7	318.0063	97.0
8	319.0087	16.3
9	337.9901	2.3
10	339.9884	2.3
11	367.1691	2.2
12	396.1092	2.6
13	433.1758	1.9
14	500.4681	1.7
15	501.4673	4.8
16	501.9682	2.4
17	502.4657	4.9
18	502.9668	2.4
19	503.4662	2.0
20	654.9867	1.9

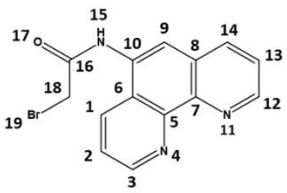

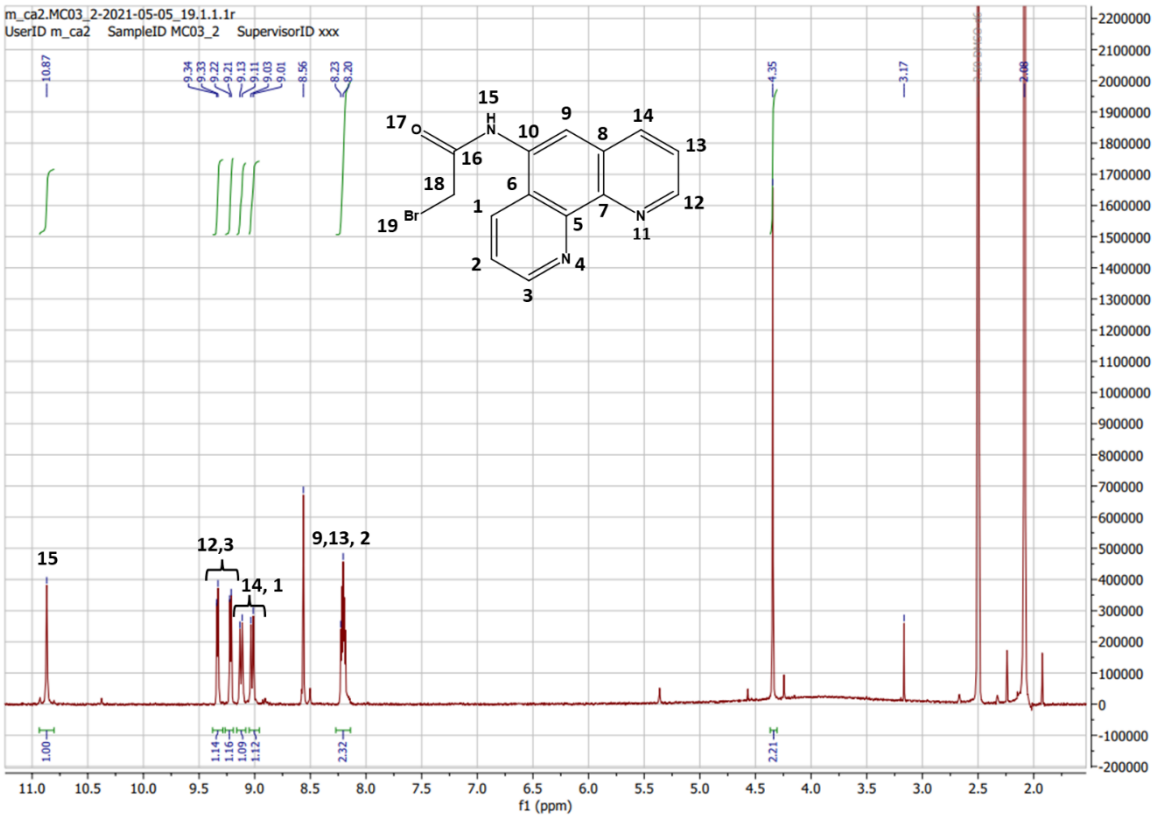

Appendix 7.D: ESI and ^{1}HNMR spectra of *N*-methyl-*N*-phenylpicolinamide

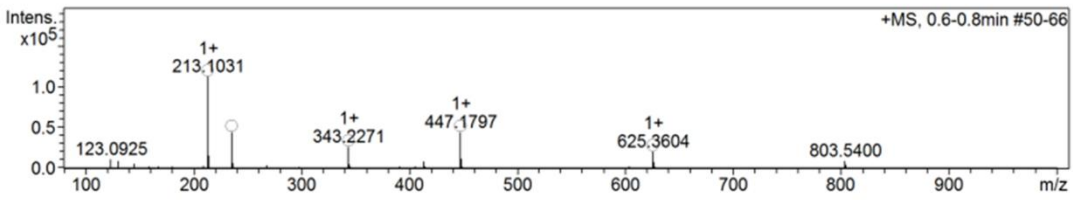

#	m/z	I %
1	123.0925	9.8
2	130.1589	8.0
3	145.1335	5.2
4	167.1148	2.4
5	180.1010	2.5
6	209.0245	3.1
7	213.1031	100.0
8	214.1047	13.9
9	235.0840	39.2
10	236.0874	5.8
11	268.1320	3.5
12	343.2271	23.5
13	344.2290	4.7
14	413.2655	7.5
15	447.1797	39.4
16	448.1824	10.6
17	625.3604	18.1
18	626.3634	7.3
19	803.5400	8.1
20	804.5453	4.1

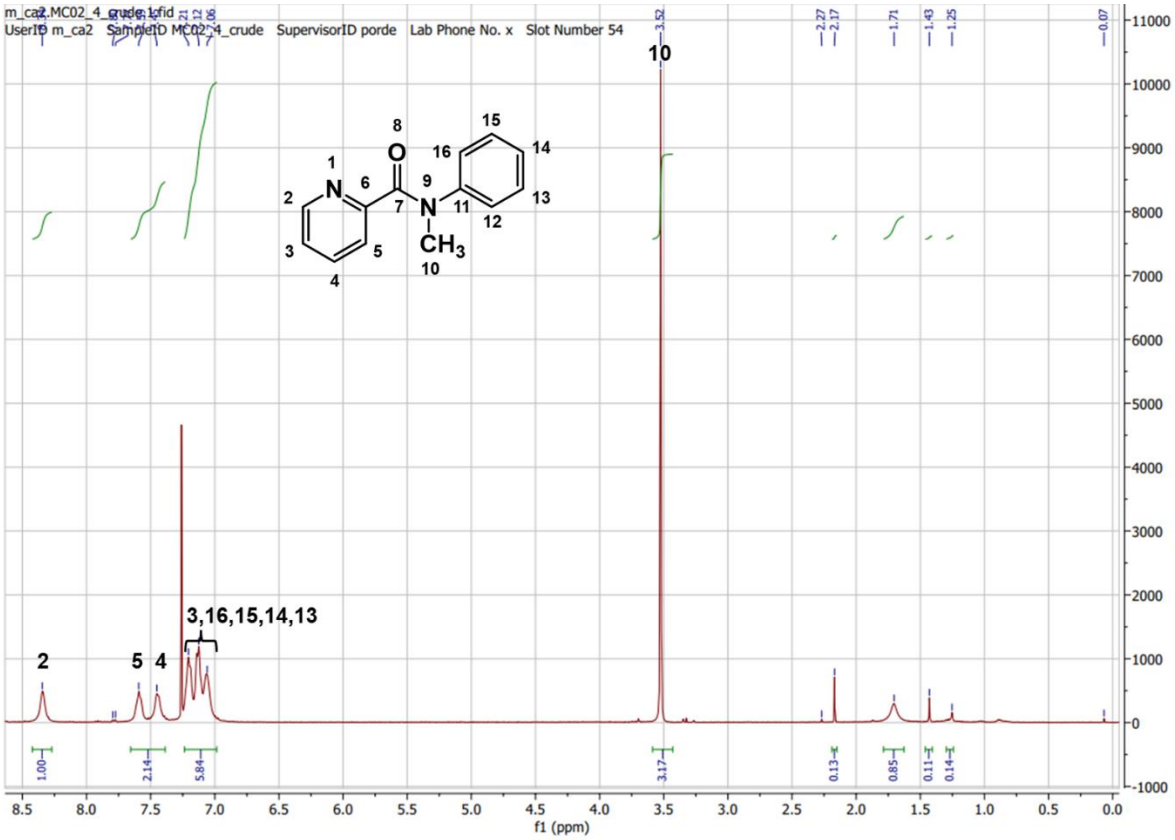

Appendix 7.E: ^{1}HNMR spectra of ethyl-N-phenylcarbamate

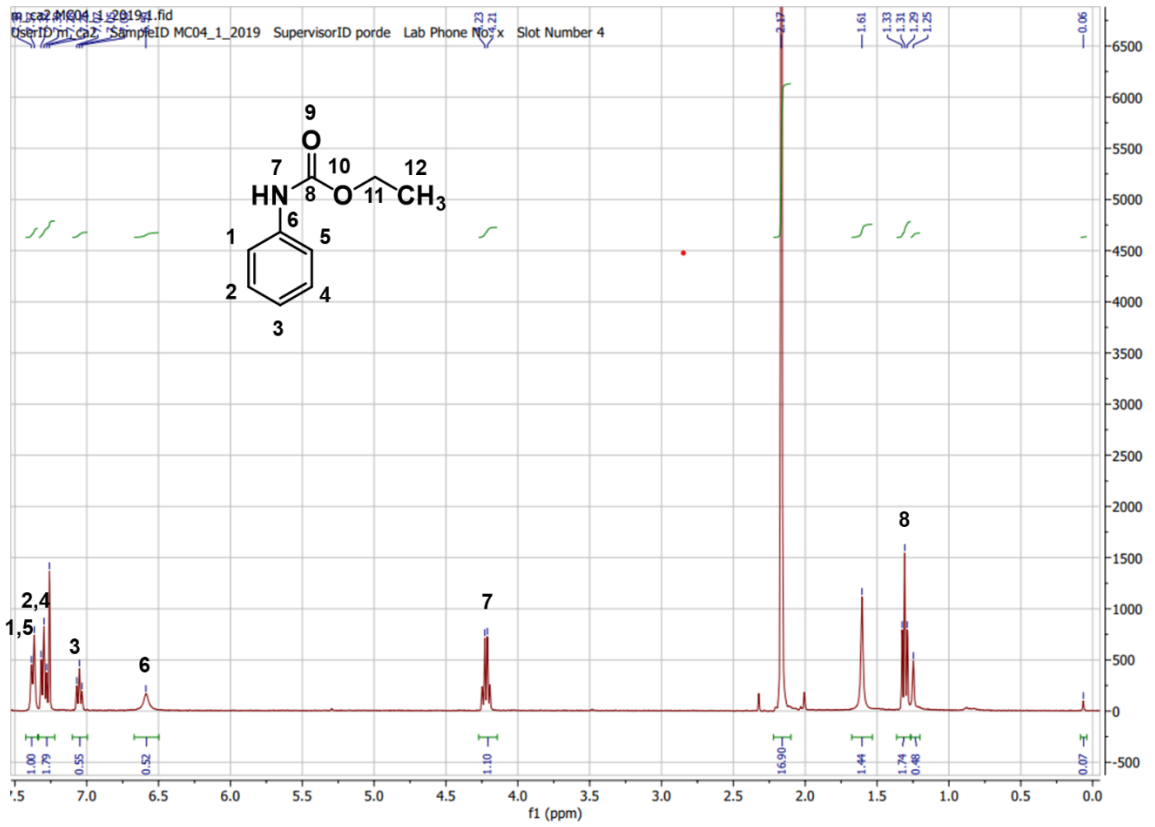

9. References

1 S. Hombach-Klonisch, M. Mehrpour, S. Shojaei, C. Harlos, M. Pitz, A. Hamai, K. Siemianowicz, W. Likus, E. Wiechec, B. D. Toyota, R. Hoshyar, A. Seyfoori, Z. Sepehri, S. R. Ande, F. Khadem, M. Akbari, A. M. Gorman, A. Samali, T. Klonisch and S. Ghavami, Glioblastoma and chemoresistance to alkylating agents: Involvement of apoptosis, autophagy, and unfolded protein response, *Pharmacol. Ther.*, 2018, **184**, 13–41.

2 F. Yun, H. Honghui, G. Jing and L. Shizhu, Effect of temozolomide combined with radiotherapy on survival and MGMT protein expression in recurrent malignant glioma patients, *Trop. J. Pharm. Res.*, 2018, **18**, 857–862.

3 Cancer Research UK, Temozolomide (Temodal), https://www.cancerresearchuk.org/about-cancer/cancer-in-general/treatment/cancer-drugs/drugs/temozolomide.

4 T. C. Johnstone, K. Suntharalingam and S. J. Lippard, The Next Generation of Platinum Drugs: Targeted Pt(II) Agents, Nanoparticle Delivery, and Pt(IV) Prodrugs, *Chem. Rev.*, 2016, **116**, 3436–3486.

5 D. Lombardo, M. A. Kiselev and M. T. Caccamo, Smart Nanoparticles for Drug Delivery Application: Development of Versatile Nanocarrier Platforms in Biotechnology and Nanomedicine, *J. Nanomater.*, 2019, **2019**, 26.

6 B. Zhang, G. Tang, J. He, X. Yan and K. Fan, Ferritin nanocage: A promising and designable multi-module platform for constructing dynamic nanoassembly-based drug nanocarrier, *Adv. Drug Deliv. Rev.*, 2021, **176**, 113892.

7 B. Tesarova, K. Musilek, S. Rex and Z. Heger, Taking advantage of cellular uptake of ferritin nanocages for targeted drug delivery, *J. Control. Release*, 2020, **325**, 176–190.

8 X. Li, F. Shao, J. Sun, K. Du, Y. Sun and F. Feng, Enhanced Copper-Temozolomide Interactions by Protein for Chemotherapy against Glioblastoma Multiforme, *ACS Appl. Mater. Interfaces*, 2019, **11**, 41935−41945.

9 World Health Organisation, Cancer, https://www.who.int/news-room/fact-sheets/detail/cancer.

10 H. Sung, J. Ferlay, R. L. Siegel, M. Laversanne, I. Soerjomataram, A. Jemal and F. Bray, Global Cancer Statistics 2020: GLOBOCAN Estimates of Incidence and Mortality Worldwide for 36 Cancers in 185 Countries, *CA. Cancer J. Clin.*, 2021, **71**, 209–249.

11 T. Dyba, G. Randi, F. Bray, C. Martos, F. Giusti, N. Nicholson, A. Gavin, M. Flego, L. Neamtiu, N. Dimitrova, R. Negrão Carvalho, J. Ferlay and M. Bettio, The European cancer burden in 2020: Incidence and mortality estimates for 40 countries and 25 major cancers, *Eur. J. Cancer*, 2021, **157**, 308–347.

12 International Agency for Research on Cancer (WHO), Estimated number of deaths in 2020, worldwide, both sexes, all ages (excl. NMSC).

13 S. M. Ansell, A. M. Lesokhin, I. Borrello, A. Halwani, E. C. Scott, M. Gutierrez, S. J. Schuster, M. M. Millenson, D. Cattry, G. J. Freeman, S. J. Rodig, B. Chapuy, A. H. Ligon, L. Zhu, J. F. Grosso, S. Y. Kim, J. M. Timmerman, M. A. Shipp and P. Armand, PD-1 Blockade with Nivolumab in Relapsed or Refractory Hodgkin's Lymphoma, *N. Engl. J. Med.*, 2014, **372**, 311–319.

14 H. Shi, W. Hugo, X. Kong, A. Hong, R. C. Koya, G. Moriceau, T. Chodon, R. Guo, D. B. Johnson, K. B. Dahlman, M. C. Kelley, R. F. Kefford, B. Chmielowski, J. A. Glaspy, J. A. Sosman, N. Van Baren, G. V Long, A. Ribas and R. S. Lo, Acquired resistance and clonal evolution in melanoma during BRAF inhibitor therapy, *Cancer Discov.*, 2014, **4**, 80–93.

15 B. G. Childs, M. Durik, D. J. Baker and J. M. Van Deursen, Cellular senescence in aging and age-related disease: From mechanisms to therapy, *Nat. Med.*, 2015, **21**, 1424–1435.

16 L. Bunton, B. A. Chabner and B. C. Knollmann, Eds., *Goodman & Gilman's The Pharmacological Basis of Therapeutichs*, McGraw-Hill, New York, 12th edn., 2011.

17 C. Holohan, S. Van Schaeybroeck, D. B. Longley and P. G. Johnston, Cancer drug resistance: an evolving paradigm, *Nat. Rev. Cancer*, 2013, **13**, 714–726.

18 M. W. Tibbitt, J. E. Dahlman and R. Langer, Emerging Frontiers in Drug Delivery, *J. Am. Chem. Soc.*, 2016, **138**, 704–717.

19 S. M. Meier-Menches and A. Casini, Design Strategies and Medicinal

Applications of Metal-Peptidic Bioconjugates, *Bioconjug. Chem.*, 2020, **31**, 1279–1288.

20 K. Hajnal, H. Gabriel, R. Aura, V. Erzsébet and S. S. Blanka, Prodrug Strategy in Drug Development, *Acta Medica Marisiensis*, 2016, **62**, 356–362.

21 R. Walther, J. Rautio and A. N. Zelikin, Prodrugs in medicinal chemistry and enzyme prodrug therapies, *Adv. Drug Deliv. Rev.*, 2017, **118**, 65–77.

22 S. Zhang, A. M. Bellinger, D. L. Glettig, R. Barman, Y. A. L. Lee, J. Zhu, C. Cleveland, V. A. Montgomery, L. Gu, L. D. Nash, D. J. Maitland, R. Langer and G. Traverso, A pH-responsive supramolecular polymer gel as an enteric elastomer for use in gastric devices, *Nat. Mater.*, 2015, **14**, 1065–1071.

23 R. Tong, H. D. Hemmati, R. Langer and D. S. Kohane, Photoswitchable nanoparticles for triggered tissue penetration and drug delivery, *J. Am. Chem. Soc.*, 2012, **134**, 8848–8855.

24 Y. Matsumura and H. Maeda, A New Concept for Macromolecular Therapeutics in Cancer Chemotherapy: Mechanism of Tumoritropic Accumulation of Proteins and the Antitumor Agent Smancs, *Cancer Res.*, 1986, **46**, 6387–6392.

25 H. Cabral and K. Kataoka, Progress of drug-loaded polymeric micelles into clinical studies, *J. Control. Release*, 2014, **190**, 465–476.

26 H. Kobayashi, R. Watanabe and P. L. Choyke, Improving conventional enhanced permeability and retention (EPR) effects; What is the appropriate target?, *Theranostics*, 2014, **4**, 81–89.

27 R. van der Meel, L. J. C. Vehmeijer, R. J. Kok, G. Storm and E. V. B. van Gaal, Ligand-targeted particulate nanomedicines undergoing clinical evaluation: Current status, *Adv. Drug Deliv. Rev.*, 2013, **65**, 1284–1298.

28 M. Swierczewska, S. Lee and X. Chen, Inorganic nanoparticles for multimodal molecular imaging, *Mol. Imaging*, 2011, **10**, 3–16.

29 J. J. Giner-Casares, M. Henriksen-Lacey, M. Coronado-Puchau and L. M. Liz-Marzán, Inorganic nanoparticles for biomedicine: Where materials scientists meet medical research, *Mater. Today*, 2016, **19**, 19–28.

30 F. Y. Kong, J. W. Zhang, Z. X. Wang, R. F. Li, W. J. Wang and W. Wang, Unique roles of gold nanoparticles in drug delivery, targeting and imaging applications, *Molecules*.

31 C. E. Probst, P. Zrazhevskiy, V. Bagalkot and X. Gao, Quantum dots as a platform for nanoparticle drug delivery vehicle design, *Adv. Drug Deliv. Rev.*, 2013, **65**, 703–718.

32 K. H. Son, J. H. Hong and J. W. Lee, Carbon nanotubes as cancer therapeutic carriers and mediators, *Int. J. Nanomedicine*, 2016, **11**, 5163–5185.

33 Wahajuddin and Arora, Superparamegnetic iron oxide nanoparticles: magnetic nanoplatforms as drug carriers, *Int. J. Nanomedicine*, 2012, **2012**, 3445–3471.

34 F. Dilnawaz, Multifunctional mesoporous silica nanoparticles for cancer therapy and imaging, *Curr. Med. Chem.*

35 C. E. Probst, P. Zrazhevskiy, V. Bagalkot and X. Gao, Quantum dots as a platform for nanoparticle drug delivery vehicle design, *Adv. Drug Deliv. Rev.*, 2013, **65**, 703–718.

36 C. T. Matea, T. Mocan, F. Tabaran, T. Pop, O. Mosteanu, C. Puia, C. Iancu and L. Mocan, Quantum dots in imaging, drug delivery and sensor applications, *Int. J. Nanomedicine*, 2017, **12**, 5421–5431.

37 K. Sreejivungsa, N. Suchaichit, P. Moosophon and A. Chompoosor, Light-Regulated Release of Entrapped Drugs from Photoresponsive Gold Nanoparticles, *J. Nanomater.*, 2016, **2016**, 7.

38 Z. Chen, A. Zhang, X. Wang, J. Zhu, Y. Fan, H. Yu and Z. Yang, The Advances of Carbon Nanotubes in Cancer Diagnostics and Therapeutics, *J. Nanomater.*, 2017, **2017**, 13.

39 N. G. Sahoo, H. Bao, Y. Pan, M. Pal, M. Kakran, H. K. F. Cheng, L. Li and L. P. Tan, Functionalized carbon nanomaterials as nanocarriers for loading and delivery of a poorly water-soluble anticancer drug: A comparative study, *Chem. Commun.*, 2011, **47**, 5235–5237.

40 K. H. Son, J. H. Hong and J. W. Lee, Carbon nanotubes as cancer therapeutic carriers and mediators, *Int. J. Nanomedicine*, 2016, **11**, 5163–5185.

41 P. B. Santhosh and N. P. Ulrih, Multifunctional superparamagnetic iron oxide nanoparticles: Promising tools in cancer theranostics, *Cancer Lett.*, 2013, **336**, 8–17.

42 I. Y. Kim, E. Joachim, H. Choi and K. Kim, Toxicity of silica nanoparticles depends on size, dose, and cell type, *Nanomedicine Nanotechnology, Biol. Med.*, 2015, **11**, 1407–1416.

43 J. J. Hu, L. H. Liu, Z. Y. Li, R. X. Zhuo and X. Z. Zhang, MMP-responsive theranostic nanoplatform based on mesoporous silica nanoparticles for tumor imaging and targeted drug delivery, *J. Mater. Chem. B*, 2016, **4**, 1932–1940.

44 T. Thanh, H. Thi, E. H. Pilkington, D. H. Nguyen and J. S. Lee, The Importance of Poly (ethylene glycol) Alternatives for Overcoming PEG Immunogenicity in Drug, *Polymers (Basel).*, 2020, **12**, 298.

45 Y. Zhao, D. Y. Alakhova, J. O. Kim, T. K. Bronich and A. V. Kabanov, A simple way to enhance Doxil® therapy: Drug release from liposomes at the tumor site by amphiphilic block copolymer, *J. Control. Release*, 2013, **168**, 61–69.

46 E. Bernabeu, G. Helguera, M. J. Legaspi, L. Gonzalez, C. Hocht, C. Taira and D. A. Chiappetta, Paclitaxel-loaded PCL-TPGS nanoparticles: In vitro and in vivo performance compared with Abraxane®, *Colloids Surfaces B Biointerfaces*, 2014, **113**, 43–50.

47 O. C. Farokhzad and R. Langer, Impact of Nanotechnology on Drug Delivery, *ACS Nano*, 2009, **3**, 16–20.

48 F. Gu, L. Zhang, B. A. Teply, N. Mann, A. Wang, A. F. Radovic-Moreno, R. Langer and O. C. Farokhzad, Precise engineering of targeted nanoparticles by using self-assembled biointegrated block copolymers, *Proc. Natl. Acad. Sci.*, 2008, **105**, 2586–2591.

49 S. E. Lipowsky R., in *Handbook of Biological Physics vol. 1*, Elsevier, Amsterdam, 1995, pp. 213–303.

50 A. Khosa, S. Reddi and R. N. Saha, Nanostructured lipid carriers for site-specific drug delivery, *Biomed. Pharmacother.*, 2018, **103**, 598–613.

51 T. Tagami, W. D. Foltz, M. J. Ernsting, C. M. Lee, I. F. Tannok, J. P. May and

Shyh-Dar Li, MRI moniotoring of intratumoral drug delivery and prediction of the therapeutic effect with a multifunctional thermosensitive liposome, *Biomaterials*, 2011, **32**, 6570–6578.

52 H.-I. Chan and M.-K. Yeh, Clinical development of liposome-based drugs: formulation, characterization, and therapeutic efficacy, *Int. J. Nanomedicine*, 2012, **7**, 49–60.

53 Y.-Y. Won, A. K. Brannan, H. T. Davis and F. S. Bates, Cryogenic transmission electron microscopy (cryo-TEM) of micelles and vesicles formed in water by poly(ethylene oxide)-based block copolymer, *J. Phys. Chem. B*, 2002, **106**, 3354–3364.

54 H. S. Yoo and T. G. Park, Biodegradable polymeric micelles composed of doxorubicin conjugated PLGA–PEG block copolymer, *J. Control. Release*, 2001, **70**, 63–70.

55 H. Vu-Quang, M. S. Vinding, T. Nielsen, M. G. Ullisch, N. C. Nielsen and J. Kjems, Theranostic tumor targeted nanoparticles combining drug delivery with dual near infrared and 19F magnetic resonance imaging modalities, *Nanomedicine Nanotechnology, Biol. Med.*, 2016, **12**, 1873–1884.

56 A. Gandhi, A. Paul, O. S. Sen and K. K. Sen, Studies on thermoresponsive polymers: phase behaviour, drug delivery and biomedical applications, *Asian J. Pharm. Sci.*, 2015, **10**, 99–107.

57 M. Masserini, Nanoparticles for Brain Drug Delivery, *ISRN Biochem.*, 2013, **2013**, 1–18.

58 D. Ha, N. Yang and V. Nadithe, Exosomes as therapeutic drug carriers and delivery vehicles across biological membranes: current perspectives and future challenges, *Acta Pharm. Sin. B*, 2016, **6**, 287–296.

59 A. V. Vlassov, S. Magdaleno, R. Setterquist and R. Conrad, Exosomes: current knowledge of their composition, biological functions, and diagnostic and therapeutic potentials, *Biochim. Biophys. Acta*, 2012, **1820**, 940–8.

60 T. Yang, P. Martin, B. Fogarty, A. Brown, K. Schurman, R. Phipps, V. Yin, P. Lockman and S. Bai, Exosome delivered anticancer drugs across the blood-brain barrier for brain cancer therapy, *Pharm. Res.*, 2015, **32**, 2003–2014.

61 Y. Tian, S. Li, J. Song, T. Ji, M. Zhu, G. Anderson, J. Wei and G. Nie, A doxorubicin delivery platform using engineered natural membrane vesicels exosomes for targeted tumo therapy, *Biomaterials*, 2014, **35**, 2383–2390.

62 J. Woodburn, The epidermal growth factor receptor and its inhibition in cancer therapy, *Pharmacol. Ther.*, 1999, **82**, 241–250.

63 S. Hong, D. W. Choi, H. N. Kim, C. G. Park, W. Lee and H. H. Park, Protein-based nanoparticles as drug delivery systems, *Pharmaceutics*, 2020, **12**, 1–28.

64 A. Jain, S. K. Singh, S. K. Arya, S. C. Kundu and S. Kapoor, Protein Nanoparticles: Promising Platforms for Drug Delivery Applications, *ACS Biomater. Sci. Eng.*, 2018, **4**, 3939–3961.

65 M. J. Rohovie, M. Nagasawa and J. R. Swartz, Virus-like Particles: Next-Generation Nanoparticles for Targeted Therapeutic Delivery., *Bioeng. Transl. Med.*, 2017, **2**, 43–57.

66 A. Roldao, M. C. M. Mellado, L. R. Castilho, M.˜T. Carrondo and P. M. J.Alves, Virus-like Particles in Vaccine Development, *Expert Rev. Vaccines*, 2010, **9**, 1149−1176.

67 W. J. Gradishar, Albumin-Bound Paclitaxel: A next-Generation Taxane, *Expert Opin. Pharmacother.*, 2006, **7**, 1041−1053.

68 A. I. Kuruppu, L. Turyanska, T. D. Bradshaw, S. Manickam, B. P. Galhena, P. Paranagama and R. De Silva, Apoferritin and Dps as drug delivery vehicles: Some selected examples in oncology, *Biochim. Biophys. Acta - Gen. Subj.*, 2022, **1866**, 130067.

69 C. Zhang, X. Zhang and G. Zhao, Ferritin nanocage: a versatile nanocarrier utilized in the field of food, nutrition, and medicine, *Nanomaterials*, 2020, **10**, 1–25.

70 A. Yau, J. Lee and Y. Chen, Nanomaterials for protein delivery in anticancer applications, *Pharmaceutica*, 2021, **13**, 1–23.

71 K. Raemdonck, K. Braeckmans, J. Demeester and S. C. De Smedt, Merging the best of both worlds: Hybrid lipid-enveloped matrix nanocomposites in drug

delivery, *Chem. Soc. Rev.*, 2014, **43**, 444–472.

72 C. Li, J. Zhang, Y. J. Zu, S. F. Nie, J. Cao, Q. Wang, S. P. Nie, Z. Y. Deng, M. Y. Xie and S. Wang, Biocompatible and biodegradable nanoparticles for enhancement of anti-cancer activities of phytochemicals, *Chin. J. Nat. Med.*, 2015, **13**, 641–652.

73 S. Rani and T. Ritter, The Exosome - A Naturally Secreted Nanoparticle and its Application to Wound Healing, *Adv. Mater.*, 2016, **28**, 5542–5552.

74 G. T. Hermanson, *Bioconjugate Techniques*, Elsevier, Amsterdam, Third., 2013.

75 D. G. Rawale, K. Thakur, S. R. Adusumalli and V. Rai, Chemical Methods for Selective Labeling of Proteins, *European J. Org. Chem.*, 2019, **2019**, 6749–6763.

76 Y. Zhang, K.-Y. Park, K. F. Suazo and M. D. Distefano, Recent progress in enzymatic protein labelling techniques and their applications, *Chem. Soc. Rev.*, 2018, **47**, 9106–9136.

77 T. Narancic, S. A. Almahboub and K. E. O'Connor, Unnatural amino acids: production and biotechnological potential, *World J. Microbiol. Biotechnol.*, 2019, **35**, 1–11.

78 S. B. Gunnoo and A. Madder, Chemical Protein Modification through Cysteine, *ChemBioChem*, 2016, **17**, 529–553.

79 S. D. Fontaine, R. Reid, L. Robinson, G. W. Ashley and D. V. Santi, Long-term stabilization of maleimide-thiol conjugates, *Bioconjug. Chem.*, 2015, **26**, 145–152.

80 P. Ochtrop and C. P. R. Hackenberger, Recent advances of thiol-selective bioconjugation reactions, *Curr. Opin. Chem. Biol.*, 2020, **58**, 28–36.

81 A. Younes, U. Yasothan and P. Kirkpatrick, Bentuximab vedotin, *Nat. Rev. Drug Discov.*, 2012, **11**, 19–20.

82 S. C. Alley, D. R. Benjamin, S. C. Jeffrey, N. M. Okeley, D. L. Meyer, R. J. Sanderson and P. D. Senter, Contribution of linker stability to the activities of anticancer immunoconjugates, *Bioconjug. Chem.*, 2008, **19**, 759–765.

83 H. Liu, J. Bolleddula, A. Nichols, L. Tang, Z. Zhao and C. Prakash, Metabolism of bioconjugate therapeutics: why, when, and how?, *Drug Metab. Rev.*, 2020, **52**, 66–124.

84 P. Sapra, A. Hooper, C. O'Donnell and H. Gerber, Investigational antibody drug conjugates for solid tumors, *Expert Opin. Investig Drugs*, 2011, **20**, 1131–1149.

85 J. Shia, D. Klimstra, J. Nitzkorski, P. Low, M. Gonen, R. Landmann, M. Weiser, W. Franklin, F. Prendergast, L. Murphy, L. Tang, L. Temple, J. Guillem, W. Wong and P. Paty, Immunohistochemical expression of folate receptor alpha in colorectal carcinoma: patterns and biological significance, *Hum. Pathol.*, 2008, **39**, 498–505.

86 J. Reddy, E. Westrick, H. Santhapuram, S. Howard, M. Miller, M. Vetzel, I. Vlahov, R. Chari, V. Goldmacher and C. Leamon, Folate receptor-specific antitumor activity of EC131, a folate-maytansinoid conjugate, *Cancer Res.*, 2007, **67**, 6376–6382.

87 G. Liu, E. A. Wold and J. Zhou, Applications of Bioorthogonal Chemistry in Tumor-Targeted Drug Discovery, *Curr. Top. Med. Chem.*, 2019, **19**, 892–897.

88 S. K. Sharma and K. D. Bagshawe, Antibody Directed Enzyme Prodrug Therapy (ADEPT): Trials and tribulations, *Adv. Drug Deliv. Rev.*, 2017, **118**, 2–7.

89 A. B. Silver, E. K. Leonard, J. R. Gould and J. B. Spangler, Engineered antibody fusion proteins for targeted disease therapy, *Trends Pharmacol. Sci.*, 2021, **42**, 1064–1081.

90 V. Capucha, E. Mendes, A. P. Francisco and M. J. Perry, Development of triazene prodrugs for ADEPT strategy: New insights into drug delivery system based on carboxypeptidase G2 activation, *Bioorg. Med. Chem. Lett.*, 2012, **22**, 6903–6908.

91 Y. Yang, H. Aloysius, D. Inoyama, Y. Chen and L. Hu, Enzyme-mediated hydrolytic activation of prodrugs, *Acta Pharm. Sin. B*, 2011, **1**, 143–159.

92 I. Tranoy-Opalinski, T. Legigan, R. Barat, J. Clarhaut, M. Thomas, B. Renoux and S. Papot, β-Glucuronidase-responsive prodrugs for selective cancer chemotherapy: An update, *Eur. J. Med. Chem.*, 2014, **74**, 302–313.

93 Z. Karjoo, X. Chen and A. Hatefi, Progress and problems with the use of suicide genes for targeted cancer therapy, *Adv. Drug Deliv. Rev.*, 2016, **99**, 113–128.

94 B. Albada and N. Metzler-Nolte, Organometallic-peptide bioconjugates: synthetic strategies and medicinal applications, *Chem. Rev.*, 2016, **116**, 11797–11839.

95 G. Gasser, M. A. Neukamm, A. Ewers, O. Brosch, T. Weyhermuller and N. Metzler-Nolte, Synthesis and characterization of dicobalthexacarbonyl-alkyne derivatives of amino acids, peptides, and peptide nucleic acid (PNA) monomers, *Inorg. Chem.*, 2009, **48**, 3157−3166.

96 C. Imberti, F. Lermyte, E. P. Friar, P. B. O'Connor and P. J. Sadler, Facile protein conjugation of platinum for light-activated cytotoxic payload release, *Chem. Commun.*, 2021, **57**, 7645–7648.

97 S. Mukhopadhyay, C. M. Barnes, A. Haskel, S. M. Short, K. R. Barnes and S. J. Lippard, Conjugated platinum(IV)- peptide complexes for targeting angiogenic tumor vasculature., *Bioconjug. Chem.*, 2008, **19**, 39−49.

98 R. Huang, Y. Sun, X. Y. Zhang, B. W. Sun, Q. C. Wang and J. Zhu, Biological evaluation of a novel herceptin-platinum (II) conjugate for efficient and cancer cell specific delivery., *Biomed. Pharmacother.*, 2015, **73**, 116−122.

99 N. Curado, G. Dewaele-Le Roi, S. Poty, J. S. Lewis and M. Contel, Trastuzumab gold-conjugates: Synthetic approach and in vitro evaluation of anticancer activities in breast cancer cell lines., *Chem. Commun.*, 2019, **55**, 1394−1397.

100 S. D. Köster, H. Alborzinia, S. Can, S. Kitanovic, I., Wölfl, R. Rubbiani, I. Ott, P. Riesterer, A. Prokop and et al Merz, K., A spontaneous gold(I)-azide alkyne cycloaddition reaction yields gold-peptide bioconjugates which overcome cisplatin resistance in a p53-mutant cancer cell line., *Chem. Sci.*, 2012, **3**, 2062−2072.

101 J. Serment-Guerrero, M. E. Bravo-Gomez, E. Lara-Rivera and L. Ruiz-Azuara, Genotoxic assessment of the copper chelated compounds Casiopeinas:Clues about their mechanism of action, *J. Inorg. Biochem.*, 2017, **166**, 68–75.

102 L. F. Hernández-Ayala, M. Flores-Álamo, S. Escalante-Tovar, R. Galindo-

Murillo, J. C. García-Ramos, J. García-Valdés, V. Gómez-Vidales, K. Reséndiz-Acevedo, Y. Toledano-Magaña and L. Ruiz-Azuara, Synthesis, characterization, theoretical studies and biological activity of coordination compounds with essential metals containing N4-donor ligand 2,9-di(ethylaminomethyl)-1,10-phenanthroline, *Inorganica Chim. Acta*, 2018, **470**, 187–196.

103 Y. Rufino-González, M. Ponce-Macotela, J. C. García-Ramos, M. N. Martínez-Gordillo, R. Galindo-Murillo, A. González-Maciel, R. Reynoso-Robles, A. Tovar-Tovar, M. Flores-Alamo, Y. Toledano-Magaña and L. Ruiz-Azuara, Antigiardiasic activity of Cu(II) coordination compounds: Redox imbalance and membrane damage after a short exposure time, *J. Inorg. Biochem.*, 2019, **195**, 83–90.

104 S. G. Davila-Manzanilla, Y. Figueroa-de-Paz, C. Mejia and L. Ruiz-Azuara, Synergistic effects between a copper-based metal Casiopeína III-ia and cisplatin, *Eur. J. Med. Chem.*, 2017, **129**, 266–274.

105 J. Serment-Guerrero, P. Cano-Sanchez, E. Reyes-Perez, F. Velazquez-Garcia, M. E. Bravo-Gomez and L. Ruiz-Azuara, Genotoxicity of the copper antineoplastic coordination complexes casiopeinas®, *Toxicol. Vitr.*, 2011, **25**, 1376–1384.

106 P. Zhang, H. Huang, S. Banerjee, G. J. Clarkson, C. Ge, C. Imberti and P. J. Sadler, Nucleus-Targeted Organoiridium–Albumin Conjugate for Photodynamic Cancer Therapy, *Angew. Chemie - Int. Ed.*, 2019, **58**, 2350–2354.

107 F. Rosati and G. Roelfes, Artificial Metalloenzymes, *ChemCatChem*, 2010, **2**, 916–927.

108 F. Schwizer, Y. Okamoto, T. Heinisch, Y. Gu, M. M. Pellizzoni, V. Lebrun, R. Reuter, V. Köhler, J. C. Lewis and T. R. Ward, *Chem. Rev.*, 2018, 118, 142–231.

109 M. Jeschek, S. Panke and T. R. Ward, Artificial Metalloenzymes on the Verge of New-to-Nature Metabolism, *Trends Biotechnol.*, 2018, **36**, 60–72.

110 W. Ghattas, V. Dubosclard, A. Wick, A. Bendelac, R. Guillot, R. Ricoux and J. P. Mahy, Receptor-Based Artificial Metalloenzymes on Living Human Cells, *J.*

Am. Chem. Soc., 2018, **140**, 8756–8762.

111 K. Tsubokura, K. K. H. Vong, A. R. Pradipta, A. Ogura, S. Urano, T. Tahara, S. Nozaki, H. Onoe, Y. Nakao, R. Sibgatullina, A. Kurbangalieva, Y. Watanabe and K. Tanaka, In Vivo Gold Complex Catalysis within Live Mice, *Angew. Chemie - Int. Ed.*, 2017, **56**, 3579–3584.

112 T.-C. Chang, K. Vong, T. Yamamoto and T. Katsunori, Prodrug Activation by Gold Artificial Metalloenzyme-Catalyzed Synthesis of Phenanthridinium Derivatives via Hydroamination, *Angew. Chem. Int. Ed. Engl.*, 2021, **60**, 12446–12454.

113 K. Vong, T. Tahara, S. Urano, I. Nasibullin, K. Tsubokura, Y. Nakao, A. Kurbangalieva, H. Onoe, Y. Watanabe and K. Tanaka, Disrupting tumor onset and growth via selective cell tagging (SeCT) therapy, *Sci. Adv.*, 2021, **7**, 1–12.

114 A. M. Koorts and M. Viljoen, Ferritin and ferritin isoforms I: Structure-function relationships, synthesis, degradation and secretion, *Arch. Physiol. Biochem.*, 2007, **113**, 30–54.

115 F. Funk, J. -P Lenders, R. Crichton and W. Schneider, Reductive mobilisation of ferritin iron, *Eur. J. Biochem.*, 1985, **152**, 167–172.

116 I. Moglia, M. Santiago, Á. Olivera-Nappa and M. Soler, An optimized low-cost protocol for standardized production of iron-free apoferritin nanocages with high protein recovery and suitable conformation for nanotechnological applications, *J. Inorg. Biochem.*, 2018, **183**, 184–190.

117 G. Jutz, P. Van Rijn, B. Santos Miranda and A. Böker, Ferritin: A versatile building block for bionanotechnology, *Chem. Rev.*, 2015, **115**, 1653–1701.

118 H. Chen, S. Zhang, C. Xu and G. Zhao, Engineering protein interfaces yields ferritin disassembly and reassembly under benign experimental conditions, *Chem. Commun.*, 2016, **52**, 7402–7405.

119 S. Yin, K. Davey, S. Dai, Y. Liu and J. Bi, A critical review of ferritin as a drug nanocarrier: Structure, properties, comparative advantages and challenges, *Particuology*, 2022, **64**, 65–84.

120 A. Patriati, N. Suparno, G. T. Sulungbudi, M. Mujamilah and E. G. R. Putra,

Structural change of apoferritin as the effect of ph change: Dls and sans study, *Indones. J. Chem.*, 2020, **20**, 1178–1183.

121 F. Carmona, M. Poli, M. Bertuzzi, A. Gianoncelli, F. Gangemi and P. Arosio, Study of ferritin self-assembly and heteropolymer formation by the use of Fluorescence Resonance Energy Transfer (FRET) technology, *Biochim. Biophys. Acta - Gen. Subj.*, 2017, **1861**, 522–532.

122 M. Kim, Y. Rho, K. S. Jin, B. Ahn, S. Jung, H. Kim and M. Ree, PH-dependent structures of ferritin and apoferritin in solution: Disassembly and reassembly, *Biomacromolecules*, 2011, **12**, 1629–1640.

123 L. Chen, G. Bai, R. Yang, J. Zang, T. Zhou and G. Zhao, Encapsulation of β-carotene within ferritin nanocages greatly increases its water-solubility and thermal stability, *Food Chem.*, 2014, **149**, 307–312.

124 S. Mazzucchelli, M. Truffi, F. Baccarini, M. Beretta, L. Sorrentino, M. Bellini, M. A. Rizzuto, R. Ottria, A. Ravelli, P. Ciuffreda, D. Prosperi and F. Corsi, H-Ferritin-nanocaged olaparib: A promising choice for both BRCA-mutated and sporadic triple negative breast cancer, *Sci. Rep.*, 2017, **7**, 1–15.

125 M. R. Ruggiero, D. Alberti, V. Bitonto and S. G. Crich, Ferritin: A platform for MRI contrast agents delivery, *Inorganics*, 2019, **7**, 15.

126 T. R. Daniels, T. Delgado, G. Helguera and M. L. Penichet, The transferrin receptor part II: Targeted delivery of therapeutic agents into cancer cells, *Clin. Immunol.*, 2006, **121**, 159–176.

127 K. Fan, X. Jia, M. Zhou, K. Wang, J. Conde, J. He, J. Tian and X. Yan, Ferritin Nanocarrier Traverses the Blood Brain Barrier and Kills Glioma, *ACS Nano*, 2018, **12**, 4105–4115.

128 M. Liang, H. Tan, J. Zhou, T. Wang, D. Duan, K. Fan, J. He, D. Cheng, H. Shi, H. S. Choi and X. Yan, Bioengineered H-Ferritin Nanocages for Quantitative Imaging of Vulnerable Plaques in Atherosclerosis, *ACS Nano*, 2018, **12**, 9300–9308.

129 L. Zhang, L. Li, A. Di Penta, U. Carmona, F. Yang, R. Schöps, M. Brandsch, J. L. Zugaza and M. Knez, H-Chain Ferritin: A Natural Nuclei Targeting and Bioactive Delivery Nanovector, *Adv. Healthc. Mater.*, 2015, **4**, 1305–1310.

130 D. W. Rice, B. Dean, J. M. A. Smith, J. L. White, G. C. Ford and P. M. Harrison, Structural homology between mouse liver and horse spleen ferritins, *FEBS Lett.*, 1985, **181**, 165–168.

131 S. Stefanini, S. Cavallo, C. Q. Wang, P. Tataseo, P. Vecchini, A. Giartosio and E. Chiancone, Thermal stability of horse spleen apoferritin and human recombinant H apoferritin, *Arch. Biochem. Biophys.*, 1996, **325**, 58–64.

132 G. Palmisano, M. Pagliaro, Z. Yang, X. Wang, H. Diao, J. Zhang, H. Li and Z. Guo, Encapsulation of platinum anticancer drugs by apoferritin, *Chem. Commun.*, 2007, **7345**, 3–6.

133 D. M. Monti, G. Ferraro and A. Merlino, Ferritin-based anticancer metallodrug delivery: Crystallographic, analytical and cytotoxicity studies, *Nanomedicine Nanotechnology, Biol. Med.*, 2019, **20**, 101997.

134 A. F. Breen, D. Scurr, M. L. Cassioli, G. Wells and N. R. Thomas, Protein Encapsulation of Experimental Anticancer Agents 5F 203 and Phortress : Towards Precision Drug Delivery, *Int. J. Nanomedicine*, 2019, **14**, 9525–9534.

135 G. Ferraro, S. Ciambellotti, L. Messori and A. Merlino, Cisplatin Binding Sites in Human H-Chain Ferritin, *Inorg. Chem.*, 2017, **56**, 9064–9070.

136 E. Falvo, E. Tremante, R. Fraioli, C. Leonetti, C. Zamparelli, A. Boffi, V. Morea, P. Ceci and P. Giacomini, Antibody-drug conjugates: targeting melanoma with cisplatin encapsulated in protein-cage nanoparticles based on human ferritin †, *Nanoscale*, 2013, **5**, 12278.

137 A. I. Kuruppu, L. Zhang, H. Collins, L. Turyanska, N. R. Thomas and T. D. Bradshaw, An Apoferritin-based Drug Delivery System for the Tyrosine Kinase Inhibitor Gefitinib, *Adv. Healthc. Mater.*, 2015, **4**, 2816–2821.

138 K. Bouzinab, H. S. Summers, M. F. G. Stevens, C. J. Moody, N. R. Thomas, P. Gershkovich, N. Weston, M. B. Ashford, T. D. Bradshaw and L. Turyanska, Delivery of Temozolomide and N3-Propargyl Analog to Brain Tumors Using an Apoferritin Nanocage, *ACS Appl. Mater. Interfaces*, 2020, **12**, 12609–12617.

139 D. Belletti, F. Pederzoli, F. Forni, M. A. Vandelli, G. Tosi and B. Ruozi, Protein cage nanostructure as drug delivery system: magnifying glass on apoferritin, *Expert Opin. Drug Deliv.*, 2017, **14**, 825–840.

140 C. Wang, C. Zhang, Z. Li, S. Yin, Q. Wang, F. Guo, Y. Zhang, R. Yu, Y. Liu and Z. Su, Extending Half Life of H-Ferritin Nanoparticle by Fusing Albumin Binding Domain for Doxorubicin Encapsulation, *Biomacromolecules*, 2018, **19**, 773–781.

141 S. Zhang, J. Zang, H. Chen, M. Li, C. Xu and G. Zhao, The Size Flexibility of Ferritin Nanocage Opens a New Way to Prepare Nanomaterials, *Small*, 2017, **13**, 1–6.

142 W. Wang, L. Wang, G. Li, G. Zhao, X. Zhao and H. Wang, AB loop engineered ferritin nanocages for drug loading under benign experimental conditions, *Chem. Commun.*, 2019, **55**, 12344–12347.

143 D. J. E. Huard, K. M. Kane and F. Akif Tezcan, Re-engineering protein interfaces yields copper-inducible ferritin cage assembly, *Nat. Chem. Biol.*, 2013, **9**, 169–176.

144 C. Gu, T. Zhang, C. Lv, Y. Liu, Y. Wang and G. Zhao, His-Mediated Reversible Self-Assembly of Ferritin Nanocages through Two Different Switches for Encapsulation of Cargo Molecules, *ACS Nano*, 2020, **14**, 17080–17090.

145 Y. Luo, X. Wang, D. Du and Y. Lin, Hyaluronic acid-conjugated apoferritin nanocages for lung cancer targeted drug delivery, *Biomater. Sci.*, 2015, **3**, 1386–1394.

146 R. Yang, Y. Liu, C. Blanchard and Z. Zhou, Channel directed rutin nano-encapsulation in phytoferritin induced by guanidine hydrochloride, *Food Chem.*, 2018, **240**, 935–939.

147 X. Liu, W. Jin and E. C. Theil, Opening protein pores with chaotropes enhances Fe reduction and chelation of Fe from the ferritin biomineral, *Proc. Natl. Acad. Sci. U. S. A.*, 2003, **100**, 3653–3658.

148 A. Ma-Ham, H. Wu, J. Wang, X. Kang, Y. Zhang and Y. Lin, Apoferritin-based nanomedicine platform for drug delivery: Equilibrium binding study of daunomycin with DNA, *J. Mater. Chem.*, 2011, **21**, 8700–8708.

149 Z. Wang, S. Zhang, R. Zhang, X. Chen, G. Sun, M. Zhou, Q. Han, B. Zhang, Y. Zhao, B. Jiang, Y. Yang, X. Yan and K. Fan, Bioengineered Dual-Targeting Protein Nanocage for Stereoscopical Loading of Synergistic

Hydrophilic/Hydrophobic Drugs to Enhance Anticancer Efficacy, *Adv. Funct. Mater.*, 2021, **31**, 1–15.

150 Z. Zhen, W. Tang, H. Chen, X. Lin, T. Todd, G. Wang, T. Cowger, X. Chen and J. Xie, RGD-modified apoferritin nanoparticles for efficient drug delivery to tumors, *ACS Nano*, 2013, **7**, 4830–4837.

151 X. Liu, W. Wei, S. Huang, S. S. Lin, X. Zhang, C. Zhang, Y. Du, G. Ma, M. Li, S. Mann and D. Ma, Bio-inspired protein-gold nanoconstruct with core-void-shell structure: Beyond a chemo drug carrier, *J. Mater. Chem. B*, 2013, **1**, 3136–3143.

152 T. R. Daniels, T. Delgado, J. A. Rodriguez, G. Helguera and M. L. Penichet, The transferrin receptor part I: Biology and targeting with cytotoxic antibodies for the treatment of cancer, *Clin. Immunol.*, 2006, **121**, 144–158.

153 K. Wetz and R. R. Crichton, Chemical Modification as a Probe of the Topography and Reactivity of Horse-Spleen Apoferritin, *Eur. J. Biochem.*, 1976, **61**, 545–550.

154 M. Zhai, Y. Wang, L. Zhang, M. Liang, S. Fu, L. Cui, M. Yang, W. Gong, Z. Li, L. Yu, X. Xie, C. Yang, Y. Yang and C. Gao, Glioma targeting peptide modified apoferritin nanocage, *Drug Deliv.*, 2018, **25**, 1013–1024.

155 L. Vannucci, E. Falvo, M. Fornara, P. Di Micco, O. Benada, J. Krizan, J. Svoboda, K. Hulikova-Capkova, V. Morea, A. Boffi and P. Ceci, Selective targeting of melanoma by PEG-masked protein-based multifunctional nanoparticles, *Int. J. Nanomedicine*, 2012, **7**, 1489–1509.

156 E. Falvo, E. Tremante, A. Arcovito, M. Papi, N. Elad, A. Boffi, V. Morea, G. Conti, G. Toffoli, G. Fracasso, P. Giacomini and P. Ceci, Improved Doxorubicin Encapsulation and Pharmacokinetics of Ferritin-Fusion Protein Nanocarriers Bearing Proline, Serine, and Alanine Elements, *Biomacromolecules*, 2016, **17**, 514–522.

157 M. Khoshnejad, C. F. Greineder, K. W. Pulsipher, C. H. Villa, B. Altun, D. C. Pan, A. Tsourkas, I. J. Dmochowski and V. R. Muzykantov, Ferritin Nanocages with Biologically Orthogonal Conjugation for Vascular Targeting and Imaging, *Bioconjug. Chem.*, 2018, **29**, 1209–1218.

158 W. Wang, Z. Liu, X. Zhou, Z. Guo, J. Zhang, P. Zhu, S. Yao and M. Zhu, Ferritin nanoparticle-based SpyTag/SpyCatcher-enabled click vaccine for tumor immunotherapy, *Nanomedicine Nanotechnology, Biol. Med.*, 2019, **16**, 69–78.

159 E. Valero, S. Tambalo, P. Marzola, M. Ortega-Muñoz, F. J. López-Jaramillo, F. Santoyo-González, J. De Dios López, J. J. Delgado, J. J. Calvino, R. Cuesta, J. M. Domínguez-Vera and N. Gálvez, Magnetic nanoparticles-templated assembly of protein subunits: A new platform for carbohydrate-based MRI nanoprobes, *J. Am. Chem. Soc.*, 2011, **133**, 4889–4895.

160 T. Ueno, M. Abe, K. Hirata, S. Abe, M. Suzuki, N. Shimizu, M. Yamamoto, M. Takata and Y. Watanabe, process of accumulation of metal ions on the interior surface of apo-ferritin: Crystal structures of a series of apo-ferritins containing variable quantities of pd(ii) ions, *J. Am. Chem. Soc.*, 2009, **131**, 5094–5100.

161 M. Suzuki, M. Abe, T. Ueno, S. Abe, T. Goto, Y. Toda, T. Akita, Y. Yamada and Y. Watanabe, Preparation and catalytic reaction of Au/Pd bimetallic nanoparticles in Apo-ferritin, *Chem. Commun.*, 2009, 4871–4873.

162 G. Ferraro, G. Petruk, L. Maiore, F. Pane, A. Amoresano, M. A. Cinellu, D. M. Monti and A. Merlino, Caged noble metals: Encapsulation of a cytotoxic platinum(II)-gold(I) compound within the ferritin nanocage, *Int. J. Biol. Macromol.*, 2018, **115**, 1116–1121.

163 D. M. Monti, G. Ferraro, G. Petruk, L. Maiore, F. Pane, A. Amoresano, M. A. Cinellu and A. Merlino, Ferritin nanocages loaded with gold ions induce oxidative stress and apoptosis in MCF-7 human breast cancer cells, *Dalt. Trans.*, 2017, **46**, 15354–15362.

164 G. Ferraro, D. M. Monti, A. Amoresano, N. Pontillo, G. Petruk, F. Pane, M. A. Cinellu and A. Merlino, Gold-based drug encapsulation within a ferritin nanocage: X-ray structure and biological evaluation as a potential anticancer agent of the Auoxo3-loaded protein, *Chem. Commun.*, 2016, **52**, 9518–9521.

165 R. Fan, S. W. Chew, V. V. Cheong and B. P. Orner, Fabrication of gold nanoparticles inside unmodified horse spleen apoferritin, *Small*, 2010, **6**, 1483–1487.

166 B. Maity, S. Abe and T. Ueno, Observation of gold sub-nanocluster nucleation within a crystalline protein cage, *Nat. Commun.*, 2017, **8**, 1–9.

167 M. B. Gawande, A. Goswami, F. X. Felpin, T. Asefa, X. Huang, R. Silva, X. Zou, R. Zboril and R. S. Varma, Cu and Cu-Based Nanoparticles: Synthesis and Applications in Catalysis, *Chem. Rev.*, 2016, **116**, 3722–3811.

168 A. Musa, M. B. Ahmad, M. Z. Hussein, S. Mohd Izham, K. Shameli and H. Abubakar Sani, Synthesis of Nanocrystalline Cellulose Stabilized Copper Nanoparticles, *J. Nanomater.*, 2016, **2016**, 7.

169 N. V. Suramwar, S. R. Thakare and N. T. Khaty, One pot synthesis of copper nanoparticles at room temperature and its catalytic activity, *Arab. J. Chem.*, 2016, **9**, S1807–S1812.

170 M. I. Din and R. Rehan, Synthesis , Characterization , and Applications of Copper Nanoparticles, *Anal. Lett.*, 2017, **50**, 50–62.

171 M. Ceolín, N. Gálvez, P. Sánchez, B. Fernández and J. M. Domínguez-Vera, Structural Aspects of the Growth Mechanism of Copper Nanoparticles Inside Apoferritin, *Eur. J. Inorg. Chem.*, 2008, **2008**, 795–801.

172 O. D. Petrucci, R. J. Hilton, J. K. Farrer and R. K. Watt, A ferritin photochemical synthesis of monodispersed silver nanoparticles that possess antimicrobial properties, *J. Nanomater.*, 2019, **2019**, 8.

173 X. Liu, W. Wei, C. Wang, H. Yue, D. Ma, C. Zhu, G. Ma and Y. Du, Apoferritin-camouflaged Pt nanoparticles: Surface effects on cellular uptake and cytotoxicity, *J. Mater. Chem.*, 2011, **21**, 7105–7110.

174 B. Maity, Y. Hishikawa, D. Lu and T. Ueno, Recent progresses in the accumulation of metal ions into the apo-ferritin cage: Experimental and theoretical perspectives, *Polyhedron*, 2019, **172**, 104–111.

175 R. Xing, X. Wang, C. Zhang, Y. Zhang, Q. Wang, Z. Yang and Z. Guo, Characterization and cellular uptake of platinum anticancer drugs encapsulated in apoferritin, *J. Inorg. Biochem.*, 2009, **103**, 1039–1044.

176 B. Maity, K. Fujita and T. Ueno, Use of the confined spaces of apo-ferritin and virus capsids as nanoreactors for catalytic reactions, *Curr. Opin. Chem. Biol.*, 2015, **25**, 88–97.

177 S. Abe, K. Hirata, T. Ueno, K. Morino, N. Shimizu, M. Yamamoto, M. Takata,

E. Yashima and Y. Watanabe, Polymerization of phenylacetylene by rhodium complexes within a discrete space of apo-ferritin, *J. Am. Chem. Soc.*, 2009, **131**, 6958–6960.

178 L. Mosca, E. Falvo, P. Ceci, E. Poser, I. Genovese, G. Guarguaglini, G. Colotti, L. Mosca, E. Falvo, P. Ceci, E. Poser, I. Genovese, G. Guarguaglini and G. Colotti, Use of Ferritin-Based Metal-Encapsulated Nanocarriers as Anticancer Agents, *Appl. Sci.*, 2017, **7**, 101.

179 M. Ismael, A. Abdou and A. M. Abdel-Mawgoud, Synthesis, Characterization, Modeling, and Antimicrobial Activity of FeIII, CoII, NiII, CuII, and ZnII Complexes Based on Tri-substituted Imidazole Ligand, *Zeitschrift fur Anorg. und Allg. Chemie*, 2018, **644**, 1203–1214.

180 R. Laghaei, D. G. Evans and R. D. Coalson, Metal binding sites of human H-chain ferritin and iron transport mechanism to the ferroxidase sites: A molecular dynamics simulation study, *Proteins Struct. Funct. Bioinforma.*, 2013, **81**, 1042–1050.

181 Y. Jin, J. He, K. Fan and X. Yan, Ferritin variants: Inspirations for rationally designing protein nanocarriers, *Nanoscale*, 2019, **11**, 12449–12459.

182 P. D. Hempstead, S. J. Yewdall, A. R. Fernie, D. M. Lawson, P. J. Artymiuk, D. W. Rice, G. C. Ford and P. M. Harrison, Comparison of the three-dimensional structures of recombinant human H and horse L ferritins at high resolution, *J. Mol. Biol.*, 1997, **268**, 424–448.

183 L. Chen, G. Bai, S. Yang, R. Yang, G. Zhao, C. Xu and W. Leung, Encapsulation of curcumin in recombinant human H-chain ferritin increases its water-solubility and stability, *Food Res. Int.*, 2014, **62**, 1147–1153.

184 G. Yahioglu and P. Sammes, 1-10-Phenanthroline: A Versatile Ligand, *Chem. Soc. Rev.*, 1994, **23**, 327–344.

185 M. Khoshnejad, H. Parhiz, V. V. Shuvaev, I. J. Dmochowski and V. R. Muzykantov, Ferritin-based drug delivery systems: Hybrid nanocarriers for vascular immunotargeting, *J. Control. Release*, 2018, **282**, 13–24.

186 B. R. Lee, H. K. Ko, J. H. Ryu, K. Y. Ahn, Y. H. Lee, S. J. Oh, J. H. Na, T. W. Kim, Y. Byun, I. C. Kwon, K. Kim and J. Lee, Engineered Human Ferritin

Nanoparticles for Direct Delivery of Tumor Antigens to Lymph Node and Cancer Immunotherapy, *Sci. Rep.*, 2016, **6**, 35182.

187 M. E. Bravo-Gómez, C. Campero-Peredo, D. García-Conde, M. J. Mosqueira-Santillán, J. Serment-Guerrero and L. Ruiz-Azuara, DNA-binding mode of antitumoral copper compounds (Casiopeinas®) and analysis of its biological meaning, *Polyhedron*, 2015, **102**, 530–538.

188 I. Fábián, Kinetics of Ternary Complex Formation with the (Nitriloacetato)copper(II) Complex, *Inorg. Chem.*, 1993, **32**, 1184–1190.

189 A. von Zelewsky and J. M. Bemtgen, Formation of Ternary Copper(II) Complexes at the Surface of Silica Gel As Studied by ESR Spectroscopy, *Inorg. Chem.*, 1982, **21**, 1771–1777.

190 K. Ozutsumi and T. Kawashima, Structure of copper(II)-bpy and -phen complexes: EXAFS and spectrophotometric studies on the structure of copper(II) complexes with 2,2′-bipyridine and 1,10-phenanthroline in aqueous solution, *Inorganica Chim. Acta*, 1991, **180**, 231–238.

191 P. Gameiro, C. Rodrigues, T. Baptista, I. Sousa and B. de Castro, Solution studies on binary and ternary complexes of copper(II) with some fluoroquinolones and 1,10-phenanthroline: Antimicrobial activity of ternary metalloantibiotics, *Int. J. Pharm.*, 2007, **334**, 129–136.

192 C. Marzano, M. Pellei, F. Tisato and C. Santini, Copper Complexes as Anticancer Agents, *Anticancer. Agents Med. Chem.*, 2009, **9**, 185–211.

193 C. Lüdtke, S. Sobottka, J. Heinrich, P. Liebing, S. Wedepohl, B. Sarkar and N. Kulak, Forty Years after the Discovery of Its Nucleolytic Activity: [Cu(phen)2]2+ Shows Unattended DNA Cleavage Activity upon Fluorination, *Chem. - A Eur. J.*, 2021, **27**, 3273–3277.

194 K. J. Catalan, S. Jackson, J. D. Zubkowski and D. L. Perry, Copper (II) nitrate compounds with heterocyclic ligands: structures of [Cu(NO3)(2,2'-dipyridyl)2][NO3]H2O and [Cu(H2O)(1,10-phenanthroline)2][NO3]2, *Polyhedron*, 1995, **14**, 2165 2171.

195 A. Draksharapu, A. J. Boersma, M. Leising, A. Meetsma, W. R. Browne and G. Roelfes, Binding of copper(ii) polypyridyl complexes to DNA and

consequences for DNA-based asymmetric catalysis, *Dalt. Trans.*, 2015, **44**, 3647–3655.

196 L. Xue, D. Deng and J. Sun, Magnetoferritin: Process, Prospects, and Their Biomedical Applications, *Int. J. Mol. Sci.*, 2019, **20**, 2426.

197 M. Salavati-Niasari and F. Davar, Synthesis of copper and copper(I) oxide nanoparticles by thermal decomposition of a new precursor, *Mater. Lett.*, 2009, **63**, 441–443.

198 A. F. Wright and J. S. Nelson, Theory of the copper vacancy in cuprous oxide, *J. Appl. Phys.*, 2002, **92**, 5849–5851.

199 *CRC Handbook of Chemistry and Physics*, Boca Raton, FL, 62nd edn., 1981.

200 I. Moglia, M. Santiago, S. Guerrero, M. Soler, A. Olivera-Nappa and M. J. Kogan, Enhanced cellular uptake of H-chain human ferritin containing gold nanoparticles, *Pharmaceutics*, 2021, **13**, 1966.

201 N. A. P. Franken, H. M. Rodermond, J. Stap, J. Haveman and C. van Bree, Clonogenic assay of cells in vitro, *Nat. Protoc.*, 2006, **1**, 2315–2319.

202 A. Erxleben, Interactions of copper complexes with nucleic acids, *Coord. Chem. Rev.*, 2018, **360**, 92–121.

203 T. Hirohama, Y. Kuranuki, E. Ebina, T. Sugizaki, H. Arii, M. Chikira, P. T. Selvi and M. Palaniandavar, Copper(II) complexes of 1,10-phenanthroline-derived ligands: Studies on DNA binding properties and nuclease activity, *J. Inorg. Biochem.*, 2005, **99**, 1205–1219.

204 D. K. Chand, H. Schneider, A. Bencini and A. Bianchi, Affinity and Nuclease Activity of Macrocyclic Polyamines and their CuII Complexes, *Chem. - A Eur. J.*, 2000, 4001–4008.

205 J. T. Wang, Q. Xia, X. H. Zheng, H. Y. Chen, H. Chao, Z. W. Mao and L. N. Ji, An effective approach to artificial nucleases using copper(ii) complexes bearing nucleobases, *Dalt. Trans.*, 2010, **39**, 2128–2136.

206 R. R. Davies and M. D. Distefano, A semisynthetic metalloenzyme based on a protein cavity that catalyzes the enantioselective hydrolysis of ester and amide substrates, *J. Am. Chem. Soc.*, 1997, **119**, 11643–11652.

207 M. J. Macdonald, L. D. Lavis, D. Hilvert and S. H. Gellman, Evaluation of the Ser-His Dipeptide, a Putative Catalyst of Amide and Ester Hydrolysis, *Org. Lett.*, 2016, **18**, 3518–3521.

208 A. Polyzos, A. B. Hughes and J. R. Christie, Catalysis of aryl ester hydrolysis in the presence of metallomicelles containing a copper(II) diethylenetriamine derivative, *Langmuir*, 2007, **23**, 1872–1879.

209 S. S. Xue, M. Zhao, Z. F. Ke, B. C. Cheng, H. Su, Q. Cao, Z. K. Cao, J. Wang, L. N. Ji and Z. W. Mao, Enantioselective Hydrolysis of Amino Acid Esters Promoted by Bis(β-cyclodextrin) Copper Complexes, *Sci. Rep.*, 2016, **6**, 1–9.

210 W. G. DeGraff and J. B. Mitchell, Evaluation of a Tetrazolium-based Semiautomated Colorimetric Assay: Assessment of Chemosensitivity Testing, *Cancer Res.*, 1987, **47**, 936–942.

211 P. Nunes, I. Correia, F. Marques, A. P. Matos, M. M. C. Dos Santos, C. G. Azevedo, J. L. Capelo, H. M. Santos, S. Gama, T. Pinheiro, I. Cavaco and J. C. Pessoa, Copper Complexes with 1,10-Phenanthroline Derivatives: Underlying Factors Affecting Their Cytotoxicity, *Inorg. Chem.*, 2020, **59**, 9116–9134.

212 J. O. Pinho, J. D. Amaral, R. E. Castro, C. M. P. Rodrigues, A. Casini, G. Soveral and M. M. Gaspar, Copper complex nanoformulations featuring highly promising therapeutic potential in murine melanoma models, *Nanomedicine*, 2019, **14**, 835–850.

213 B. J. Denny, L. L. H. Tsang, J. A. Slack, R. T. Wheelhouse and M. F. G. Stevens, NMR and Molecular Modeling Investigation of the Mechanism of Activation of the Antitumor Drug Temozolomide and Its Interaction with DNA, *Biochemistry*, 1994, **33**, 9045–9051.

214 Q. Pan, X. J. Yang, H. M. Wang, X. T. Dong, W. Wang, Y. Li and J. M. Li, Chemoresistance to Temozolomide in Human Glioma Cell Line U251 is Associated with Increased Activity of O 6-methylguanine-DNA Methyltransferase and Can be Overcome by Metronomic Temozolomide Regimen, *Cell Biochem. Biophys.*, 2012, **62**, 185–191.

215 K. Du, Q. Xia, H. Heng and F. Feng, Temozolomide-Doxorubicin Conjugate as a Double Intercalating Agent and Delivery by Apoferritin for Glioblastoma

Chemotherapy, *ACS Appl. Mater. Interfaces*, 2020, **12**, 34599–34609.

216 T. Waghule, V. K. Rapalli, G. Singhvi, S. Gorantla, A. Khosa, S. K. Dubey and R. N. Saha, Design of temozolomide-loaded proliposomes and lipid crystal nanoparticles with industrial feasible approaches: comparative assessment of drug loading, entrapment efficiency, and stability at plasma pH, *J. Liposome Res.*, 2021, **31**, 158–168.

217 Y. Liu, H. Wang, J. Wei, R. Zhou, Z. Chen and H. Liang, Synthesis and crystal structure of a cadmium complex of temozolomide, *J. Chem. Res.*, 2012, **36**, 520–522.

218 X. Li, K. Du, J. Sun and F. Feng, Apoferritin as a Carrier of Cu(II) Diethyldithiocarbamate and Biomedical Application for Glutathione-Responsive Combination Chemotherapy, *ACS Appl. Bio Mater.*, 2020, **3**, 654–663.

219 S. M. Russell and P. M. Harrison, Heterogeneity in horse ferritins. A comparative study of surface charge, iron content and kinetics of iron uptake, *Biochem. J.*, 1978, **175**, 91–104.

220 A. I. Kuruppu, L. Zhang, H. Collins, L. Turyanska, N. R. Thomas and T. D. Bradshaw, An Apoferritin-based Drug Delivery System for the Tyrosine Kinase Inhibitor Gefitinib, *Adv. Healthc. Mater.*, 2015, **4**, 2816–2821.

221 T. Waghule, R. Narayan Saha and G. Singhvi, UV spectroscopic method for estimation of temozolomide: Application in stability studies in simulated plasma pH, degradation rate kinetics, formulation design, and selection of dissolution media, *Spectrochim. Acta - Part A Mol. Biomol. Spectrosc.*, 2021, **258**, 119848.

222 K. Bhattacharjee and P. K. Shukla, A DFT study of reactions of methyldiazonium ion with DNA/RNA nucleosides: Investigating effect of sugar moiety on methylation pattern of bases, *Int. J. Quantum Chem.*, 2014, **114**, 1637–1644.

223 L. Li, Y. Huang, T. Shi, Y. Xu, M. Hyytiainen, J. Keski-Oja, Q. Jiang, Y. Hu and Z. Du, EGF/EGFR upregulates and cooperates with Netrin-4 to protect glioblastoma cells from DNA damage-induced senescence, *BMC Cancer*, 2018, **18**, 1215.

224 L. Tang, Y. Feng, S. Gao, Q. Mu and C. Liu, Nanotherapeutics Overcoming the Blood-Brain Barrier for Glioblastoma Treatment, *Front. Pharmacol.*, 2021, **12**, 1–11.

225 N. Song, J. Zhang, J. Zhai, J. Hong, C. Yuan and M. Liang, Ferritin: A Multifunctional Nanoplatform for Biological Detection, Imaging Diagnosis, and Drug Delivery, *Acc. Chem. Res.*, 2021, **54**, 3313–3325.

226 I. Moglia, M. Santiago, Á. Olivera-nappa and M. Soler, An optimized low-cost protocol for standardized production of iron-free apoferritin nanocages with high protein recovery and suitable conformation for nanotechnological applications, *J. Inorg. Biochem.*, 2018, **183**, 184–190.

227 M. Liang, K. Fan, M. Zhou, D. Duan, J. Zheng, D. Yang, J. Feng and X. Yan, H-ferritin-nanocaged doxorubicin nanoparticles specifically target and kill tumors with a single-dose injection, *Proc. Natl. Acad. Sci. U. S. A.*, 2014, **111**, 14900–14905.

228 Y. Zhao, M. Liang, X. Li, K. Fan, J. Xiao, Y. Li, H. Shi, F. Wang, H. S. Choi, D. Cheng and X. Yan, Bioengineered Magnetoferritin Nanoprobes for Single-Dose Nuclear-Magnetic Resonance Tumor Imaging, *ACS Nano*, 2016, **10**, 4184–4191.

229 L. Li, M. Muñoz-Culla, U. Carmona, M. P. Lopez, F. Yang, C. Trigueros, D. Otaegui, L. Zhang and M. Knez, Ferritin-mediated siRNA delivery and gene silencing in human tumor and primary cells, *Biomaterials*, 2016, **98**, 143–151.

230 M. Bellini, S. Mazzucchelli, E. Galbiati, S. Sommaruga, L. Fiandra, M. Truffi, M. A. Rizzuto, M. Colombo, P. Tortora, F. Corsi and D. Prosperi, Protein nanocages for self-triggered nuclear delivery of DNA-targeted chemotherapeutics in Cancer Cells, *J. Control. Release*, 2014, **196**, 184–196.

231 Sung Il Yoon and Mark R. Walter, Identification and Characterization of a +1 Frameshift Observed during the Expression of Epstein-Barr Virus IL-10 in Escherichia coli, *Protein Expr Purif.*, 2007, **53**, 132–137.

232 G. L. Rosano and E. A. Ceccarelli, Recombinant protein expression in Escherichia coli: Advances and challenges, *Front. Microbiol.*, 2014, **5**, 1–17.

233 A. Bernard and M. Payton, Fermentation and Growth of Escherichia coli for

Optimal Protein Production , *Curr. Protoc. Protein Sci.*, 1995, **00**, 1–18.

234 M. Sibley and J. M. Ward, A cell engineering approach to enzyme-based fed-batch fermentation, *Microb. Cell Fact.*, 2021, **20**, 1–16.

235 G. W. Luli and W. R. Strohl, Comparison of growth, acetate production, and acetate inhibition of Escherichia coli strains in batch and fed-batch fermentations, *Appl. Environ. Microbiol.*, 1990, **56**, 1004–1011.

236 M. Szenk, K. A. Dill and A. M. R. de Graff, Why Do Fast-Growing Bacteria Enter Overflow Metabolism? Testing the Membrane Real Estate Hypothesis, *Cell Syst.*, 2017, **5**, 95–104.

237 E. N. Kosobokova, K. A. Skrypnik and V. S. Kosorukov, Overview of fusion tags for recombinant proteins, *Biochem.*, 2016, **81**, 187–200.

238 W. T. Booth, C. R. Schlachter, S. Pote, N. Ussin, N. J. Mank, V. Klapper, L. R. Offermann, C. Tang, B. K. Hurlburt and M. Chruszcz, Impact of an N-terminal polyhistidine tag on protein thermal stability, *ACS Omega*, 2018, **3**, 760–768.

239 W. Pan, Y. Wang and N. Wang, A new metal affinity NCTR25 tag as a better alternative to the His-tag for the expression of recombinant fused proteins, *Protein Expr. Purif.*, 2019, **164**, 105477.

240 J. E. Tropea, S. Cherry and D. S. Waugh, Expression and purification of soluble His6-tagged TEV protease, *Methods Mol. Biol.*, 2009, **498**, 297–307.

241 T. D. Parks, K. K. Leuther, E. D. Howard, S. A. Johnston and W. G. Dougherty, *Anal. Biochem.*, 1994, 216, 413–417.

242 J. C. Lewis, Artificial metalloenzymes and metallopeptide catalysts for organic synthesis, *ACS Catal.*, 2013, **3**, 2954–2975.

243 C. Zhang, E. V. Vinogradova, A. M. Spokoyny, S. L. Buchwald and B. L. Pentelute, *Angew. Chemie - Int. Ed.*, 2019, 58, 4810–4839.

244 A. Kumar, S. Mao, N. Dimasi and C. Gao, Design and validation of linkers for site-specific preparation of antibody–drug conjugates carrying multiple drug copies per cysteine conjugation site, *Int. J. Mol. Sci.*, 2020, **21**, 1–11.

245 A. Maruani, M. E. B. Smith, E. Miranda, K. A. Chester, V. Chudasama and S.

Caddick, A plug-and-play approach to antibody-based therapeutics via a chemoselective dual click strategy, *Nat. Commun.*, 2015, **6**, 2–10.

246 R. C. Camacho, S. You, K. E. D'Aquino, W. Li, Y. Wang, J. Gunnet, J. Littrell, J. S. Qi, L. Kang, W. Jian, M. MacDonald, T. Tat, D. Steiner, Y. M. Zhang, J. Lanter, R. Patch, R. Zhang, J. Li, S. Edavettal, W. Edwards, T. Dinh, L. Y. Wang, J. Connor, M. Hunter, E. Chi, R. V. Swanson, J. N. Leonard and M. A. Case, Conjugation of a peptide to an antibody engineered with free cysteines dramatically improves half-life and activity, *MAbs*, 2020, **12**, 11.

247 B. G. Hill, C. Reily, J. Y. Oh, M. S. Johnson and A. Landar, Methods for the determination and quantification of the reactive thiol proteome, *Free Radic. Biol. Med.*, 2009, **47**, 675–683.

248 J. Lan and R. Zenobi, Characterizing the iron loading pattern of ferritin using high-mass matrix-assisted laser desorption ionization mass spectrometry, *Rapid Commun. Mass Spectrom.*, 2019, **33**, 1855–1860.

249 R. Kehm, T. Baldensperger, J. Raupbach and A. Höhn, Protein oxidation - Formation mechanisms, detection and relevance as biomarkers in human diseases, *Redox Biol.*, 2021, **42**, 101901.

250 C. Molinaro, A. Martoriati, L. Pelinski and K. Cailliau, Copper complexes as anticancer agents targeting topoisomerases i and ii, *Cancers (Basel).*, 2020, **12**, 1–26.

251 J. C. García-Ramos, A. G. Gutiérrez, A. Vázquez-Aguirre, Y. Toledano-Magaña, A. L. Alonso-Sáenz, V. Gómez-Vidales, M. Flores-Alamo, C. Mejía and L. Ruiz-Azuara, The mitochondrial apoptotic pathway is induced by Cu(II) antineoplastic compounds (Casiopeínas®) in SK-N-SH neuroblastoma cells after short exposure times, *BioMetals*, 2017, **30**, 43–58.